INVESTIGATION OF LIQUID-VAPOR INTERACTIONS IN A CONSTANT AREA CONDENSING EJECTOR

by

EDWARD KENNETH LEVY

B.S., University of Maryland
(1963)

S.M., Massachusetts Institute of Technology
(1964)

SUBMITTED IN PARTIAL FULFILLMENT

OF THE REQUIREMENTS FOR THE

DEGREE OF DOCTOR OF

SCIENCE

at the

MASSACHUSETTS INSTITUTE OF TECHNOLOGY

June, 1967

Signature of Author ....
Department of Mechanical Engineering
May 26, 1967

Certified by ....
Thesis Supervisor

Accepted by ....
Chairman, Departmental Committee on Graduate Students

INVESTIGATION OF LIQUID-VAPOR INTERACTIONS IN A CONSTANT AREA CONDENSING EJECTOR

by

Edward Kenneth Levy

"Submitted to the Department of Mechanical Engineering on May 26, 1967 in partial fulfillment of the requirement for the degree of Doctor of Science."

ABSTRACT

A detailed investigation of the liquid-vapor interactions occurring within a constant area steam-water condensing ejector is described. Axial static and radial impact pressure profiles were obtained. These data which correspond to a limited range of inlet vapor conditions and a wide range of inlet liquid velocities reveal the presence of three flow regimes based on inlet liquid velocity. Complete condensation caused by a condensation shock is shown to occur only within the High Inlet Liquid Velocity Regime. Evidence is given of the occurrence and importance of liquid jet breakup. It is shown that the presence of supersonic vapor flow is a necessary but not sufficient condition for the existence of the condensation shock.

Two one-dimensional mixing section analyses are described. Digital computer solutions of the analyses are presented which show the effects of interfacial heat transfer and friction on the flow variables. It is shown that the coefficient of heat transfer from the interface to the liquid jet is of the order of 100 BTU/ft^{2}sec°F. This compares favorably with the results of other studies on the heat transfer rates to turbulent water jets with condensation.

Thesis Supervisor: George A. Brown
Title: Associate Professor of Mechanical Engineering

ACKNOWLEDGEMENTS

To the many individuals who contributed in one way or another to this research I give my thanks.

In particular I thank my thesis advisor, Professor George Brown, for the advice and encouragement which he gave me during our two-year association. Professor Brown is not only a stimulating teacher but also a selfless individual. He possesses the characteristics which every thesis student looks for when selecting an advisor. I am very fortunate to have had this opportunity to work with him.

In addition I am grateful to Professor S. William Gouse, Jr., Professor Philip G. Hill and Professor Warren M. Rohsenow for serving as members of my thesis committee, and also to Professor Peter Griffith. The many discussions which I have had with each of these gentlemen were of considerable help to me in my research.

My wife, Nancy, has been an invaluable partner throughout my Doctoral program. She has served as the chief bread-winner of the family, and gave freely of her leisure hours when the time came to type the rough draft of the thesis.

This research was performed through the Department of Mechanical Engineering and the Research Laboratory of Electronics of the Massachusetts Institute of Technology and was sponsored by agencies of the United States Government.

The work was done in part at the Computation Center at the Massachusetts Institute of Technology, Cambridge, Massachusetts.

TABLE OF CONTENTS

LIST OF FIGURES

LIST OF TABLES

NOMENCLATURE

A	cross sectional area
A_w	cross sectional area of duct
F_{LV}	interfacial shear force
F_{VL}	interfacial shear force
F_p	wall pressure force
F_τ	wall shear force
F_w	wall shear force
L_I	influence length
M	vapor Mach number
M_c	critical vapor Mach number
P	pressure; static pressure
P_T	static pressure at mixing section inlet
P_x	static pressure
$P_{\mathbb{C}}$	centerline impact pressure
P_{oy}	vapor impact pressure
P_{ox}	vapor stagnation pressure
P_{impact}	impact pressure
Q_L	interfacial heat transfer rate
R	gas constant
R_w	radius of duct
T	temperature
V	velocity
V_i	interfacial velocity

X_{ml} length of supersonic region

f friction factor

h specific enthalpy

h^o specific stagnation enthalpy

$\hat{h}$ heat transfer coefficient

k ratio of specific heats

m mass flow rate (used synonymously with w)

m_c condensation rate

q vapor quality

r radius

r_L radius of liquid jet

s specific entropy

w mass flow rate (used synonymously with m)

x axial distance from nozzle exit plane

ρ density

τ shear stress

Subscripts

a inlet plane to region of condensation shock

e exit

f saturated liquid

LV; VL at liquid-vapor interface

L liquid

oL	inlet liquid stagnation
og	inlet vapor stagnation
v	vapor

Abbreviations

BPVC	Back pressure valve closed
BPVO	Back pressure valve open
CE	Condensing ejector
OCVA	Overall Control Volume Analysis

CHAPTER I

INTRODUCTION

The investigation described below is that of a one-component two-phase jet pump called a condensing ejector (CE). The CE combines a subcooled liquid stream and a vapor stream producing a liquid stream wiih a stagnation pressure which can be higher than that of either of the two inlet flows.

The CE is composed of a pair of inlet nozzles, a convergent mixing section, a constant area section, and a diffuser (Figure 1). (Although the liquid is shown at the tube centerline in Figure 1, the reverse configuration is possible; i.e., liquid at the wall and vapor at the centeline). The fluid streams are accelerated in the nozzles at the exit planes of which the vapor is at a high temperature and velocity compared to the temperature and velocity of the liquid. The streams are then brought into contact in the mixing section. Due to the large temperature difference and the high relative velocity between the jets, a high rate of heat transfer is established. Vapor condenses onto the liquid stream, and the momentum of the liquid increases accordingly. It has been observed that for certain combinations of inlet conditions it is possible to cause the remaining vapor to condense within a short distance in the constant area section if the back pressure control valve is closed sufficiently. The rapid condensation process which results in a steep rise has been called a condensation shock. (This is not to be confused with the condensation shock associated with the phenomenon of supersaturation in nozzles.) The stream, now completely liquid, flows through the diffuser.

Many applications have been suggested for the CE, including use in liquid-metal MHD power cycles, as condensers in Rankine cycles and in underwater propulsion systems. Liquid metal MHD power cycles require a device which can efficiently convert thermal energy to stagnation pressure at the inlet to the MHD generator. The CE could be such a device (Refs. 6 through 9). The numerous Rankine-cycle space power systems under development require that the working fluid, after leaving the turbine, be condensed to a liquid state. The condenser must operate in a nearly zero gravity environment. This precludes the use of any conventional surface condenser which requires a gravity force to remove the condensate from condensing surfaces. The CE operates independently of gravity, has high condensation rates and hence is compact, and in addition may provide an appreciable pressure rise to circulate the liquid through the remainder of the flow loop. For deep running torpedoes with an open-cycle turbine system, the relatively low gas pressure of the turbine exhaust must be increased somehow to match the relatively higher pressures of the environment. The exhaust gases and sea water could be supplied to a CE to produce the required pressure rise. In this case, the exhaust gases are multicomponent so that mass diffusion phenomena and noncondensable gas components have an important effect on the overall performance of the device.

Over the past decade considerable research effort has been expended toward the development of high performance CE's for the applications mentioned above. Hays (Ref. 1) has obtained pressure performance data using constant area and convergent-divergent condensing ejectors with mercury as the working fluid. His tests were conducted with the liquid at the centerline and the vapor at the wall. Platt (Ref. 2), interested in condenser applications of the CE, obtained pressure and temperature performance data for a steam-water CE with a divergent mixing section. All of his tests were conducted with the steam at the centerline and the liquid at the wall. Kaye and Rivas (Ref. 3) and Brown and Miguel (Refs. 4 and 5) all have been engaged in two-component CE studies with an ultimate goal of applying the CE to underwater propulsion systems.

In addition to the experimental activities described above, several papers have been published which concern themselves with the prediction of overall CE performance. These include Refs. 10, 11, and 12. All of these analyses are similar in that they combine the conservation relations with certain boundary conditions and the requirement that the vapor condenses completely. From this they are able to predict the exit state of the resultant liquid stream. Analyses of this type will be denoted as Overall Control Volume Analyses (OCVA).

At the beginning of the current research program, the author conducted an extensive test program to determine the performance of a particular convergent-divergent, steam-water CE. This device operated with the liquid at the centerline and the vapor at the wall. The convergent annular steam nozzle had a 0.461 ID and a 1.351 OD (See Figure 8); the liquid nozzle diameter was 0.400 inches at the mixing section inlet. The convergent mixing section was tapered from an inlet diameter of 1.351 inches to an exit diameter of 0.626 inches. The ratio of total inlet flow area to total exit area was 5/1 (see Chapter III and Figure 10 for a detailed description of the 5/1 test section). The data from this device are shown in Figure 2. Here P_{oL} is the inlet liquid stagnation pressure, P_{og} the inlet vapor stagnation pressure, and P_{oe} the exit stagnation pressure.

Each of the data was obtained by starting the liquid and vapor flows with the back pressure valve open. The valve was then slowly closed until the pressure rise shown in Figure 1 was positioned as far forward as possible within the constant area section. The data were obtained at inlet vapor stagnation pressures from 19.6 to 48.5 psia. It appears that within this range of inlet vapor pressures, the pressure performance of the device is independent of vapor stagnation pressure. Note also that over the entire range of inlet pressure ratios tested the exit stagnation pressure is greater than both the inlet vapor stagnation pressure and the inlet liquid stagnation pressure. The device can operate as a pump!

Curve A is the theoretical pressure performance obtained from the Overall Control Volume Analysis (OCVA) (see Chapter II and Ref. 10). This curve was calculated by assuming that complete condensation occurred, that the wall friction force was negligible, and the wall pressure force was the same as that which would have occurred if the static pressure in the convergent section had been constant. (It was necessary to make these assumptions about the wall forces because the actual forces were not determined experimentally. More recent experiments, Chapter IV, suggest that the forces which were assumed for the calculations were too high.)

In the range $P_{og}/P_{oL} > 1.25$ the data were approximately 8% above curve A. This discrepancy is due to overestimation of the wall forces in the theoretical calculations. In general, the agreement between the theory and data is quite good in this range. However in the range $0 < P_{oL}/P_{og} < 1.25$, the measured exit pressure ratio decreased sharply with decreasing inlet stagnation pressure ratio. At $P_{og}/P_{oL} = 0.85$, the data were 30% below the predicted values.

It is clear from the data above that the OCVA predicts quite well the pressure performance of the device over a wide range of inlet pressure ratios. However, it is also clear that at low inlet pressure ratios, the OCVA does not adequately describe the flow. (It will be shown in Chapter IV that at low values of P_{og}/P_{oL} the assumption that complete condensation occurs is invalid.) From Eqs. 1 and 3 in Chapter II it is seen also that although the OCVA does indicate the performance which one would expect for a given mixing section contraction ratio and nozzle inlet flow area ratio, it does not furnish information on what shape the mixing section walls should have or how long the constant area section should be. These, after all, are related to the rate processes occurring within the device; the OCVA ignores such phenomena. It would appear then that the individual interested in designing a high performance CE needs more information than the OCVA can supply. This is especially true of operations at low inlet pressure ratios.

The present study is a detailed analytical and experimental investigation of the liquid-vapor interactions occurring within the mixing section region. To simplify the problem somewhat the study was limited to flows in constant area mixing sections. Detailed axial and radial profiles were obtained of the flows, and in addition visual observations of the flows were made.

The goal of the research was to study over a limited range of inlet vapor conditions the effect of variations of inlet liquid velocity on the behavior of the liquid and vapor streams and on the overall performance of the device. It was also intended to determine whether liquid jet breakup is a significant factor and to obtain clues to the nature of the condensation shock and to the conditions which are necessary for the existence of the shock.

In addition, it was intended to develop a mixing section analysis based on the one-dimensional rod-annulus model and to determine how well such a model describes the real flow. Throughout the entire research program efforts were made to uncover as many of the existing CE problem areas as possible. It was felt that the definition of such potential areas of future research would be useful at this stage of CE development.

Two earlier investigations have dealt with the CE liquid-vapor interaction problem. Ref. 13 is an experimental study in which radial and axial profiles were obtained from a central steam jet and an annular water jet. At its outer surface, the water stream, a free jet, was not confined by solid walls. Because of the difference in test conditions, boundary conditions, and geometrical configuration, the results of Ref. 13 are not directly applicable to the CE which is presently being studied. Ref. 14 is an analytical study of the interactions occurring between a central liquid jet and a concentric annular gas stream confined in a duct. This study is similar to the mixing section analyses which are presented in Chapter II.

CHAPTER II

ANALYSES OF THE CONDENSING EJECTOR

In this section, three analyses of the CE are described. The first, the Overall Control Volume Analysis (OCVA), is used to predict the overall performance of the device. The conservation equations are combined with the appropriate boundary conditions and the requirement that the vapor condenses completely. Using these relations the exit state of the resultant liquid stream can be determined. Unlike the OCVA, the two remaining analyses, the slug and shear model analyses, take into account the rate processes occurring between the interacting liquid and vapor streams. They can be used to provide detailed axial profiles of the liquid and vapor states.

Overall Control Volume Analysis (OCVA)

Consider a duct of arbitrary cross sectional area and the control volume pictured in Figure 3 . A vapor and its subcooled liquid enter the control volume through surface "a"; it is desired to calculate the static pressure, temperature, and velocity at "e" assuming that the vapor condenses completely in the region from "a" to "e". It is to be noted that the analysis applies regardless of whether "a" and "e" are separated by an infinitesimal or finite distance.

Assumptions

(1) State "e" is that of a subcooled or saturated liquid.

(2) The flow is steady.

(3) For purposes of calculation of mass, momentum, and enthalpy fluxes, the liquid and vapor streams at "a" are each one-dimensional and are characterized by the bulk values of velocity and temperature. The same is true of the liquid flow at "e".

(4) The static pressures at "a" and "e" do not vary across the duct and are denoted as P_a and P_e.

(5) The liquid is incompressible. $\therefore$ $\rho_a = \rho_e \equiv \rho_L$

(6) The total flow is adiabatic; there is no heat transferred through the duct walls.

Continuity requires that

$$\rho_L V_L A_L + \rho_v V_v A_v = \rho_L V_e A_e$$

or

$$m_L + m_v = m_e \quad .$$

Solving for the exit velocity, this becomes

$$V_e = \frac{m_L + m_v}{\rho_L A_e} \tag{1}$$

The momentum equation in the axial direction yields

$$\rho_L V_e^2 A_e - \rho_v V_v^2 A_v - \rho_L V_L^2 A_L = p_a A_a - p_e A_e + F_p - F_\tau \tag{2}$$

Here F_p and F_τ are the axial components of the wall pressure force and the wall shear force which act on the control volume. Solving for the exit static pressure and combining Eqs. 1 and 2, there results the relation

$$p_e = \frac{m_v V_v + m_L V_L}{A_e} - \frac{(m_L + m_v)^2}{\rho_L A_e^2} + \frac{F_p - F_\tau}{A_e} + p_a \frac{A_a}{A_e} \tag{3}$$

For a given geometry, if all the conditions at "a" are known and if the value of the term $\frac{F_p - F_\tau}{A_e}$ can be determined, then Equations 1 and 3 are easily solved for the exit velocity and exit static pressure. The exit enthalpy is obtained from the first law of thermodynamics which for adiabatic flow requires that

$$h_e = \left(\frac{1}{w_L + w_v}\right)\left[w_L\left(h_L + \frac{V_L^2}{2}\right) + w_v\left(h_v + \frac{V_v^2}{2}\right)\right] - \frac{V_e^2}{2} \tag{4}$$

To determine whether the calculated single phase liquid exit state is a possible end state two additional conditions must be satisfied.

(1) The specific static enthalpy of the liquid at "e" must be less than or equal to the enthalpy of saturated liquid at the exit pressure P_e.

$$h_e \leq h_f \tag{5}$$

(2) The second law of thermodynamics must be satisfied.

$$(m_L + m_v)\, s_e \geq m_L s_L + m_v s_v \tag{6}$$

Brown (Ref. 10) in a generalized treatment of the overall control volume problem assumed that the wall shear forces are negligible and that the wall pressure force is equal to the force which would act if the static pressure in the condensation region ("a" to "e") were constant.

That is, $F_t = 0$ and $F_p = P_a(A_e - A_a)$.

With these assumptions Eq. 3 becomes

$$p_e = \frac{m_v V_v + m_L V_L}{A_e} - \frac{(m_L + m_v)^2}{\rho_L A_e^2} + p_a \tag{7}$$

In the constant area case, Eq. 3 reduces to

$$p_e = \frac{m_v V_v + m_L V_L}{A} - \frac{(m_L + m_v)^2}{\rho_L A^2} - \frac{F_\tau}{A} + p_a \tag{8}$$

In this case F_τ is the only force acting at the wall of the device.

This analysis is used for the predictions shown in Figures 2 and 50.

Analysis of the Liquid Vapor Interactions

Consider a two-phase liquid-vapor flow in a cylindrical duct. The liquid flows axially at the duct centerline with the shape of a rod; the vapor flows axially in the annular region between the liquid and the duct wall. The vapor which is saturated or slightly super-heated condenses at the surface of the subcooled liquid jet.

For the rod-annulus flow described above, it is possible to form a number of models all of which exhibit various features of the real flow, and to write a consistent set of equations for each one. (Ref. 14 the treatment of a multicomponent two-phase rod-annulus flow is an example of such an analysis). Two models are considered here. The first is that of a one-dimensional slug flow. It handles the difficult problem of modeling the interfacial velocity and the interfacial drag force by assuming the condensate enters the liquid control volume with the tangential velocity of the vapor and by setting the interfacial shear force equal to zero. The second, a quasi-one-dimensional analysis, permits the interfacial velocity to have a value between the bulk velocity of the liquid and that of the vapor. In addition it provides for a non-zero interfacial shear force.

<u>One-Dimensional Rod Annulus Flow - Slug Flow Model</u>

Three control volumes are pictured in Figure 4 with the corresponding terms which enter into the continuity, momentum and energy equations. The liquid control volume, I, of length dx, has been drawn to the middle of the infinitesimally thin vapor interface. On one side of the control surface there exists only the liquid phase and on the other side, only vapor. The annular vapor control volume, II, extends from the interface to the tube wall. The third control volume, III, is infinitesimally thin and encloses those regions on both sides of the liquid vapor interface.

Assumptions

1. Within both the liquid and vapor regions the velocity and temperature profiles are one-dimensional with the characteristic values of velocity and temperature given by V_V, V_L, T_V, and T_L.

2. The static pressure varies with axial distance only. At any x, the static pressure is uniform from wall to wall.

3. The flow is steady.

4. The liquid is incompressible.

5. The flow is cylindrically symmetrical; the liquid jet is a smooth cylindrical jet which can change radius with axial distance. Atomization and liquid jet breakup do not occur.

6. The condensate crosses the liquid vapor interface with a tangential velocity equal to the local vapor velocity.

7. The wall shear force F_W acts on the vapor control volume but the drag term at the liquid vapor interface is assumed to be zero.

8. The vapor is saturated or slightly superheated. The temperature at the liquid-vapor interface is equal to the saturation temperature corresponding to the local static pressure. Heat transfer from the vapor to the liquid-vapor interface is negligible.

9. The total flow is adiabatic; heat transfer through the outer wall is negligible.

10. Axial heat conduction is negligible.

Continuity requires that

$$\rho_L \, d \left(V_L A_L \right) = m_c \tag{9}$$

and

$$d \left(\rho_v V_v A_v \right) = - m_c \tag{10}$$

Here m_c is the amount of condensate which crosses the liquid vapor interface from x to x + dx per unit time. The area terms A_L and A_v are given by

$$A_L = \pi \, r_L^2 \tag{11}$$

and

$$A_v = \pi \left(R_w^2 - r_L^2 \right) \tag{12}$$

The axial momentum equations for the liquid and vapor control volumes become

$$\rho_L \, d \left(V_L^2 A_L \right) + A_L \, dp = m_c V_v \tag{13}$$

and

$$d \left(\rho_v V_v^2 A_v \right) + A_v \, dp = - m_c V_v - F_w \tag{14}$$

The term F_w is the axial component of the wall shear force acting from x to x + dx. This is of the form

$$F_w = 2\pi R_w \, dx \, \tau_w \tag{15}$$

where τ_w is the wall shear stress.

In addition the first law of thermodynamics requires that

$$\rho_L d\left(V_L A_L\left[h_L + \frac{V_L^2}{2}\right]\right) = m_c\left(h_v + \frac{V_v^2}{2}\right) \tag{16}$$

and

$$d\left(\rho_v V_v A_v\left[h_v + \frac{V_v^2}{2}\right]\right) = -m_c\left[h_v + \frac{V_v^2}{2}\right] \tag{17}$$

The vapor energy equation (Eq. 17) can also be written as

$$m_v\, d\left(h_v + \frac{V_v^2}{2}\right) = 0 \tag{18}$$

This indicates that that vapor which does not condense in the region from x to x + dx undergoes an adiabatic change of state. Equations 9 through 17 coupled with equations of state for the vapor and liquid phases

$$h_v = h_v(\rho_v, p) \tag{19a}$$

$$h_L = h_L(T_L) \tag{19b}$$

and the geometrical relation

$$dA_w = dA_v + dA_L \tag{20}$$

form an independent set of equations from which the nine variables dV_L, dh_L, dT_L, dA_L, dV_v, dh_v, $d\rho_v$, dA_v, and dP can be determined. This is true, provided that dA_w, m_c and F_w have been specified. Note that Eq. 20 reduces to $dA_v + dA_L = 0$ for the case of flow in a constant area duct.

The third control volume (Figure 4d) is used to relate the condensation flux m_c to the heat transfer coefficient $\hat{h}$ defined by Eq. 22. An energy balance for the third control volume requires that

$$Q_L = m_c \left(h_v - h_L + \frac{V_v^2 - V_L^2}{2} \right) \tag{21}$$

The term Q_L is the heat transfer rate from the liquid-vapor interface to the liquid core within the region from x to x + dx. The heat transfer coefficient is thus defined by

$$\hat{h} = \frac{Q_L}{2\pi r_L \, dx \left(T_{sat} - T_L \right)} \tag{22}$$

<u>Method of Solution - Constant Area Duct</u>

For flow in a constant area duct, Eqs. 9 through 20 can be rearranged to the following forms:

$$C_{12} \, d\rho_v + C_{13} \, dp = \gamma_1 \tag{23}$$

$$C_{22} \, dp + C_{23} \, dh_L = \gamma_2 \tag{24}$$

$$C_{32} \, d\rho_v + C_{33} \, dh_v + C_{34} \, dp = \gamma_3 \tag{25}$$

$$h_v = h_v (\rho_v , p) \tag{26a}$$

$$h_L = h_L (T_L) \tag{26b}$$

$$dA_L = \frac{\beta_1 - b_{13} \, dp}{b_{11}} \tag{27}$$

$$dA_v = - dA_L \tag{28}$$

$$dV_L = \frac{\alpha_1 - a_{11} \, dA_L}{a_{13}} \tag{29}$$

$$d\,V_v = \frac{\alpha_2 - a_{21}\,dA_L - a_{25}\,d\rho_v}{a_{24}} \tag{30}$$

Here the quantities a_{ij}, b_{ij}, c_{ij}, γ_k, β_k, and α_k are given by the following expressions.

$$C_{12} = -A_v V_v^2$$

$$C_{13} = A_v + A_L \frac{\rho_v V_v^2}{\rho_L V_L^2}$$

$$C_{22} = -A_L V_L$$

$$C_{23} = \rho_L A_L V_L$$

$$C_{32} = -A_v V_v^3$$

$$C_{33} = \rho_v A_v V_v$$

$$C_{34} = A_L \frac{\rho_v}{\rho_L} \frac{V_v^3}{V_L^2}$$

$$a_{11} = \rho_L V_L$$

$$a_{13} = \rho_L A_L$$

$$a_{21} = -\rho_v V_v$$

$$a_{25} = A_v V_v$$

$$a_{24} = \rho_v A_v$$

$$b_{13} = A_L$$

$$b_{11} = -\rho_L V_L^2$$

$$\alpha_1 = m_c$$

$$\alpha_2 = -m_c$$

$$\beta_1 = m_c \left(V_v - 2 V_L \right)$$

$$\gamma_1 = -F_w + m_c V_v + m_c \frac{\rho_v V_v^2}{\rho_L V_L^2} \left(V_v - 2V_L \right)$$

$$\gamma_2 = m_c \left[h_v - h_L + \frac{\left(V_v - V_L \right)^2}{2} \right]$$

$$\gamma_3 = m_c \left[\frac{V_v^2}{2} + \left(V_v - 2V_L \right) \frac{\rho_v V_v^3}{\rho_L V_L^2} \right]$$

Vapor Equation of State

At this point additional steps cannot be taken without more specific information on the vapor equation of state. The two cases described below were those treated during the present investigation.

1. The vapor is superheated with its equilibrium state defined by the independent variables static pressure and vapor temperature. Here $\rho_v = \rho_v(p,T_v)$ and $h_v = h_v(p,T_v)$. These relations are available in both equation and tabular form in Ref. 15.

2. The vapor is saturated with its equilibrium state defined by the two independent variables static pressure and mass quality. The mass quality q is defined as the ratio of vapor mass flow to the total mass flow in an equilibrium mixture. In this case

$$\rho_v = \rho_v\,(p\,,\,q) \qquad \text{and} \qquad h_v = h_v\,(p,q)$$

Superheated Vapor

Equations 23 through 26 can be manipulated further and arranged into the following forms.

$$C_{12}\,\rho_v(p,T_v)_{x+dx} + C_{13}\,p_{x+dx} = \gamma_1 - C_{12}\,\rho_{v_x} - C_{13}\,p_x \tag{31}$$

$$C_{22}\,p_{x+dx} + C_{23}\,h_L(T_L)_{x+dx} = \gamma_2 - C_{22}\,p_x - C_{23}\,h_{L_x} \tag{32}$$

$$C_{32}\,\rho_v\,(p\,,T_v)_{x+dx} + C_{33}\,h_v\,(p,T_v)_{x+dx} + C_{43}\,p_{x+dx}$$
$$= \gamma_3 - C_{32}\,\rho_{v_x} - C_{33}\,h_{v_x} - C_{34}\,p_x \tag{33}$$

$$h_v = h_v\,(p\,,T_v) \qquad \text{and} \qquad \rho_v = \rho_v\,(p\,,T_v) \tag{34}$$

Hence Equations 31, 33, and 34 can be solved by iteration for the values of p, T_v, h_v, and ρ_v at x + dx. These then can be substituted into Equations 32, 26b, 27, 28, 29, and 30 to determine h_L, T_L, A_L, A_v, V_L and V_v at x + dx.

Saturated Vapor

Equations 23 through 26 become

$$C_{12}\,\rho_v\,(p\,,q)_{x+dx} + C_{13}\,p_{x+dx} = \gamma_1 - C_{12}\,\rho_{vx} - C_{13}\,p_x \tag{35}$$

$$C_{22}\,p_{x+dx} + C_{23}\,h_L\,(T_L)_{x+dx} = \gamma_2 - C_{22}\,p_x - C_{23}\,h_{L\,x} \tag{36}$$

$$C_{32}\, \rho_v(p,q)_{x+dx} + C_{33}\, h_v(p,q)_{x+dx} + C_{43}\, p_{x+dx} = \gamma_3 - C_{32}\, \rho_{vx} - C_{33}\, h_{vx} - C_{43}\, p_x \tag{37}$$

$$h_v = h_v(p,q) \qquad \text{and} \qquad \rho_v = \rho_v(p,q) \tag{38}$$

Equations 35, 37, and 38 are easily solved for the values of p, q, h_v, and ρ_v at x + dx and then h_L, T_L, A_L, V_L and V_v at x + dx are determined as before.

Boundary Conditions

At the mixing section inlet (x = 0) all of the conditions required to initiate a "marching" solution of the type described above are available. This then formed the starting point for all of the solutions which will be presented in Chapter 5. Some difficulty was encountered in selecting the proper value of vapor velocity used to initiate the calculations. As will be demonstrated later in this chapter, the rod model requires that the vapor be supersonic in order that it be accelerated to higher values of Mach number. For this reason it was found necessary to initiate the calculations with vapor Mach numbers slightly greater than unity.

Digital Computer Solutions

A computer program for use on an IBM 7090 digital computer was written to solve the mixing section Equations 27 through 30, 31 through 34, and 35 through 38. The state equations for the liquid and vapor phases taken from Ref. 15 were written in the form of subprograms which were used in conjunction with the main mixing section program. The actual details of the computer programs are not included in this report. Such information may be obtained by contacting the author or his thesis advisor, Professor George Brown.

Formulation of the Perfect Gas - Slug Model Equations

The final form of the conservation equations is much easier to interpret if it is assumed that the vapor is a perfect gas. These equations are rederived below using the perfect gas law as the vapor equation of state. It is to be noted that the effect of variations in total flow area are included in this development. The restriction of a constant area test section does not apply here.

As before, the liquid continuity and axial momentum equations are

$$\rho_L (A_L \, dV_L + V_L \, dA_L) = m_c \tag{39}$$

and

$$\frac{dP}{P} = -\frac{\rho_L V_L \, dV_L}{P} - \frac{m_c}{W_L} \frac{\rho_L (V_L^2 - V_L V_v)}{P} \tag{40}$$

The elimination of $\frac{dV_L}{V_L}$ from Eqs. 39 and 40 results in

$$\frac{dP}{P} = \frac{\rho_L V_L^2}{P} \frac{dA_L}{A_L} + \frac{\rho_L V_L^2}{P} \left(\frac{V_v}{V_L} - 2 \right) \frac{m_c}{W_L} \tag{41}$$

The vapor equation of state is

$$\frac{dP}{P} = \frac{dT_v}{T_v} + \frac{d\rho_v}{\rho_v} \tag{42}$$

The vapor Mach number is defined as

$$M \equiv \frac{V_v}{\sqrt{k R T_v}} \tag{43}$$

where k is the ratio of specific heats and R the gas constant.

Equation 43 can also be expressed in the form

$$\frac{dV_v^2}{V_v^2} = \frac{dM^2}{M^2} + \frac{dT_v}{T_v} \tag{44}$$

Vapor continuity requires that

$$\frac{dV_v}{V_v} + \frac{dA_v}{A_v} + \frac{d\rho_v}{\rho_v} = -\frac{m_c}{w_v} \tag{45}$$

The vapor axial momentum equation becomes

$$-\frac{dP}{P} = \frac{F_w}{PA_v} + kM^2 \frac{dV_v^2}{2V_v^2} \tag{46}$$

For the vapor, the first law requires that

$$\frac{M^2(k-1)}{2} \frac{dV_v^2}{V_v^2} + \frac{dT_v}{T_v} = 0 \tag{47}$$

Eliminating $\frac{dT_v}{T_v}$ from Eqs. 42 and 44 and then equating the density term to that in Eq. 45 one obtains

$$\frac{dM^2}{M^2} = \frac{dV_v^2}{2V_v^2} - \frac{m_c}{w_v} - \frac{dA_v}{A_v} - \frac{dP}{P} \tag{48}$$

Combining Eqs. 44 and 47, one obtains

$$\frac{dM^2}{M^2} = \left[1 + \frac{M^2}{2}(k-1)\right] \frac{dV_v^2}{V_v^2} \tag{49}$$

Combining Eqs. 48 and 49, one obtains

$$\left[\frac{1}{2} + \frac{M^2}{2}(k-1)\right]\frac{dV_v^2}{V_v^2} = -\frac{m_c}{w_v} - \frac{dA_v}{A_v} - \frac{dP}{P} \tag{50}$$

and then combining this with Eq. 46 one obtains

$$\frac{(M^2-1)}{kM^2}\frac{dP}{P} = \frac{1+M^2(k-1)}{kM^2}\frac{F_w}{pA_v} - \frac{m_c}{w_v} - \frac{dA_v}{A_v} \tag{51}$$

But $\quad A_L + A_v = A_w$

or

$$dA_L + dA_v = dA_w \tag{52}$$

or

$$-\frac{dA_v}{A_v} = \frac{dA_L}{A_L}\frac{A_L}{A_v} - \frac{dA_w}{A_w}\frac{A_w}{A_v} \tag{53}$$

Hence Eq. 51 becomes

$$\left(\frac{A_L}{A_v}\right)\frac{dA_L}{A_L} = \left(\frac{A_w}{A_v}\right)\frac{dA_w}{A_w} + \frac{m_c}{w_v} - \frac{(1+M^2(k-1))}{kM^2}\frac{F_w}{pA_v} + \frac{(M^2-1)}{kM^2}\frac{dp}{p} \tag{54}$$

From Eq. 41

$$\frac{dA_L}{A_L} = \frac{P}{\rho_L V_L^2}\frac{dP}{p} - \left(\frac{V_v}{V_L} - 2\right)\frac{m_c}{w_L}$$

Combining this with Eq. 54 and rearranging terms

$$\frac{dP}{p} = \left\{\frac{1}{\frac{kpM^2}{\rho_L V_L^2}\frac{A_L}{A_v} - (M^2-1)}\right\}\left\{\left[kM^2\frac{A_w}{A_v}\right]\frac{dA_w}{A_w} + \left[kM^2\left(1+\left(\frac{V_v}{V_L}-2\right)\frac{A_L}{A_v}\frac{W_v}{W_L}\right)\right]\frac{m_c}{w_v} - \left[(1+M^2(k-1))\right]\frac{F_w}{pA_v}\right\} \tag{55}$$

Combining Eqs. 51 and 55 and solving for $\dfrac{dA_v}{A_v}$

$$\begin{aligned}\frac{dA_v}{A_v} = &\left\{\frac{1}{\frac{k p M^2}{\rho_L V_L^2}\frac{A_L}{A_v} - (M^2-1)}\right\}\left\{-\left[(M^2-1)\frac{A_w}{A_v}\right]\frac{dA_w}{A_w} - \left[\frac{k p M^2}{\rho_L V_L^2}\frac{A_L}{A_v}\right.\right.\\ &\left.\left. + (M^2-1)\left(\frac{V_v}{V_L}-2\right)\frac{A_L}{A_v}\frac{w_v}{w_L}\right]\frac{m_c}{w_v} + \left[\frac{p}{\rho_L V_L^2}\frac{A_L}{A_v}\left(1+M^2(k-1)\right)\right]\frac{F_w}{pA_v}\right\}\end{aligned} \tag{56}$$

Similarly it can be shown that

$$\begin{aligned}\frac{dA_L}{A_L} = &\left\{\frac{1}{\frac{k p M^2}{\rho_L V_L^2}\frac{A_L}{A_v} - (M^2-1)}\right\}\left\{\left[\frac{k p M^2}{\rho_L V_L^2}\frac{A_w}{A_v}\right]\frac{dA_w}{A_w} + \left[\frac{k p M^2}{\rho_L V_L^2}\right.\right.\\ &\left.\left. + (M^2-1)\left(\frac{V_v}{V_L}-2\right)\frac{w_v}{w_L}\right]\frac{m_c}{w_v} - \left[\frac{p}{\rho_L V_L^2}\left(1+M^2(k-1)\right)\right]\frac{F_w}{pA_v}\right\}\end{aligned} \tag{57}$$

$$\begin{aligned}\frac{1}{2}\frac{dV_v^2}{V_v^2} = &\left\{\frac{1}{\frac{k p M^2}{\rho_L V_L^2}\frac{A_L}{A_v} - (M^2-1)}\right\}\left\{-\left[\frac{A_w}{A_v}\right]\frac{dA_w}{A_w} - \left[1 + \left(\frac{V_v}{V_L}-2\right)\frac{A_L}{A_v}\frac{w_v}{w_L}\right]\frac{m_c}{w_v}\right.\\ &\left. + \left[1 - \frac{p}{\rho_L V_L^2}\frac{A_L}{A_v}\right]\frac{F_w}{pA_v}\right\}\end{aligned} \tag{58}$$

$$\begin{aligned}\frac{dT_v}{T_v} = &\left\{\frac{M^2(k-1)}{\frac{k p M^2}{\rho_L V_L^2}\frac{A_L}{A_v} - (M^2-1)}\right\}\left\{+\left[\frac{A_w}{A_v}\right]\frac{dA_w}{A_w} + \left[\left(1 + \left(\frac{V_v}{V_L}-2\right)\frac{A_L}{A_v}\frac{w_v}{w_L}\right)\right]\frac{m_c}{w_v}\right.\\ &\left. - \left[1 - \frac{p}{\rho_L V_L^2}\frac{A_L}{A_v}\right]\frac{F_w}{pA_v}\right\}\end{aligned} \tag{59}$$

$$\frac{dM^2}{M^2} = \left\{ \frac{2\left[1+\frac{M^2}{2}(k-1)\right]}{\frac{kpM^2}{\rho_L V_L^2}\frac{A_L}{A_v} - (M^2-1)} \right\} \left\{ -\left[\frac{A_w}{A_v}\right]\frac{dA_w}{A_w} - \left[1+\left(\frac{V_v}{V_L}-2\right)\frac{A_L w_v}{A_v w_L}\right]\frac{m_c}{w_v} \right.$$

$$\left. + \left[1 - \frac{p}{\rho_L V_L^2}\frac{A_L}{A_v}\right]\frac{F_w}{p A_v} \right\} \qquad (60)$$

$$\frac{d\rho_v}{\rho_v} = \left\{ \frac{1}{\frac{kpM^2 A_L}{\rho_L V_L^2 A_v} - (M^2-1)} \right\} \left\{ \left[M^2\frac{A_w}{A_v}\right]\frac{dA_w}{A_w} + \left[M^2\left(1+\left(\frac{V_v}{V_L}-2\right)\frac{A_L}{A_v}\frac{w_v}{w_L}\right)\right] \right. \qquad (61)$$

$$\left. - \left[1 + \frac{pM^2}{\rho_L V_L^2}(k-1)\frac{A_L}{A_v}\right]\frac{F_w}{pA_v} \right\}$$

For the vapor the isentropic stagnation pressure is given by

$$\frac{dP_{ov}}{P_{ov}} = \frac{dP}{P} + \frac{\frac{kM^2}{2}}{1+\frac{k-1}{2}M^2}\frac{dM^2}{M^2} \qquad (62)$$

This reduces to

$$\frac{dP_{ov}}{P_{ov}} = -\frac{F_w}{pA_v} \qquad (63)$$

Also

$$\frac{1}{2}\frac{dV_L^2}{V_L^2} = \left\{ \frac{1}{\frac{kpM^2}{\rho_L V_L^2}\frac{A_L}{A_v} - (M^2-1)} \right\} \left\{ -\left[\frac{kpM^2}{\rho_L V_L^2}\frac{A_w}{A_v}\right]\frac{dA_w}{A_w} + \left[\frac{p}{\rho_L V_L^2}\left(1+M^2(k-1)\right)\right]\frac{F}{p} \right. \qquad (64)$$

$$\left. + \left[\frac{kpM^2}{\rho_L V_L^2}\left(\frac{w_v}{w_L}\frac{A_L}{A_v}-1\right) - (M^2-1)\frac{w_v}{w_L}\left(\frac{V_v}{V_L}-1\right)\right]\frac{m_c}{w_v} \right\}$$

Properties of the Equations

Equations 55 through 64 very clearly illustrate the features which are built into the rod-annulus slug-flow model. All of the dependent variables except for dP_{ov} are influenced by a change in total flow area $\frac{dA_w}{A_w}$, by the condensation rate $\frac{m_c}{w_v}$, and by the wall shear term $\frac{F_w}{PA_v}$. The vapor stagnation pressure $\frac{dP_{ov}}{P_{ov}}$ is a function of wall shear only. In addition all of the relations except for the dP_{ov} term have the quantity $\frac{kpM^2}{\rho_L V_L^2}\frac{A_L}{A_v} - (M^2 - 1)$ appearing in the denominator.

For the regions of interest in this investigation the expressions for $\frac{dp}{p}$ and $\frac{dM^2}{M^2}$ can be approximated by the following expressions. (Similar simplifications would follow for the other dependent variables.)

$$\frac{dP}{P} \sim \left\{\frac{1}{\frac{kpM^2}{\rho_L V_L^2}\frac{A_L}{A_v} - (M^2-1)}\right\}\left\{\left[kM^2\frac{A_w}{A_v}\right]\frac{dA_w}{A_w} + \left[kM^2\right]\frac{m_c}{w_v} - \left[1 + M^2(k-1)\right]\frac{F_w}{PA_v}\right\} \tag{65}$$

$$\frac{dM^2}{M^2} \sim \left\{\frac{2\left[1+\frac{M^2}{2}(k-1)\right]}{\frac{kpM^2A_L}{\rho_L V_L^2 A_v} - (M^2-1)}\right\}\left\{-\left[\frac{A_w}{A_v}\right]\frac{dA_w}{A_w} - \frac{m_c}{w_v} + \frac{F_w}{PA_v}\right\} \tag{66}$$

These equations are of the form

$$\frac{dP}{P} \sim \left\{\frac{1}{\frac{kpM^2A_L}{\rho_L V_L^2 A_v} - (M^2-1)}\right\}\left\{a_{11}\frac{dA_w}{A_w} + a_{12}\frac{m_c}{w_v} - a_{13}\frac{F_w}{PA_v}\right\} \tag{67}$$

and

$$\frac{dM^2}{M^2} \sim \left\{ \frac{1}{\frac{kpM^2}{\rho_L V_L^2}\frac{A_L}{A_v} - (M^2-1)} \right\} \left\{ -a_{21}\frac{dA_w}{A_w} - a_{22}\frac{m_c}{w_v} + a_{23}\frac{F_w}{pA_v} \right\} \tag{68}$$

where a_{ij} is positive. In addition, $\frac{F_w}{pA_v} > 0$ and for condensation, $\frac{m_c}{w_v} > 0$.

There are several possible cases depending on the value of the denominator D. (Note: $D \equiv \frac{kpM^2}{\rho_L V_L^2} \frac{A_L}{A_v} - (M^2 - 1)$).

Case (i): $M < 1$

Here $D > 0$ and Eqs. 67 and 68 are of the form

$$\frac{dP}{P} \sim \left\{ b_{11}\frac{dA_w}{A_w} + b_{12}\frac{m_c}{w_v} - b_{13}\frac{F_w}{pA_v} \right\} \tag{69}$$

$$\frac{dM^2}{M^2} \sim \left\{ -b_{21}\frac{dA_w}{A_w} - b_{22}\frac{m_c}{w_v} + b_{23}\frac{F_w}{pA_v} \right\} \tag{70}$$

where b_{ij} is positive.

This case is similar to that of one-dimensional single-phase subsonic gas flow in a duct. An area increase increases the static pressure and decreases the Mach number; mass ejection (as with condensation) increases the pressure and decreases the Mach number; and the wall shear force decreases the pressure and increases the Mach number

Case (ii): $M = 1$

The conclusions are the same as for case (i). (Note that unlike single-phase gas flow in a duct, the rod-annulus slug flow model permits the vapor Mach number to attain a value of unity without requiring that the denominator be zero).

Case (iii): $M > 1$ and $\dfrac{kpM^2}{\rho_L V_L^2} \dfrac{A_L}{A_v} > (M^2 - 1)$

The conclusions are the same as for case (i).

Case (iv): $M > 1$ and $\dfrac{kpM^2}{\rho_L V_L^2} \dfrac{A_L}{A_v} = (M^2 - 1)$

Here $D = 0$. In general the numerators of Eqs. 67 and 68 are non-zero. Hence the derivatives dp/p and dM^2/M^2 are equal to infinity. Since physically this cannot occur, it would appear that the equations derived for the slug flow do not represent the actual situation when $D = 0$.

Case (v): $M > 1$ and $\dfrac{kpM^2}{\rho_L V_L^2} \dfrac{A_L}{A_v} < (M^2 - 1)$

Here $D < 0$ and Eqs. 67 and 68 are of the form

$$\frac{dp}{p} \sim \left\{ -b_{11} \frac{dA_w}{A_w} - b_{12} \frac{m_c}{w_v} + b_{13} \frac{F_w}{pA_v} \right\} \quad (71)$$

$$\frac{dM^2}{M^2} \sim \left\{ +b_{21} \frac{dA_w}{A_w} + b_{22} \frac{m_c}{w_v} - b_{13} \frac{F_w}{pA_v} \right\} \quad (72)$$

where b_{ij} is positive.

This case is similar to that of one-dimensional single-phase supersonic gas flow in a duct. An area increase decreases the static pressure and increases the Mach number; mass ejection decreases the static pressure and increases the Mach number; and the wall shear force increases the pressure and decreases the Mach number.

One-Dimensional Rod-Annulus Flow - Shear Flow Model

The control volumes are pictured in Figure 5 with the corresponding terms which enter into the continuity, momentum, and energy equations. The liquid control volume, of length dx, has been drawn inside of the liquid-vapor interface. The vapor control volume extends from the liquid side of the liquid-vapor interface to the tube wall. A third control volume (Figure 5e) extends from a vapor streamline near the liquid vapor interface to the liquid side of the liquid vapor interface.

Figure 5b shows the velocity and temperature profiles in the vicinity of the liquid-vapor interface.

Assumptions

(1) For purposes of calculation of mass, momentum, and enthalpy fluxes, the liquid and vapor streams are one-dimensional with the characteristic values of velocity and temperature given by V_v, V_L, T_v, and T_L.

(2) The axial component of velocity at the liquid vapor

interface is V_i; the condensate crosses the interface with the velocity V_i.

(3) The static pressure varies with axial distance only. At any x, the static pressure is uniform from wall to wall. (Radial pressure drop calculations indicate that this is a reasonable assumption.)

(4) The liquid is incompressible.

(5) The flow is steady.

(6) The flow is cylindrically symmetrical; the liquid jet is a smooth cylindrical jet which can change radius with axial distance.

(7) The vapor is saturated or slightly superheated. The temperature at the liquid-vapor interface is equal to the local saturation temperature. Heat transfer from the vapor to the liquid-vapor interface is negligible.

(8) The total flow is adiabatic.

(9) Axial heat conduction is negligible.

Continuity requires that

$$\rho_L \, d \left(V_L A_L \right) = m_c \tag{73}$$

and

$$d \left(\rho_v V_v A_v \right) = - m_c \tag{74}$$

Here m_c is the amount of condensate which crosses the liquid-vapor interface from x to x + dx per unit time. The area terms A_L and A_V

are given by

$$A_L = \pi r_L^2 \tag{75}$$

and

$$A_V = \pi \left(R_w^2 - r_L^2 \right) \tag{76}$$

The axial momentum equations become

$$\rho_L \, d\left(V_L^2 A_L\right) + A_L \, dp = m_c V_i + F_{LV} \tag{77}$$

$$d\left(\rho_V V_V^2 A_V\right) + A_V \, dp = - m_c V_i - F_{LV} - F_w \tag{78}$$

The term F_w is the axial component of the wall shear force acting from x to x + dx; F_{LV} is the axial component of the interfacial shear term. These are of the form

$$F_w = 2\pi R_w \, dx \, \tau_w \tag{79}$$

$$F_{LV} = 2\pi r_L \, dx \, \tau_{LV} \tag{80}$$

The first law of thermodynamics requires that

$$\rho_L \, d\left(V_L A_L \left(h_L + \frac{V_L^2}{2}\right)\right) = Q_L + W_k + m_c\left(h_f + \frac{V_i^2}{2}\right) \tag{81}$$

and

$$d\left(\rho_V V_V A_V \left(h_V + \frac{V_V^2}{2}\right)\right) = - Q_L - W_k - m_c\left(h_f + \frac{V_i^2}{2}\right) \tag{82}$$

The term W_k is the interfacial shear work. This is

$$W_k = \left| F_{Lv} V_i \right| \tag{83}$$

Equations 73 through 78, 81 and 82 coupled with equations of state for the vapor and liquid phases

$$h_v = h_v(\rho_v, p) \tag{84}$$

$$h_L = h_L(T_L) \tag{85}$$

and the geometrical relation

$$dA_w = dA_v + dA_L \tag{86}$$

form an independent set of equations from which the nine variables dV_L, dh_L, dT_L, dA_L, dV_v, dh_v, $d\rho_v$, dA_v, and dp can be determined. This is true provided that m_c, F_w, Vi, F_{Lv}, Q_L, dA_w, and W_k are specified.

The term Q_L represents the heat transfer rate from the liquid-vapor interface to the liquid core. This is related to the condensation flux by means of the energy balance for the control volume drawn around the interface region (Figure 5e); that is

$$Q_L + W_k = m_c \left(h_v - h_f + \frac{V_v^2 - V_i^2}{2} \right) \tag{87}$$

After some manipulation the liquid and vapor energy equations become

$$\rho_L \, d\left(V_L A_L \left(h_L + \frac{V_L^2}{2}\right)\right) = m_c \left(h_v + \frac{V_v^2}{2}\right) \tag{88}$$

and

$$d\left(h_v + \frac{V_v^2}{2}\right) = 0 \tag{89}$$

Equation 89 requires that the vapor which does not condense within the distance x to x + dx undergo an adiabatic change of state. The heat transfer term can be used to define a condensation heat transfer coefficient; that is,

$$\hat{h} \equiv \frac{Q_L}{2\pi r_L \, dx \left(T_{sat} - T_L\right)} \tag{90}$$

The interfacial velocity V_i can be determined by considering an infinitesimally thin control volume drawn around the liquid-vapor interface. (See Figure 5f). The condensate enters and leaves the control volume with the tangential velocity V_i. F_{vL} is the shear force acting on the vapor side of the interface and F_{Lv} is the force on the liquid side. Hence momentum considerations require that

$$\tau_{vL} = \tau_{Lv} \tag{91}$$

Defining the force coefficients f_{vL} and f_{Lv} as

$$f_{vL} \equiv \frac{\tau_{vL}}{\frac{\rho_v}{2}\left(V_v - V_i\right)^2} \tag{92a}$$

and

$$f_{Lv} \equiv \frac{\tau_{Lv}}{\frac{\rho_L}{2}\left(V_i - V_L\right)^2} \tag{92b}$$

combining Eqs. 91, 92a and 92b, and solving for V_i one obtains

$$V_i = \frac{V_v + \sqrt{\frac{f_{Lv}\,\rho_L}{f_{vL}\,\rho_v}}\; V_L}{1 + \sqrt{\frac{f_{Lv}\,\rho_L}{f_{vL}\,\rho_v}}} \tag{93}$$

Defined in this manner, V_i is a function of the liquid and vapor densities and velocities and of the two unknown force coefficients f_{vL} and f_{Lv}. (In the absence of condensation, if the liquid-vapor interface were an infinitesimally thin wall, then f_{vL} and f_{Lv} would be the same as the conventional Fanning friction factors for flow past a smooth wall.)

If $\frac{f_{Lv}}{f_{vL}} \sim 1$, then Eq. 93 reduces to

$$V_i = \frac{V_v + \sqrt{\frac{\rho_L}{\rho_v}}\; V_L}{1 + \sqrt{\frac{\rho_L}{\rho_v}}} \tag{94}$$

Method of Solution

The shear model equations were solved in the same manner as the slug model equations (See page 16). The same boundary conditions were utilized and as with the slug flow equations, a computer program, written for use on an IBM 7090 digital computer, was utilized in conjunction with the exact vapor equations of state to determine the axial profiles of the liquid and vapor states.

Formulation of the Perfect Gas Shear Model Equations

As was the case with the slug model equations, the shear model equations are greatly simplified if the vapor is a perfect gas.

The liquid continuity and axial momentum relations are

$$\rho_L \left(A_L \, dV_L + V_L \, dA_L \right) = m_c \tag{95}$$

and

$$\frac{dP}{P} = -\frac{\rho_L V_L \, dV_L}{P} - \frac{m_c}{w_L} \frac{\rho_L \left(V_L^2 - V_L V_i \right)}{P} + \frac{F_{LV}}{P \, A_L} \tag{96}$$

The elimination of $\frac{dV_L}{V_L}$ from Eq. 95 and 96 results in

$$\frac{dP}{P} = \frac{\rho_L V_L^2}{P} \frac{dA_L}{A_L} + \frac{\rho_L V_L^2}{P} \left(\frac{V_i}{V_L} - 2 \right) \frac{m_c}{w_L} + \frac{F_{LV}}{P A_L} \tag{97}$$

The vapor equation of state is

$$\frac{dP}{P} = \frac{dT_v}{T_v} + \frac{d\rho_v}{\rho_v} \tag{98}$$

The vapor Mach number is defined as

$$M \equiv \frac{V_v}{\sqrt{k R T_v}} \tag{99}$$

Equation 99 can also be expressed in the form

$$\frac{dV_v^2}{V_v^2} = \frac{dM^2}{M^2} + \frac{dT_v}{T_v} \tag{99a}$$

Vapor continuity requires that

$$\frac{dV_v}{V_v} + \frac{dA_v}{A_v} + \frac{d\rho_v}{\rho_v} = -\frac{m_c}{w_v} \tag{100}$$

The vapor axial momentum equation becomes

$$-\frac{dP}{P} = \frac{F_w}{PA_v} + \frac{F_{Lv}}{PA_v} + \frac{kM^2}{2}\frac{dV_v^2}{V_v^2} + kM^2\left(\frac{V_i}{V_v} - 1\right)\frac{m_c}{w_v} \tag{101}$$

For the vapor, the first law requires that

$$\frac{dT_v}{T_v} + \frac{M^2}{2}(k-1)\frac{dV_v^2}{V_v^2} = 0 \tag{102}$$

In operations similar to those performed with the slug model equations, Eqs. 95 through 102 can be manipulated and rearranged to the following forms.

$$\frac{dP}{P} = \left\{\frac{kM^2}{\frac{kPM^2}{\rho_L V_L^2}\frac{A_L}{A_v} - (M^2-1)}\right\}\left\{\left[\frac{A_w}{A_v}\right]\frac{dA_w}{A_w} - \left[\frac{1+M^2(k-1)}{kM^2}\right]\frac{F_w}{PA_v} - \left[\frac{1+M^2(k-1)}{kM^2} - \frac{P}{\rho_L V_L^2}\right]\frac{F_{Lv}}{PA_v} + \left[1 + \left(\frac{V_i}{V_L} - 2\right)\frac{w_v}{w_L}\frac{A_L}{A_v} - \left(\frac{V_i}{V_v} - 1\right)\left(1 + M^2(k-1)\right)\right]\frac{m_c}{w_v}\right\} \tag{103}$$

$$\frac{dA_v}{A_v} = \left\{\frac{1}{\frac{kPM^2}{\rho_L V_L^2}\frac{A_L}{A_v} - (M^2-1)}\right\}\left\{\left[1-M^2\right]\frac{A_w}{A_v}\frac{dA_w}{A_w} + \left[\left(1+M^2(k-1)\right)\frac{P}{\rho_L V_L^2}\frac{A_L}{A_v}\right]\frac{F_w}{PA_v}\right.$$

$$+\left[\frac{P}{\rho_L V_L^2}\left(1-M^2+\left[1+M^2(k-1)\right]\frac{A_L}{A_v}\right]\frac{F_{Lv}}{PA_v} + \left[(1-M^2)\left(\frac{V_i}{V_L}-2\right)\frac{w_v}{w_L}\frac{A_L}{A_v}\right.$$

$$\left. + \left\{\frac{V_i}{V_v}-1\right\}\left\{1+M^2(k-1)\right\}\frac{PkM^2}{\rho_L V_L^2}\frac{A_L}{A_v} - \frac{PkM^2}{\rho_L V_L^2}\frac{A_L}{A_v}\right]\frac{m_c}{w_v}\right\} \tag{104}$$

$$\frac{1}{2}\frac{dV_v^2}{V_v^2} = \left\{\frac{1}{\frac{PkM^2}{\rho_L V_L^2}\frac{A_L}{A_v} - (M^2-1)}\right\}\left\{-\left[\frac{A_w}{A_v}\right]\frac{dA_w}{A_w} + \left[1-\frac{P}{\rho_L V_L^2}\frac{A_L}{A_v}\right]\frac{F_w}{PA_v}\right.$$

$$+\left[1-\frac{P}{\rho_L V_L^2}\frac{A_L}{A_v} - \frac{P}{\rho_L V_L^2}\right]\frac{F_{Lv}}{PA_v} - \left[1+\left(\frac{V_i}{V_L}-2\right)\left(\frac{w_v}{w_L}\frac{A_L}{A_v}\right)\right.$$

$$\left. - \left(\frac{V_i}{V_v}-1\right)\left(kM^2\right)\left(1-\frac{P}{\rho_L V_L^2}\frac{A_L}{A_v}\right)\right]\frac{m_c}{w_v}\right\}$$

(105)

$$\frac{dM^2}{M^2} = \left\{\frac{2+M^2(k-1)}{\frac{PkM^2}{\rho_L V_L^2}\frac{A_L}{A_v} - (M^2-1)}\right\}\left\{-\left[\frac{A_w}{A_v}\right]\frac{dA_w}{A_w} + \left[1-\frac{P}{\rho_L V_L^2}\frac{A_L}{A_v}\right]\frac{F_w}{PA_v}\right.$$

$$+\left[1-\frac{P}{\rho_L V_L^2}\frac{A_L}{A_v} - \frac{P}{\rho_L V_L^2}\right]\frac{F_{Lv}}{PA_v} - \left[1+\left(\frac{V_i}{V_L}-2\right)\left(\frac{w_v}{w_L}\frac{A_L}{A_v}\right)\right.$$

$$\left. - \left(\frac{V_i}{V_v}-1\right)\left(kM^2\right)\left(1-\frac{P}{\rho_L V_L^2}\frac{A_L}{A_v}\right)\right]\frac{m_c}{w_v}\right\}$$

(106)

$$
\begin{aligned}
\frac{d\rho_v}{\rho_v} = & \left\{ \frac{1}{\dfrac{PkM^2}{\rho_L V_L^2}\dfrac{A_L}{A_v} - (M^2-1)} \right\} \left\{ \left[M^2 \frac{A_w}{A_v} \right] \frac{dA_w}{A_w} - \left[1 + M^2(k-1)\frac{P}{\rho_L V_L^2}\frac{A_L}{A_v} \right] \frac{F_w}{PA_v} \right. \\
& - \left[1 - \frac{PM^2}{\rho_L V_L^2}\left(k - M^2(k-1)\left(1 + \frac{A_L}{A_v}\right)\right)\right] \frac{F_{Lv}}{PA_v} + \left[M^2 \left(1 + \left(\frac{V_i}{V_L} - 2\right) \frac{w_v}{w_L}\frac{A_L}{A_v} \right. \right. \\
& \left. \left. \left. - \left(\frac{V_i}{V_v} - 1\right)(k)\left(1 + M^2(k-1)\frac{P}{\rho_L V_L^2}\frac{A_L}{A_v}\right)\right)\right] \frac{m_c}{w_v} \right\}
\end{aligned}
\tag{107}
$$

$$
\begin{aligned}
\frac{dT_v}{T_v} = & \left\{ \frac{M^2(k-1)}{\dfrac{PkM^2}{\rho_L V_L^2}\dfrac{A_L}{A_v} - (M^2-1)} \right\} \left\{ \left[\frac{A_w}{A_v} \right] \frac{dA_w}{A_w} - \left[1 - \frac{P}{\rho_L V_L^2}\frac{A_L}{A_v} \right] \frac{F_w}{PA_v} \right. \\
& - \left[1 - \frac{PM^2}{\rho_L V_L^2}\left(1 + \frac{A_L}{A_v}\right)\right] \frac{F_{Lv}}{PA_v} + \left[1 + \left(\frac{V_i}{V_L} - 2\right) \frac{w_v}{w_L}\frac{A_L}{A_v} \right. \\
& \left. \left. - kM^2\left(\frac{V_i}{V_v} - 1\right)\left(1 - \frac{P}{\rho_L V_L^2}\frac{A_L}{A_v}\right)\right] \frac{m_c}{w_v} \right\}
\end{aligned}
\tag{108}
$$

$$
\frac{dP_{0v}}{P_{0v}} = -\frac{(F_w + F_{Lv})}{PA_v} + kM^2\left(1 - \frac{V_i}{V_v}\right)\frac{m_c}{w_v}
\tag{109}
$$

Properties of the Shear Model Equations

All of the dependent variables except for dP_{ov} are influenced by a change in total flow area $\frac{dA_w}{A_w}$, by the condensation rate $\frac{m_c}{w_v}$, by the wall shear term $\frac{F_w}{PA_v}$, and by the interfacial shear term $\frac{F_{Lv}}{PA_v}$. The vapor stagnation pressure $\frac{dP_{ov}}{P_{ov}}$ is independent of the area terms. In addition, all of the equations except for the dP_{ov} relation have the quantity $[\frac{kPM^2}{\rho_L V_L^2} \frac{A_L}{A_v} - (M^2 - 1)]$ appearing in the denominator.

For the regions of interest in this investigation the expressions for $\frac{dP}{P}$ and $\frac{dM^2}{M^2}$ can be approximated by the following expressions. (As before, similar simplifications would follow for the other dependent variables.)

$$\frac{dP}{P} \sim \left\{\frac{k M^2}{\frac{kPM^2 A_L}{\rho_L V_L^2 A_v} - (M^2-1)}\right\}\left\{\left[\frac{A_w}{A_v}\right]\frac{dA_w}{A_w} - \left[\frac{1+M^2(k-1)}{kM^2}\right]\frac{F_w+F_{Lv}}{PA_v} + \left[1+\left(1-\frac{V_i}{V_v}\right)\left(1+M^2(k-1)\right)\right]\frac{m_c}{w_v}\right\} \tag{110}$$

$$\frac{dM^2}{M^2} \sim \left\{\frac{2+M^2(k-1)}{\frac{kPM^2 A_L}{\rho_L V_L^2 A_v} - (M^2-1)}\right\}\left\{-\left[\frac{A_w}{A_v}\right]\frac{dA_w}{A_w} + [1]\frac{F_w+F_{Lv}}{PA_v} - \left[1+\left(1-\frac{V_i}{V_v}\right)kM^2\right]\frac{m_c}{w_v}\right\} \tag{111}$$

But $V_i/V_v \leq 1$; therefore Eqs. 110 and 111 are of the form

$$\frac{dP}{P} \sim \left\{\frac{1}{\frac{kPM^2 A_L}{\rho_L V_L^2 A_v} - (M^2-1)}\right\}\left\{a_{11}\frac{dA_w}{A_w} - a_{12}\frac{F_w+F_{Lv}}{PA_v} + a_{13}\frac{m_c}{w_v}\right\} \tag{112}$$

$$\frac{dM^2}{M^2} \sim \left\{ \frac{1}{\frac{kPM^2 A_L}{\rho_L V_L^2 A_v} - (M^2-1)} \right\} \left\{ - a_{21} \frac{dA_w}{A_w} + a_{22} \frac{F_w + F_{Lv}}{PA_v} - a_{23} \frac{m_c}{w_v} \right\} \tag{113}$$

where a_{ij} is positive.

In addition, $\frac{F_w + F_{Lv}}{PA_v} > 0$ and for condensation, $\frac{m_c}{w_v} > 0$.

As was true for the slug model, there are several possible cases depending on the value of the denominator D, $(D \equiv \frac{PkM^2}{\rho_L V_L^2} \frac{A_L}{A_v} - (M^2-1))$

<u>Case</u> (i): $M < 1$

Here $D > 0$ and Eqs. 112 and 113 are of the form

$$\frac{dP}{P} \sim \left\{ b_{11} \frac{dA_w}{A_w} - b_{12} \frac{F_w + F_{Lv}}{PA_v} + b_{13} \frac{m_c}{w_v} \right\} \tag{114}$$

$$\frac{dM^2}{M^2} \sim \left\{ - b_{21} \frac{dA_w}{A_w} + b_{22} \frac{F_w + F_{Lv}}{PA_v} - b_{23} \frac{m_c}{w_v} \right\} \tag{115}$$

where b_{ij} is positive.

This case is similar to that of one-dimensional single-phase subsonic gas flow in a duct. An area increase increases the static pressure and decreases the Mach number; mass ejection (as with condensation) increases the pressure and decreases the Mach number, and the shear forces decrease the pressure and increase the Mach number.

Case (ii): $M = 1$

The conclusions are the same as for Case (i). (Note that unlike single-phase gas flow in a duct, the rod-annulus shear model permits the vapor Mach number to attain a value of unity without requiring that the denominator be zero.

Case (iii): $M > 1$ and $\frac{kpM^2}{\rho_L V_L{}^2} \frac{A_L}{A_V} > (M^2 - 1)$

The conclusions are the same as for case (i).

Case (iv): $M > 1$ and $\frac{kpM^2}{\rho_L V_L{}^2} \frac{A_L}{A_V} = (M^2 - 1)$

Here $D = 0$. In general the numerators of Eqs. 112 and 113 are non-zero. Hence the derivatives $\frac{dp}{p}$ and $\frac{dM^2}{M^2}$ are equal to infinity.

Case (v): $M > 1$ and $\frac{kpM^2}{\rho_L V_L{}^2} \frac{A_L}{A_v} < (M^2 - 1)$

Here $D < 0$ and Eqs. 112 and 113 are of the form

$$\frac{dP}{P} \sim \left\{ -b_{11} \frac{dA_w}{A_w} + b_{12} \frac{F_w + F_{Lv}}{pA_v} - b_{13} \frac{m_c}{w_v} \right\} \tag{116}$$

and

$$\frac{dM^2}{M^2} \sim \left\{ b_{21} \frac{dA_w}{A_w} - b_{22} \frac{F_w + F_{Lv}}{pA_v} + b_{33} \frac{m_c}{w_v} \right\} \tag{117}$$

where b_{ij} is positive.

This case is similar to that of one-dimensional single-phase supersonic gas flow in a duct. An area increase decreases the static pressure and increases the Mach number; mass ejection decreases the static pressure and increases the Mach number; and the shear terms increase the static pressure and decrease the Mach number.

Comparison of the Slug and Shear Models

As might be expected, the two flow models discussed above are quite similar in many respects. Both models require the vapor phase to undergo adiabatic changes of state. In neither case does the flow choke at a vapor Mach number of unity but instead the equations "blow up" when the Mach number attains the critical value given by

$$\frac{M_c^2 - 1}{M_c^2} = \frac{k_e P}{\rho_L V_L^2} \frac{A_L}{A_V} \tag{118}$$

With both models the effect of friction forces is to cause the vapor Mach number to go towards the critical value; on the other hand, the condensation process causes the Mach number to go away from the critical value. With both models frictional effects cause the vapor isentropic stagnation pressure to decrease; the shear model allows the vapor stagnation pressure to increase with the condensation flux m_c/w_v.

As stated earlier there are also basic differences between the two models; the slug model demands that the condensate cross the liquid-vapor interface with a tangential velocity equal to the local vapor velocity and in addition does not permit shear forces to act at the interface. Herein lies the main weakness of the slug model. Consider, for example, the isothermal rod-annulus flow of a low speed liquid jet and a high speed subsonic noncondensable gas stream in a constant area duct. In this case condensation does not occur. According to the slug model equations, the liquid velocity will increase under the influence of the wall shear force only. Physical intuition suggests, however, that the shear force acting at the gas-liquid interface will have a much greater effect on the liquid jet velocity than the wall shear force. The slug model is unable to account for such interfacial forces.

The shear model, on the other hand, does admit the existence of interfacial shear forces. It requires, however, a detailed knowledge of the velocity profile at the interface; and herein lies the main weakness of the shear model. In a real flow the interface is not a smooth cylindrical surface but instead a complicated two-phase region. To attempt to define an interface velocity for such a confused region is indeed a difficult task!

It is not obvious at this stage of CE research which is the better flow model. Some will argue that under the circumstances the slug model is the one which should be used while others will argue just the opposite. It is believed by the author that both models have something to offer: the slug model is simple and uncluttered while the shear model accounts for certain phenomena which the former cannot. For this reason computer calculations have been made using both. These will be presented in detail in Chapter V .

CHAPTER III

EXPERIMENTAL APPARATUS

The steam-water condensing ejector test facility pictured schematically in Figure 6 is composed of three main units: the stagnation chamber, the liquid and vapor nozzles, and the test section.

Stagnation Chamber

The stagnation chamber (Figure 7) is a 7 inch diameter, 12 inch long section of stainless steel pipe capped on both ends with face plates held together by a series of tie rods. Water enters through the 1 inch diameter hole in the rear face plate, flows through the duct located on the chamber axis and is then accelerated in the water nozzle attached to the end of the duct. The water duct has a double wall construction with thermal insulation packed in the annular space between the walls to minimize heat transfer between the steam and water. The four positioning rods are used to give the water duct rigidity and to aid in the centering of the liquid nozzle. Steam enters symmetrically through the two 2 inch holes normal to the axis of the chamber, flows axially along the exterior of the water duct and is accelerated in the annular nozzle before entering the test section. For a more complete description of the stagnation chamber and a commentary on some of the decisions and factors which affected the ultimate design, see Reference 16.

Nozzles

Two sets of brass liquid-vapor nozzles were used during the course of the experimental program.

Nozzles LN 1 - VN 1. At its exit plane, liquid nozzle LN 1 (Figure 8) has a 0.400 inch ID and a 0.461 inch OD. This nozzle is bolted to the end of the 1 inch water duct. The inner wall of the convergent annular vapor flow passage is formed by the outer surface of LN 1 and the outer wall of the vapor flow passage by VN 1. Nozzle VN 1 is bolted to the front face plate of the stagnation tank. This pair of nozzles was designed so that the position of minimum area of the vapor flow passage would occur at the nozzle exit plane. The ratio of vapor flow area to liquid flow area at this point is 11/1.

Nozzles LN 2 - VN 2. Liquid nozzle LN 2 (Figure 9) is similar in design to LN 1 but has instead a 0.441 inch ID and a 0.461 inch OD. As before the outer surface of the liquid nozzle forms the inner wall of the annular vapor flow passage; the outer wall is formed by VN 2. The outer diameter of the annular passage at the exit plane is 1.351 inch. To facilitate static pressure measurements near the geometric throat (nozzle exit plane) the section VN 2 and the test section TS3 were machined as one unit. As before the nozzles were designed so that the position of minimum area of the vapor flow passage would occur at the nozzle exit plane. The flow area ratio at the geometric throat for this pair of nozzles is 8.3/1.

Test Sections

Three test sections were used during the test program. All test sections were positioned with their axes in the horizontal plane.

Test Section TS1. Test section TS1 includes a convergent section, a constant area section, and a diffuser. The convergent section has an inlet diameter of 1.351 inches, an exit diameter of 0.626 inches, and a half angle of convergence of 2.26°. The ratio of the inlet flow area to the exit flow area is 5/1. The 0.626 inch constant area section is approximately 7 inches long and the diffuser has a half angle of divergence of 6°. The test section has a total length of 23.37 inches. (See Figure 10). The three parts of the convergent-divergent test section are held together with "screw on" flanges. This test section was used with nozzles LN1 and VN1. All parts of the convergent-divergent test section were fabricated from free machining brass.

Test Section TS2. Test section TS2, a 17-3/4 in. long constant-area section (1.351 ID) was fabricated from Emerson and Cuming Stycast 1269A epoxy resin. This material, a high temperature (400°F), colorless, transparent plastic is somewhat comparable to plexiglass in appearance. It was originally cast in the form of an annular slug (1.351 ID) and was then machined to the shape shown in Figure 11. This material is quite brittle and tends to change its dimensions with time. However, despite these disadvantages, it was found that if sufficient care was taken, the material was satisfactory for low-pressure visual flow tests. Test section TS2 was used with nozzles LN 1 and VN 1 and a brass 2°38' half angle diffuser.

Test Section TS3. Due to the limited strength of the Stycast tube a brass constant-area test section (TS3) was fabricated. Section TS3 and vapor nozzle VN 2 were machined as one integral unit (see Figure 9). This test section has a 1.351 ID and is 17-3/4 in. long. This is also used with the 2°38' half angle diffuser.

Additional Equipment

Water Pump

A modified Worthington centrifugal pump was used to raise the inlet water pressure to the desired operating level.

Back Pressure Valve

A forged steel 2 inch Jenkins Globe Valve provided back pressure control. This valve was located downstream of the test section and was separated from the test section by a 4-1/2 ft. length of 2 inch pipe.

Steam Superheaters

The steam available from the M.I.T. steam supply was saturated at approximately 200 psia. Flow-through electrical resistance heaters (9 KW total) were used to superheat the steam and thus permit accurate mass flow measurements to be made at the steam orifice plate. In addition these superheaters gave some flexibility in selecting the operating state of the vapor at the mixing section inlet.

Instrumentation

Flow Measurement

The flow rates of the inlet steam and water were determined by use of sharp-edge orifice plates with standard ASME flange pressure taps. ASME orifice flow coefficients were used to calculate the steam mass flow rates (Ref. 17). The steam density upstream of the orifice was obtained by measuring the pressure and temperature of the steam.

The water orifice plate was calibrated with a weigh tank and stop-watch.

Temperature Measurement

Thermocouples were used to measure the following quantities:

1. Bulk temperature of the steam upstream of the orifice plate
2. Inlet water temperature
3. Bulk temperature of the steam in the stagnation chamber
4. Bulk temperature of the flow in the diffuser downstream of the mixing section.

All four units were Conax Company Iron Constantan thermocouples enclosed in Magnesium Oxide insulation and stainless steel sheaths. Each was inserted radially into the flow from the wall through standard 1/8 inch Conax pressure fittings. A Model 8690 Leeds and

Northrup Potentiometer was used for signal display. This has a maximum uncertainty of ± 25 microvolts which corresponds to approximately ± 1°F over the temperature range of interest. The cold junction was an ice bath.

Pressure Measurement

Helicoid Bourdon tube test gauges were used for all pressure measurements.

The following quantities obtained from wall static pressure taps were measured during all experimental runs:

(i) The stagnation pressure of the steam upstream of the orifice plate (P_{STM})

(ii) The stagnation pressure of the steam in the stagnation tank (P_{og})

(iii) The stagnation pressure of the liquid upstream of the liquid nozzle

All other pressure measurements were made within the annular steam nozzle and the test section. For this reason, during any given run the type and location of the pressure measurements made were a function of the particular nozzles and mixing section in use at that time.

Test Section TS 1. Wall static pressure taps were located at various axial distances from the nozzle exit plane within the mixing section, constant area section, and the diffuser (see Table I). These taps were spiraled to eliminate the effects of flow asymmetries on static pressure profiles. No means were provided for impact pressure measurement.

Test Section TS 2. Wall static pressure taps were located at various axial distances from the nozzle exit plane. These taps were spiraled (Table II). In addition eleven ports were machined into the test section into which impact pressure probes were inserted. These probes could be traversed radially across the flow (Table II).

Test Section TS 3 and Vapor Nozzle VN 2. Wall static pressure taps were located within the annular vapor nozzle and also downstream within the constant area section (Table III). Eleven ports were provided within the constant area section for impact pressure probes (Table III).

In order that asymmetries in the flow could be detected by the probe traverses, the probe ports were located in such a way that both horizontal and vertical traverses of the flow could be made. The probes at x = 0.33, 3, 7 and 9 inches were positioned horizontally and those at x = 1 and 5 inches vertically. To minimize the effects of probe deflection on the radial profiles, the probes were used in diametrically opposite pairs. For example, at x = 1 inch, the top probe was traversed from the top wall radially to the mixing section centerline and the bottom probe from the bottom wall radially to the mixing section centerline. The sole exception to this was the probe at x = 0.33 inches which was used alone.

A convention was adopted for identification of the various impact probes by standing beside the test section and facing the downstream direction. The horizontal probes entering through the left wall are denoted as "Left" probes and those entering through the right wall as "Right" probes. Similarly, the vertical probes were denoted as "Top" and "Bottom" probes.

Liquid nozzles LN 1 and LN 2 and vapor nozzle VN 1 were fabricated without provisions for radial or axial pressure measurements.

Probe Construction

The impact probes were fabricated from 19 gauge (.0425 inch OD - .027 inch ID) stainless steel hypodermic needle tubing (see Figure 12). To increase the rigidity and strength of the probes the 19 gauge section was enclosed in a shorter length of 16 gauge (.065 OD - .047 ID) tubing and the two sections soldered together. The tubes were bent through a 90 degree turn with a radius of 1/4 inch. The probes were inserted into the mixing section through Swagelok tube-fittings. A 1-1/2 inch long section of 1/4 inch OD teflon rod formed the pressure seal between the Swagelok fitting and the impact probe. This seal was found to be loose enough to permit the probe to be easily traversed from one wall to the other and also tight enough to contain pressure differences up to 20 psi. This was found to be adequate for the operating pressures at which tests were conducted. The brass sleeve with the set screw was included to maintain the probe at any particular depth of immersion. At a given immersion depth the distance y between the top of the brass sleeve and the mark on the indicator was used as a measure of the radial position of the probe tip. The value of y with the probe positioned against the opposite wall was used as the reference depth.

Interpretation of Probe Measurements

With the probe tip immersed in a single-phase liquid region there was no difficulty in interpreting the resultant pressure signal. In this case the impact pressure was equal to the liquid stagnation pressure so that the local liquid velocity could be determined from the Bernoulli equation.

Within the vapor region, data reduction became slightly more involved for here compressibility effects had to be considered. In the range of static pressures and temperatures at which impact pressure measurements were made, steam behaves as a perfect gas with the ratio of specific heats equal to 1.32 (Ref. 15). For those cases in which the vapor was subsonic, the isentropic flow tables were used to calculate the vapor Mach number. For those cases in which the vapor was supersonic, the one-dimensional normal shock relations were used for evaluating the Mach number upstream of the probe tip.

An effect which should be considered when interpreting the vapor impact readings is the influence of liquid droplets on the impact pressure measurements. It has been assumed that the probe tip was situated outside the region which encloses those droplets which originated at the liquid jet surface. Atomized particles are not of concern here. Instead the droplets which were nucleated as the steam crossed the saturation line and achieved an equilibrium two-phase saturated vapor state will be considered. The reader is referred to Appendix A for a complete treatment of this problem.

Contrary to those measurements in the single-phase liquid or in the equilibrium vapor regions, the impact probe readings obtained from the two-phase region which separates the liquid and vapor regions were almost completely beyond interpretation. In most instances the two-phase impact pressure signals were extremely unsteady with high frequency oscillations with amplitudes greater than 50% of the mean pressure signal. A fluidic RC filter was used to remove the high frequency pressure fluctuations: the resultant steady-state pressure signal is that which appears in this report (e.g. see Figures 16 and 23). All that can be said of data obtained from the two-phase regions is that they indicate the presence of such unsteady flow regimes. No conclusions as to the local values of the average two-phase flow velocity or the two-phase stagnation pressure can be made.

Probe Calibration

A continuity check was made in three separate runs by using the impact pressure profiles at x = 1 inch. The velocity profiles within the liquid core were determined (e.g. see Figure 18) and from these the liquid flow rates were calculated. It was assumed that within the 1 inch axial distance, condensation of the vapor on to the liquid jet and erosion of the liquid jet surface by atomization did not significantly alter the liquid flow rate in the core region. The probe liquid flow rates calculated by this method differed from those determined from the orifice plate measurements by 1.66%, 8.6% and 5.17% for the three runs. The diameters of the impact probes were approximately 10% of the liquid jet diameters in a typical run. This alone would cause an uncertainty in the probe liquid flow rate of at least ± 10%. Hence the calculated differences in mass flow are well within the expected limits of experimental uncertainty.

P_{og}, P_{oL}, and the Nozzle Discharge Coefficients

The values of the vapor stagnation pressure measured upstream of the vapor nozzle were greater than those obtained from the impact probes just downstream of the nozzle. Similarly the liquid stagnation pressures measured upstream of the liquid nozzle were greater than those measured downstream at the mixing section inlet. Liquid nozzle discharge coefficients were determined by exhausting the liquid jet to the atmosphere. The resultant liquid discharge coefficients were in the range of 0.90 to 0.96. These values account for the observed liquid nozzle pressure losses. Calculations indicate that the vapor nozzle losses are accounted for by a vapor discharge coefficient of approximately 0.98.

All values of liquid stagnation pressure presented with the data in Chapter IV were obtained from the relation

$$P_{oL} = \frac{\rho_L V_L^2}{2} + P_T$$

where V_L is the inlet liquid velocity obtained from the mass flow measurement and P_T is the static pressure at the nozzle exit plane. The values of vapor stagnation pressure presented with the data in Chapter IV were those measured in the vapor stagnation chamber.

Hence, P_{oL} reflects the true value of the inlet liquid stagnation pressure while P_{og} is the inlet vapor stagnation pressure plus the pressure loss which occurred in the vapor nozzle.

CHAPTER IV

EXPERIMENTAL RESULTS

With the steam-water flow loop described above, the capability existed for obtaining considerable information on the dynamics of interacting liquid and vapor streams. With the wall static pressure taps located along the length of the mixing section and with the pitot probes which were used to obtain radial profiles of impact pressure, it became possible to monitor closely the radial and axial behavior of the liquid and vapor streams over the permissible range of inlet conditions. The simultaneous use of a transparent test section permitted a visual observation of the flow and aided greatly in the identification of the various flow regimes. The results of these measurements will be described in detail below.

However, before going deeply into the results, it is necessary to explain the effect on the flow of opening or closing the downstream back pressure valve. Figure 13 is a plot of several axial static pressure distributions. Curve A was obtained with the back pressure valve open as much as possible. The static pressure was 14.75 psia 0.247 inches upstream of the mixing section inlet. It dropped to a value of 11.70 psia at $x = 0$, the geometric throat of the convergent vapor nozzle and the water nozzle exit plane, and then dropped to a minimum of 2.50 psia after coming into contact with the subcooled liquid jet. Figure 14a schematically shows what the flow looked like when viewed through the walls of the transparent mixing section. Curves B through G (Figure 13) show the static pressure profiles obtained with the same inlet conditions as "A" but with the downstream valve closed by varying amounts. Curve H is the static pressure which one would expect if the vapor stream were completely condensed (see Chapter II). Note that the static pressure of "G" followed the same course as "A" up to x = 1 inch but then deviated significantly from the "A" profile. Note also that "G" was relatively flat past x = 9 inches. Figure 14b shows schematically what Run G looked like when viewed through the transparent test section. Upstream of the pressure rise the flow was a two-phase rod-annulus flow. Within the region of rising pressure the flow appeared as a milky or frothy mixture, and downstream of the pressure rise the flow appeared to be a single-phase liquid stream. This is in sharp contrast to the appearance of the flow in Run A in which the liquid and vapor jets maintained their stratified nature throughout the entire length of the mixing section. Hence by regulating the valve downstream of the mixing section it was possible to significantly alter the character of the flow in the test section. For purposes of discussion, data which are obtained with the downstream valve open as much as possible will be referred to as "Back Pressure Valve Open" Data (BPVO) and data obtained with the valve partially closed (but open sufficiently to permit the liquid and vapor streams to flow) will be labeled "Back Pressure Valve Closed" Data (BPVC).

"Back Pressure Valve Open" Data (BPVO)

As a working device the condensing ejector, of course, must function with a high back pressure or equivalently with the back pressure valve closed; for as it has already been pointed out, it is only when such conditions exist that the device will produce a high-pressure, single-phase liquid exit stream. However, in order to learn something of the behavior of the interacting liquid and vapor streams it was felt that a significant portion of the program should be devoted to that particular mode of operation which exists when the downstream valve is open. It was hoped that such a study would furnish clues which might help to answer some of the questions which were posed in Chapter I .

Figure 15, a plot of wall static pressure ratio, P_x/P_{og}, versus axial distance from the nozzle exit plane, shows the effect of inlet liquid velocity on the static pressure profiles. These data were obtained with the inlet vapor conditions set at P_{og} = 22.5 psia and $T_{og} \cong 335°F$. The inlet liquid temperature was constant at T_{liq} = 40°F and the inlet liquid velocity was permitted to vary from a low of 32.0 fps in Run I to a high of 116 fps in Run A. For all runs, the back pressure valve was open (BPVO). During Run A (V_{liq} = 116 fps) the static pressure ratio was 0.66 at a distance of 0.247 inches upstream of the geometric throat, dropped to a value of 0.53 at x = 0, and continued to decrease downstream of the throat. Similarly Run B (V_{liq} = 70.2 fps) began with P_x/P_{og} = 0.66 at x = -.247 inches, attained a value of

P_x/P_{og} = .52 at x = 0, decreased to a minimum of P_x/P_{og} = .11 at x = 6 inches, and then remained constant from x = 6 inches to x = 14 inches. Little changed when the liquid velocity was lowered to 55.9 fps (Run C). The static pressure profile for Run D behaved similarly to those of A, B and C for a distance of 8 inches but then deviated as it rose to a value of P_x/P_{og} = 0.29 at x = 14.08 inches. Upon decreasing the inlet liquid velocity even further to 38.2 fps (Run E) it was found that the static pressure ratio followed the same general trend, but then rose sharply at x = 6 inches and attained a maximum observed value of 0.43. Runs F, G and H were similar in nature to Run E although the position at which the static pressure began to rise moved upstream as the inlet liquid velocity was decreased. Finally with the inlet liquid velocity reduced to a value of 32 fps, the static pressure profile deviated from that of Runs A-H over the entire length of the mixing section. At x = -.247 inches, P_x/P_{og} was 0.64; it dropped to a value of 0.60 at x = 0 and then increased in magnitude downstream of the throat.

From this series of static pressure profiles it appears that the flow can be divided into three distinct flow regimes based on inlet liquid velocity.

I. High Inlet Liquid Velocity Flow Regime (Runs A, B, and C) - The vapor is accelerated in its convergent nozzle from stagnation conditions to a state at the geometric throat having a static pressure ratio of about 0.50. Downstream of the throat, as the vapor interacts with the subcooled liquid stream, the static pressure ratio is decreased further and then levels off. The vapor static pressure ratio at the throat and upstream of the throat is independent of the magnitudes of the inlet liquid velocity. The static pressure profile downstream of the throat is relatively insensitive to variations in inlet liquid velocity.

II. Intermediate Inlet Liquid Velocity Flow Regime (Runs E, F, G and H) - The vapor is accelerated in its convergent nozzle from stagnation conditions to a state at the geometric throat having a static pressure ratio of about 0.50. Downstream of the throat, the static pressure ratio decreases further but then rises abruptly at some axial distance and then tends to level off. The vapor static pressure at the throat and upstream of the throat is independent of the magnitude of the inlet velocity. Within the mixing region up to the axial position at which the pressure rise begins, the static pressure is relatively insensitive to variations in inlet liquid velocity. The position at which the pressure rise begins and the magnitude of the pressure rise are extremely sensitive to variations in inlet liquid velocity. The pressure rise moves upstream towards the throat as the inlet liquid velocity is reduced.

III. Low Inlet Liquid Velocity Flow Regime (Run I) - The vapor is accelerated in its convergent nozzle from stagnation conditions. At the geometric throat the static pressure ratio is greater than 0.50. Downstream of the throat, the static pressure rises and then levels off.

From the static pressure profiles of Figure 15 it is not at all obvious where the transition from the Intermediate to the High Liquid Velocity Flow Regime occurred. Indeed, by using merely the shape of the pressure profile as a criterion for transition, it becomes difficult to decide to which regime Run D should be assigned. It will be shown later that Run D belongs to Regime I. More will be said of the transition between I and II and also of that between II and III in later sections.

Each of the three liquid velocity flow regimes will now be discussed in detail.

Regime I - High Inlet Liquid Velocity (BPVO)

With P_{og} = 22.5 psia, T_{og} = 340°F, T_{liq} = 40°F, and V_{liq} = 88.5 fps radial impact pressure profiles were obtained at 1, 3, 5, 7 and 9 inches from the geometric throat. These are shown in Figure 16. The profile at 1 inch (Figure 16a) clearly shows the central cylindrical liquid jet with an impact pressure of 79 psia, an annular vapor region with an impact pressure of 17 psia, and an annular two-phase region which separates the liquid and vapor streams. (It is assumed that the points at which the measured impact pressure is a maximum lie at the interface between the liquid core and the annular two-phase region. The radial interface between the vapor region and the two-phase region is defined by the points of intersection of the lines drawn tangent to the pressure distribution within the vapor and those drawn tangent to the pressure distribution within the two-phase region.) At distances of 3 and 5 inches (Figures 16b and 16c) the liquid impact pressure increased and the vapor impact pressure decreased. In addition the single-phase liquid region decreased in diameter, the two-phase region increased in width, and the region including the liquid and two-phase regions increased in width. Further downstream at 7 inches (Figure 16d) the centerline impact pressure was higher, and the two-phase region wider although here the annular region of maximum impact pressure no longer appeared. Finally at 9 inches (Figure 16e) the two-phase region grew larger in diameter, the vapor impact pressure was lower still and the centerline impact pressure was slightly lower than at 7 inches.

The radial location of the interface between the single-phase liquid core and the two-phase annular region is indicated in Figures 16a, b, and c. But from the profiles at 7 and 9 inches, without a detailed knowledge of the radial density distribution it is difficult to determine at what radial position the single-phase liquid region ended and the two-phase region began. The fact that the centerline impact pressure at 9 inches was slightly lower than that at 7 inches is evidence however that the much lower density vapor had reached the liquid jet centerline. From this it must follow that the liquid jet had "broken up" and that the jet breakup length was between 5 and 9 inches.

It will be shown later (Figure 27) that the jet breakup length increases with liquid velocity and that at the highest inlet liquid velocity at which tests were conducted (94.7 fps) the measured values of centerline impact pressure increased with x for all values of x.

Figure 17 is a flow regime map obtained from the profiles of Figure 16. This shows the single-phase liquid core decreasing in diameter from the value of 0.44 inches (r/R = 0.33) at x = 0 to a diameter of 0.21 inches (r/R = 0.16) at an axial distance of 5 inches and then disappearing completely somewhere between 5 and 9 inches from the nozzle exit plane.

Within the single phase liquid region, the local velocity can be calculated from Bernoulli's Equation. The liquid velocity profiles calculated from the measured points given in Figures 16a, b, and c are shown in Figure 18. Curve A indicates the liquid velocity entering the mixing section at $x = 0$ as determined from the mass flow-rate measurement. The velocity at the liquid jet centerline increased from an inlet value of 88.5 fps to a value of 150 fps within an axial distance of 5 inches. As has been mentioned previously (Chapter III), liquid flow rates estimated from probe profiles at $x = 1$ inch are in close agreement with the flow rates determined from the orifice plate measurements.

Figure 19 is a plot of the centerline impact pressure versus axial distance. Here, P_L has been normalized with respect to the inlet liquid stagnation pressure P_{oL}. In addition to data at 1, 3, 5, 7, and 9 inches, there is also included on this plot a measurement obtained at $x = 0.33$ inches. It can be seen that the centerline impact pressure ratio remained fairly constant over the first inch of the mixing section before rising to a maximum and then falling.

By placing the tip of the pitot probe in the annular vapor region (see Figure 17), values of the vapor impact pressure P_{oy} were obtained at 0.33, 1, 3, 5, 7 and 9 inches. (These can be taken for instance from Figure 16). The measured values of wall static pressure and vapor impact pressure are plotted versus axial distance in Figure 20. Using the usual one-dimensional normal shock relationships for a perfect gas and values of the ratio of specific heats, k, from Ref. 15 ($k = 1.32$) the vapor Mach Number can be determined from the data in Figure 20.

Figure 21 shows the results of the calculations for Mach Number and vapor stagnation pressure. It is seen that the vapor flow was supersonic with a maximum Mach Number of ≈ 1.5. The Mach Number profile, extrapolated back to $x = 0$, yields a value of unity at the vapor nozzle exit plane. The calculated values of vapor stagnation pressure begin at 19 psia at $x = 0.33$ inches and then fall to 7.4 psia at 9 inches. A discrepancy exists between the value of P_{og} measured in the stagnation tank ($P_{og} = 22.5$ psia) and the value calculated at 0.33 inches. Calculations indicate however that for a vapor nozzle discharge coefficient of $C_d = .98$ a vapor stagnation pressure drop of 2 to 3 psi was to be expected within the vapor nozzle.

On the basis of the information presented in Figures 16 through 27 it is now possible to draw some conclusions about the liquid and vapor flows for those specific conditions at which that run was made.

(i) Within its nozzle the vapor was accelerated from stagnation conditions to the sonic velocity (approximately 1550 fps) at the geometric throat and then upon entering the mixing section was rapidly accelerated to a Mach Number of approximately 1.5.

(ii) The central liquid jet entering the mixing section at an average velocity of 88.5 fps was accelerated by the high speed vapor stream so that within an axial distance of 5 inches it attained an average velocity of approximately 150 fps. Simultaneously the liquid jet decreased in diameter as it moved downstream and became discontinuous or broken at its centerline between 5 and 9 inches from the inlet plane.

(iii) The vapor stagnation pressure decreased from its entrance value of approximately 20 psia to a value of 7.75 psia at $x = 9$ inches. Calculations indicate that the probable cause of this unusually large axial gradient in stagnation pressure was the drag force present at the liquid-vapor interface.

Regime II - Intermediate Inlet Liquid Velocity (BPVO)

Figure 22 contains a plot of the wall static pressure distribution for the following inlet conditions: $P_{og} = 22.5$ psia, $T_{og} = 331°F$, $T_L = 38°F$, $V_L = 35.8$ fps, $W_{og} = .384$ lbm/sec, and $P_{oL}/P_{og} = .88$. Note that V_L and P_{oL}/P_{og} are smaller than in the previously discussed run.

The static pressure was 11.2 psia at the nozzle exit ($x = 0$), dropped to a minimum of 5.25 psia at $x = 1$ inch, and then suddenly began to rise at an axial distance of between 2 and 4 inches from the entrance plane. This is typical of the static pressure behavior of flows which have been identified with the Intermediate Inlet Liquid Velocity Flow Regime.

Figure 23 shows the corresponding radial distributions of impact pressure. The central liquid core is evident in Figure 23a (x = 1 inch) but is not readily discernible from the four additional profiles (x = 3, 5, 7, 9 inches). The profiles at 1 and 5 inches were obtained by traversing the pitot probes vertically from the top of the mixing section to the bottom while the profiles at 3, 7 and 9 inches were obtained from horizontal traverses of the mixing region. The profile in Figure 23c gives some indication that an asymmetry developed in the flow. The liquid jet centerline fell 0.20 inches from the tube centerline within a distance of 5 inches from the nozzle exit plane. Calculations show that the gravity force could have caused a vertical deflection of no more than 0.02 inches within the 5 inch distance. No measurable amounts of liquid jet "droop" were found from the radial profiles of the high liquid velocity run. (see Figure 16c).

Figure 24 shows the axial variation of the liquid jet centerline impact pressure. The centerline impact pressure ratio reached its maximum between x = 1 and 5 inches and then rapidly fell to 3.78 at x = 9 inches.

Figure 22 also contains plots of vapor Mach number and vapor stagnation pressure. These values were obtained by the same procedure as those presented in Figure 21. As with the run previously discussed, the Mach number in Figure 22 was unity at the nozzle throat (x = 0) and then reached a maximum of approximately 1.5 within a short distance from the mixing section inlet. However, then as the wall static pressure began to rise after 2 inches, the Mach number dropped rapidly and became subsonic. It should be noted by comparing Figure 22 with 24 that dramatic changes in the character of the liquid jet and vapor stream seem to have occurred simultaneously. Liquid jet breakup occurred at a distance of between 1 and 5 inches; the wall static pressure began to rise at a distance of between 2 and 4 inches; and the vapor Mach number became subsonic at a distance of approximately 3 inches from the mixing section inlet.

Regime III - Low Inlet Liquid Velocity (BPVO)

Due to the sensitive nature of the dependence of static pressure on inlet liquid velocity in Regime III, it was not possible to obtain any probe data for this regime. It was found that random fluctuations of less than ± 2% in inlet liquid velocity caused variations of the order of ± 10% in static pressure. This, coupled with a slow drift in inlet liquid velocity which occurred over the 5 hour period required to obtain a set of probe profiles, made such measurements impossible.

On the basis of Curve I in Figure 15 and of the results for Regimes I and II, the following conclusions are drawn for the Low Inlet Liquid Velocity Flow Regime:

(i) The vapor is accelerated from stagnation conditions to subsonic velocities at the throat.

(ii) The vapor flow is subsonic over the entire mixing section length.

(iii) Liquid jet breakup occurs within a short distance from the nozzle exit plane.

The nature of the transition between Regimes II and III will now be discussed.

Subsonic-Supersonic Transition at $x = 0$

Figure 25 shows the static pressure distributions for inlet liquid velocities near the transition from Regime II to Regime III. (Note the magnified scale of the abscissa.) The transition, which was marked by an increase in static pressure within the vapor nozzle and downstream at $x = 0$, occurred at an inlet liquid velocity between 32.9 fps and 33.8 fps.

A series of runs was made at various inlet vapor stagnation pressures to determine the effect of vapor stagnation pressure on the transition liquid velocity V_{LT}. The results are shown in Figure 26 where V_{LT} at first decreased with P_{og}, reached a minimum, and then increased with P_{og}.

This subsonic-supersonic transition phenomenon has grave import for the designer. As it will later be shown, a CE forced to operate in Regime III cannot undergo a Condensation Shock and hence will not achieve the exit pressures for which it is designed.

Additional BPVO Data

The data above (Figures 16 to 26) were presented in three distinct groups to emphasize some of the similarities and differences which exist among the three inlet liquid velocity flow regimes. Now to complete the picture of BPVO operation, the following series of figures has been included. The first of these (Figure 27) is a graph of the axial variation of centerline impact pressure as a function of inlet liquid velocity. All of the runs shown on Figure 27 were made with P_{og} = 22.5 psia, T_{og} ~ 335°F, and T_L ~ 40°F. The inlet liquid velocity was varied from 33.8 to 94.7 fps. It is clear from these profiles that liquid jet breakup occurred in almost all cases and that it was especially prominent within the intermediate liquid velocity flow range (Regime II).

Figures 28 to 34 are graphs of the axial variation of vapor Mach number as a function of inlet liquid velocity. Several runs are included at each liquid velocity which was varied from 35.8 to 116 fps. The data points given by the circles, triangles, and cross marks in Figures 28 to 34 were obtained in the same manner as those in Figures 21 and 22 . That is, at x = 0.33, 1, 3, 5, 7 and 9 inches, the measured values of vapor impact pressure, P_{oy}, were divided by the local measured values of wall static pressure and this ratio was used to determine the local vapor Mach number, M. The procedure used to calculate the continuous curves was to first draw "faired" curves through the measured values of P_{oy} and the measured values of P_x (see Figure 35). Then at close intervals (for example at x = 0.33, .5, .75, 1., 1.5, 2 etc.) the local "faired" values of

P_{oy} and P_x were used to determine the Mach number M. Hence the discrete points should be considered as measured values of Mach number and the continuous curves as the best fit curves. At any given velocity and at any x, due to uncertainty in the measurement of static and impact pressure and liquid velocity, there is some variation in the "best fit" Mach number profiles from run to run. Therefore, one additional averaging procedure was followed. Each curve in Figure 36 represents the arithmetic average of the best fit Mach number profiles (the continuous curves) which are shown in Figures 28 to 34 (e.g. the curve labeled "V_L = 116 fps" is the arithmetic mean of the three continuous curves given in Figure 28).

Figure 37 obtained from Figure 36 shows as a function of inlet liquid velocity, the axial position (x_{m1} at which the vapor went from supersonic to subsonic flow. The lower limit which was taken from Figure 26 is the liquid velocity at which transition from Regime II to Regime III occurred. At this limiting velocity, the supersonic-subsonic transition occurs at x = 0. The dotted portion of the curve was obtained by extrapolating the V_L = 46 fps curve of Figure 36 to the sonic line.

Figures 38 through 41 are graphs of the axial variation of the vapor stagnation pressure as a function of inlet liquid velocity. As with Figures 28 through 34, each of the curves in Figures 38 through 41 is the best fit curve for a given run. These were obtained by the same general procedure as the Mach number curves. It is possible that the downstream portions of the 46 fps curves (Figure 41) are in error by as much as 2 or 3 psi. At a liquid velocity of 46 fps, liquid jet breakup occurred at a distance of approximately 5 inches, (see Figure 27). Hence if the droplets from the disintegrated liquid jet had drifted to the walls rapidly enough, they would have interfered with the probe readings and caused the measured impact pressures to be too high. Calculations indicate that any such errors did not significantly affect the Mach number profiles in Figures 28 through 34 . Due to the observed increase in liquid jet breakup length with inlet liquid velocity, it is also believed that such droplet probe interactions did not significantly affect the probe measurements at the higher inlet liquid velocities.

Each curve in Figure 42 represents the arithmetic average of the "best fit" profiles shown in Figures 38 through 41 . The stagnation pressure profiles appear to be independent of liquid velocity in the range from V_L = 46 to 117 fps. The stagnation pressures rose slightly with a maximum at about x = .7 inches and then decreased rapidly downstream of x = 1 inch with a slope of approximately -1.9 psi/inch

Effect of Back Pressure on Mixing Section Processes

In an attempt to relate the BPVO data described above to performance criteria for the condensing ejector, a series of tests was conducted with the Back Pressure Valve closed. Earlier the effect on the flow of partially closing the downstream valve was described in some detail. By means of illustration, several static pressure profiles were presented (Figure 13) all with the same inlet conditions, but each obtained with the downstream valve closed by a different amount. It was pointed out that if the valve were closed sufficiently, the two-phase rod-annulus flow appearing in the test section would undergo a transition to a single-phase subcooled liquid stream. This transformation was shown to occur within a short distance ($L/D \approx 10$) and to be accompanied by an increase in static pressure. This phenomenon has been reported in the literature and has been referred to as a condensation shock. By comparing curve A of Figure 13 to Figure 15 , it is clear that the data in Figure 13 fall into the High Liquid Velocity Flow Regime.

To illustrate the effect of back pressure on the static pressure within the Intermediate Liquid Velocity Flow Regime, several static pressure profiles from Regime II are plotted in Figures 43, 44, and 45. All eight curves in Figure 44 have the same inlet conditions, but were obtained with the downstream valve closed by varying amounts. Curve A was obtained with the valve open as much as possible. As is typical of Regime II data, the static pressure ratio decreased from a value of 0.52 at $x = 0$ to a low of .078 before rising sharply at $x = 6$ inches.

With the downstream valve closed sufficiently to alter the pressure within the mixing section (Curve B), it is seen that the static pressure was changed only in that region downstream of $x = 6$ inches (Point Q). (See Figure 46 for a magnified view of the region around Q). Raising the back pressure further resulted in an increase in wall static pressure over the same region (Curve C), but not upstream of Q. Hence the pressure downstream of Point Q was sensitive to variations in back pressure rising over the <u>entire</u> downstream region for any valve setting between A and C. It was found impossible to cause the point at which the pressure departed from Curve A to move downstream of Q for any valve setting between A and C. The pressure upstream of Point Q was insensitive to variations in back pressure for valve settings between A and C. During Run D, however, the pressure upstream of Q was higher than in Runs A, B, and C. The remaining curves (E through H) illustrate the effect of further increases in back pressure. (If complete condensation had occurred, a downstream pressure of 26.3 psia would have resulted. Clearly this was not the case).

Figure 47 shows what Runs A and H looked like when viewed through the transparent test section. In this case complete condensation was not made to occur by closing the valve. This should be compared to Figure 14 which shows the CE operating within the High Liquid Velocity Flow Regime. Here the condensation shock and complete condensation did occur when the valve was closed.

The data in Figures 43 and 45 are of the same type as Figure 44, but with V_L = 36.2 fps and 43.2 fps respectively.

Figure 48 was obtained from Figures 43 through 45 and shows the effect of inlet liquid velocity on that length (L_I) of the flow which is initially insensitive to back pressure. (For purposes of discussion L_I will be referred to as the influence length). Finally a cross-plot was made from Figures 37 and 48 to study the relation between the length of the supersonic region, X_{M1}, and the influence length, L_I (see Figure 49). The fact that $\frac{L_I}{X_{M1}}$ is less than unity within the intermediate liquid velocity flow regime indicates that when the back pressure was raised the axial distribution of wall static pressure was altered throughout the entire downstream subsonic region of the flow and also within a small portion of the upstream supersonic region. Stated in another way, Figure 49 indicates that increases in wall static pressure caused by closing the back pressure valve are initiated within the region of supersonic flow. This suggests that a necessary condition for the existence of the condensation shock is the presence of supersonic vapor flow.

As defined in Chapter I, a condensation shock is that process by which within a relatively short distance a rod-annular two-phase flow is transformed into a single-phase liquid stream. Supersonic vapor flow existed for all values of x in Curve A of Figure 13 (V_L = 70.6 fps) and indeed complete condensation was made to occur by raising the back pressure. (Run G - Figure 13). (Also see Figure 14). During Run A of Figure 44 (V_L = 38.6 fps) the vapor was supersonic over the first 8 inches of the mixing section. When the back pressure was raised, the static pressure rose over the downstream subsonic region and also over a portion of the upstream supersonic region. However, in sharp contrast to the high liquid velocity case, the static pressure at the last pressure tap was only 55% of that which one would expect it complete condensation had occurred. Visual observations confirmed the fact that a two-phase flow existed at the mixing section exit. Supersonic vapor flow occurred during both the 38.6 fps and the 70.6 fps run. The only difference between the inlet conditions for the two runs was in the value of the inlet liquid velocity. Hence it is clear that while the presence of supersonic vapor flow is a necessary condition for the existence of the condensation shock, it is not a sufficient condition.

Performance Data -- Back Pressure Valve Closed (BPVC)

The procedure followed for obtaining the BPVC data was: (1) with the valve open, the desired inlet conditions were established, (2) the valve was slowly closed until the rise in static pressure moved upstream to the throat. The exit static pressure, P_e, was then taken as the pressure at the last static pressure tap (x = 14.08"). This procedure was followed over a wide range of inlet pressure ratios with the inlet vapor stagnation pressure set at 22.5 psia. These data are plotted on Figure 50 . Over the entire range of inlet conditions tested, it was thermodynamically possible to attain a single phase subcooled liquid state. Neglecting wall friction and assuming complete condensation had occurred, the Overall Control Volume Analysis (see Chapter II) was used to calculate the exit static pressure P_e. This is plotted as Curve A in Figure 50 . But it is possible that wall friction could have a significant effect on P_e. With a wall shear force based on the fanning friction factor for compressible vapor flow past a smooth wall, the Overall Control Volume Analysis was once again used to calculate the exit pressure assuming that complete condensation had occurred. This is plotted as curve B. The data agree with the theory over a wide range of inlet pressure ratios but deviate quite markedly at inlet pressure ratios less than unity. The two dashed lines drawn through the data indicate a sharp break in slope at an inlet pressure ratio of 1.06.

Figure 51 relates the variation of inlet liquid velocity to the inlet pressure ratio for the nozzles LN2 - VN2 with an inlet vapor stagnation pressure of 22.5 psia. At $P_{oL}/P_{og} = 1.06$, the inlet liquid velocity was 43 fps. Referring back to Figure 15, it is seen that the 43 fps curve lies somewhere between Curves C and D. But this is approximately where the transition from Regime I to Regime II was thought to occur. Finally, from Figure 37 it appears that at $V_L = 43$ fps with the BPVO, the vapor was supersonic over the first 10.5 inches of the mixing section.

Conclusions

(i) With the BPVO, the flow can be divided into 3 inlet liquid velocity flow regimes.

(ii) Liquid jet breakup occurs within the mixing section and is most prominent at the lower inlet liquid velocities.

(iii) Liquid jet breakup is accompanied by a rapid decrease in vapor Mach number and a transition from supersonic to subsonic vapor flow.

(iv) A Condensation Shock is necessary in order to condense completely the vapor <u>within the short length of the mixing section</u>.

(v) One condition to be satisfied for the existence of a Condensation Shock is that the vapor flow must be supersonic. This is not a sufficient condition, however.

(vi) Complete condensation was shown to occur within Liquid

Velocity Regime I but not within Regimes II and III.

CHAPTER V

COMPARISON OF THEORETICAL AND EXPERIMENTAL RESULTS

The digital computer programs for the slug and shear model equations were used in an attempt to predict some of the experimentally determined static pressure and vapor Mach number variations. With the slug model, the greatest difficulty which arose was the problem of theoretically predicting the rate of heat transfer between the liquid-vapor interface and the liquid core. Numerous heat transfer correlations and theories were tried, but none of these gave values of $\hat{h}$ which when combined with the computer programs would reproduce the measured static pressure distributions.

Because of the inability to find a heat transfer rate which could be used in the analyses, the opposite approach was taken. That is, digital computer experiments were conducted using the machine to determine those values of $\hat{h}$ needed to produce the observed variations in static pressure and Mach number. Similar computer experiments were conducted with the shear model program to learn something of the effect of interfacial shear forces, heat transfer, and interface velocity on the behavior of the rod-annulus flow.

It will be shown below that both the slug and shear flow models require heat transfer coefficients of the order of 100 BTU/sec $ft^2 {}^\circ F$.

Two sources were found which report heat transfer coefficients of this order of magnitude. Zinger (Ref. 18) measured the radial and axial variations of temperature within a turbulent jet of water falling through a chamber filled with stagnant steam. The water nozzle had a 0.59 inch diameter; the inlet liquid velocities were 65 and 82 fps; the steam was saturated at pressures from 1.7 to 2 atmospheres; and the inlet liquid temperature was approximately 70°F. From his temperature profiles Zinger calculated coefficients of heat transfer from the condensing steam to the water jet based on the surface area of a cylinder whose diameter equaled the liquid nozzle diameter. For an inlet liquid velocity of 65 fps the heat transfer coefficients were found to decrease systematically from a value of 190 BTU/sec ft^2°F at 12 inches from the inlet to a value of 57 BTU/sec ft^2°F downstream at 32 inches. Data presented at 82 fps showed $\hat{h}$ varying from 185 BTU/sec ft^2°F at 16 inches from the inlet to 80 BTU/sec ft^2°F downstream at 32 inches. No values of $\hat{h}$ were reported upstream of 12 inches.

Abramovich (Ref. 19) obtained a theoretical equation for the condensation of steam on the surface of an infinite plane turbulent jet. It was assumed that a core of undisturbed flow exists throughout the length of the jet, thus the development is valid only for the initial region of flow. The velocity and temperature in the core region were assumed to be constant throughout and equal to those values at the inlet plane; the steam was assumed to be everywhere uniform in temperature; and it was assumed the steam condensing at the liquid surface had a tangential velocity of zero. The heat transfer was assumed to take place in the turbulent mixing zone between the undisturbed core region and the liquid surface. The heat transfer coefficient $\hat{h}$ was found to be

$$\hat{h} = 5.62 \; U_o \; \Phi(k) \quad \left[{}^{BTU}/_{sec\,ft^2\,{}^oF} \right] \tag{119}$$

where U_o is the inlet velocity (ft/sec). The quantity $\Phi(k)$ a function of the dimensionless parameter $k = \frac{c(T_{stm} - T_o)}{h_{fg}}$ is given in Table IV.

In addition

$c \equiv$ specific heat of the liquid

$h_{fg} \equiv$ heat of evaporation

$T_{sat} \equiv$ temperature of the steam

$T_o \equiv$ inlet liquid temperature

At a steam temperature of 212°F, a water temperature of 70°F, and a liquid velocity of 65 fps, Eq. 119 predicts an $\hat{h}$ of 140 BTU/sec ft^2°F.

Thus, although the analysis of Ref. 19 and the test conditions of Ref. 18 do not correspond perfectly to the problem of interest, they do give one a feeling for what the order of magnitude should be for the heat transfer rate to a turbulent water jet with steam condensing at its surface. In addition they give some support to the analytical results which are shown below.

Slug Model Results. In addition to the assumptions of Chapter II, the following restrictions were placed on the slug model calculations:

(i) It was assumed that the bulk vapor stream changed to an equilibrium two-phase state immediately upon crossing the saturation line. Supersaturation effects were assumed to be negligible.

(ii) In the saturated region, any dependence of the wall friction force on the vapor quality was neglected. The wall shear force F_w was taken as

$$F_w = f \frac{\rho_v V_v^2}{2} 2\pi R_w \, dx \tag{120}$$

where f is the Fanning friction factor for turbulent flow past a smooth wall.

(iii) The duct was a constant area tube.

(iv) The heat transfer rate Q_L was given as

$$Q_L = \hat{h} \, 2\pi r_L \, dx \left(T_{sat} - T_L\right) \tag{121}$$

Figure 52 shows the effect of variation of the heat transfer coefficient $\hat{h}$ on the static pressure distribution. The family of curves was computed for the initial conditions of P_{og} = 22.3 psia, T_{og} = 321°F, T_L = 40°F, and V_L = 117 fps. To initiate the calculations, an inlet vapor Mach number of 1.02 was used. This was necessary because of the properties of the rod-annulus equations at Mach numbers of unity or slightly greater than unity. (See p. 28). The points given by the triangles, circles and crosses are from the 117 fps data presented in Chapter IV. It is seen that the rate of decrease of static pressure increased with $\hat{h}$. This is in agreement with the effect of $\hat{h}$ on static pressure as predicted by Eqs. 55 and 71 of Chapter II for a perfect gas. In the range from x = 0 to 1 inch, the pressure data were correlated by a value of $\hat{h}$ = 120 BTU/ft^{2}sec°F.

Figure 53 shows the effect of $\hat{h}$ on the axial distributions of the liquid and vapor temperatures. As to be expected the bulk liquid temperature T_L increased with x and $\hat{h}$. For all three cases shown in Figure 53, the vapor crossed the saturation line within .02 inches from the inlet. The vapor temperatures shown in Figure 53 correspond to the local saturation temperature, and therefore the temperature difference $(T_{sat} - T_L)$ used for the calculation of Q_L can be taken directly from this graph.

Figure 54 shows the variations of vapor quality q and the condensation rate $\dot{m}_c/\Delta x$ with $\hat{h}$ and x. In all cases the condensation rate decreased with axial distance, dropping rapidly from an initial value of approximately 2.0 lbm/sec ft. This decrease reflects the decrease in $(T_{sat} - T_L)$ which occurred.

Figures 55 and 56 show the variations of vapor flow rate, vapor Mach number, liquid jet radius, and liquid velocity with $\hat{h}$ and x. It should be noted that the liquid jet radius decreased with both axial distance and $\hat{h}$. This is evidence of the tremendous acceleration which the liquid jet is subjected to within the framework of the slug model.

The dependence of static pressure on $\hat{h}$ (Figure 52) suggests that by properly adjusting the value of $\hat{h}$ as a function of axial position the slug model calculations can be made to agree with the data over the entire length of the constant area section. The results of this exercise are presented in Figures 57 and 58. The heat transfer coefficient was set equal to 120 BTU/sec ft^2°F in the range $0 < x < 1$ inch, to 50 from 1 inch to 6 inches, and then to 15 for $x > 6$ inches. As seen from the static pressure and Mach number profiles the agreement with the data is excellent. (This is not too surprising considering the liberties which were taken with $\hat{h}$).

Figures 59 and 60 show similar results for the P_{og} = 22 psia and V_L = 64 fps run. Here the dashed Mach number line was obtained by interpolating between the 46 and 70 fps curves of Figure 36. For this case $\hat{h}$ was set equal to 100 BTU/sec ft^2°F from the inlet to $x = 1$ inch, to 35 from 1 to 7.5 inches and then to 1 for $x > 7.5$ inches.

Figure 61 shows the computed axial variations of vapor flow rate, condensation rate, and quality for the 64 and 117 fps runs. According to the slug model the vapor crossed the saturation line quite close to the inlet ($x \sim .01$ inch); the vapor quality then decreased with axial distance and inlet liquid velocity, but then tended to level off at values of 0.92 and 0.86 for the two runs. The condensation rate curves reflect the abrupt and large changes in $\hat{h}$ which were required to obtain the agreement between the theory and experiment. The vapor flow rate decreased rapidly from initial values of approximately 0.4 lbs/sec and then leveled off at 0.24 and 0.145 lbs/sec as the condensation rate became smaller.
Figure 62 shows the effect of inlet liquid velocity on the axial variations of liquid velocity and liquid jet radius. The liquid jet

radius decreased from an initial value of .01875 ft to values of 0.016 and 0.011 ft for the two runs. Finally Figure 63 shows the axial variation of liquid and vapor temperatures for the two runs. At any x the temperature difference between the streams was roughly the same for both the 64 and 117 fps runs.

In Chapter II it was shown that for the slug model and for a perfect-gas vapor stream the variation of vapor stagnation pressure is

$$\frac{dP_{ov}}{P_{ov}} = - \frac{F_w}{p A_v} \tag{63}$$

This can be written as

$$\frac{dP_{ov}}{dx} = - \frac{\frac{F_w}{dx} P_{ov}}{A_v \quad p} \tag{122}$$

It was shown in Figure 42 in Chapter IV that the measured stagnation pressure was roughly constant from x = 0 to 1 inch and then decreased with a slope of -1.9 psi/inch. According to the slug model equation the stagnation pressure gradient should have been of the order of

$$\frac{dP_{ov}}{dx} \sim - 0.15 \frac{\text{psi}}{\text{INCH}}$$

This is an order of magnitude lower than the gradient which was measured at values of x > 1. Although the slug model was made to produce the experimentally observed static pressure and Mach number variations by the use of appropriate values of the heat transfer coefficient, it did not simultaneously yield values of stagnation pressures which are consistent with the experiments.

To summarize briefly, axial variations of vapor Mach number, vapor stagnation pressure, and static pressure produced by the slug model are consistent with the measured variations from x = 0 to x = 1 inch. For values of x > 1, agreement was obtained for Mach number and static pressure only. For x > 1 the behavior of the vapor stagnation pressure as predicted by the slug model is not consistent with the data.

Shear Model Results

In addition to the assumptions of Chapter II, the following restrictions were placed on the shear model calculations.

(i) It was assumed that the bulk vapor stream changed to an equilibrium two-phase state immediately upon crossing the saturation line. Supersaturation effects were assumed to be negligible.

(ii) In the saturated region any dependence of the wall friction force on the vapor quality was neglected. The wall shear force F_w was taken as

$$F_w = f \frac{\rho_v V_v^2}{2} 2\pi R_w \, dx \tag{123}$$

where f is the Fanning friction factor for turbulent flow past a smooth wall.

(iii) The duct was a constant area tube.

(iv) The heat transfer rate Q_L was given as

$$Q_L = \hat{h} \, 2\pi r_L \, dx \left(T_{sat} - T_L\right) \tag{124}$$

(v) The interfacial force term F_{Lv} was defined as

$$F_{Lv} = f \rho_v \frac{(V_v - V_i)^2}{2} 2\pi r_L \, dx \tag{125}$$

where f is an as yet unspecified force coefficient.

(vi) The interfacial work term W_k was assumed to be of lower order than the heat transfer term Q_L and was neglected.

Figures 64 and 65 show the effect of variations of the heat transfer coefficient $\hat{h}$ on the computed variations of static pressure and vapor Mach number. The curves were calculated for inlet conditions of P_{og} = 22.3 psia, T_{og} = 321°F, T_L = 40°F and V_L = 117 fps. The data shown here are the same as those in Figures 57 and 58. The two families of curves were computed with the force coefficient f set equal to zero and the interfacial velocity from Eq. 94 (see Chapter II).

As before an inlet vapor Mach number of 1.02 was used to initiate the calculations. It is seen that at any x the static pressure decreases with $\hat{h}$ while the Mach number increases with $\hat{h}$. This is in agreement with the effect of $\hat{h}$ on static pressure and Mach number as predicted by Eqs. 103 and 106 of Chapter II for a perfect gas.

Figures 66 and 67 show the effect of various assumptions for the interfacial velocity on the computed variations of static pressure and Mach number. All of the curves were obtained with $\hat{h}$ = 70 and f = 0. The interfacial velocity was varied from $V_i = V_L$ to $V_i = 3V_L$. The expression

$$V_i = \frac{V_L + \sqrt{\rho_v/\rho_L}\; V_v}{1 + \sqrt{\rho_v/\rho_L}} \tag{94}$$

yields values of V_i of the order of $V_i \sim 1.3\ V_L$.

Because of the relative independence of the shear model calculations from the particular model used for V_i all of the remaining calculations were made with the interfacial velocity set equal to the local liquid velocity. Figures 68 and 69 show the effects of variations of the interfacial force coefficient on the shear model calculations. At any x, the static pressure increases with f while the vapor Mach number decreases with f. This is in agreement with the effect of f on static pressure and Mach number as predicted by Eq. 103 and 106 of Chapter II. Note the unusually high values of f needed to significantly affect the calculations. The vapor Reynolds number was of the order of magnitude of 10^5 or 10^6. For a smooth wall, this corresponds to a Fanning friction factor of 0.004.

For the case of an inlet liquid velocity of 117 fps a series of digital computer experiments were run to determine the values of $\hat{h}$ and f required for agreement between the shear model calculations and the data. For a perfect gas, Eq. 109 from Chapter II is

$$\frac{dP_{ov}}{P_{ov}} = \frac{-\left(F_w + F_{Lv}\right)}{P\,A_v} + k M^2 \left(1 - \frac{V_i}{V_v}\right) \frac{m_c}{w_v} \tag{109}$$

This gives the relation between the change in vapor stagnation pressure and the friction forces and condensation rate which must be satisfied locally within the flow. Eq. 109 can be written as

$$\frac{\frac{dP_{ov}}{P_{ov}}}{dx} = -\frac{\left(\frac{F_w}{dx} + \frac{f\rho_v(V_v - V_i)^2}{2} 2\pi r_L\right)}{PA_v} + kM^2\left(1 - \frac{V_i}{V_v}\right)\frac{\frac{m_c}{dx}}{w_v} \tag{126}$$

As it was shown above, the vapor stagnation pressure obeyed the relation

$$\frac{dP_{ov}}{dx} \sim 0 \tag{127}$$

from $0 < x < 1$ inch and decreased according to

$$\frac{dP_{ov}}{dx} \sim 1.9 \ \text{psi}/\text{inch} \tag{128}$$

for $x > 1$ inch (see Figure 42). Equations 126, 127 and 128 were combined to furnish relations of constraint between f and $\hat{h}$. By systematically varying $\hat{h}$ and f subject to the stagnation pressure constraints, agreement was obtained between the Mach number, static pressure, and vapor stagnation data and the shear model calculations. The results of these calculations are shown in Figures 70 and 71. From x = 0 to 1 inch the values of $\hat{h}$ and f required were $\hat{h}$ = 100 BTU/ft^{2}sec°F and f = 0.6. Similarly in the region from x = 1.0 to 3.6 inches, $\hat{h}$ and f were taken as $\hat{h}$ = 80 BTU/ft^{2}sec°F and f = 0.65.

CHAPTER VI

CONCLUSIONS

A detailed analytical and experimental investigation of the liquid-vapor interactions occurring within a constant area condensing ejector has been conducted. Axial and radial profiles were obtained of the flows over a limited range of inlet vapor conditions to study the effect of variations of inlet liquid velocity on the behavior of the liquid and vapor streams and on the overall pressure performance of the device. These data suggest that the flows can be divided into three separate regimes based on inlet liquid velocity. The High Liquid Velocity Flow Regime (I) is characterized by supersonic vapor flow over a considerable length of the mixing section. Within Regime I complete condensation was achieved within a relatively short distance by partially closing the back pressure control valve and thus establishing a condensation shock. The overall pressure performance data from this Regime are in agreement with the performance predicted by the Overall Control Volume Analysis.

Within the Intermediate Liquid Velocity Flow Regime (II) the vapor streams were supersonic over only a short upstream length of the mixing section. Within Regime II it was not possible to achieve complete condensation of the vapor stream within the length of the mixing section or to establish a condensation shock. The overall pressure performance was lower than that predicted by the OCVA.

Within the Low Inlet Liquid Velocity Flow Regime (III) the vapor was subsonic over the entire length of the mixing section. Complete condensation was not achieved when the back pressure was raised; it was not possible to establish a condensation shock.

Liquid jet breakup occurred at all but the highest inlet liquid velocities at which probe profiles were taken (88.5 and 94.7 fps). The breakup length increased with inlet liquid velocity. Occurring simultaneously with the breakup of the liquid jet was an increase in static pressure and a decrease in vapor Mach number. With sufficiently short breakup lengths the vapor became subsonic downstream of the initial supersonic region.

It was found that a necessary but not sufficient condition for the existence of the condensation shock is the presence of a supersonic vapor flow.

Two mixing section analyses based on a one-dimensional rod-annulus flow model were written and programmed with the exact equations of state on an IBM 7090 digital computer. The slug flow model requires that the condensate leaves the vapor control volume with the bulk vapor velocity and that no forces exist at the liquid vapor interface. The shear flow model permits the condensate to leave the vapor control volume with a velocity less than the bulk vapor velocity and also allows the existence of an interfacial shear force. To predict the observed pressure and Mach number variations both models require high rates of heat transfer from the liquid-vapor interface to the liquid core; these being characterized by heat transfer coefficients of the order of 100 btu/ft^{2}sec$^\circ$F. In addition, the shear model requires interface friction coefficients of the order of unity. Excellent agreement was obtained between the shear model calculations and the measured values of static pressure, vapor Mach number, and vapor stagnation pressure by using appropriate values of the heat transfer coefficient and the interfacial friction factor. From similar calculations using the slug model program with appropriate values of the heat transfer coefficient, agreement was obtained over the entire mixing section length between the experimental and theoretical static pressure and vapor Mach number variations. However, agreement between the slug theory and the vapor stagnation pressure data was obtained over the first inch of the mixing section only.

CHAPTER VII

RECOMMENDATIONS FOR FUTURE RESEARCH

It is not unusual for a research program of as wide a scope as the present one to generate a significant number of potential subjects for future research. This investigation is not deficient in this respect.

There are many possible variations and extensions of the test program which the author has just completed. These include the following:

(1) A detailed study should be run to determine the effect of variations in inlet vapor stagnation pressure on the behavior of the liquid and vapor streams and on the overall pressure performance of the device. The data of Figure 2 which represent a range of inlet vapor stagnation pressures from 20 to 50 psia show no noticeable effects of variation of inlet vapor pressure on overall performance. The upper limit should be extended and data obtained on the liquid-vapor interactions at higher pressures.

(2) The effects of varying the amount of subcooling of the liquid stream and the amount of superheating of the inlet vapor could be of considerable importance. As an example, consider the extreme situation in which the liquid enters the device as a

saturated liquid stream and the vapor as saturated vapor at the same static pressure. In this case the heat transfer between the streams will be quite low and hence the drag effects will predominate. The behavior of the streams would be substantially different from the case of a large inlet temperature difference.

(3) All of the data presented here were obtained with a convergent vapor nozzle. The vapor entered the mixing section as either a subsonic or sonic stream. The effects on performance of low subsonic and supersonic inlet vapor Mach numbers should be investigated.

(4) The effects of changes of inlet geometry on the behavior of the two streams and on overall performance should be carefully examined. The diameter of the inlet liquid jet is important because of its connection with the liquid jet breakup phenomena. According to Brown's OCVA (Ref. 10) the ratio of inlet vapor flow area to inlet liquid flow area must be considered when predicting the overall performance of the device.

(5) It is shown in Ref. 10 that the overall pressure performance increases if a convergent test section is used. Clearly an investigation on the effect of mixing section shape on total performance and on the mixing section interactions should be undertaken.

The above problems are all of concern to the individual faced with the task of designing a high performance device.

However, there are several other pertinent problems of an even more basic nature. These are described below.

(1) One glaring weakness of the mixing section analyses presented here was that the values of the heat transfer coefficients which were used were all assumed rather than theoretically predicted. It is extremely important that more information on the heat transfer be made available. This is a problem which must be solved before the mixing section analysis can become an effective design tool.

(2) Liquid jet breakup was shown to occur with breakup lengths as short as an inch or two occurring at the lower liquid velocities. To the knowledge of the author there is nothing available in the literature which can be used to predict such short lengths for breakup. Ref. 20, a study of the disintegration of liquid streams issuing into quiescent regions, does present some data on the subject; however, calculations based on these data predict breakup lengths of the order of 2 ft. Some basic studies of the effect of a high velocity coflowing condensing vapor stream on jet breakup should be conducted.

(3) Research on the rate of atomization of liquid jets should be expanded. Most research has been directed toward determining the terminal droplet size as a function of a large number of variables. However, little effort has been directed toward determining the rate at which droplets are torn from the jet surface. Knowledge of the subject is almost nonexistent at the relative velocities of the magnitude of those encountered in the CE.

That this is an important phenomenon in the CE is evident from the width of the two-phase regions which are shown in Figures 16 and 23. In addition the friction factors required by the shear model analyses ($f \sim .6$) suggest the presence of considerable droplet-vapor interactions within the two-phase regions.

(4) Efforts should be made to learn more about the condensation shock. The additional conditions required for the existence of the shock should be determined. In addition, a program should be initiated to investigate the effects of the various flow quantities on the length of the shock and on shock stability. This information becomes important when determining how long the constant area portion of the convergent-divergent CE should be (see Figure 1) and whether or not the shock will remain in a stable position within the constant area portion.

It is quite conceivable that investigations directed along the lines of the first five recommendations will add substantially to the second group of research subjects listed in this Chapter.

APPENDIX A

ESTIMATE OF THE ERRORS CAUSED BY DROPLET-PROBE INTERACTIONS

In this section the influence of liquid droplets on the vapor impact probe measurements is discussed. Those droplets which originate at the central liquid jet and are formed by erosion of the jet surface are not of concern here. Instead the droplets which are nucleated as the steam crosses the saturation line and achieves an equilibrium two-phase state are considered. It is assumed that the vapor quality is high; the fluid will be treated as a gas carrying with it liquid droplets of uniform size. The droplets are assumed to be very small compared to the probe diameter and at great distances upstream of the probe tip the droplets and gas are assumed to have the same velocity. Dussourd and Shapiro (Ref. 21) consider the problem of the aerodynamic interactions between the droplets and the gas both inside and outside of the probe. It is shown that the droplets must undergo a momentum decrease as they cross the vapor streamlines just upstream of the probe. Consequently the gas pressure in the probe is greater than it would be if the gas were to be decelerated without the droplets being present. The external over pressure is expressed as

$$\frac{\left(P_{meas.} - P_o\right)_e}{\frac{1}{2}\rho_v V_{v_\infty}^2 \left(\frac{w_L}{w_v}\right)_\infty} = 2\left[1 - \frac{V_L}{V_{v_\infty}}\right]\bar{e} \tag{A1}$$

where $\bar{e}$ the capture efficiency is given as a function of the dimensionless number $\theta = \frac{3}{4} \frac{\rho_{v\infty}}{\rho_L} \frac{D_{probe}}{D_{drop}}$

For droplets with an average diameter of 10 microns, for a vapor quality of q = 0.87 (This, the lowest of the values of q determined by the slug model program (see Figure 61), is used because it will give the largest value for the calculated overpressure), and for an upstream gas velocity of 2000 fps, Eq. A1 predicts the external overpressure to be of the order of +.1 psi.

The overpressure caused by interactions inside of the probe can be estimated from the relation

$$\left(P_{meas.} - P_o\right)_i = \frac{W_L V_{L\infty}}{A_{PROBE}} \tag{A2}$$

The local liquid flow rate into the probe W_L is equal to

$$W_L = (1-q)\, W_{TOTAL} \frac{A_{PROBE}}{A_{TOTAL}} \bar{e} \tag{A3}$$

Hence,

$$\left(P_{meas.} - P_o\right)_i = (1-q) \frac{W_{TOTAL}}{A_{TOTAL}} V_{L\infty} \bar{e} \tag{A4}$$

For a droplet diameter of 10 microns, a vapor quality of 0.87, a local vapor flow rate of 0.15 lbm/sec (this was taken from the slug flow calculation at x = 9 in. and V_L = 117 fps (see Figure 61)), and a vapor velocity of 2000 fps, Eq. A4 yields

$$\left(P_{meas.} - P_o\right)_i \sim +0.85 \text{ psi}$$

Hence by using the lowest estimates of vapor quality from the mixing section calculations, a maximum probe error of 0.95 psi is estimated.

APPENDIX B

BIOGRAPHY

The author was born in Baltimore, Maryland in 1942. He received his secondary education in the Baltimore City public school system graduating from the Baltimore Polytechnic Institute in 1960. He entered the University of Maryland in 1960 and received a B.S. in Mechanical Engineering in 1963. Entering M.I.T. in 1963 he received an S.M. degree in 1964 and then after working briefly as an Engineer at the United States Naval Ordnance Laboratory, returned to M.I.T. in 1965 and commenced his Doctoral program.

BIBLIOGRAPHY

1. L. Hays, "Investigation of Condensers Applicable to Space Power Systems - Part II Jet Condensers," Rept. 1588, Electro-Optical Systems, Inc., Pasadena, Calif., (Nov., 1962).

2. R. Platt, "Investigation of a Jet Condenser for Space Power," NASA TND-3045.

3. J. Kaye and M. Rivas, "Experimental and Analytical Study of Two-Component Two-Phase Flow in an Ejector with Condensation," Dept. of Mech. Eng., M.I.T., Camb., Mass., (March 15, 1957).

4. J. Miguel and G.A. Brown, "An Analytical and Experimental Investigation of a Condensing Ejector with a Condensable Vapor," AIAA Paper 64-469, Washington, D.C. (June, 1964).

5. G.A. Brown and J. Miguel, "An Experimental Investigation of the Effects of a Non-Condensable Gas on Condensing Ejector Performance," AIAA Paper 66-674 (June, 1966).

6. G.A. Brown and E.K. Levy, "Liquid-Metal MHD Power Generation with Condensing Ejector Cycles," Paper SM-74/171, Int. Symp. on MHD Electric Power Generation, Salzburg, Austria (July, 1966).

7. W. D. Jackson and G.A. Brown, "Liquid Metal MHD Power Generator Utilizing the Condensing Ejector," Patent Disclosure, M.I.T., Camb., Mass. (Oct. 15, 1962).

8. G.A. Brown and K.S. Lee, "A Liquid Metal MHD Power Generation Cycle Using a Condensing Ejector," Paper 60, Int. Symp. of MHD Electric Power Generation, Paris, France (July, 1964).

9. M. Petrick, "Liquid-Metal MHD," IEEE Spectrum, pp. 137-151 (March, 1965).

10. G.A. Brown, "An Analysis of Performance Data from the NUOS Condensuctor Test Facility with a New Theory for the Variable Area Condensuctor-I Steam-Water Operation," Rept. 44, Joseph Kaye Co., Camb., Mass. (Jan., 1962).

11. J. Burgers and A. Ghaffari, "On the Application of Steam Driven Water Jets for Propulsion," NBS Rept. 5307 (May, 1957).

12. P. Chiarulli and R. Dressler, "Condensation Interfaces in Two-Phase Flows," J. Applied Physics, Vol. 28, No. 9, pp. 990, (Sept., 1957).

13. J. Levy, "The Mixing of Vapor and Liquid Jets," Aero-Jet General Corp., Rept. 1344, (Oct., 1957).

14. S.W. Gouse and J. Leigh, "Heat, Mass, and Momentum Transfer between a High Velocity Liquid Jet and a Concentric Gas Stream in an Axisymmetric Channel," Joseph Kaye and Co., Rept. 67 (Jan., 1965).

15. J. Keenan and F. Keyes, Thermodynamic Properties of Steam, John Wiley and Sons, Inc., 1936.

16. B.T. Lubin, "Design and Construction of a Steam-Water Condensing Ejector Test Facility", Dept. of Mech. Eng., M.I.T., Cambridge, Mass. (Sept., 1965).

17. ASME, "Power Test Codes 19.5, 4-1959 - Flow Measurement".

18. N.M. Zinger, "Heating of a Jet of Water in a Vapor-Filled Space", Problems of Heat Transfer during a Change of State: A Collection of Articles, ed. by S.S. Kutateladze, AEC TR-3405 (1953).

19. G. Abramdvich, The Theory of Turbulent Jets, M.I.T. Press, Cambridge, Mass. (1963).

20. C.C. Miesse, "Correlation of Experimental Data on the Disintegration of Liquid Jets", Industrial and Engineering Chemistry, Vol. 47, No. 9 (Sept. 1955).

21. J.L. Dussourd and A.H. Shapiro, "A Deceleration Probe for Measuring Stagnation Pressure and Velocity of a Particle-laden Gas Stream", Dept. of Mech. Eng., Gas Turbine Laboratory, M.I.T., Cambridge, Mass. (May 1955).

22. A.H. Shapiro, The Dynamics and Thermodynamics of Compressible Fluid Flow, Vol. I, Ronald Press, New York (1953).

TABLE I

LOCATION OF STATIC PRESSURE TAPS IN TEST SECTION TS1

x inches	
.25	Convergent Section
1.25	
2.25	
3.25	
4.25	
5.25	
6.25	
7.25	
8.25	
9.25	
12.11	Constant Area Section
12.61	
13.11	
13.61	
14.11	
14.61	
15.11	
15.61	
19.86	Diffuser
21.86	

TABLE II

LOCATION OF STATIC PRESSURE TAPS AND PROBE PORTS IN TEST SECTION TS2

x (static) in.	x (probe port) in.	x (probe tip) in.	
0.38			
2.00	2.00	1.00	Right
5.00	2.00	1.00	Left
8.00	4.00	3.00	Top
11.00	4.00	3.00	Bottom
14.00	6.00	5.00	Top
	6.00	5.00	Bottom
	8.00	7.00	Right
	8.00	7.00	Left
	10.00	9.00	Right
	10.00	9.00	Left
	15.00	14.00	Bottom

(Note: Probe tips are 1 inch upstream of probe ports.)

TABLE III

LOCATION OF STATIC PRESSURE TAPS AND PROBE PORTS IN TEST SECTION TS3

x (static) in.	x (probe port) in.	x (probe tip) in.
- 0.243	1.33	.33 Right
- 0.65	2.00	1.00 Top
+ 0.18	2.00	1.00 Bottom
+ 0.38	4.00	3.00 Right
+ 0.58	4.00	3.00 Left
+ 0.83	6.00	5.00 Top
+ 1.08	6.00	5.00 Bottom
+ 2.08	8.00	7.00 Right
+ 4.08	8.00	7.00 Left
+ 6.08	10.00	9.00 Right
+ 8.08	10.00	9.00 Left
+ 10.08		
+ 12.08		
+ 14.08		

(Note: Probe tips are 1 inch upstream of probe ports).

(Note: Negative x is upstream of nozzle exit plane).

TABLE IV

FUNCTION $\Phi(k)$ FROM ABRAMOVICH'S ANALYSIS

k	$\Phi(k)$
0.002	0.100
0.007	0.149
0.016	0.198
0.031	0.246
0.053	0.288
0.084	0.332
0.123	0.370
0.172	0.401
0.233	0.432

From Ref. 19.

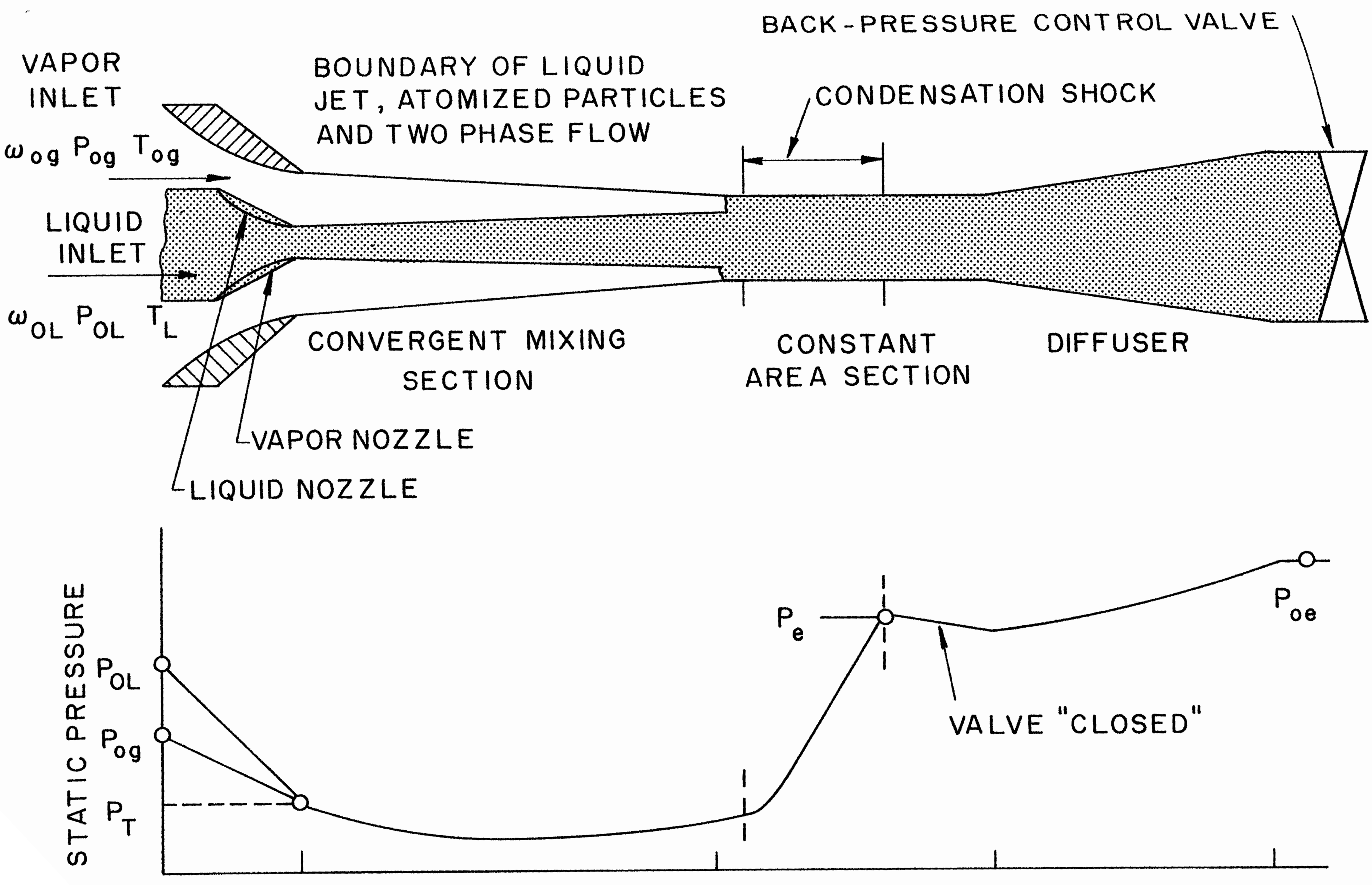

FIG. I TYPICAL CONDENSING EJECTOR PROCESSES AND PRESSURE DISTRIBUTION

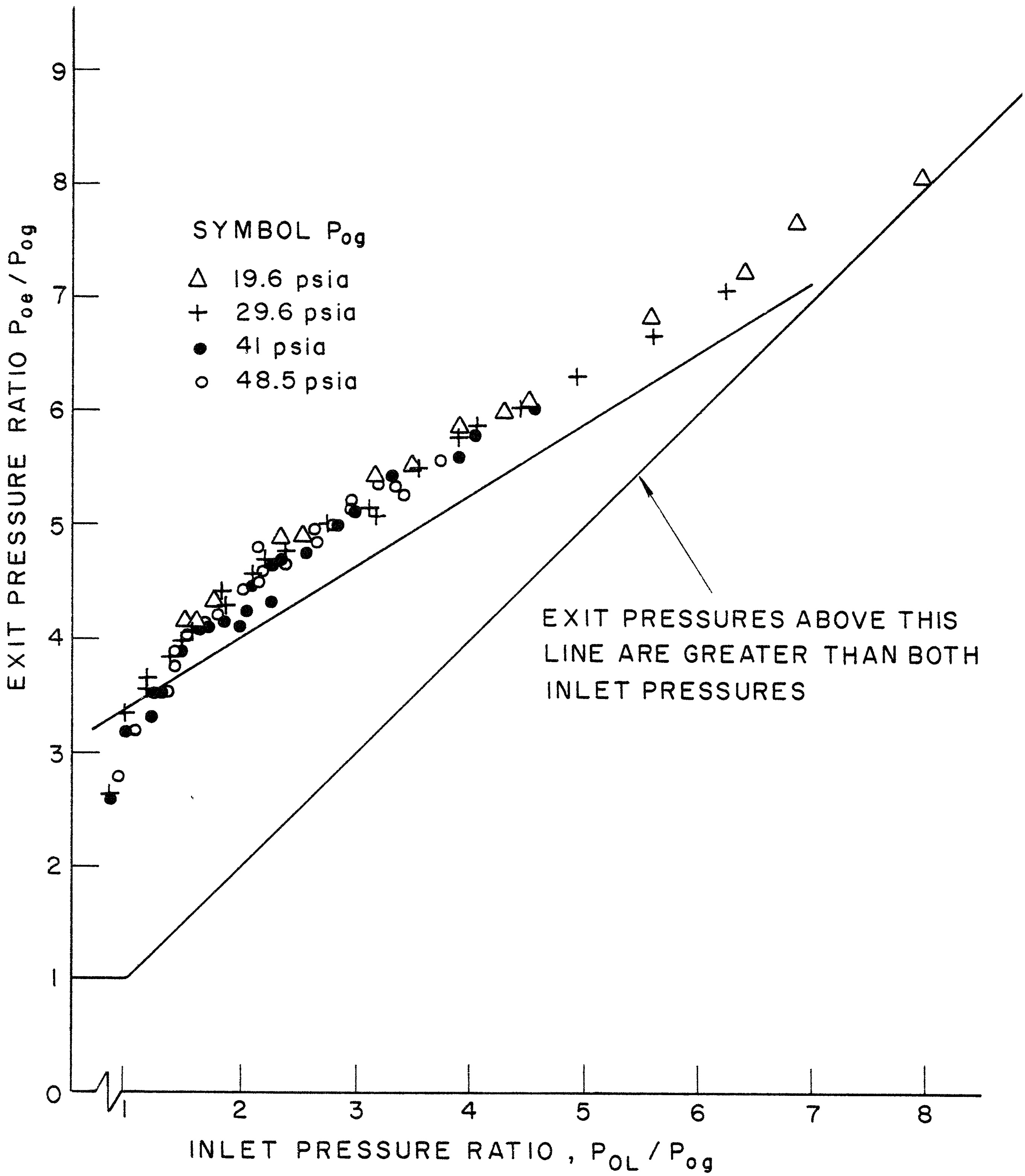
EXIT PRESSURE RATIO P_{oe} / P_{og}
INLET PRESSURE RATIO , P_{OL} / P_{og}
SYMBOL P_{og}
19.6 psia
29.6 psia
41 psia
48.5 psia
EXIT PRESSURES ABOVE THIS LINE ARE GREATER THAN BOTH INLET PRESSURES
0
1
2
3
4
5
6
7
8
9

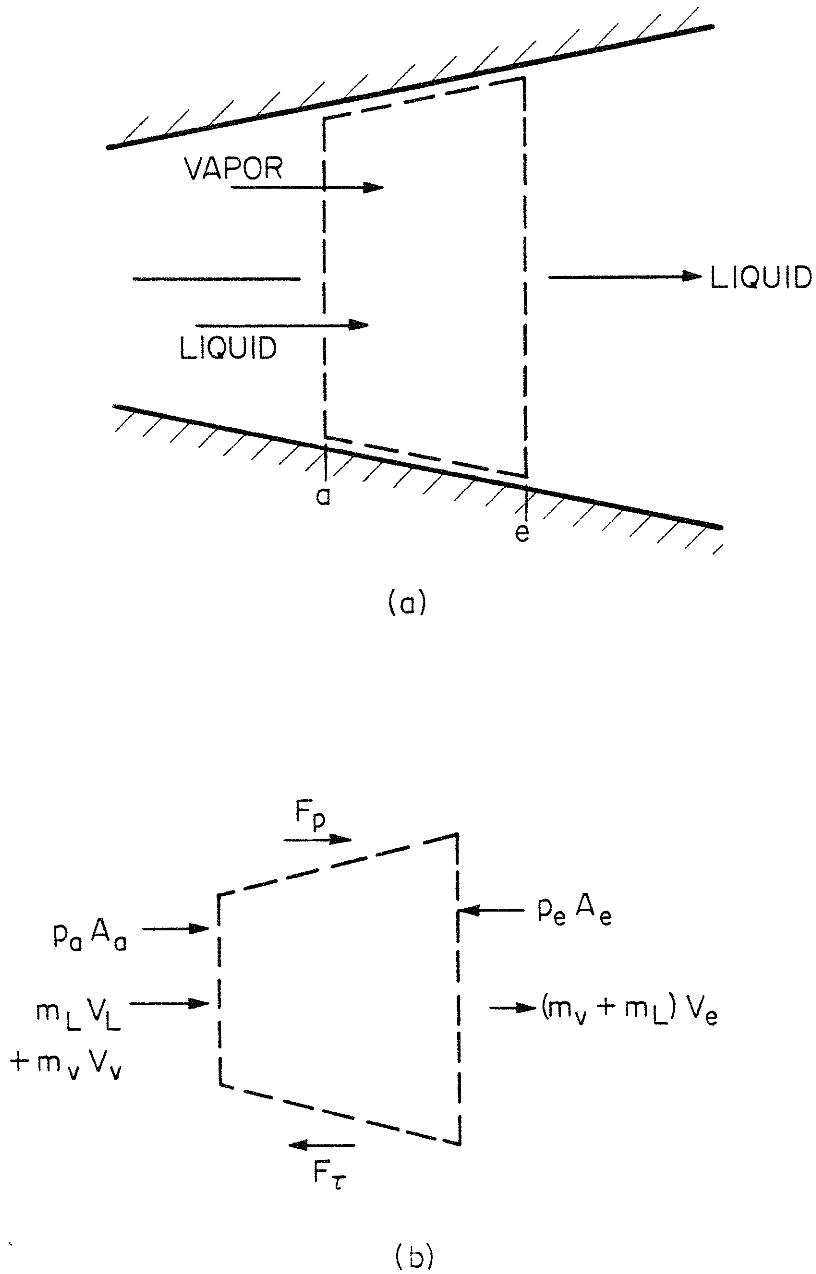

FIGURE 3 CONTROL VOLUME FOR THE OVERALL CONTROL VOLUME ANALYSIS

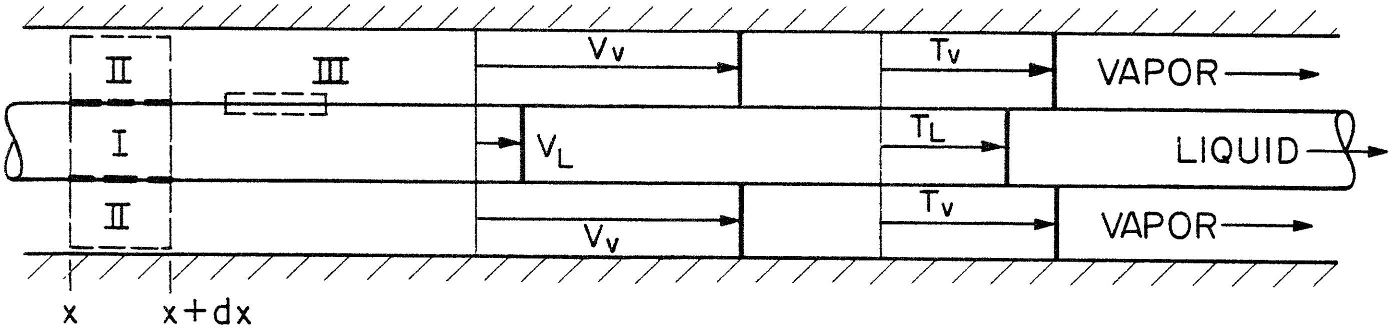

FIGURE 4a CONTROL VOLUMES, TEMPERATURE AND VELOCITY PROFILES FOR SLUG MODEL

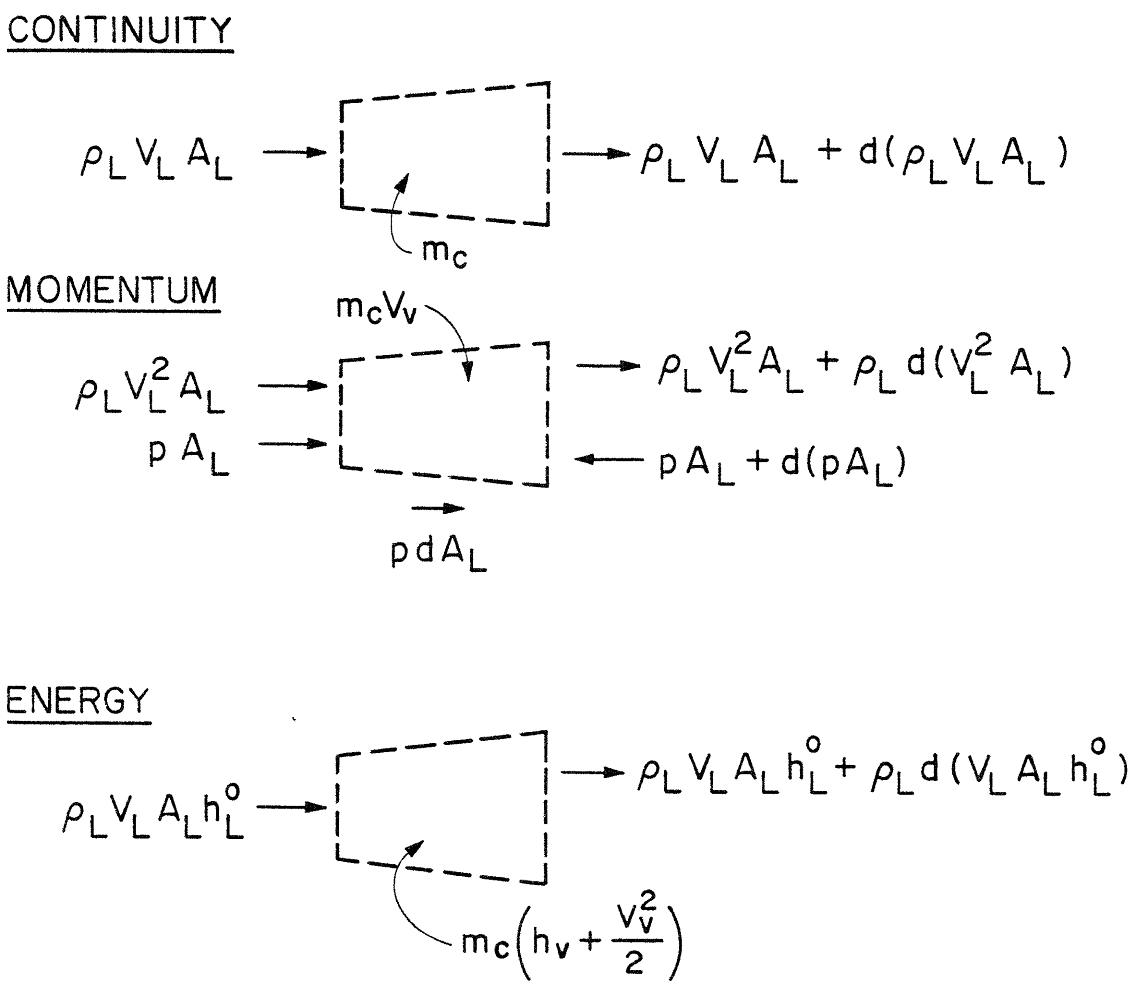

FIGURE 4b TERMS APPEARING IN CONSERVATION EQUATIONS FOR LIQUID CORE

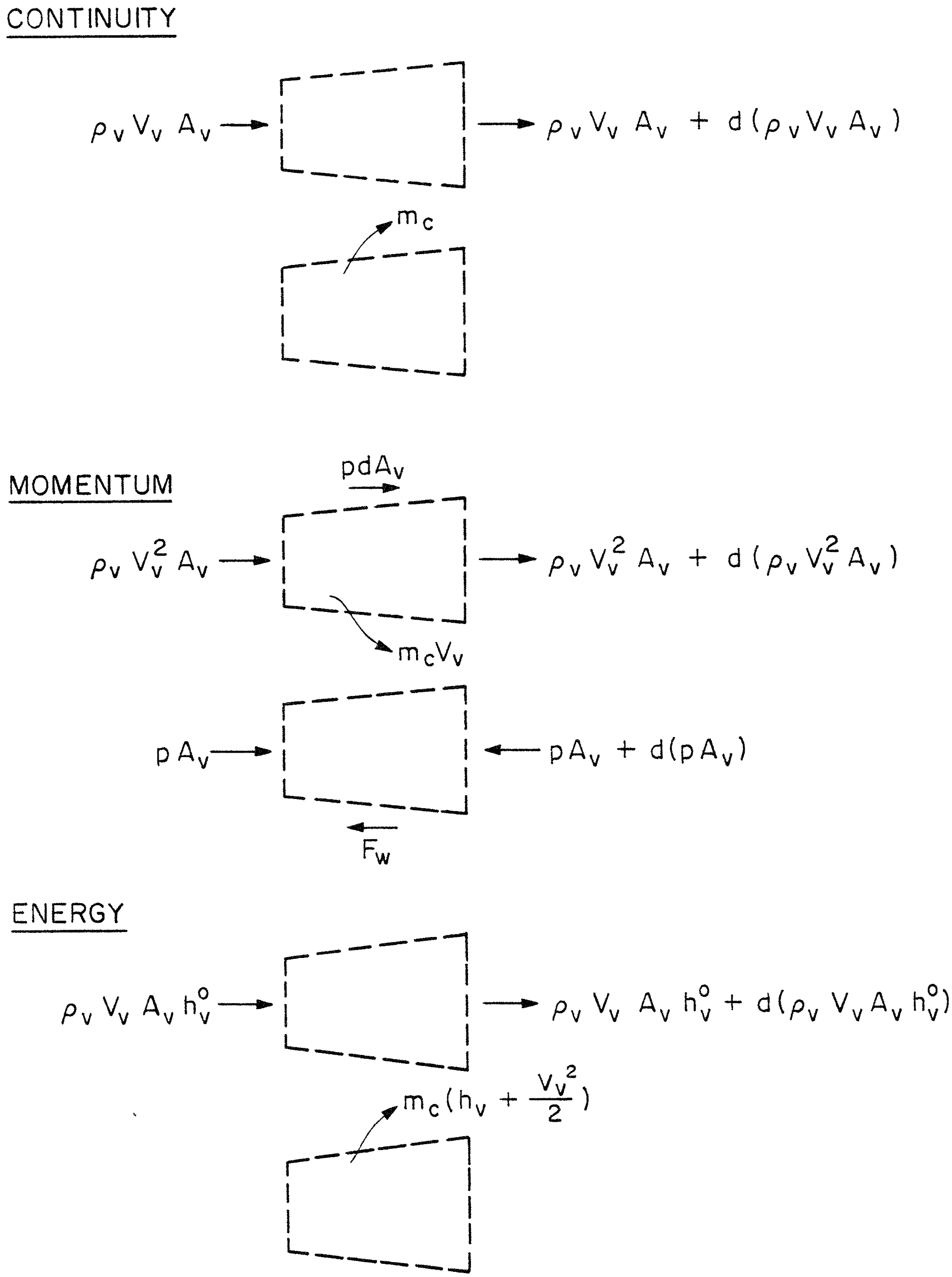

FIGURE 4c TERMS APPEARING IN CONSERVATION EQUATIONS FOR VAPOR ANNULUS

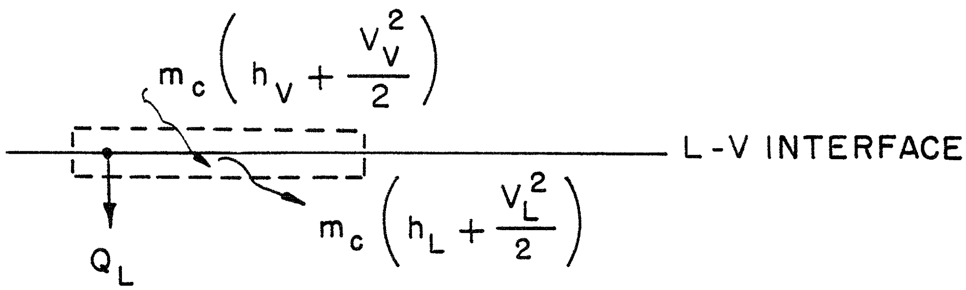

FIG. 4d TERMS APPEARING IN ENERGY EQUATION FOR CONTROL VOLUME III

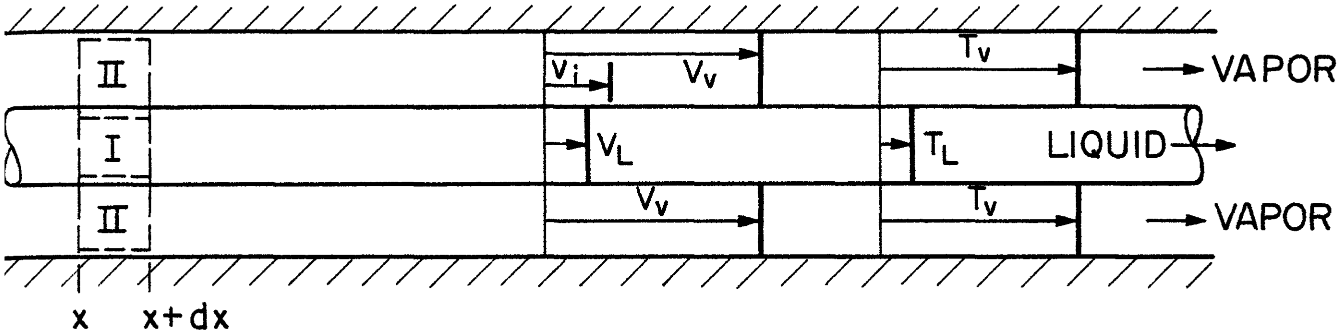

FIGURE 5a CONTROL VOLUMES, TEMPERATURE AND VELOCITY PROFILES FOR SHEAR MODEL

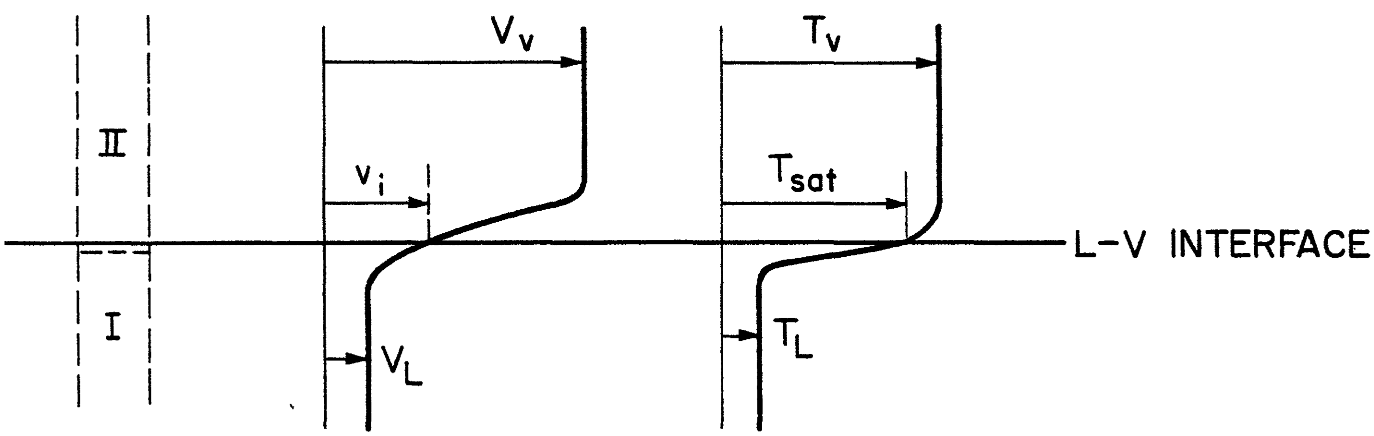

FIGURE 5b TEMPERATURE AND VELOCITY PROFILES IN THE VICINITY OF THE LIQUID-VAPOR INTERFACE

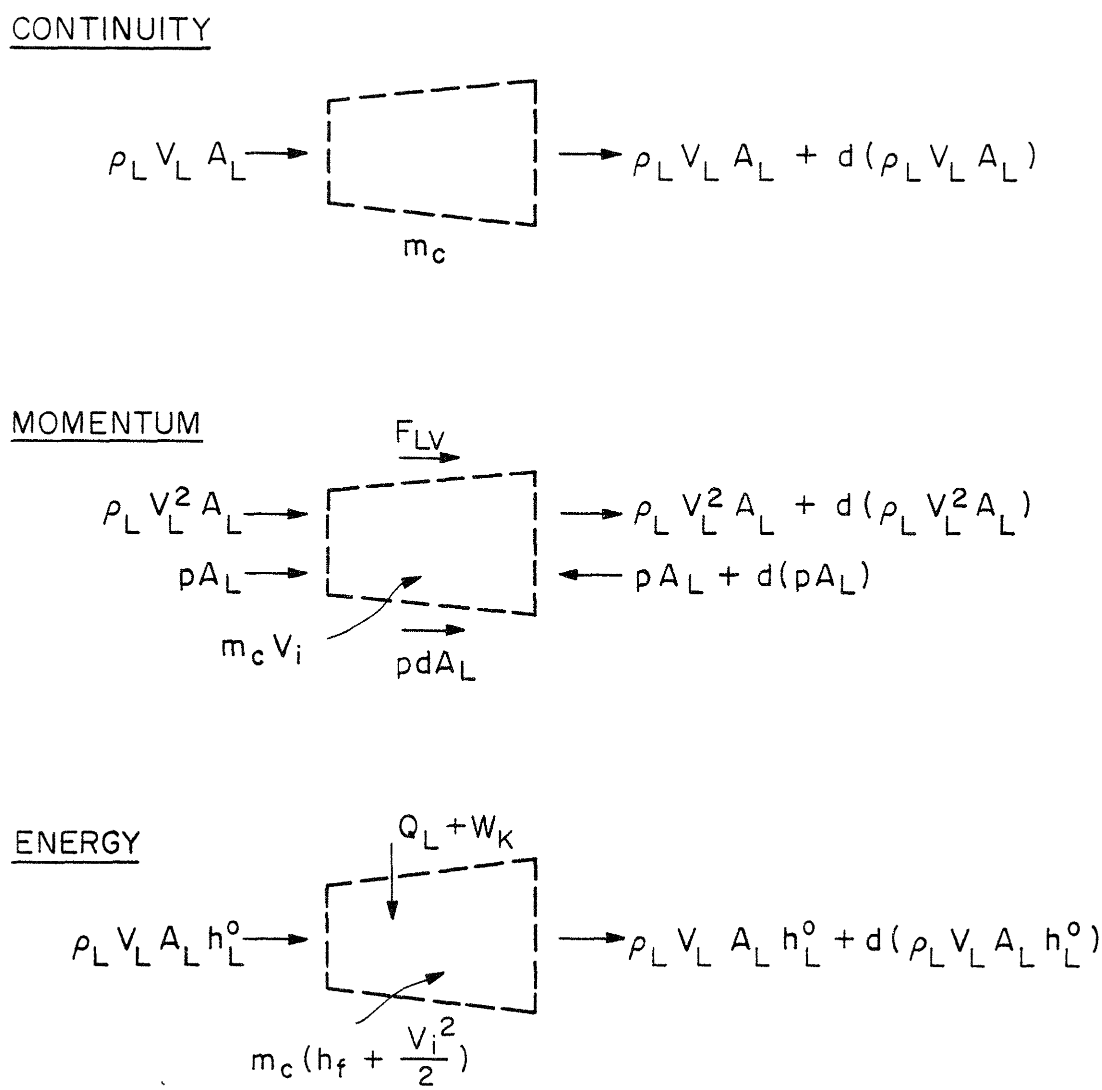

FIGURE 5c TERMS APPEARING IN CONSERVATION EQUATIONS FOR CONTROL VOLUME I

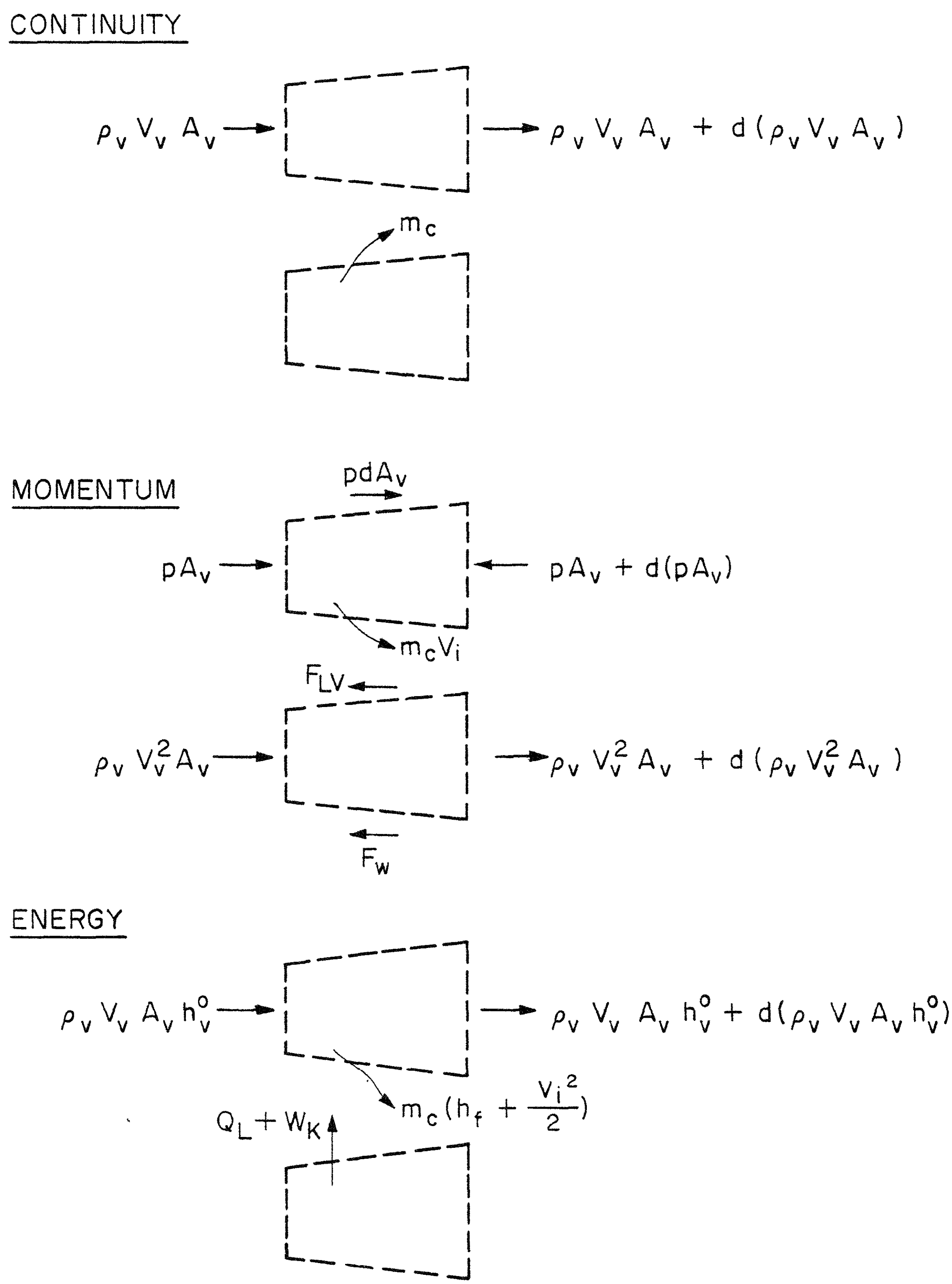

FIGURE 5d TERMS APPEARING IN CONSERVATION EQUATIONS FOR CONTROL VOLUME II

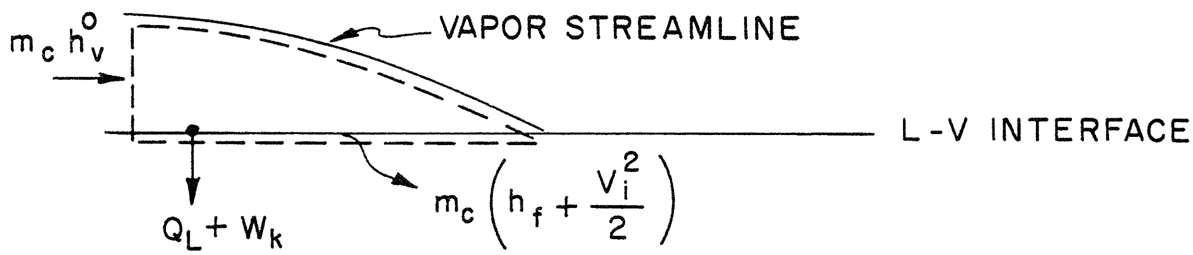

FIG. 5e CONTROL VOLUME III FOR THE SHEAR MODEL

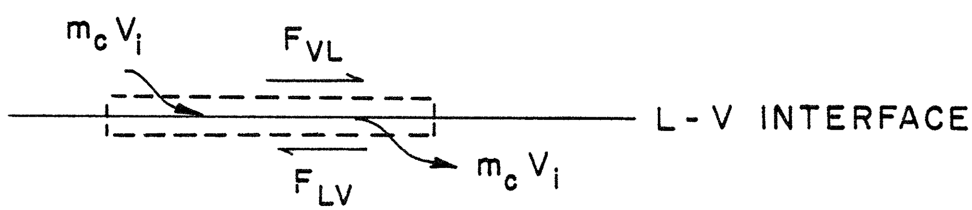

FIG. 5f CONTROL VOLUME FOR INTERFACIAL MOMENTUM EQUATION

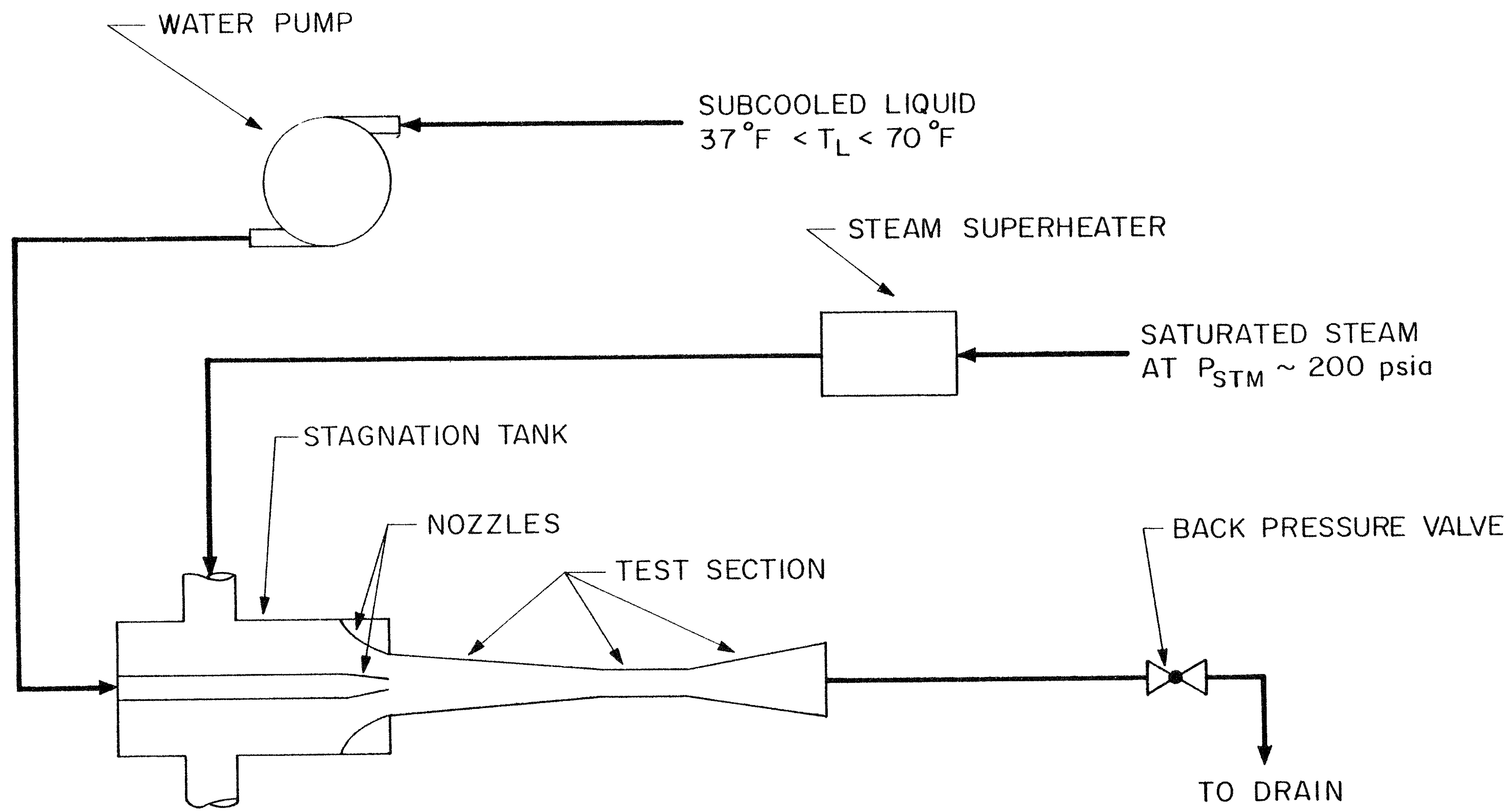

FIGURE 6 DIAGRAM OF STEAM–WATER CONDENSING EJECTOR TEST FACILITY

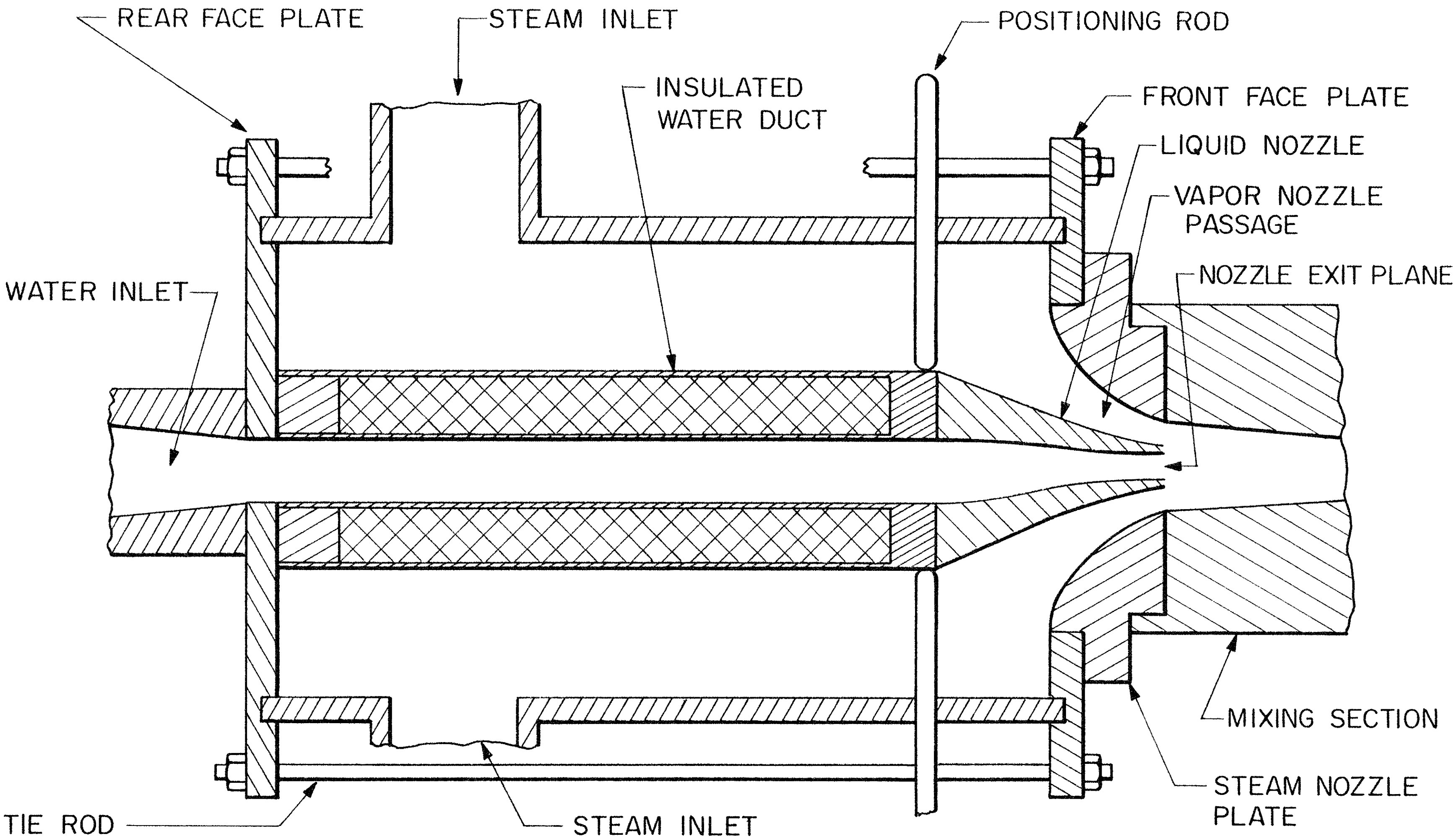

FIGURE 7 DIAGRAM OF STAGNATION CHAMBER WITH LIQUID AND VAPOR NOZZLES

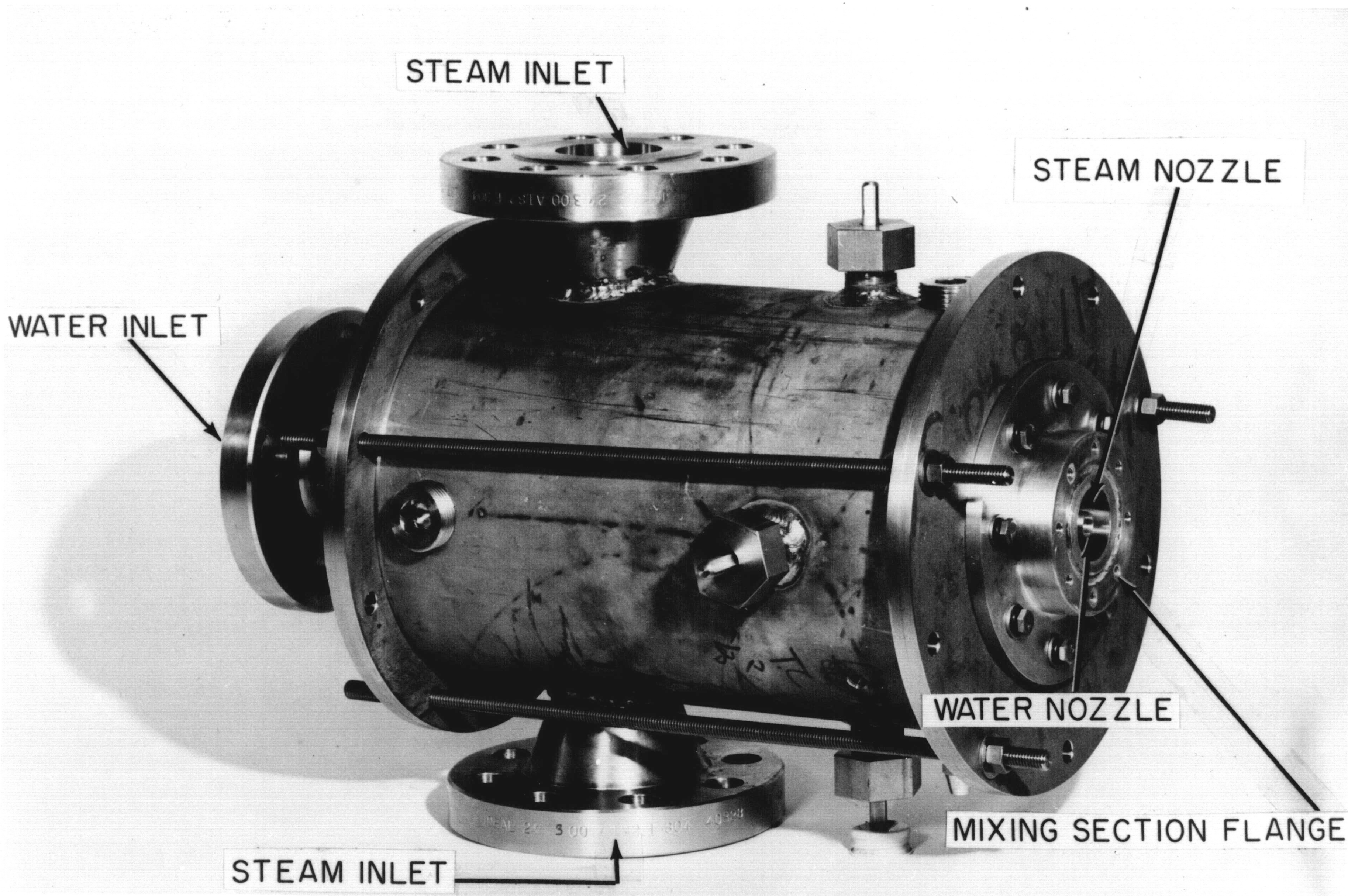

FIGURE 7a. STAGNATION CHAMBER.

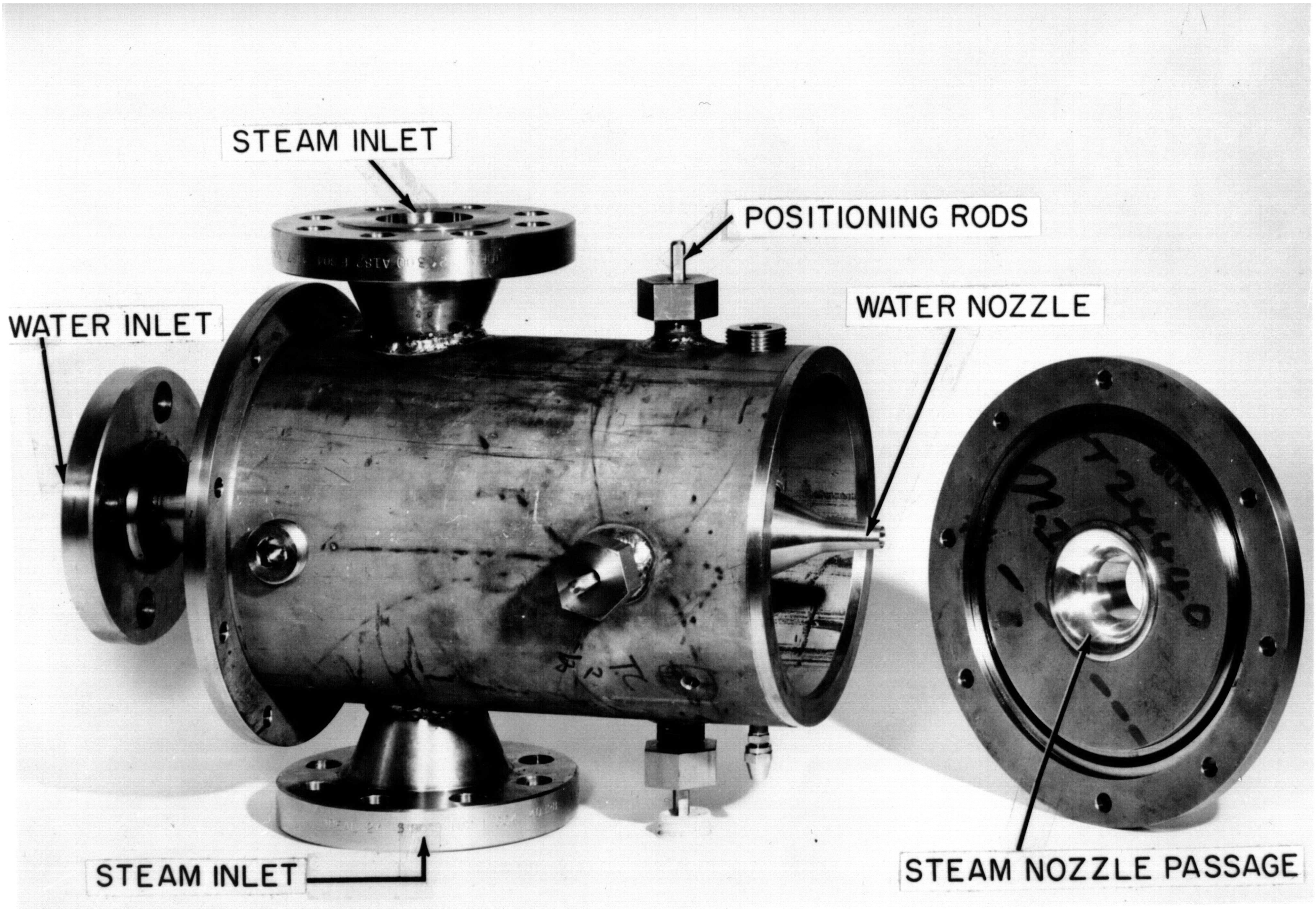

FIGURE 7b. STAGNATION CHAMBER.

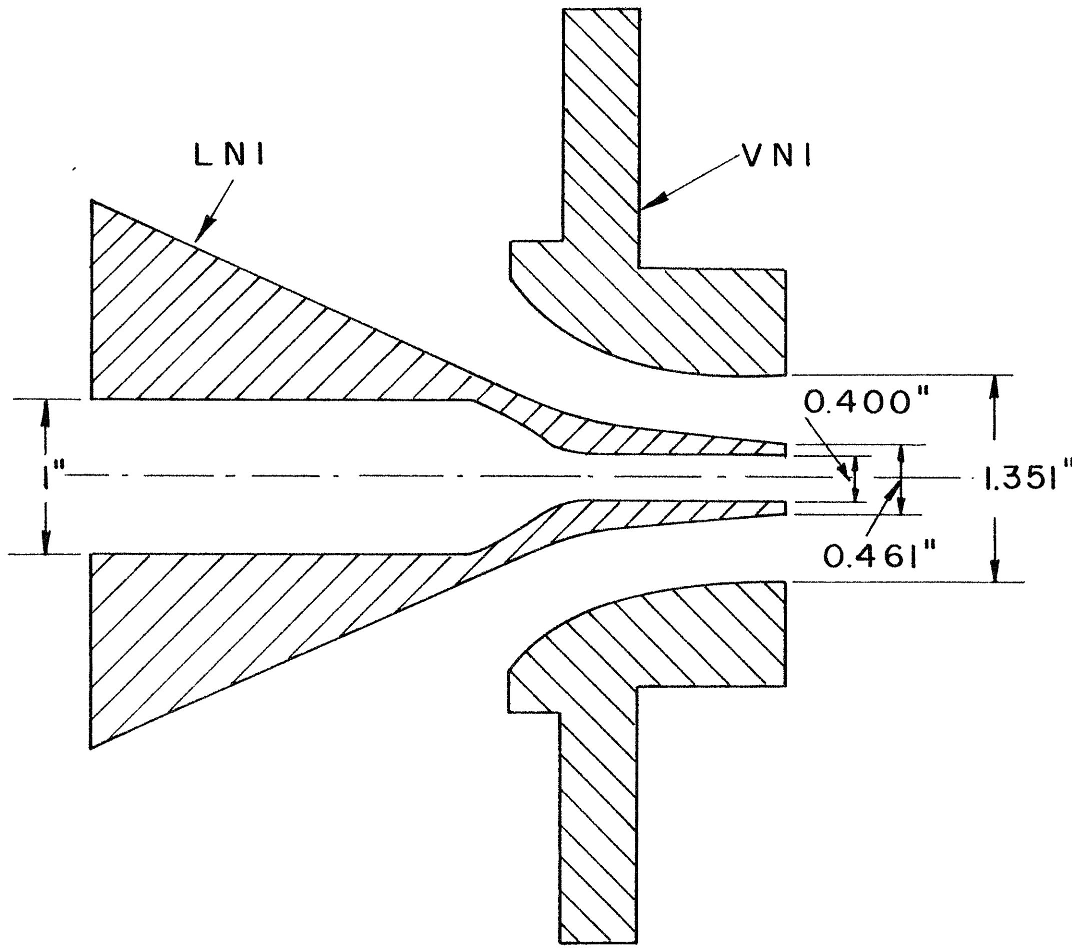

FIG. 8 LIQUID AND VAPOR NOZZLES LN1 - VN1

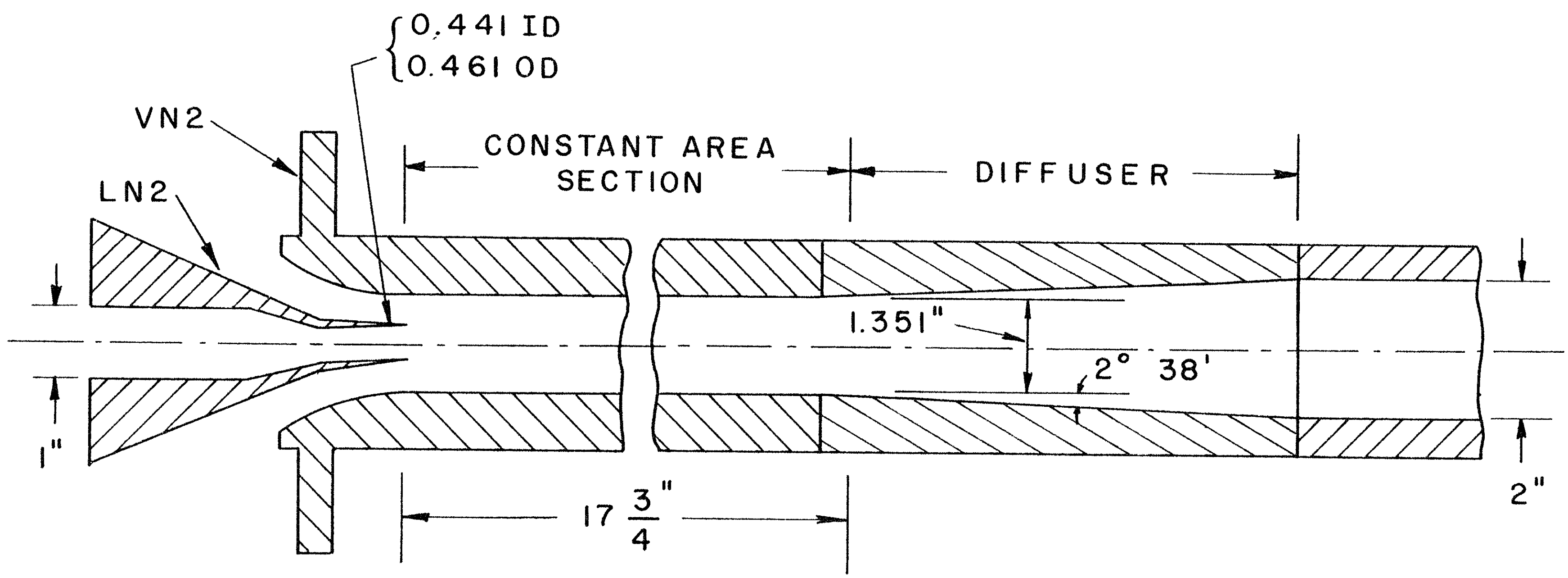

FIG. 9 LIQUID AND VAPOR NOZZLES LN2 - VN2 AND CONSTANT AREA TEST SECTION TS 3

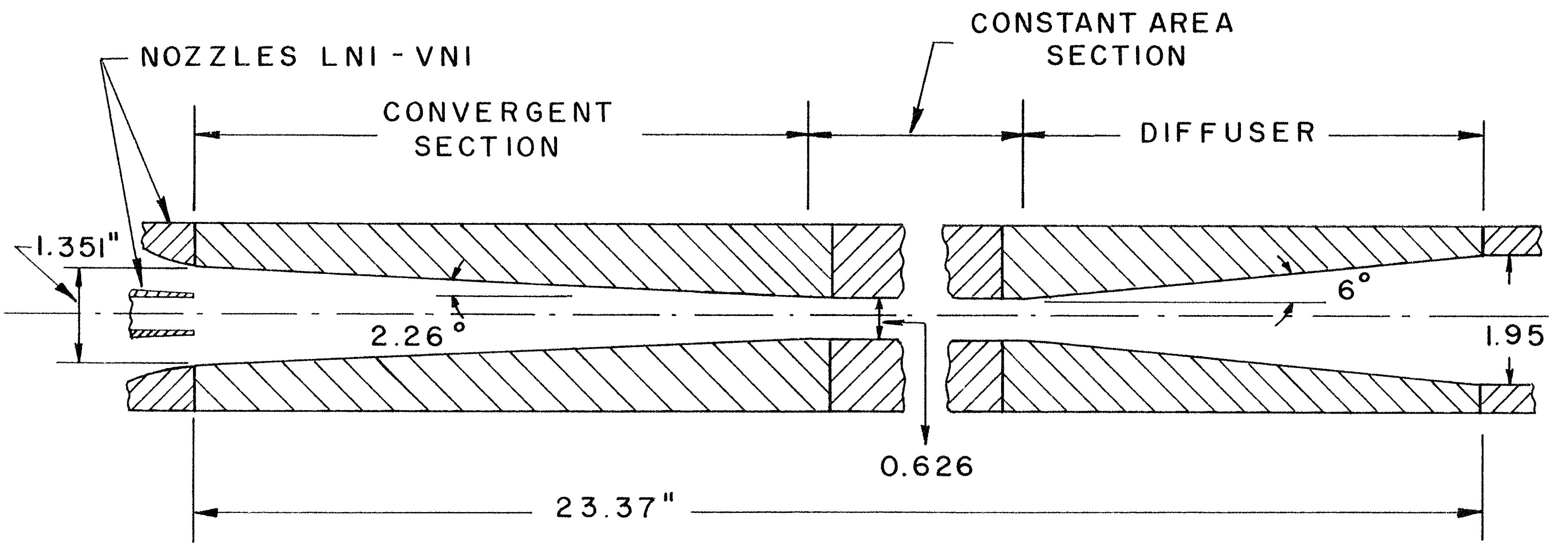

FIG. 10 5/1 CONVERGENT - DIVERGENT TEST SECTION TSI

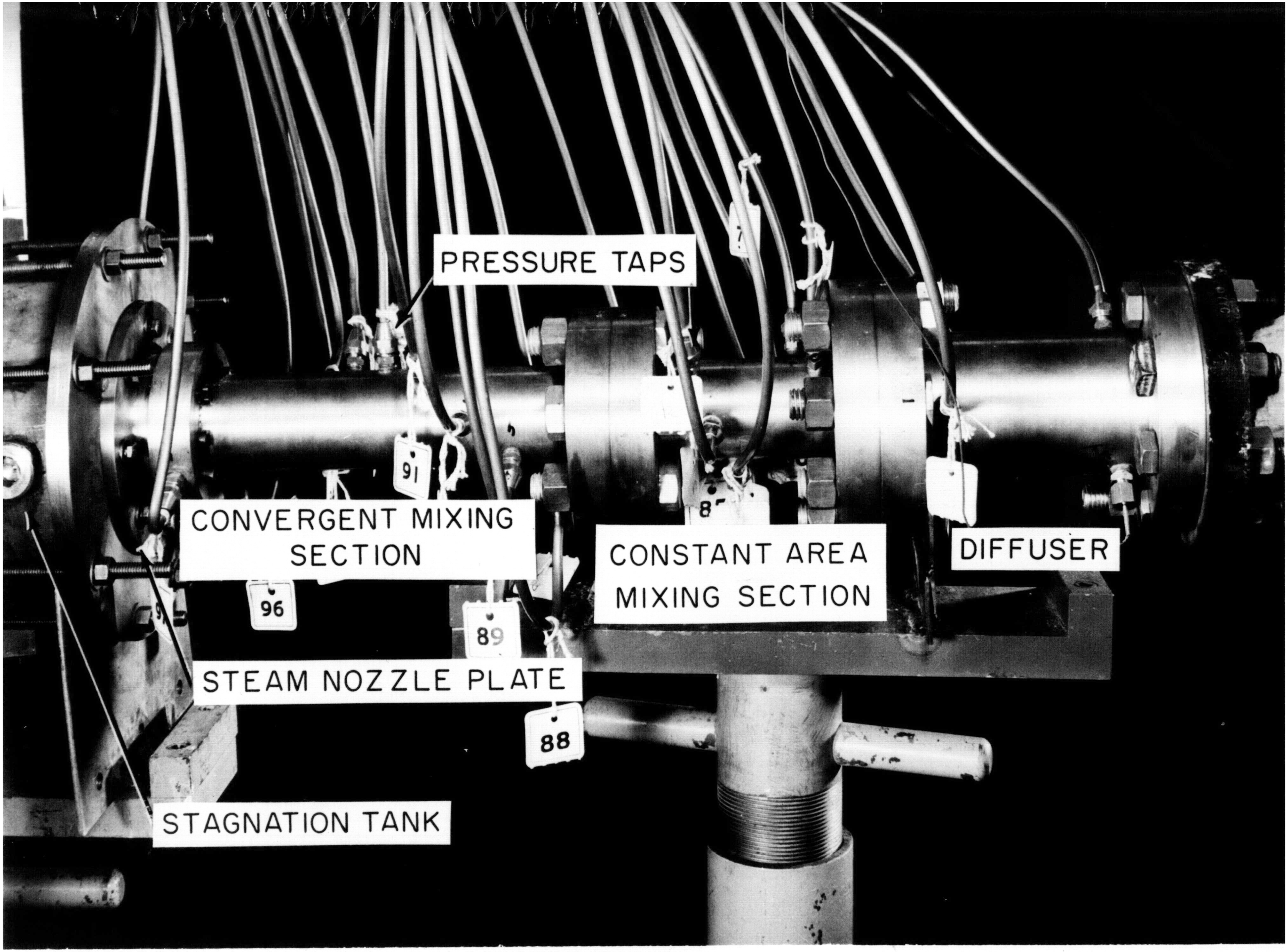

FIGURE 10a. TEST SECTION TS1.

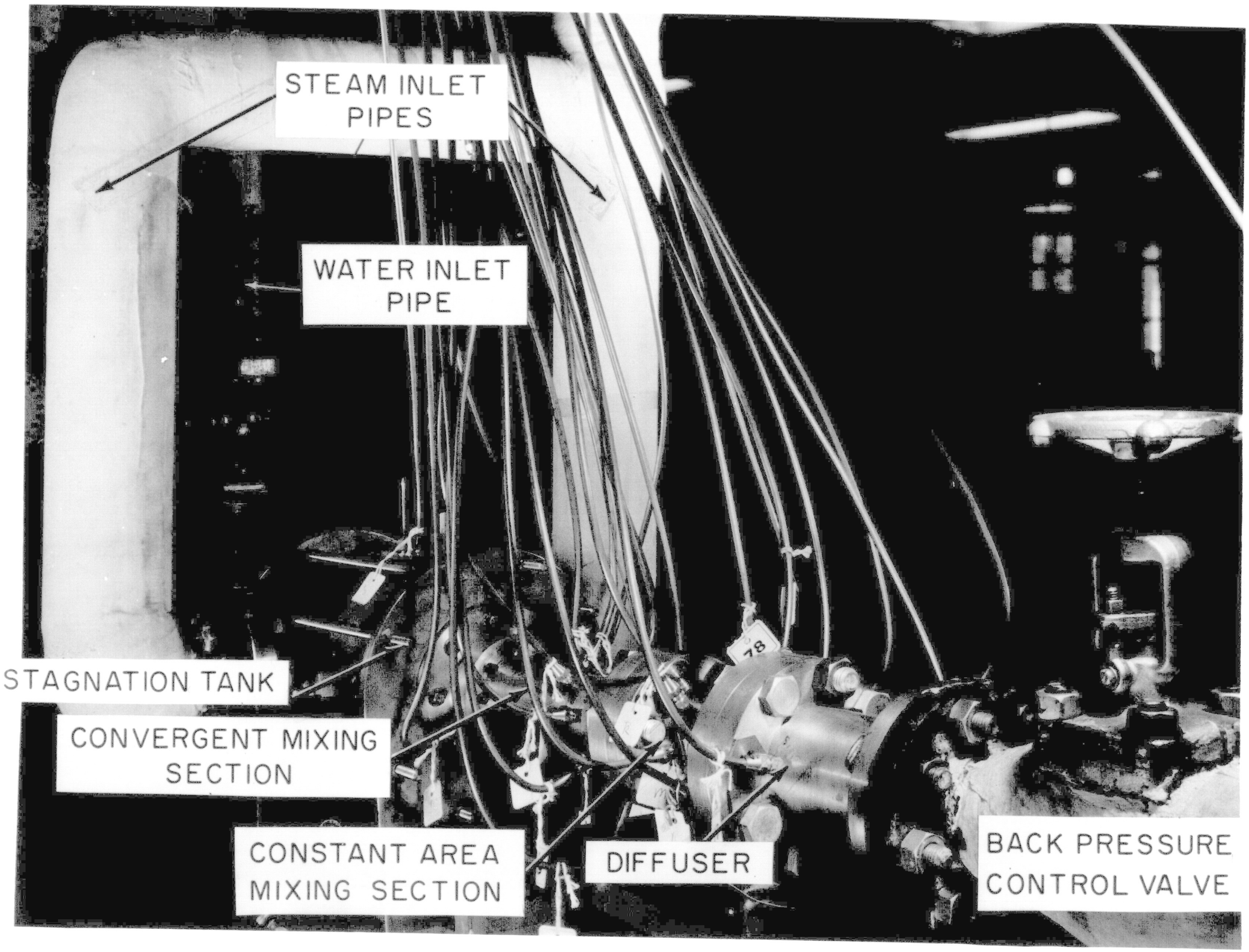

FIGURE 10b. TEST SECTION TS1.

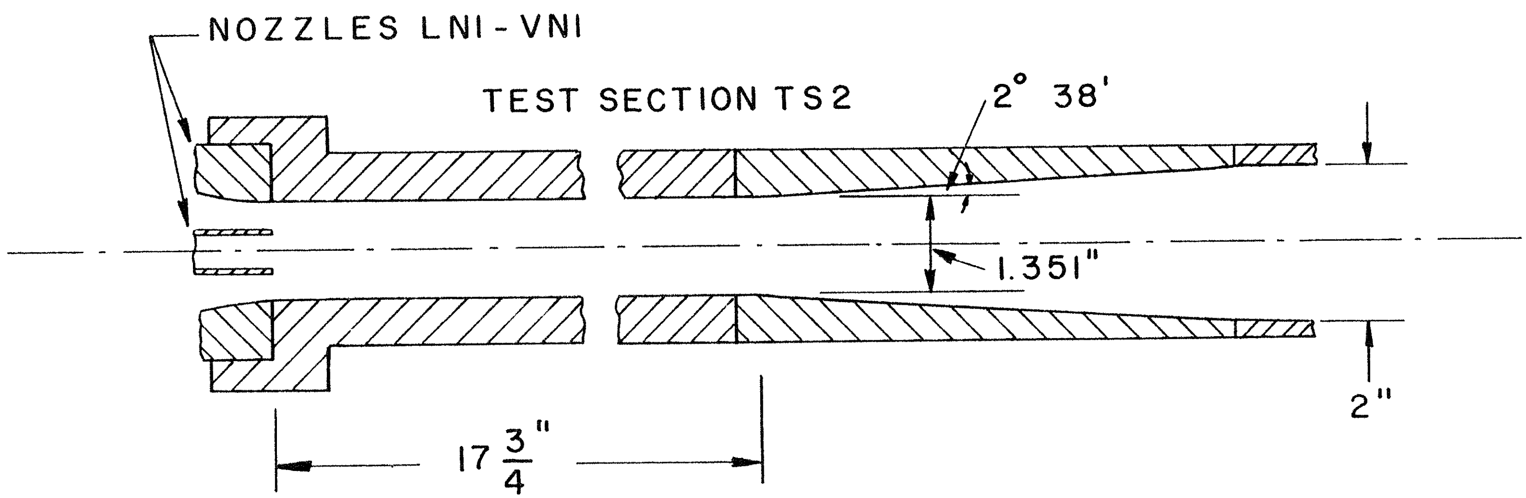

FIG. II PLASTIC CONSTANT AREA TEST SECTION TS2

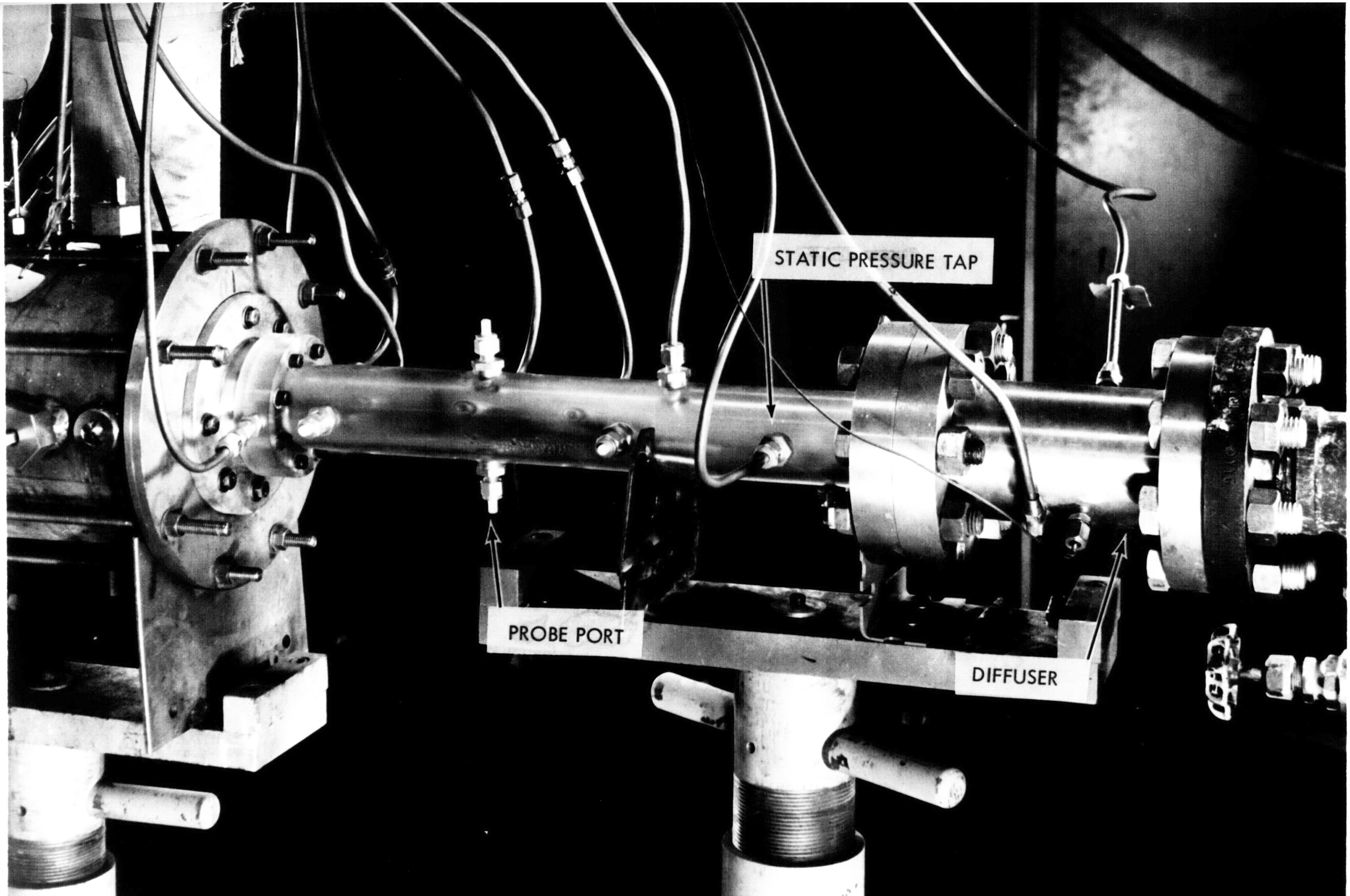

FIGURE IIa PLASTIC TEST SECTION

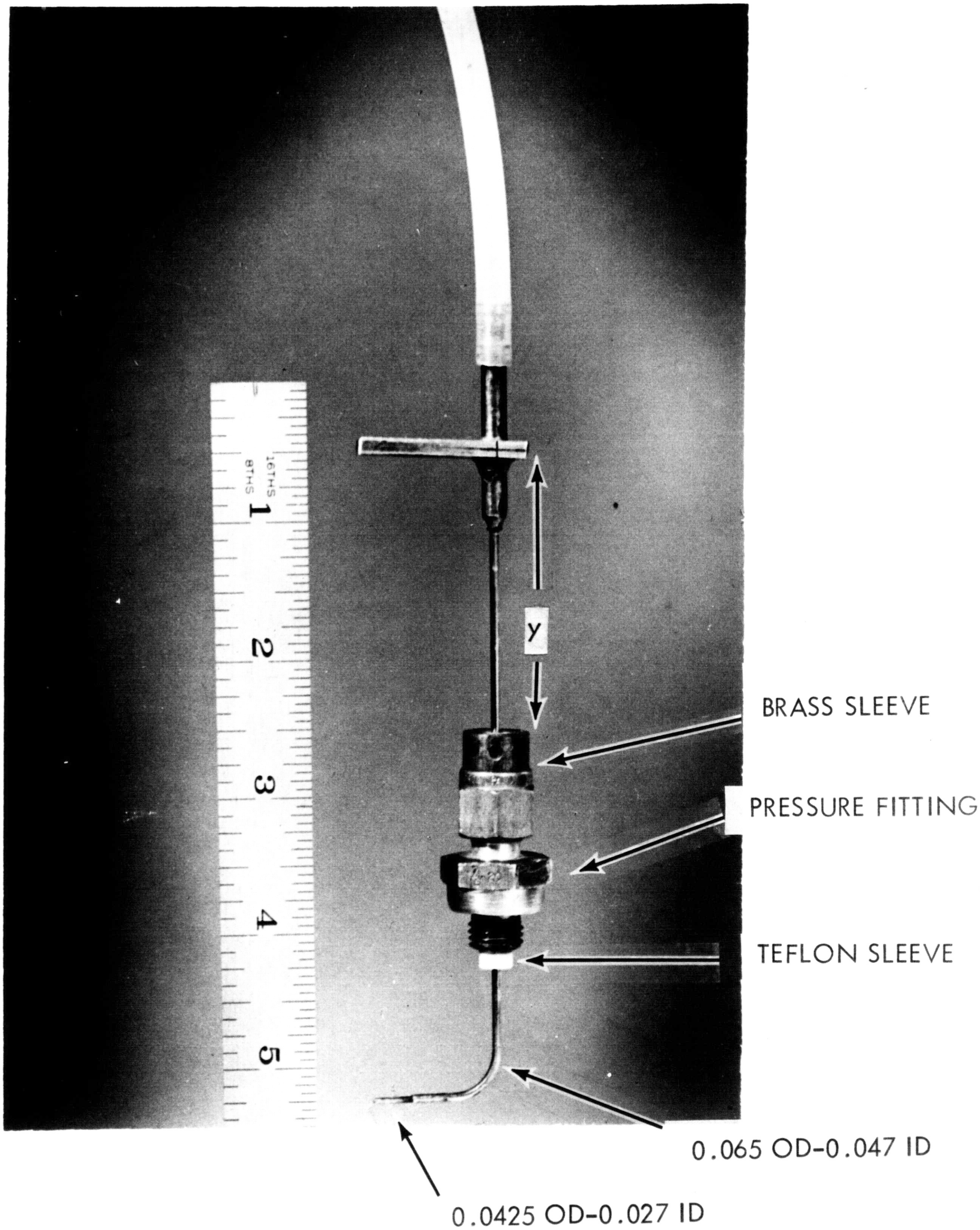

FIGURE 12 DETAILS OF AN IMPACT PRESSURE PROBE

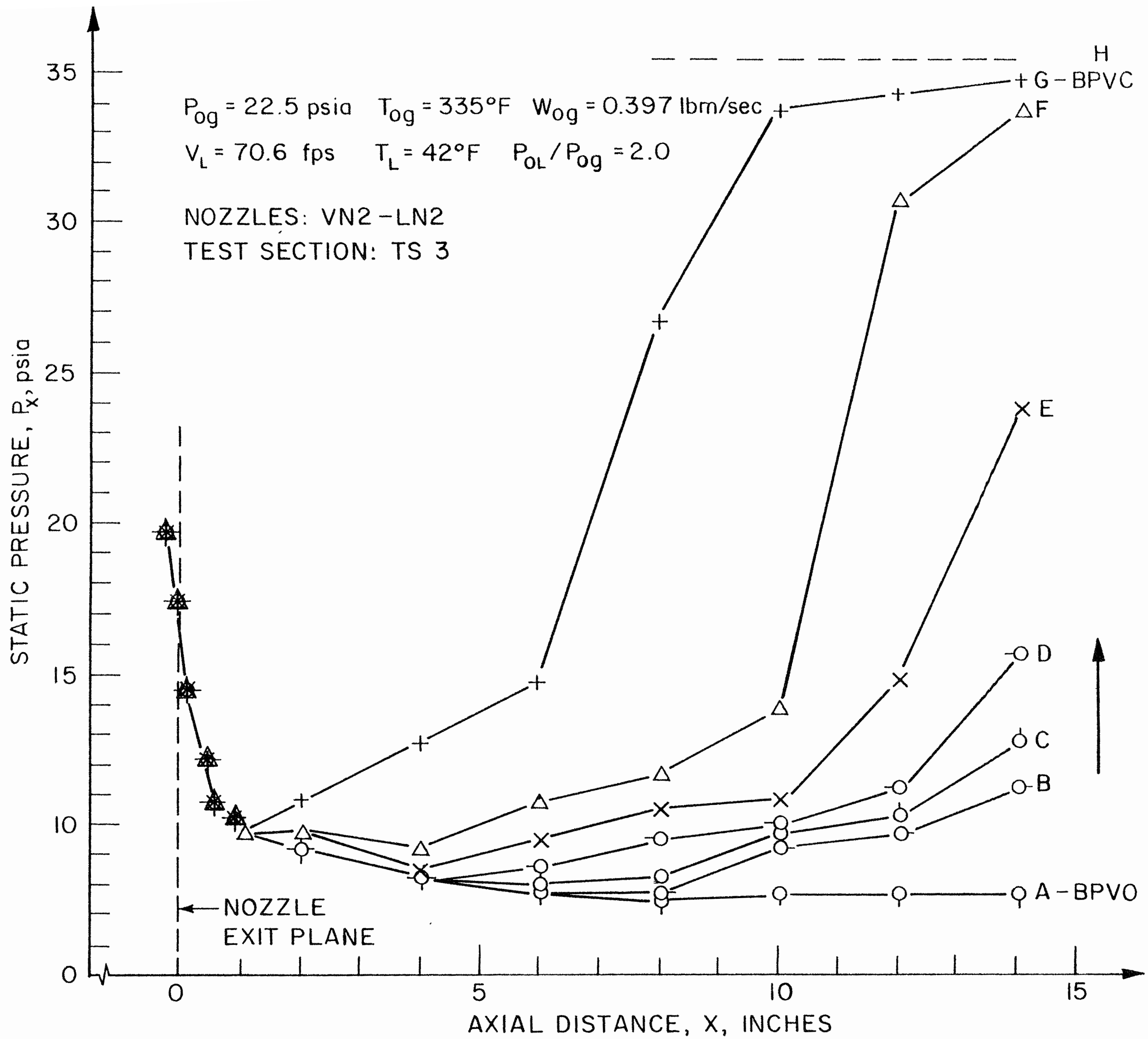

FIGURE 13 EFFECT OF BACK PRESSURE ON AXIAL PRESSURE DISTRIBUTION

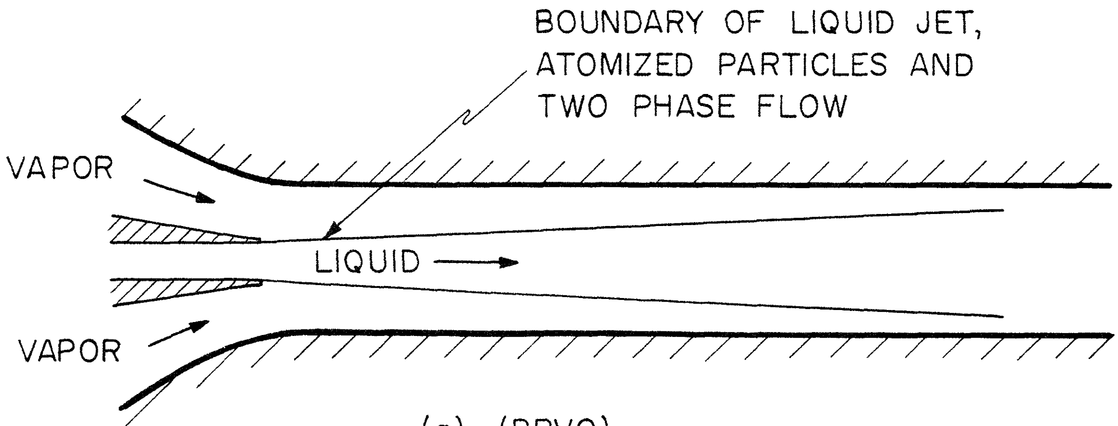

(a) (BPVO)

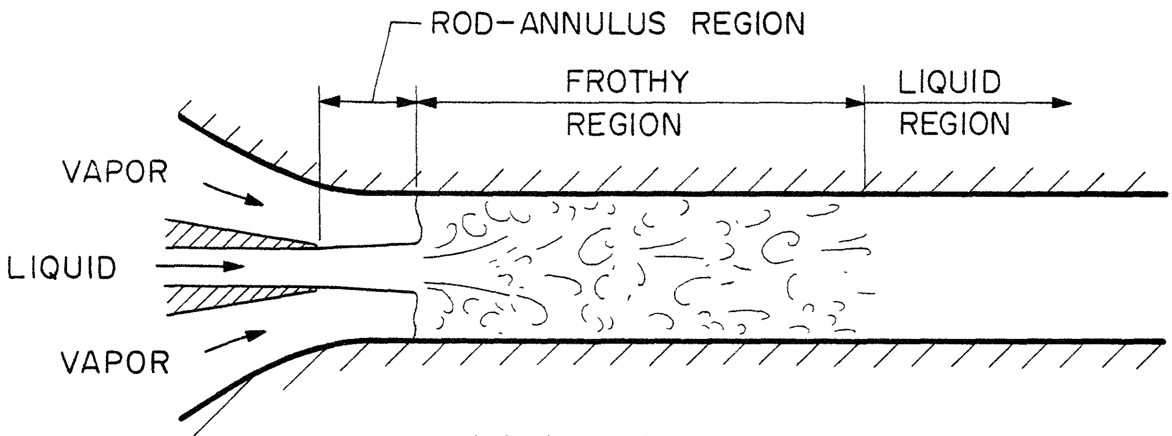

(b) (BPVC)

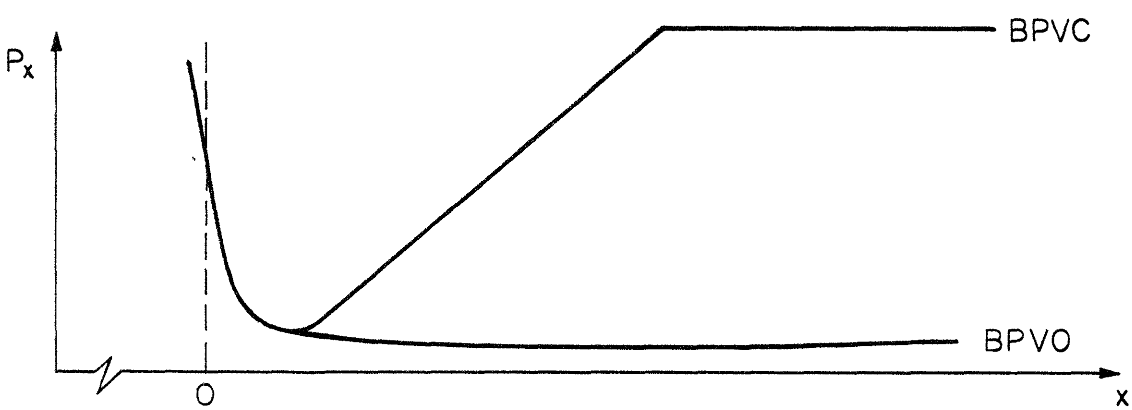

(c) PRESSURE DISTRIBUTIONS

FIGURE 14 DIAGRAM OF CE OPERATION AT p_{og} = 22.5 psia AND V_L = 70.6 fps WITH BPVO AND BPVC

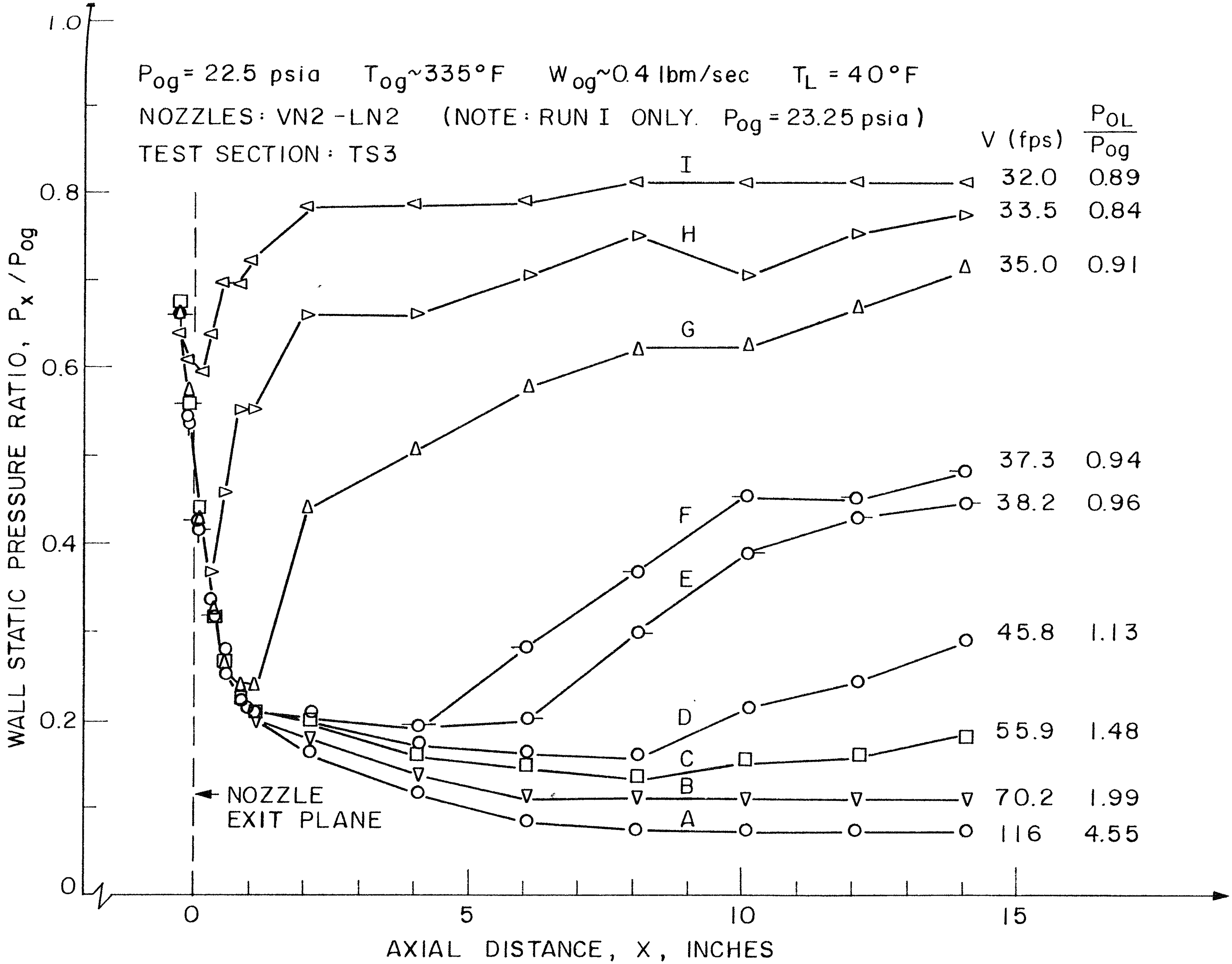

FIGURE 15 EFFECT OF INLET LIQUID VELOCITY ON AXIAL PRESSURE DISTRIBUTION (BPVO)

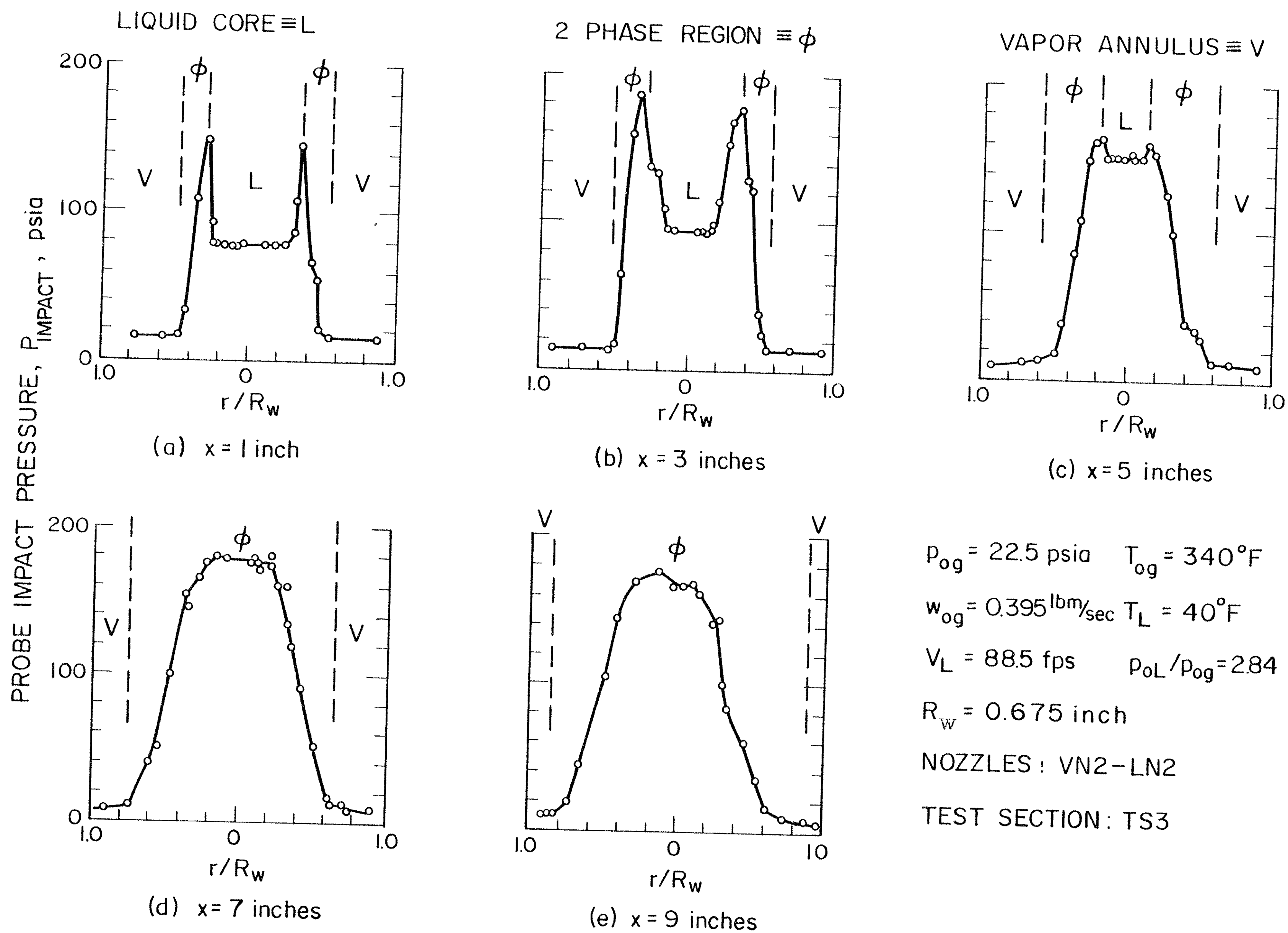

p_{og} = 22.5 psia T_{og} = 340°F

w_{og} = 0.395 lbm/sec T_L = 40°F

V_L = 88.5 fps p_{oL}/p_{og} = 2.84

R_W = 0.675 inch

NOZZLES: VN2-LN2

TEST SECTION: TS3

FIGURE 16 RADIAL IMPACT PRESSURE PROFILES

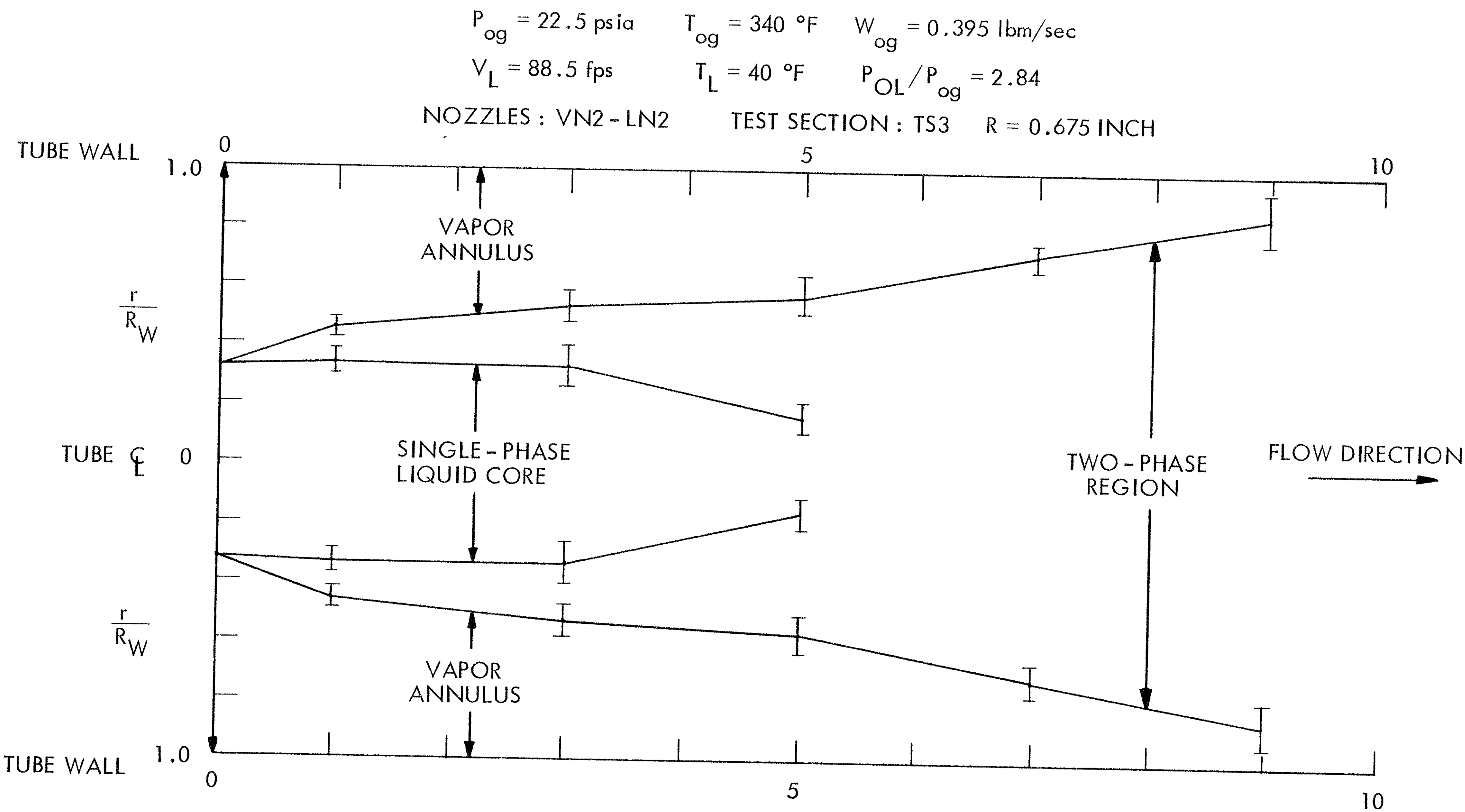

FIGURE 17. BOUNDARIES OF SINGLE - PHASE AND TWO - PHASE FLOW REGIONS (BPVO)

P_{og} = 22.5 psia T_{og} = 340 °F W_{og} = 0.395 lbm/sec
V_L = 88.5 fps T_L = 40 °F P_{OL}/P_{og} = 2.84

NOZZLES : VN2 - LN2 TEST SECTION : TS3 R = 1.351 INCHES

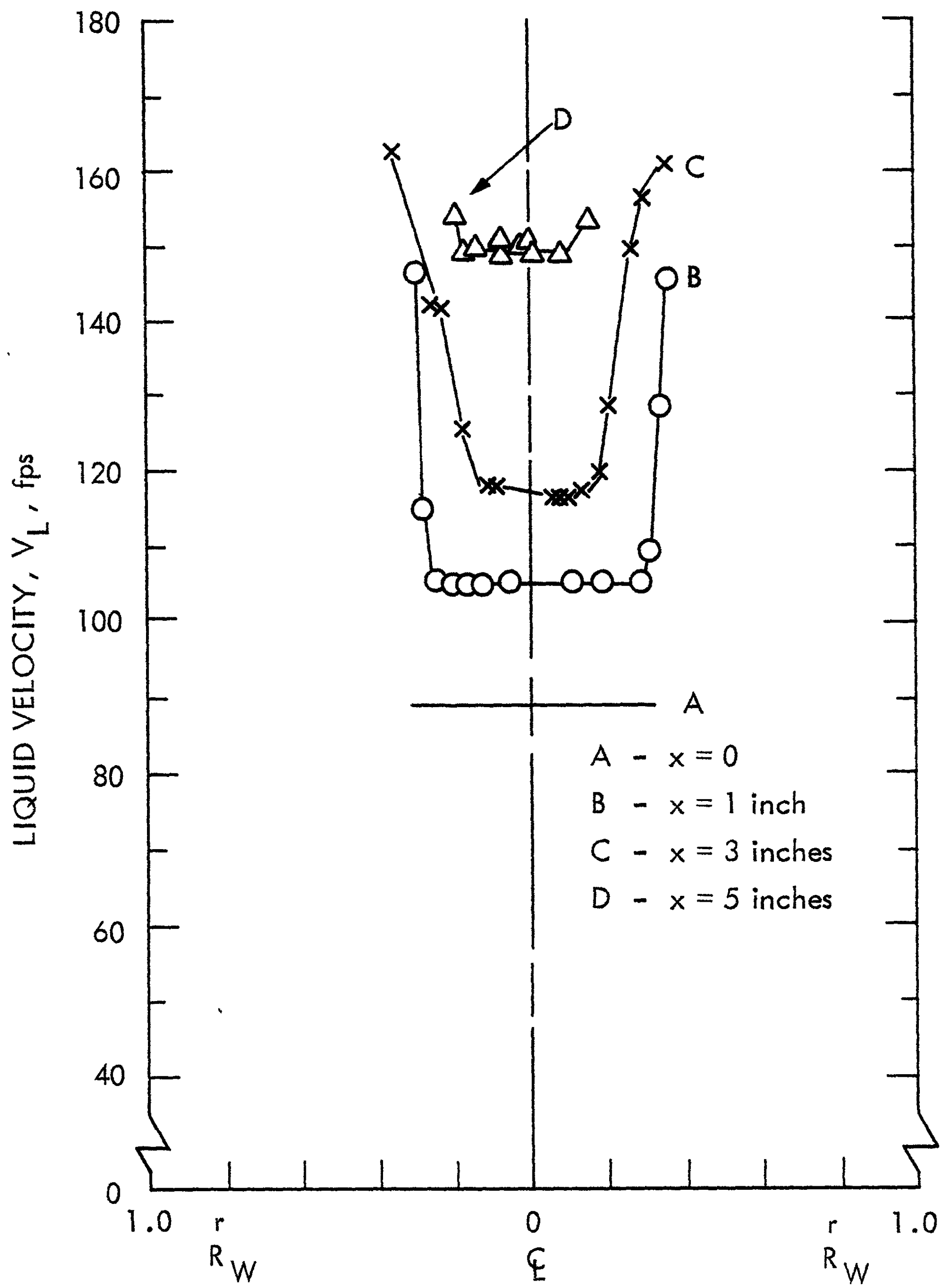

FIGURE 18. RADIAL VELOCITY PROFILES WITHIN LIQUID CORE REGION (BPVO)
(POINTS CALCULATED FROM PROFILES OF FIGURE 16 a, b, c)

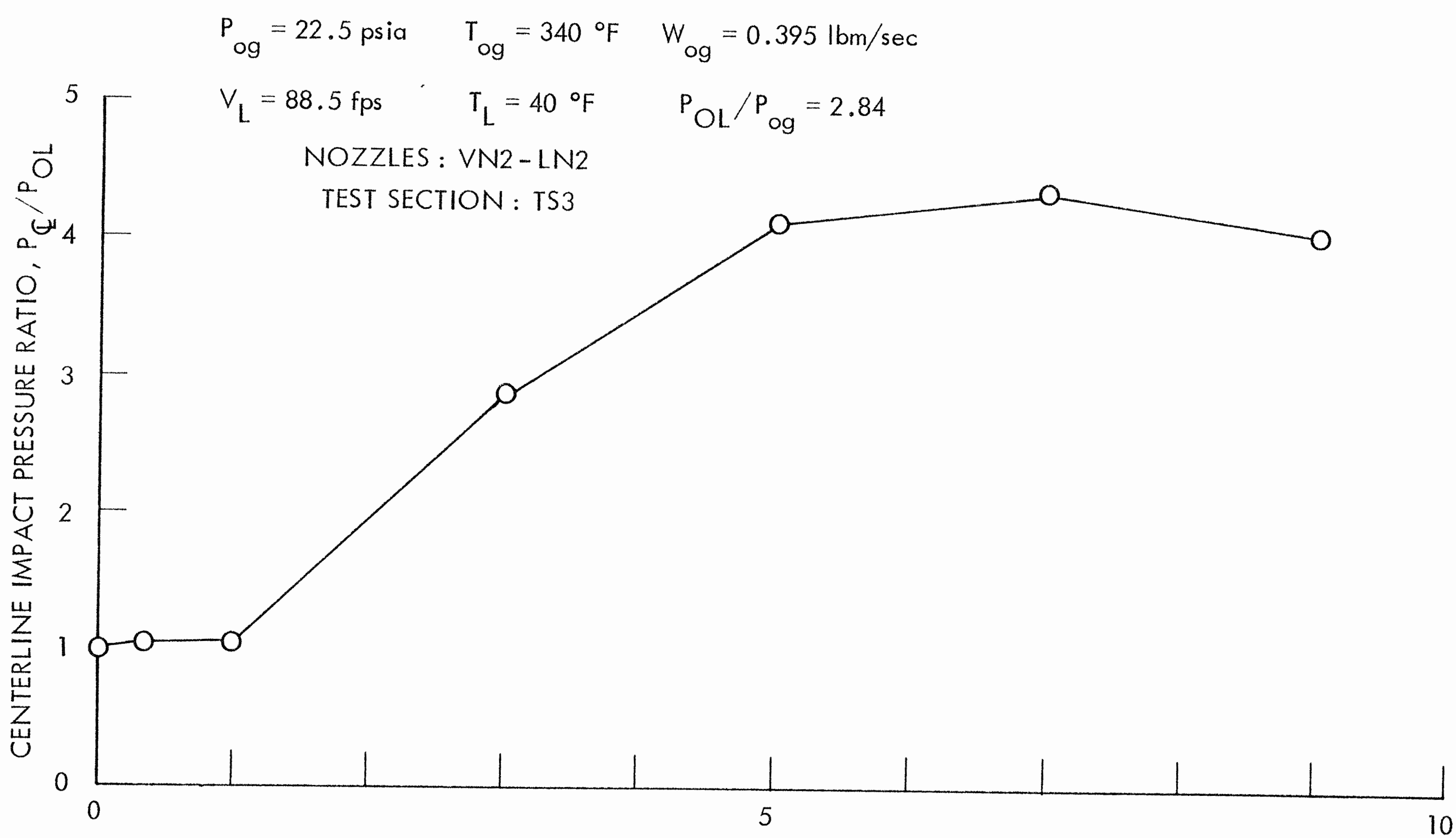

FIGURE 19. AXIAL VARIATION OF CENTERLINE IMPACT PRESSURE (BPVO)

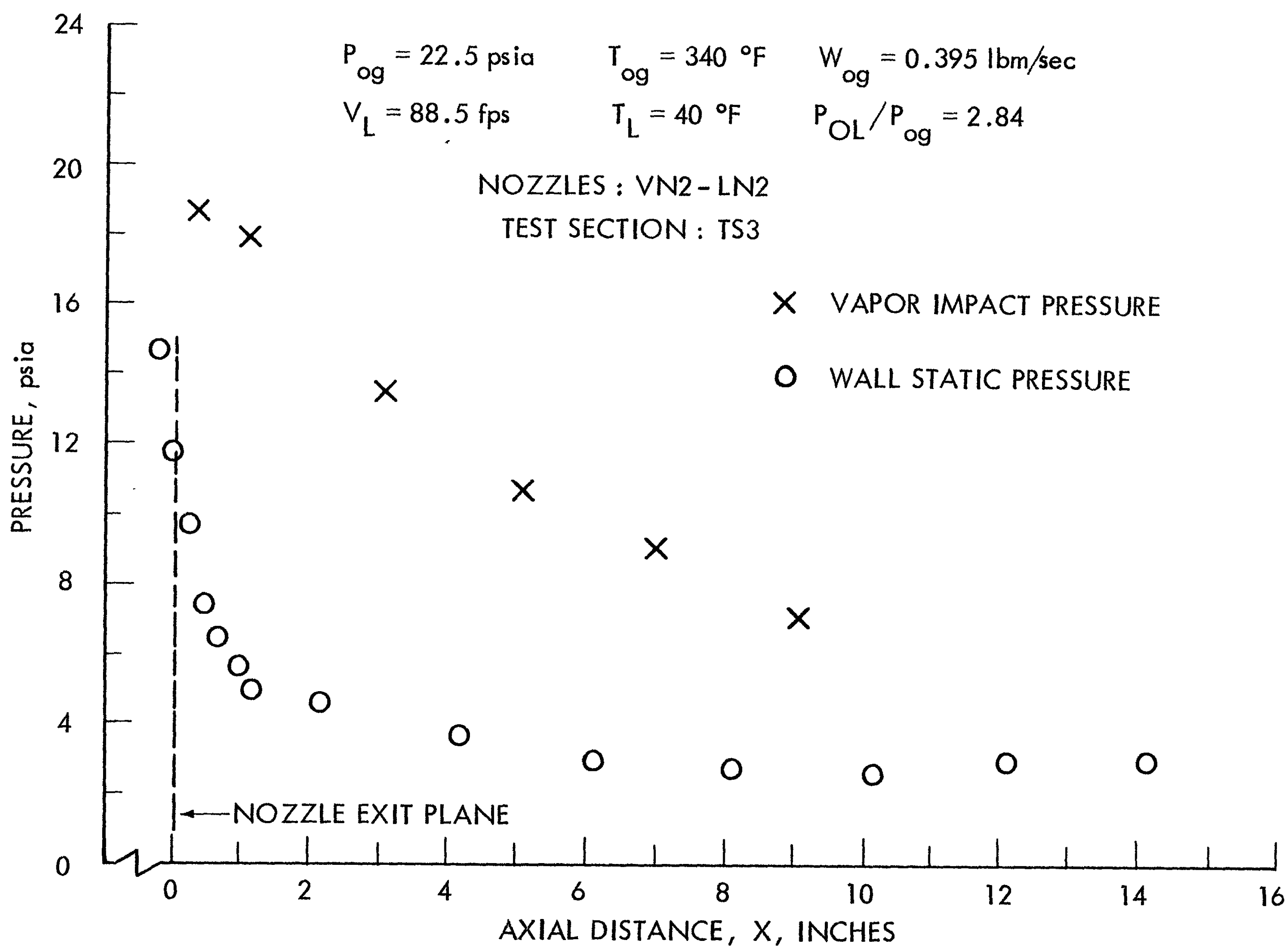

FIGURE 20. AXIAL VARIATION OF VAPOR IMPACT PRESSURE AND WALL STATIC PRESSURE (BPVO)

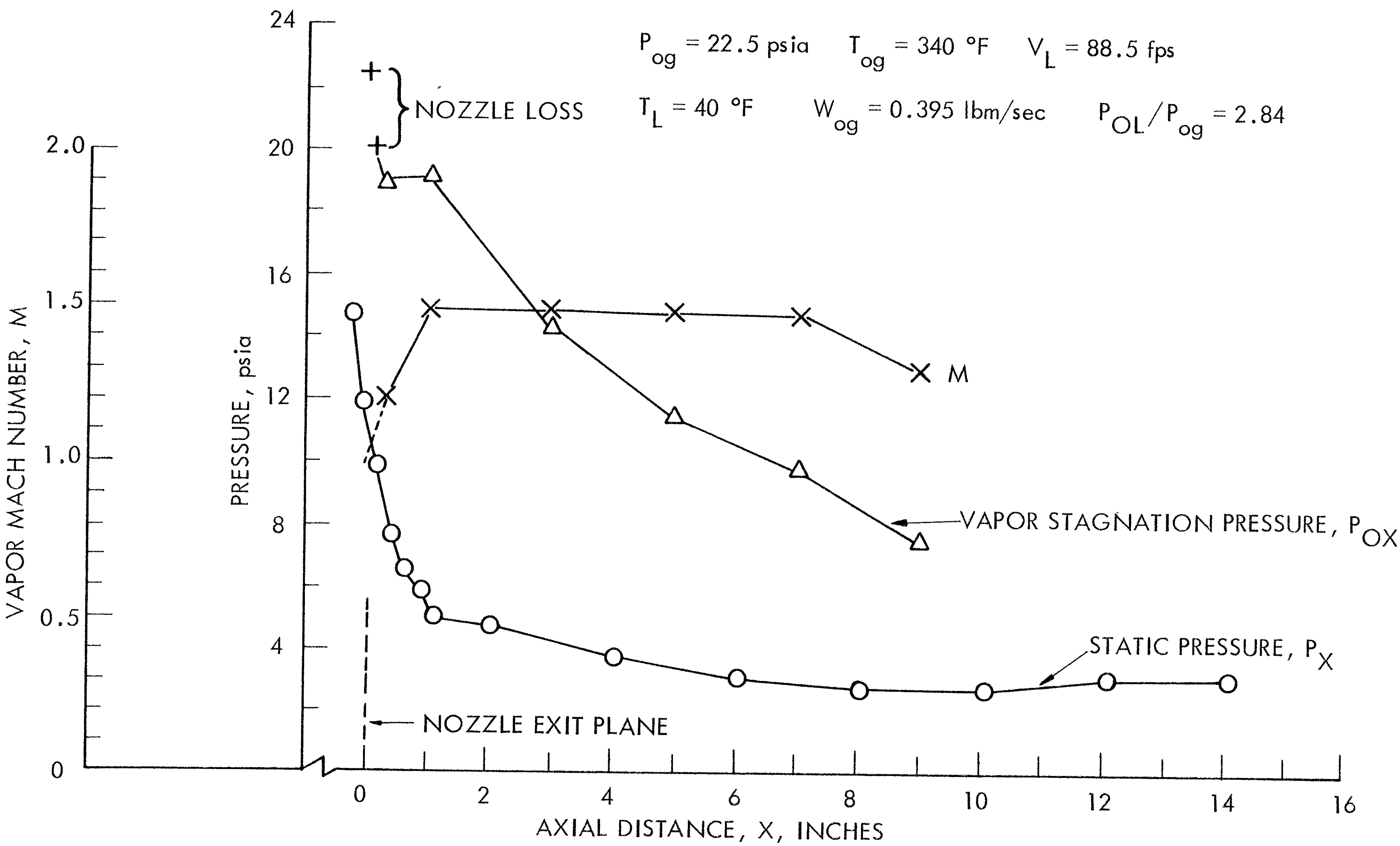

FIGURE 21 AXIAL VARIATION OF VAPOR MACH NUMBER, VAPOR STAGNATION PRESSURE, AND WALL STATIC PRESSURE (BPVO)

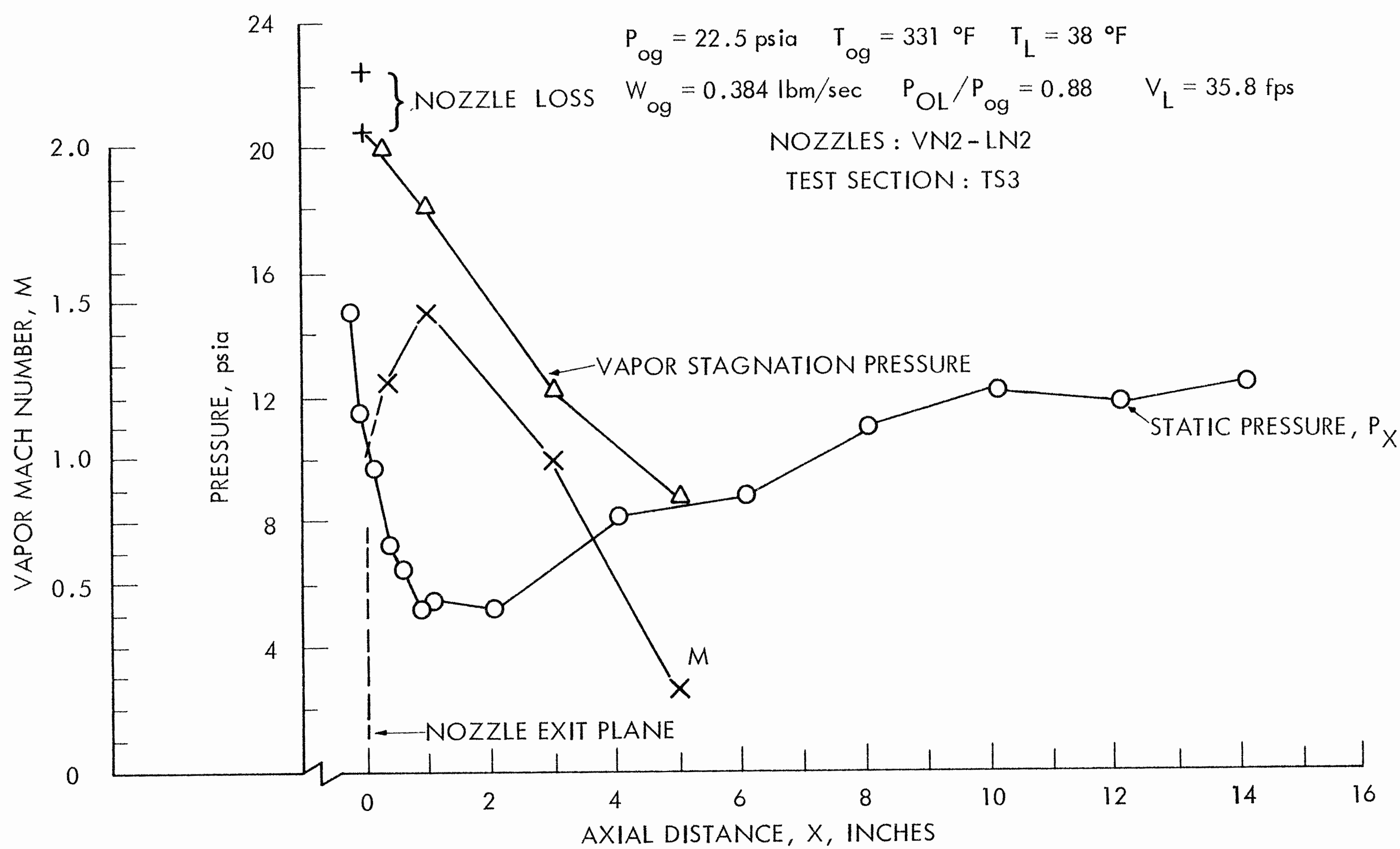

FIGURE 22. AXIAL VARIATION OF VAPOR MACH NUMBER, VAPOR STAGNATION PRESSURE AND WALL STATIC PRESSURE (BPVO)

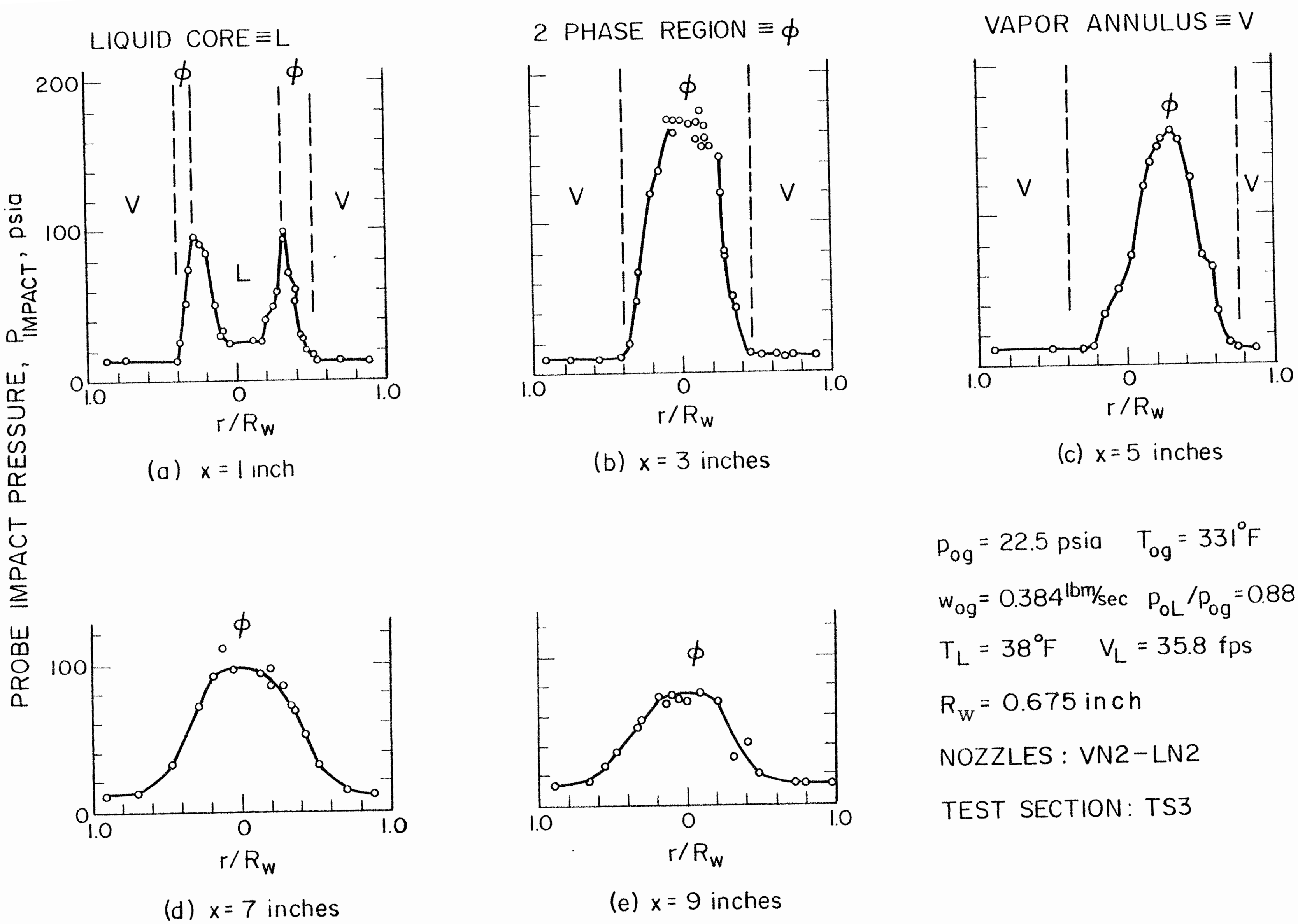

FIGURE 23 RADIAL IMPACT PRESSURE PROFILES

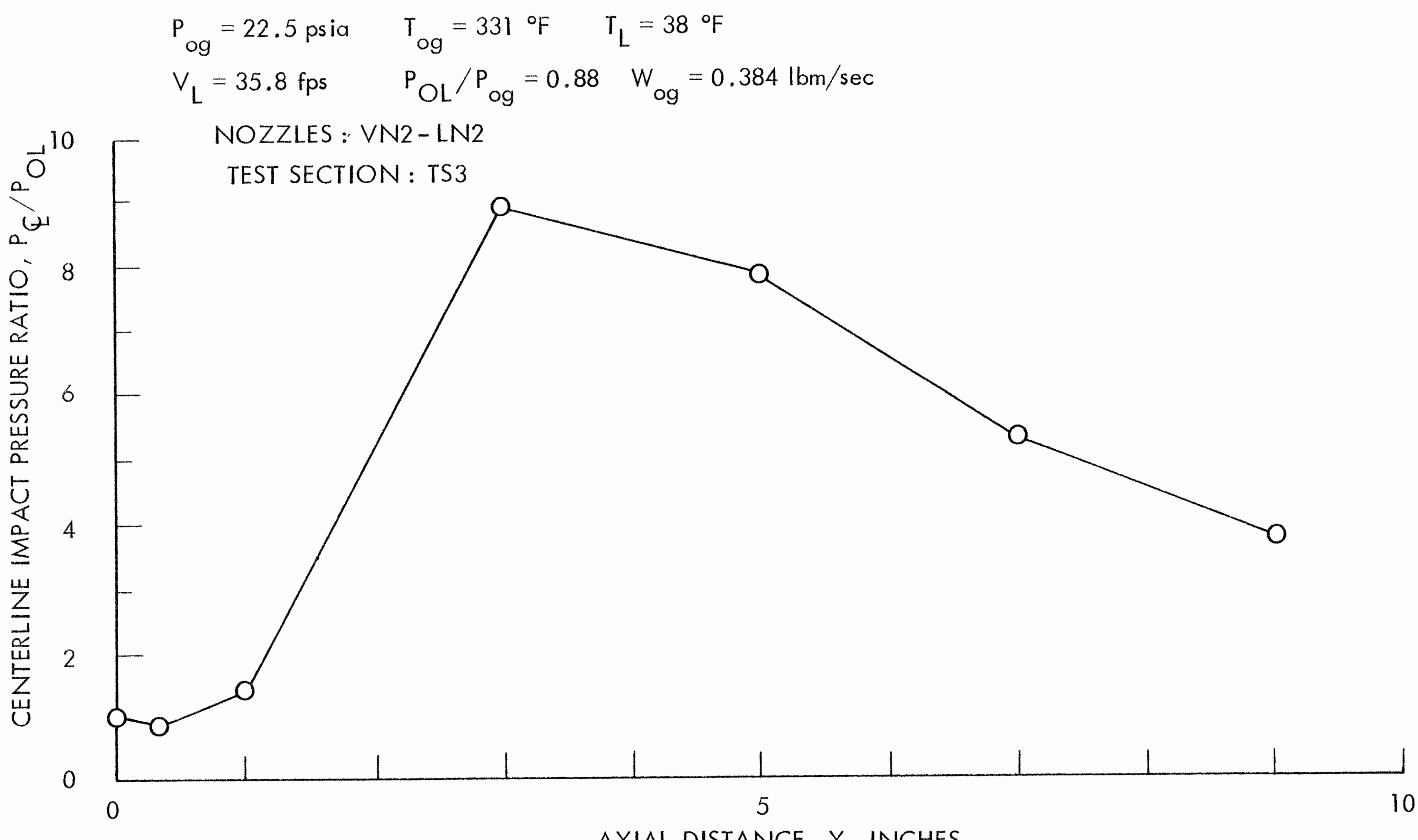

FIGURE 24. AXIAL VARIATION OF CENTERLINE IMPACT PRESSURE (BPVO)

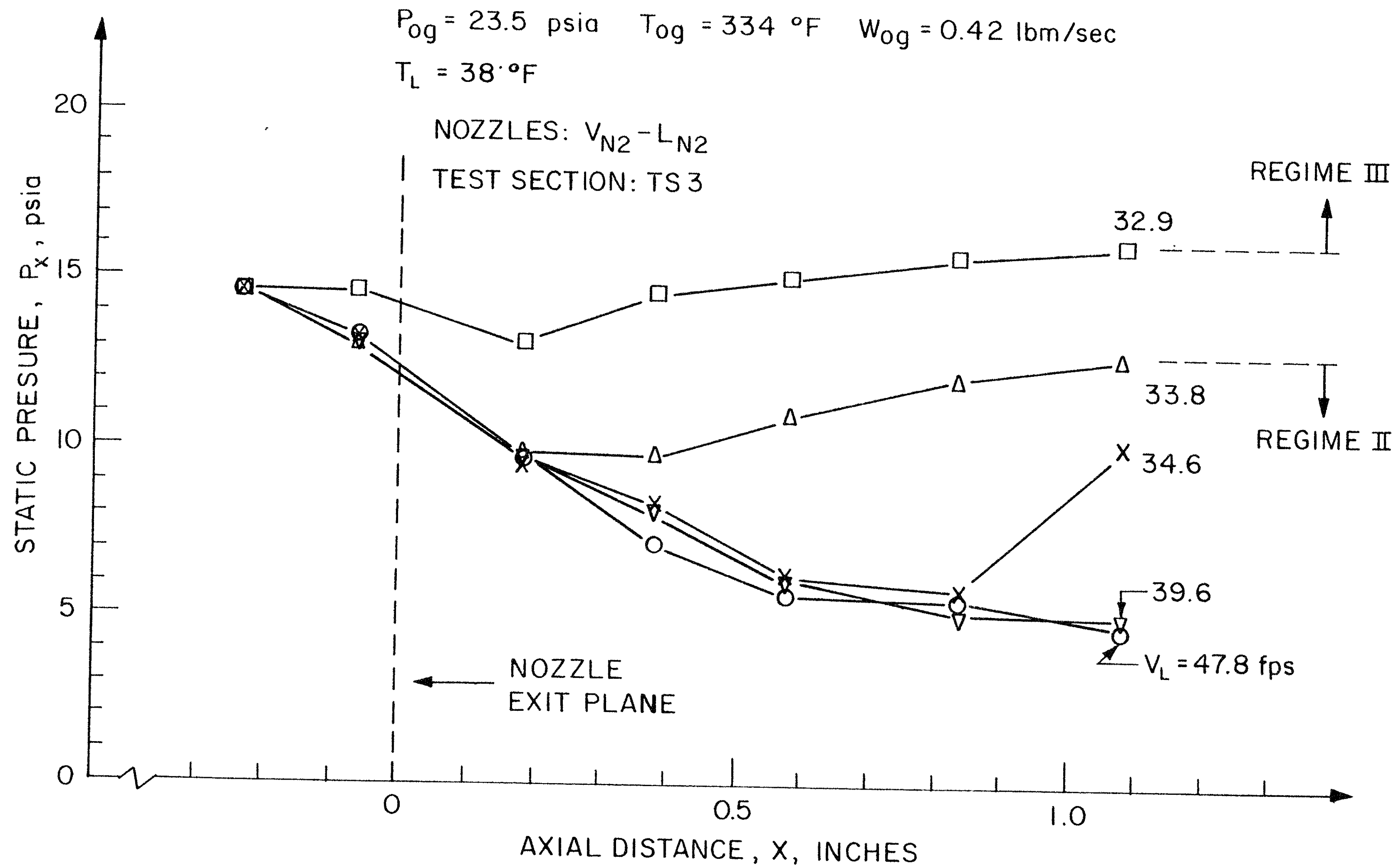

FIGURE 25 SUBSONIC-SUPERSONIC TRANSITION AT THE MIXING SECTION INLET. (BPVO)

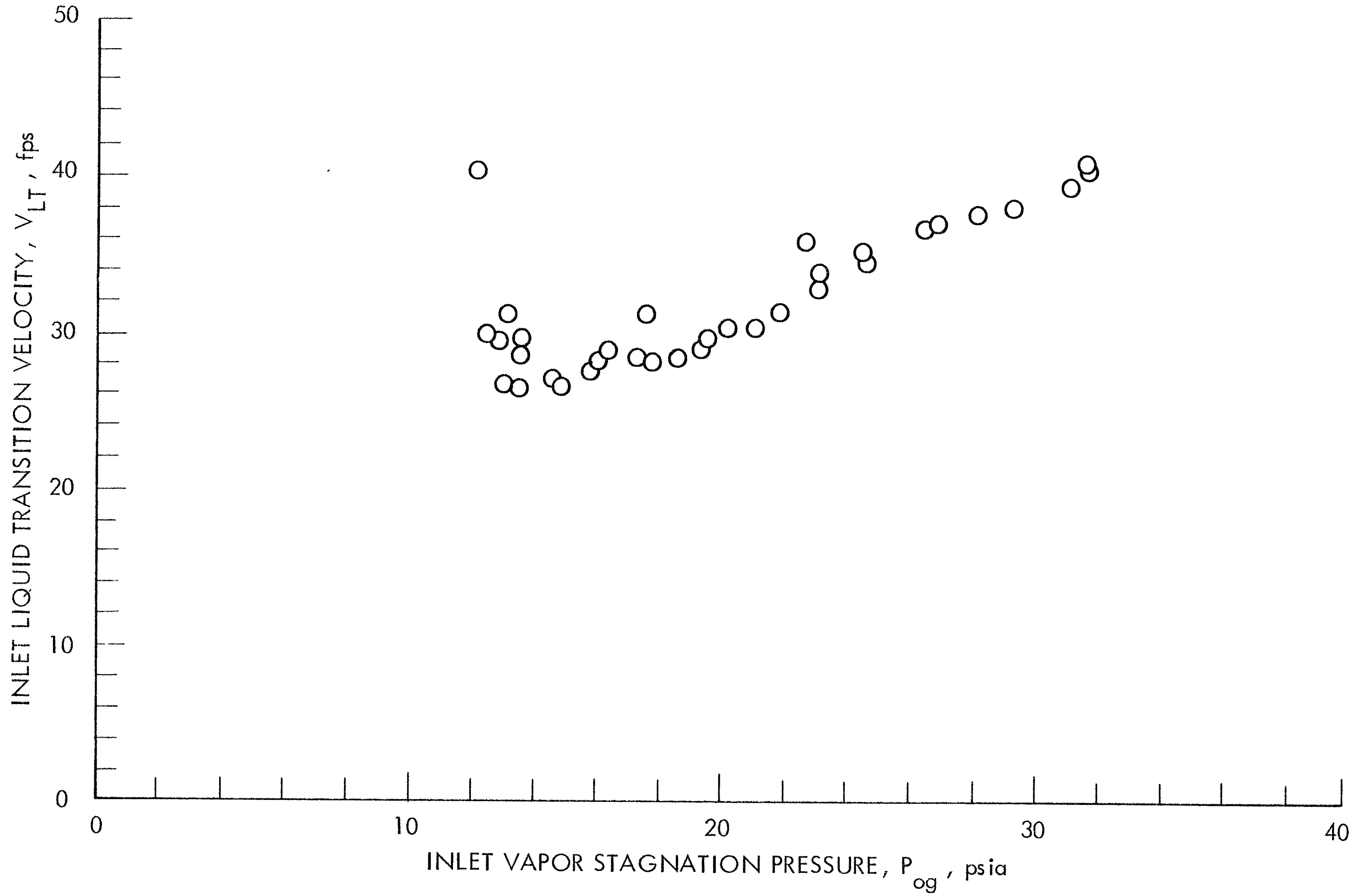

FIGURE 26. VARIATION OF LIQUID TRANSITION VELOCITY WITH INLET VAPOR STAGNATION PRESSURE (BPVO)

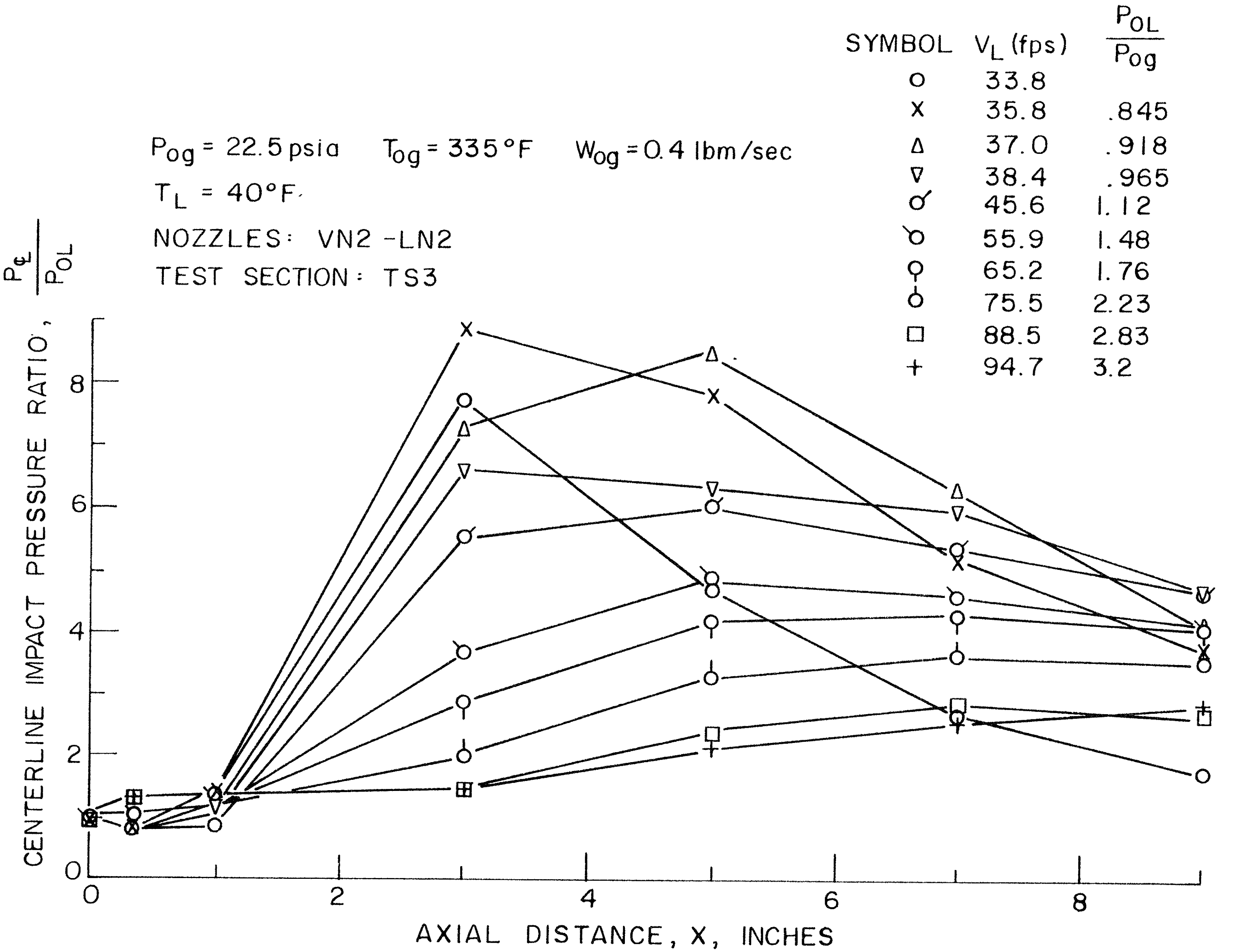

FIGURE 27 EFFECT OF INLET LIQUID VELOCITY ON VARIATION OF CENTERLINE IMPACT PRESSURE (BPVO)

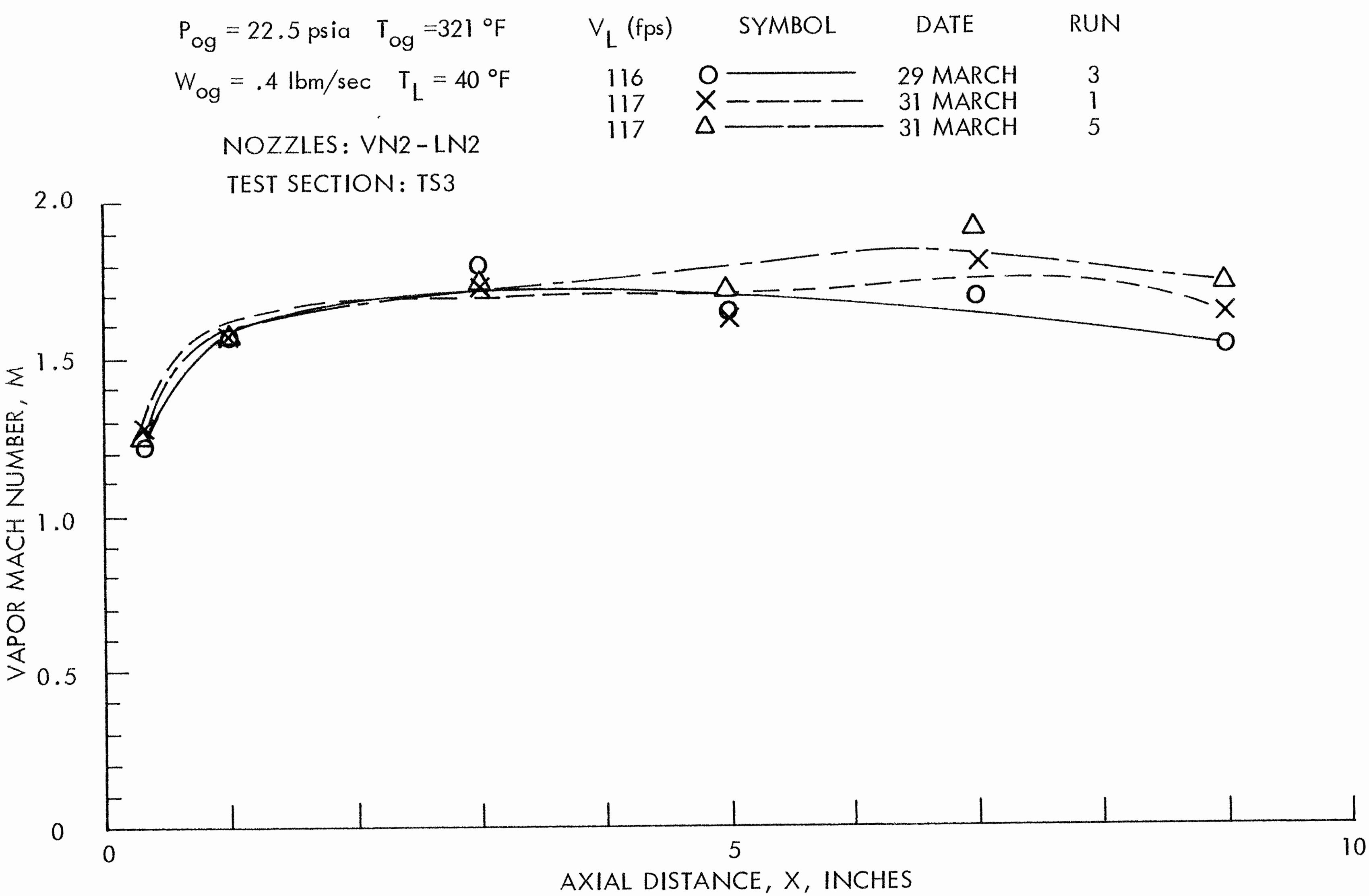

FIGURE 28. AXIAL VARIATION OF VAPOR MACH NUMBER

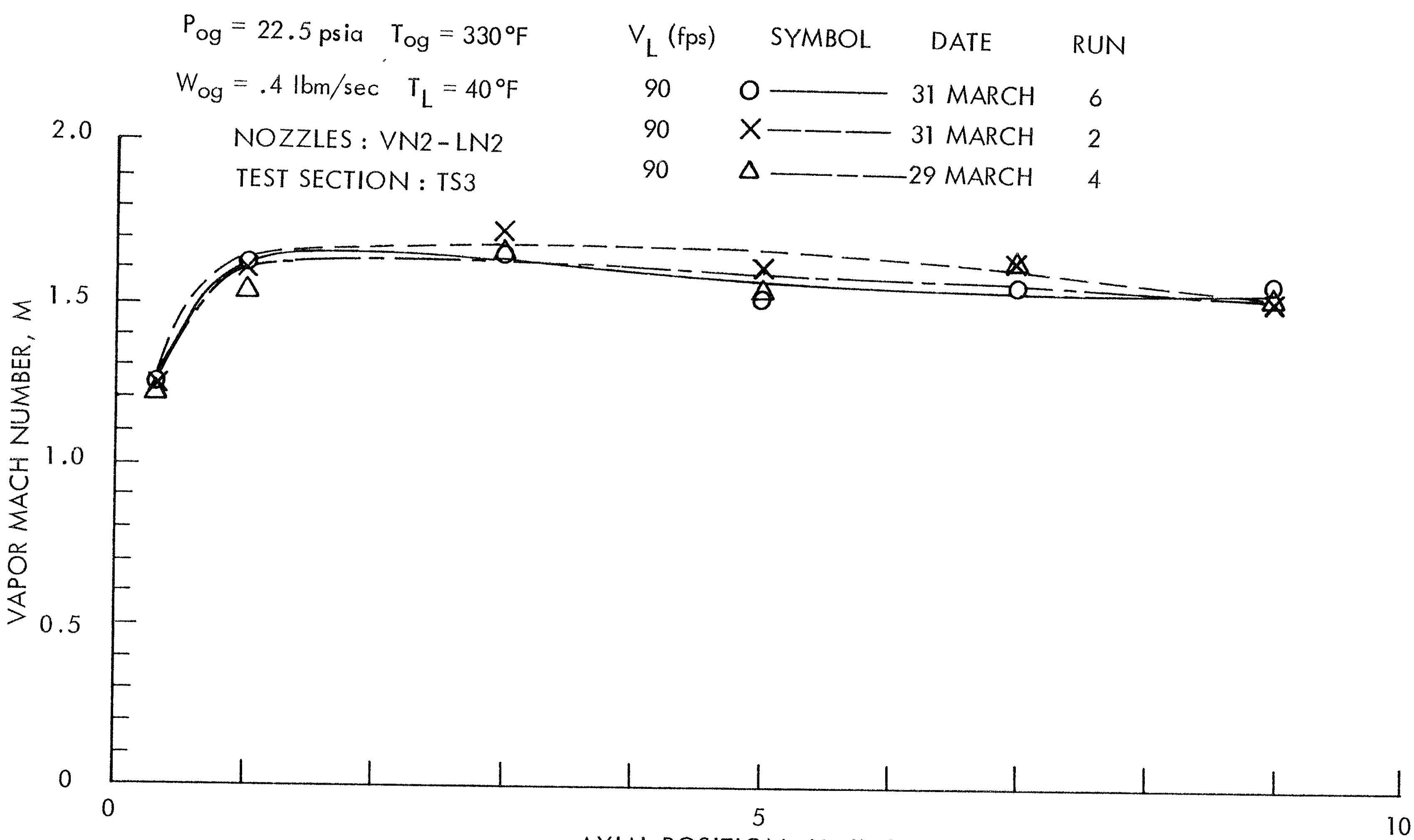

FIGURE 29. AXIAL VARIATION OF VAPOR MACH NUMBER

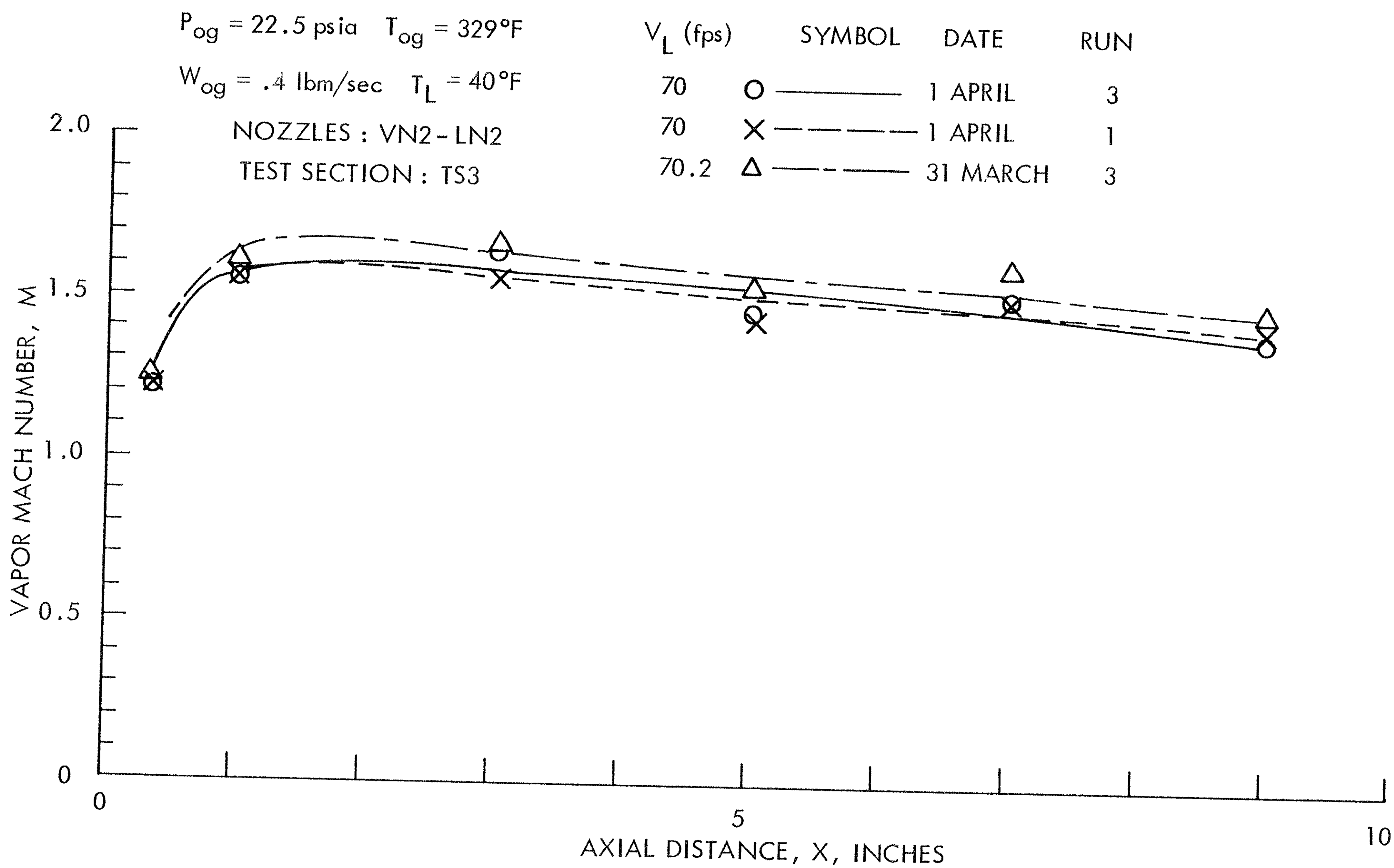

FIGURE 30. AXIAL VARIATION OF VAPOR MACH NUMBER

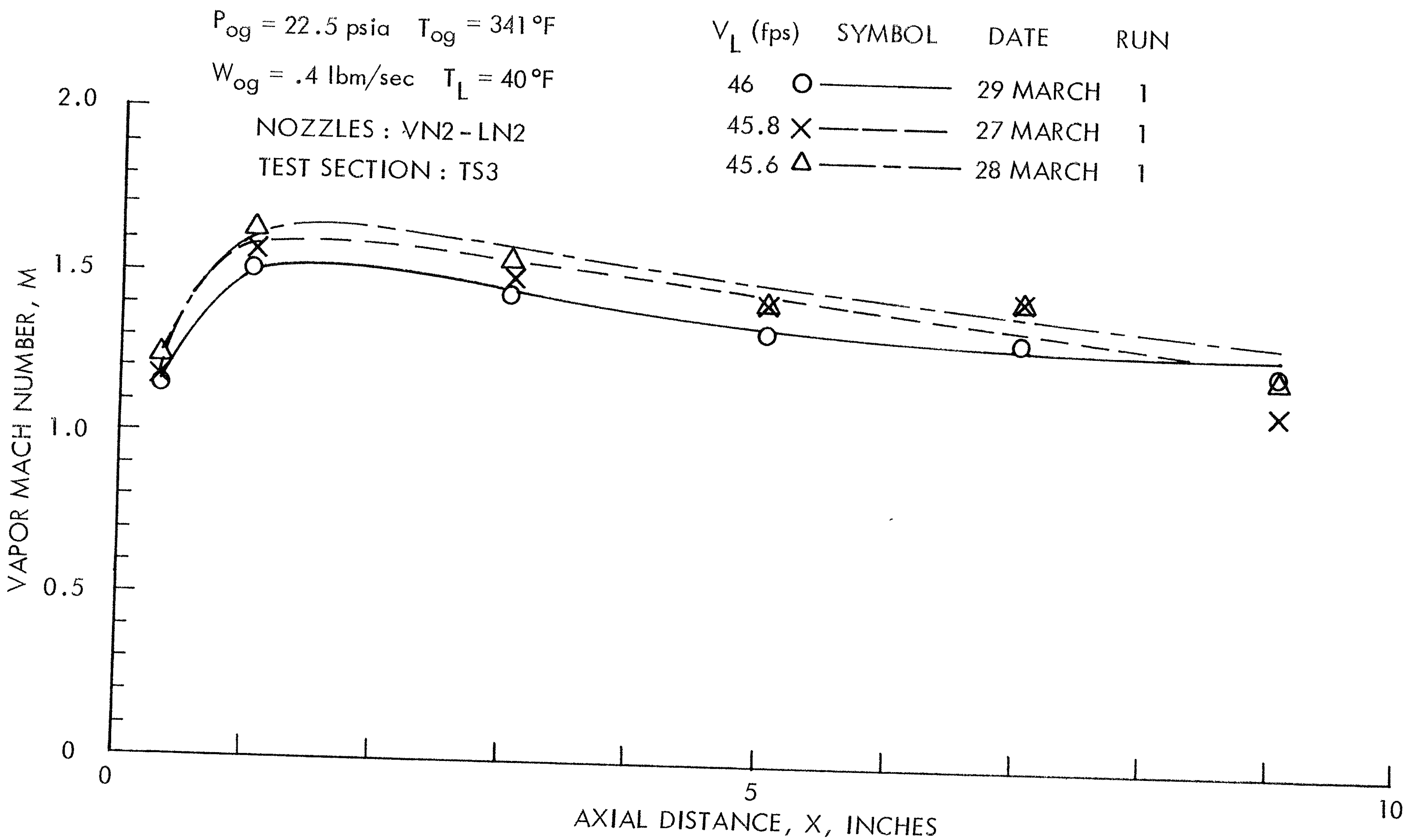

FIGURE 31. AXIAL VARIATION OF VAPOR MACH NUMBER

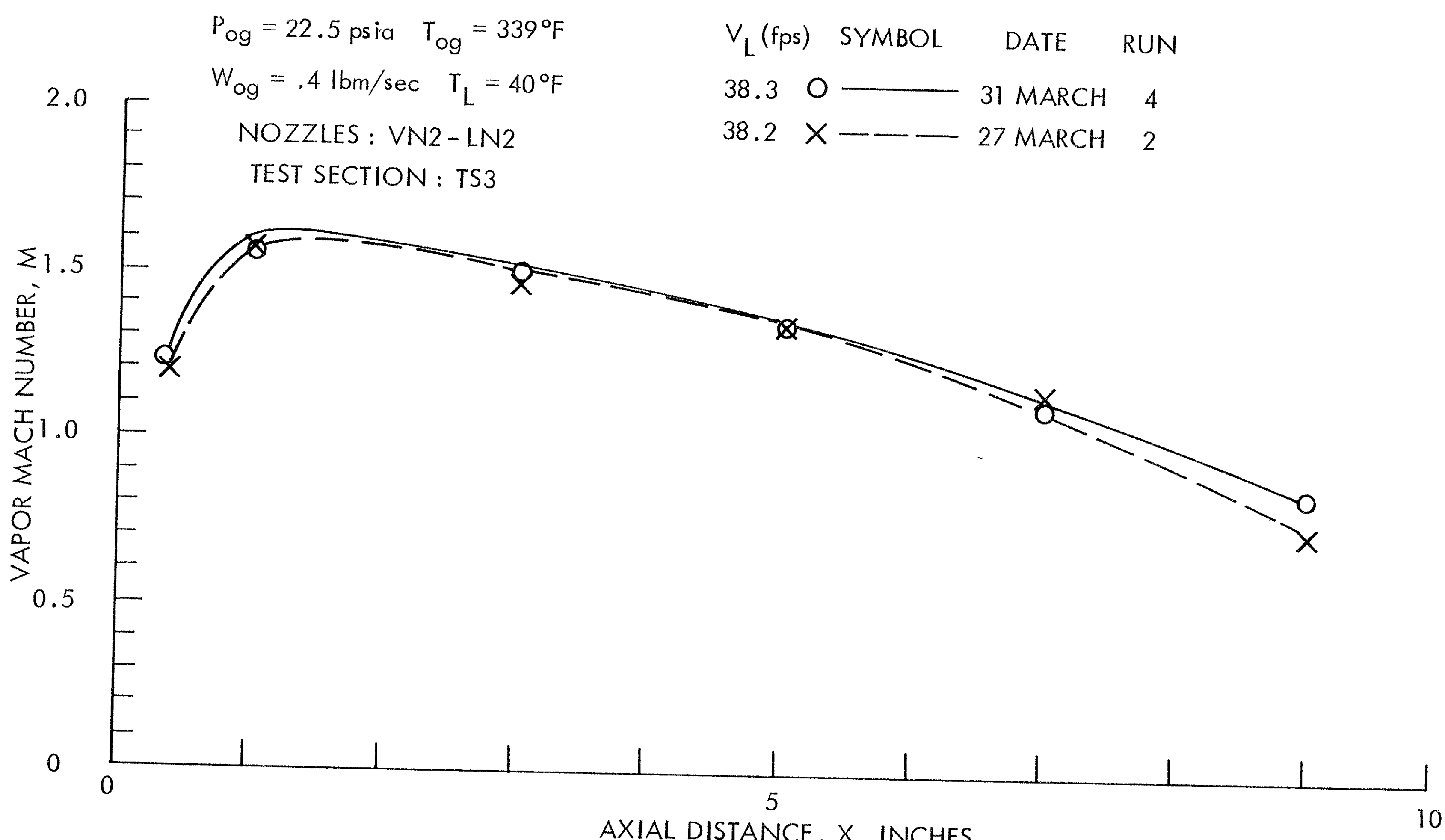

FIGURE 32. AXIAL VARIATION OF VAPOR MACH NUMBER

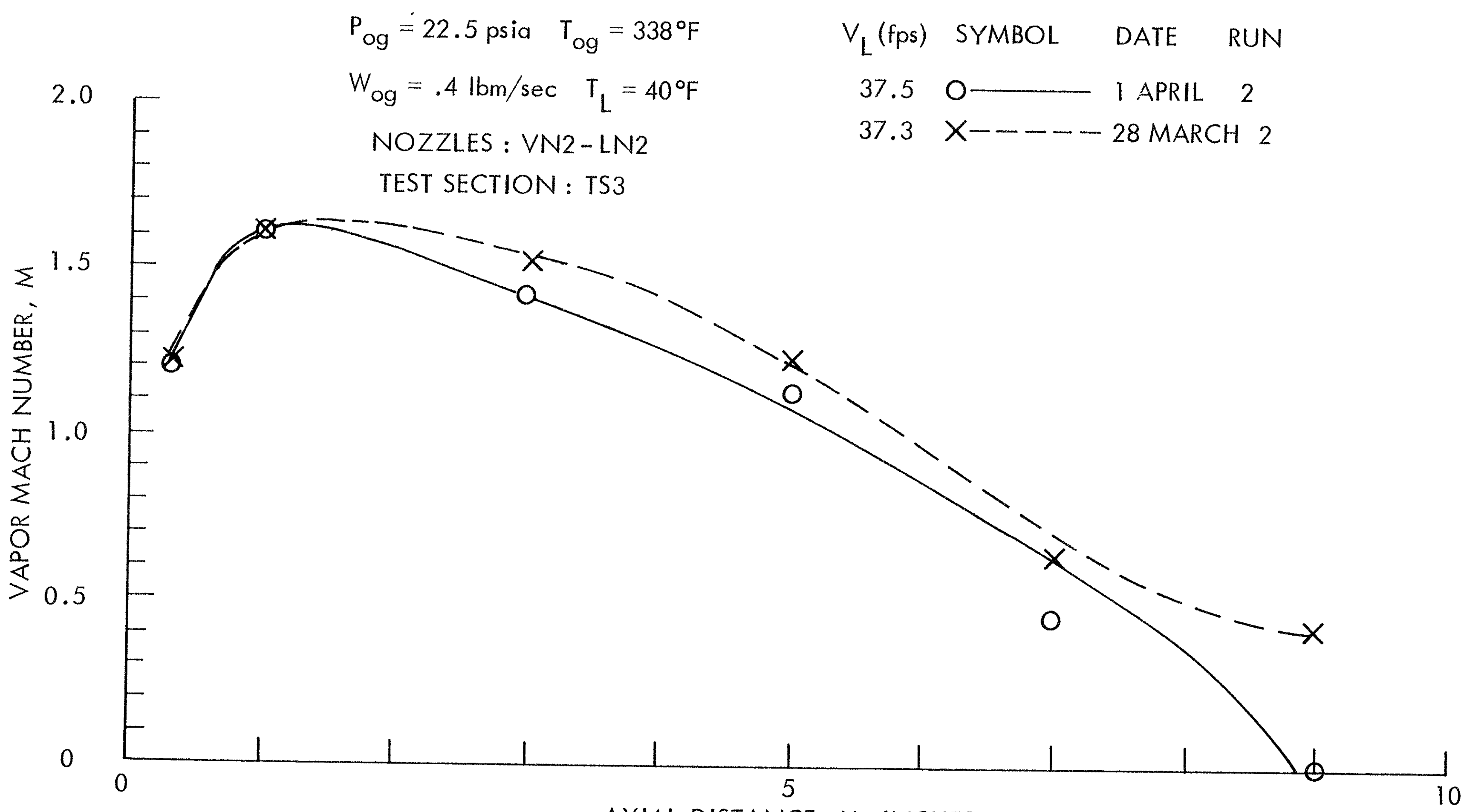

FIGURE 33. AXIAL VARIATION OF VAPOR MACH NUMBER

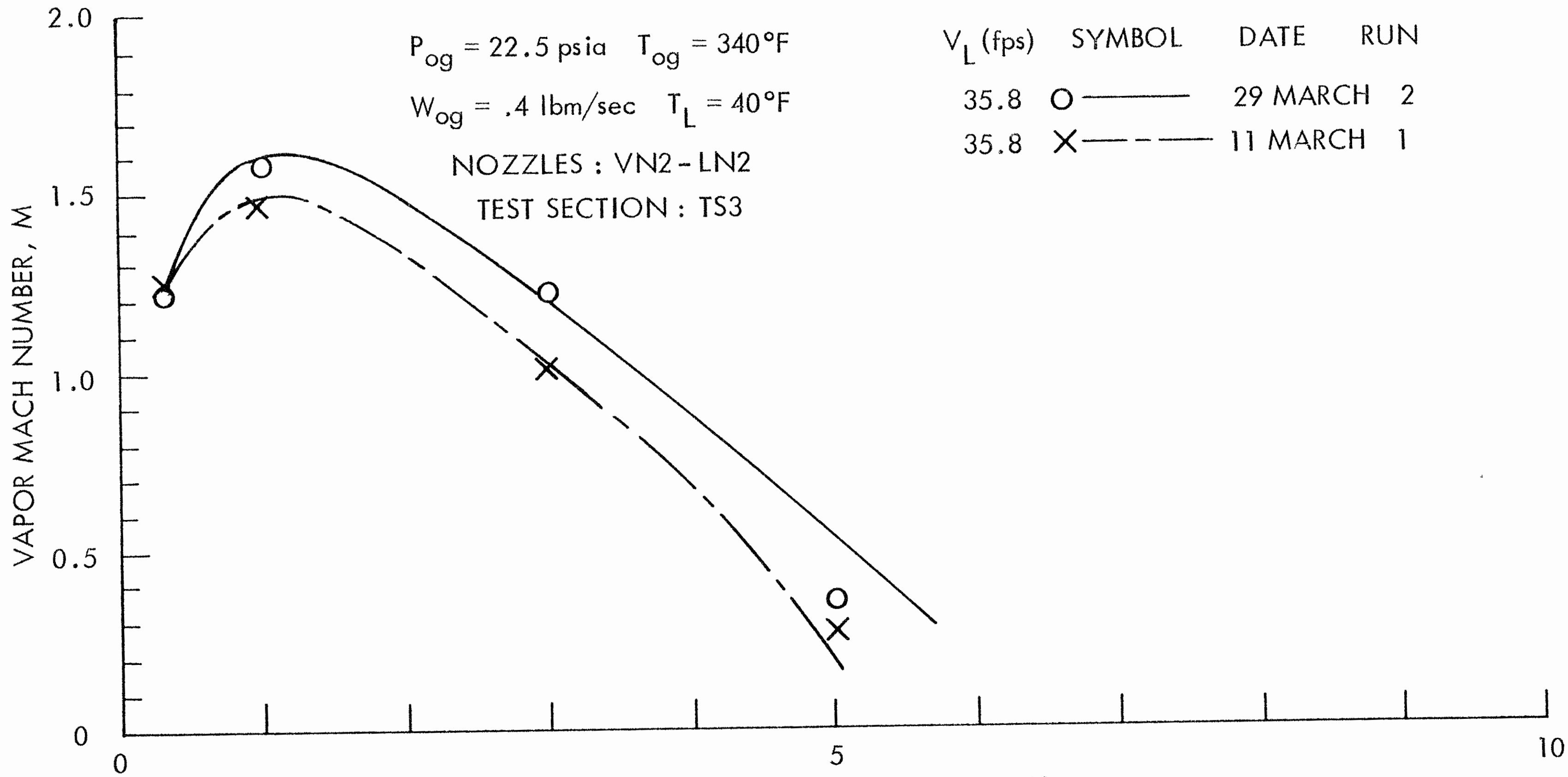

FIGURE 34. AXIAL VARIATION OF VAPOR MACH NUMBER

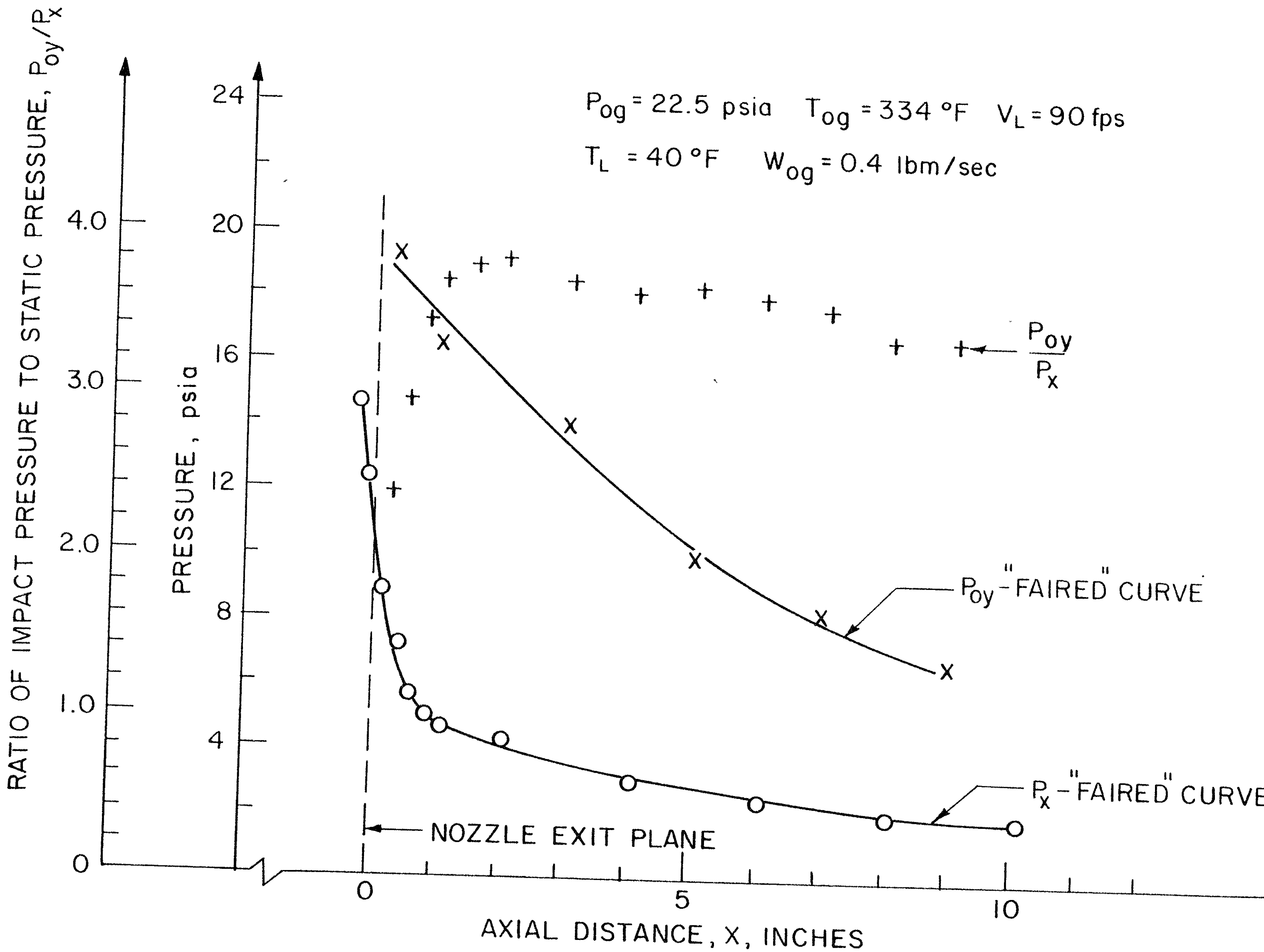

FIGURE 35 CONSTRUCTION OF BEST FIT MACH NUMBER PROFILES

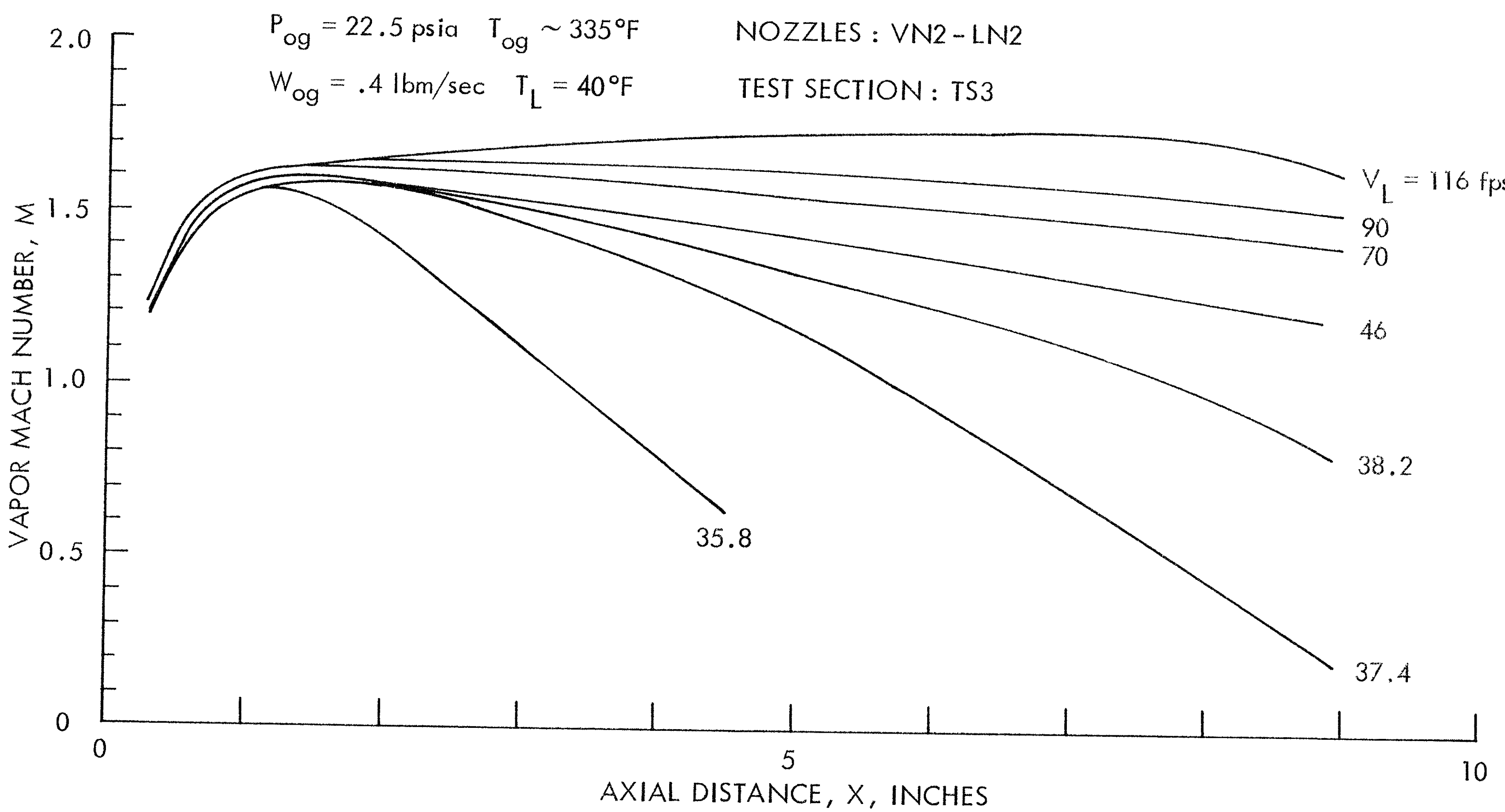

FIGURE 36. EFFECT OF INLET LIQUID VELOCITY ON VAPOR MACH NUMBER DISTRIBUTION

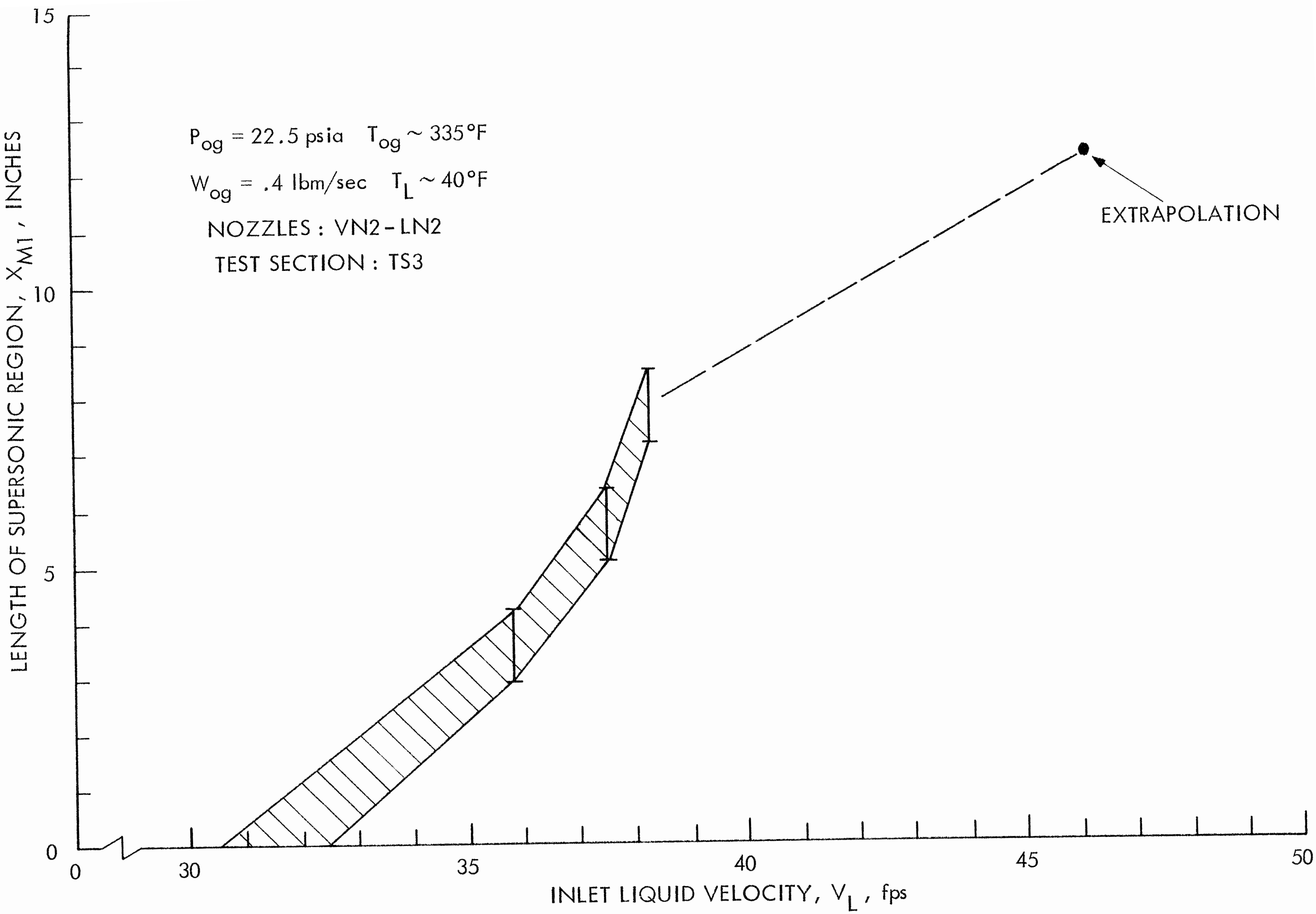

FIGURE 37. VARIATION OF LENGTH OF SUPERSONIC REGION WITH INLET LIQUID VELOCITY

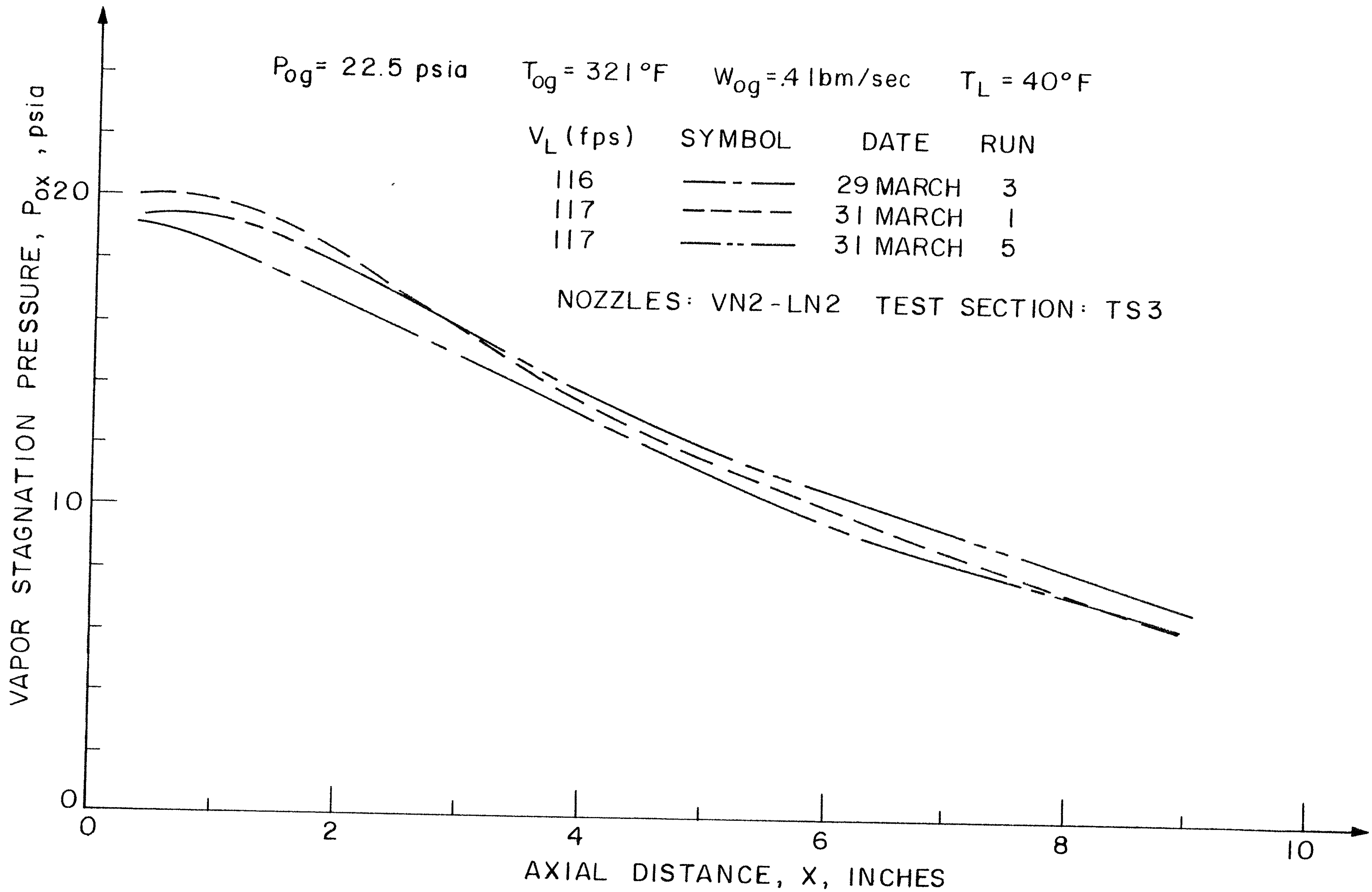

FIGURE 38 AXIAL VARIATION OF VAPOR STAGNATION PRESSURE

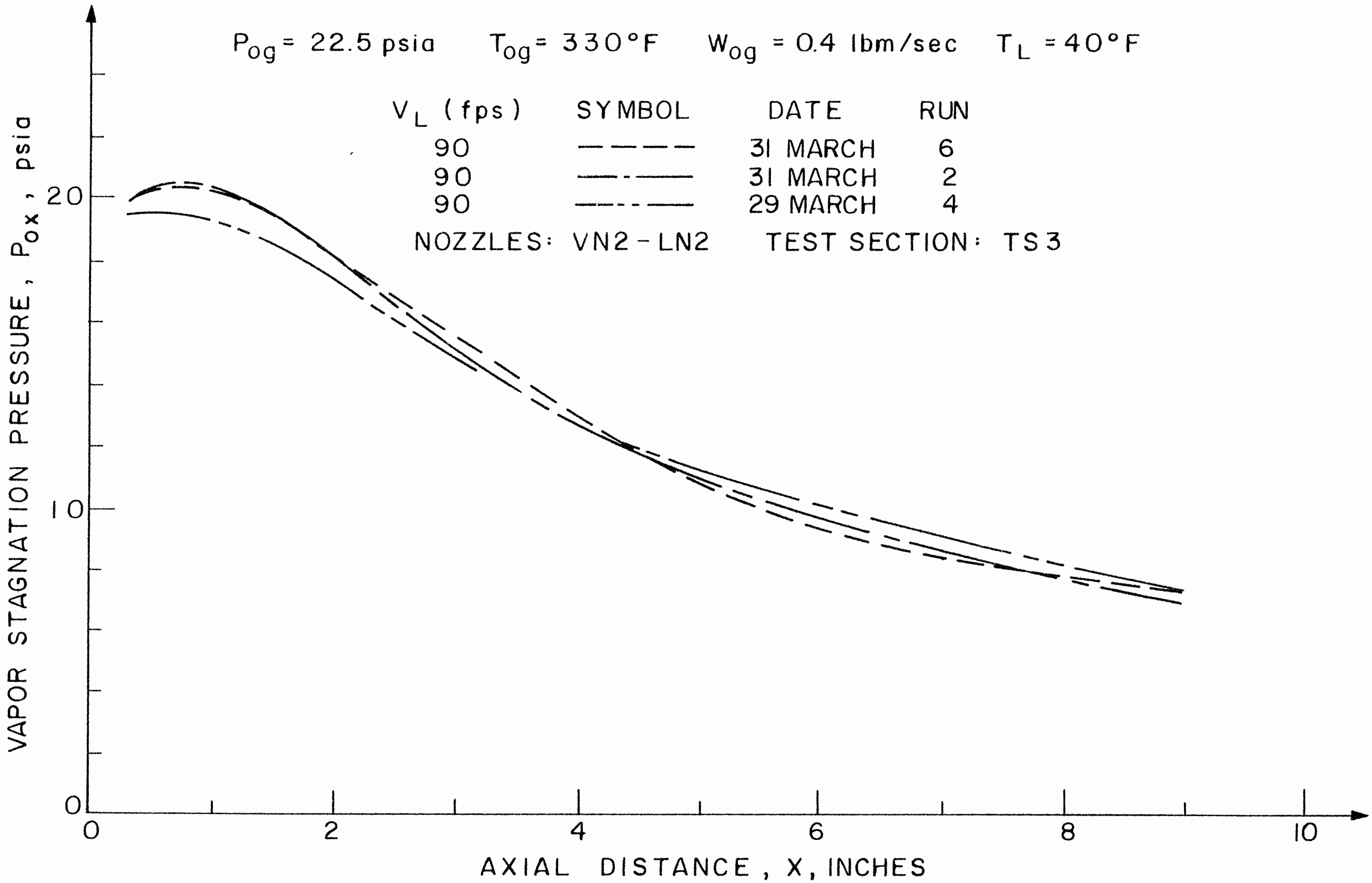

FIGURE 39 AXIAL VARIATION OF VAPOR STAGNATION PRESSURE

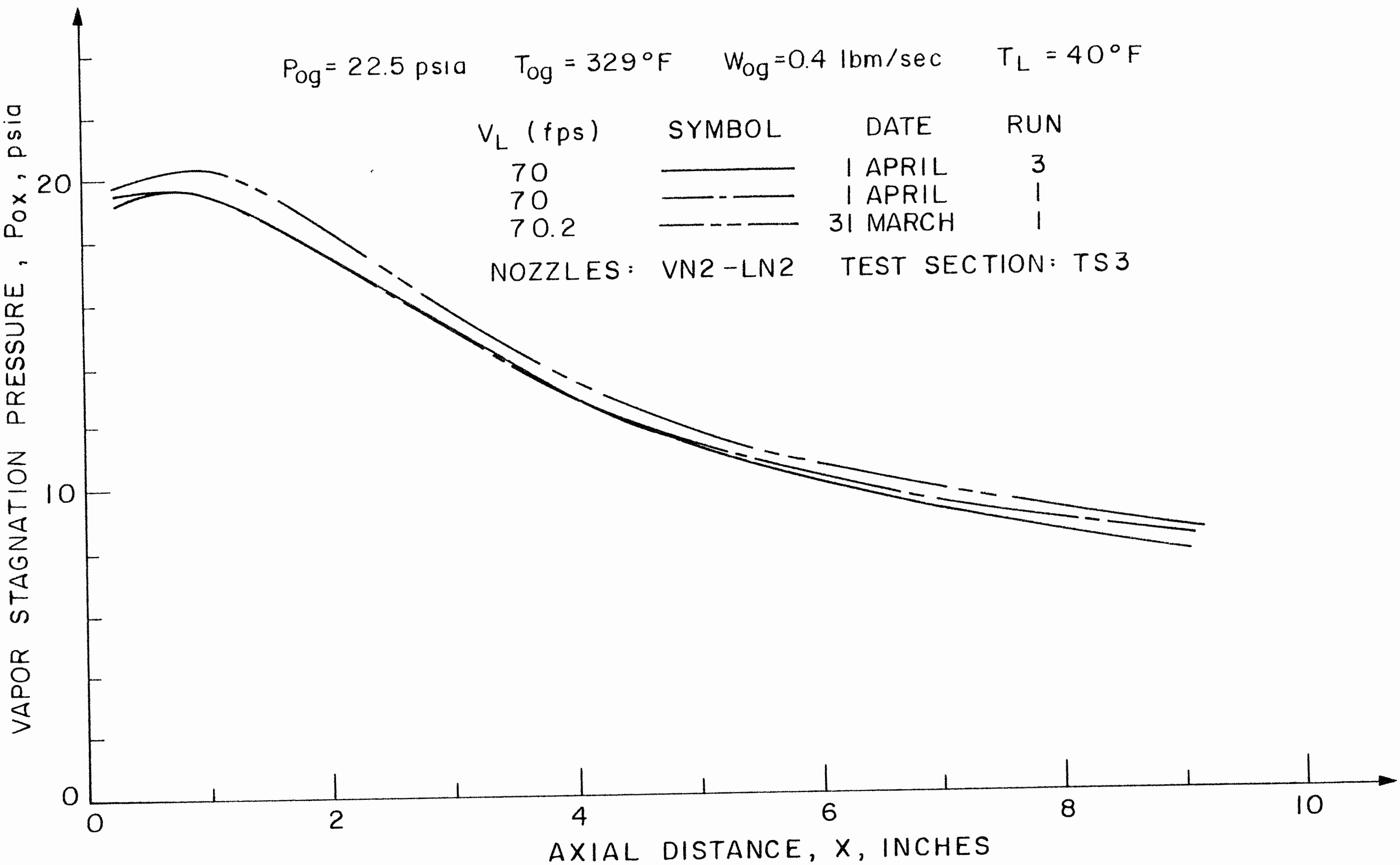

FIGURE 40 AXIAL VARIATION OF VAPOR STAGNATION PRESSURE

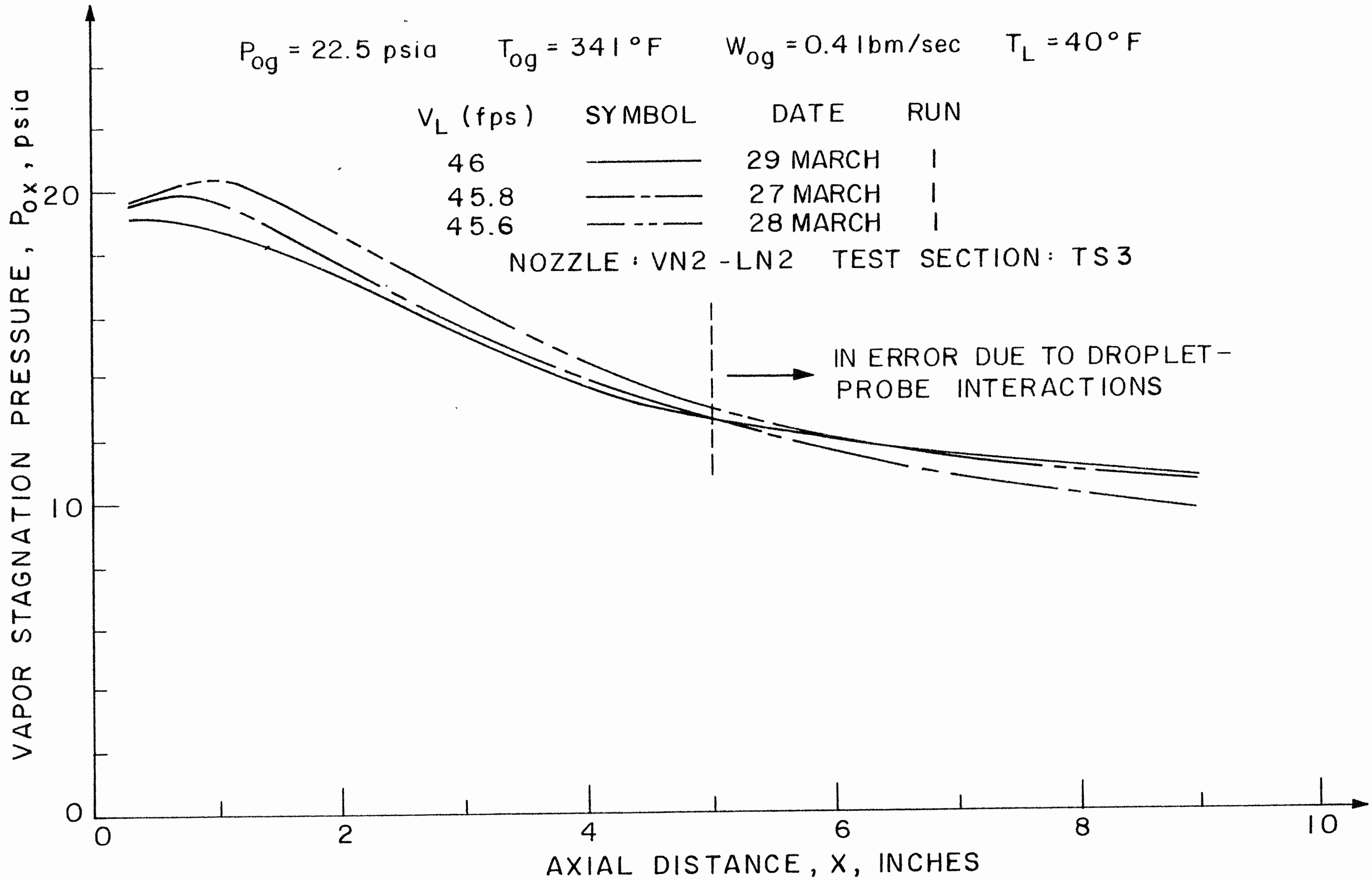

FIGURE 41 AXIAL VARIATION OF VAPOR STAGNATION PRESSURE

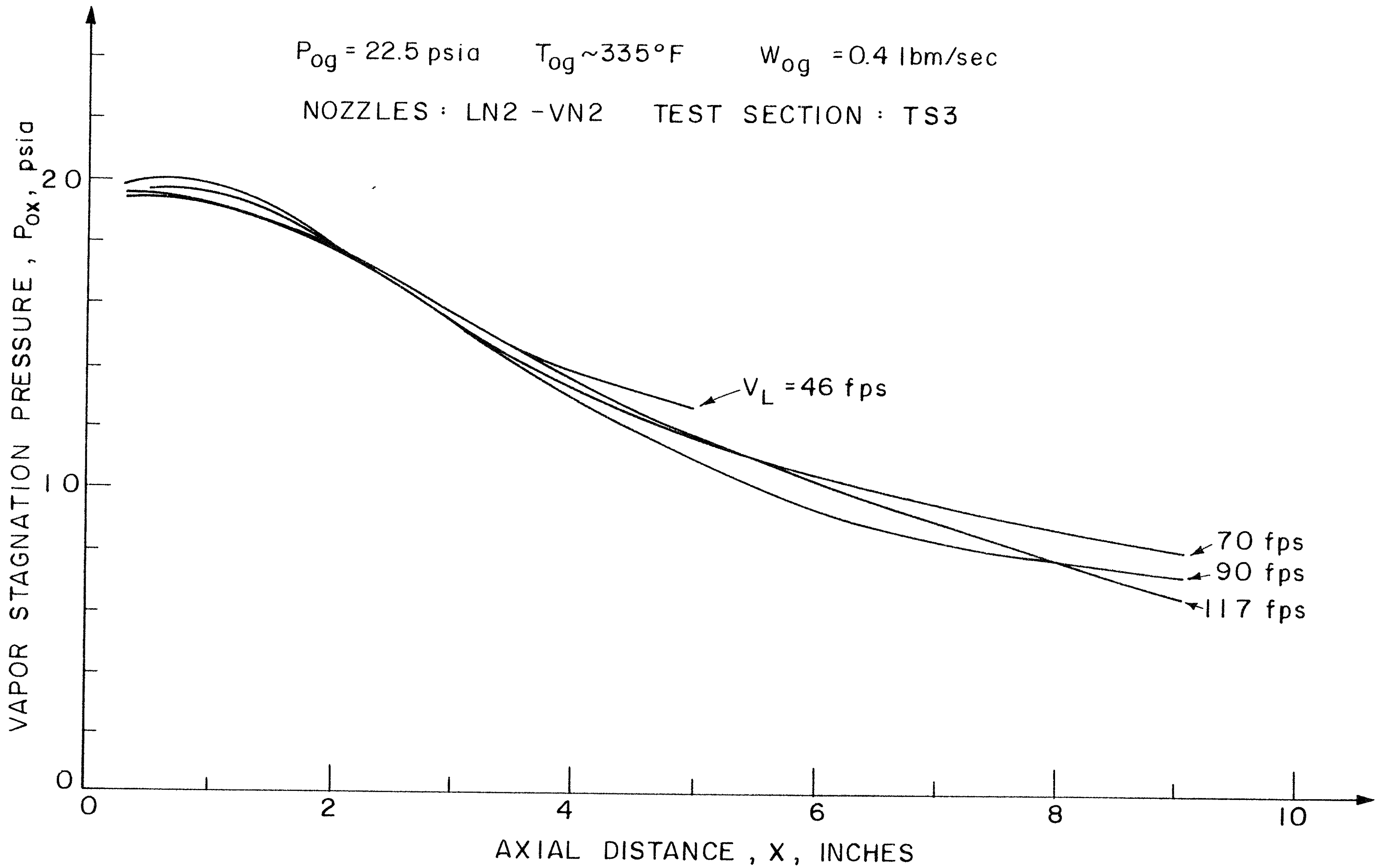

FIGURE 42 EFFECT OF INLET LIQUID VELOCITY ON AXIAL VARIATION OF VAPOR STAGNATION PRESSURE

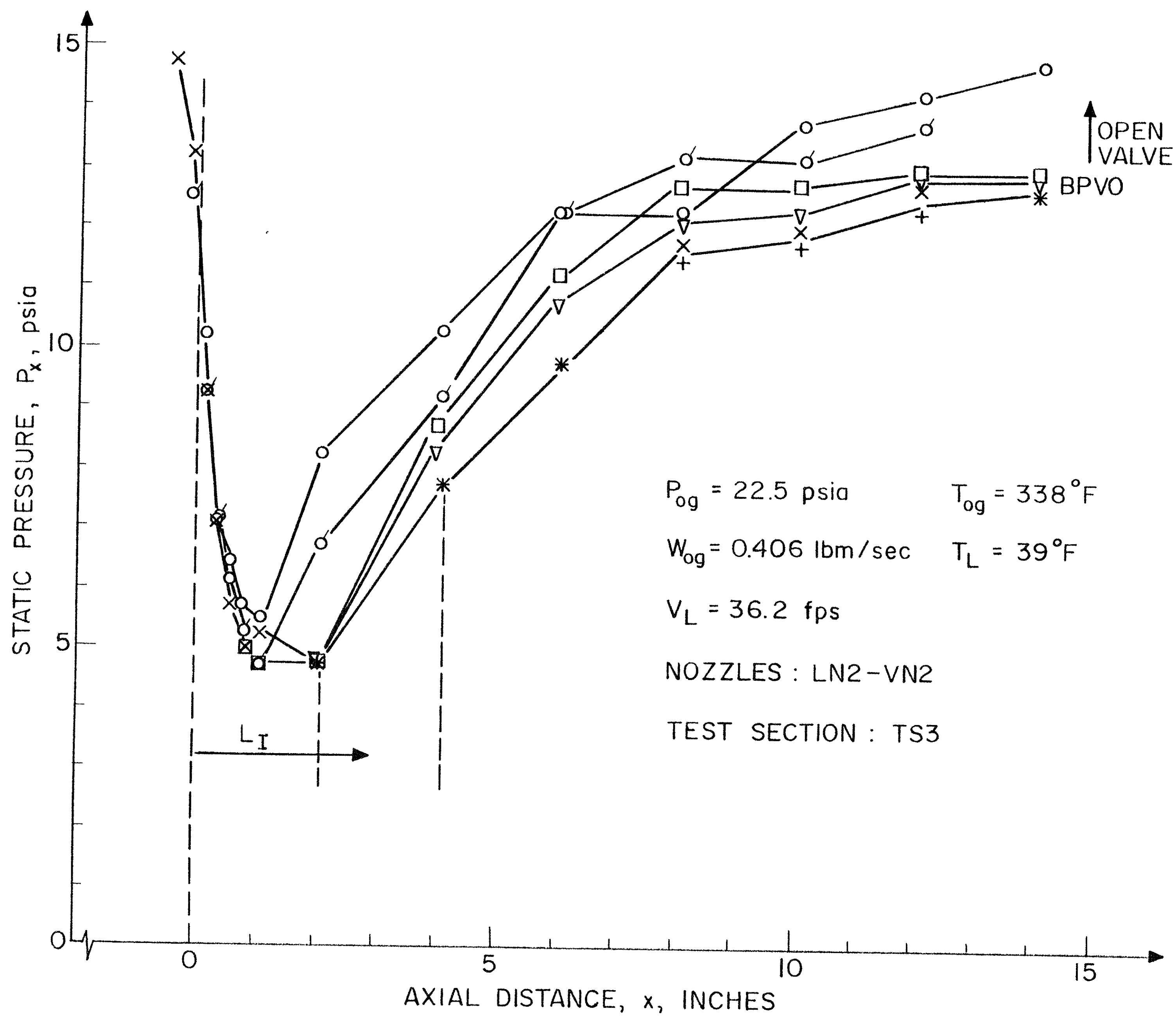

FIGURE 43 EFFECT OF BACK PRESSURE ON WALL STATIC PRESSURE DISTRIBUTION

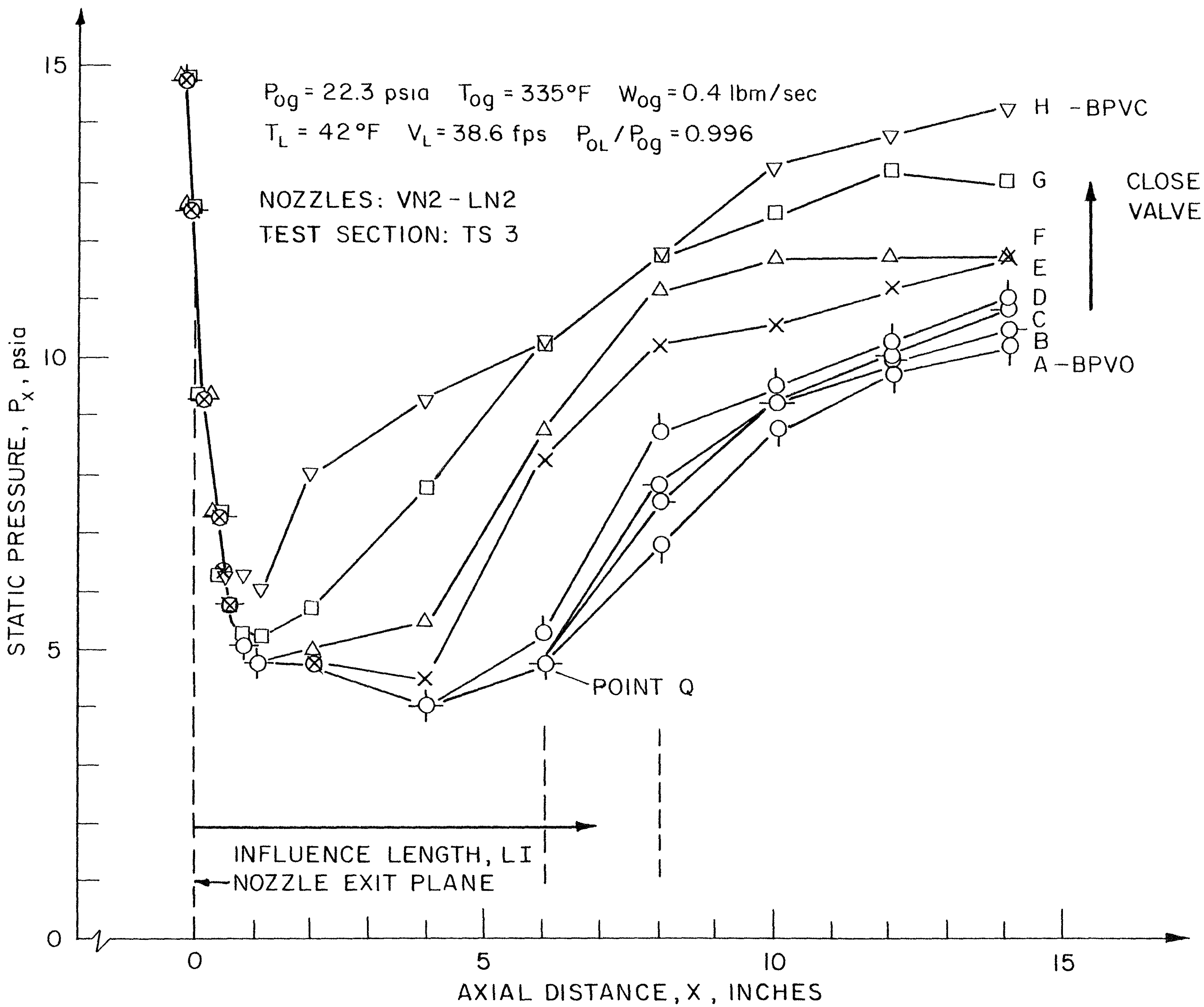

FIGURE 44 EFFECT OF BACK PRESSURE ON AXIAL PRESSURE DISTRIBUTION

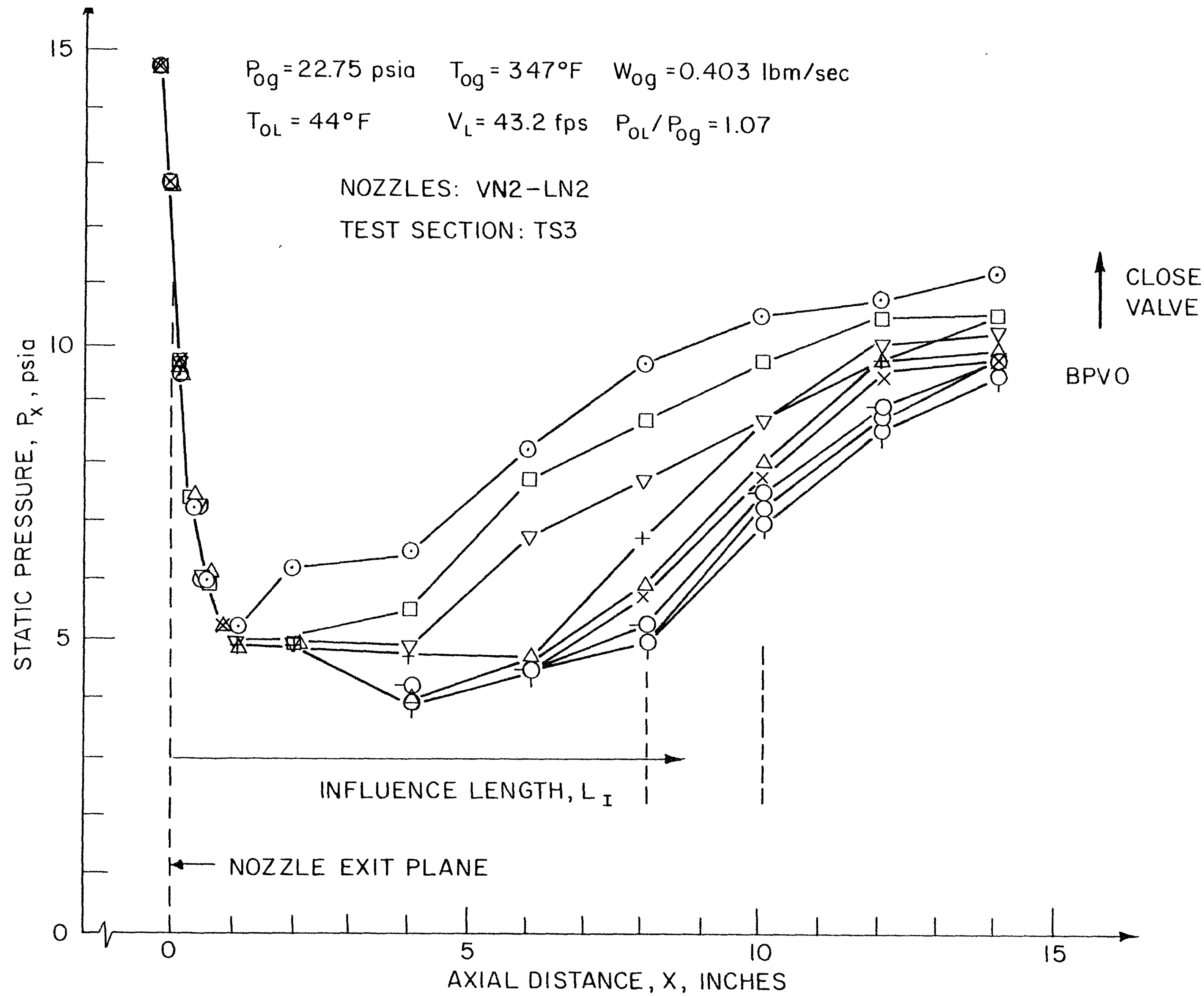

FIGURE 45 EFFECT OF BACK PRESSURE ON AXIAL PRESSURE DISTRIBUTION

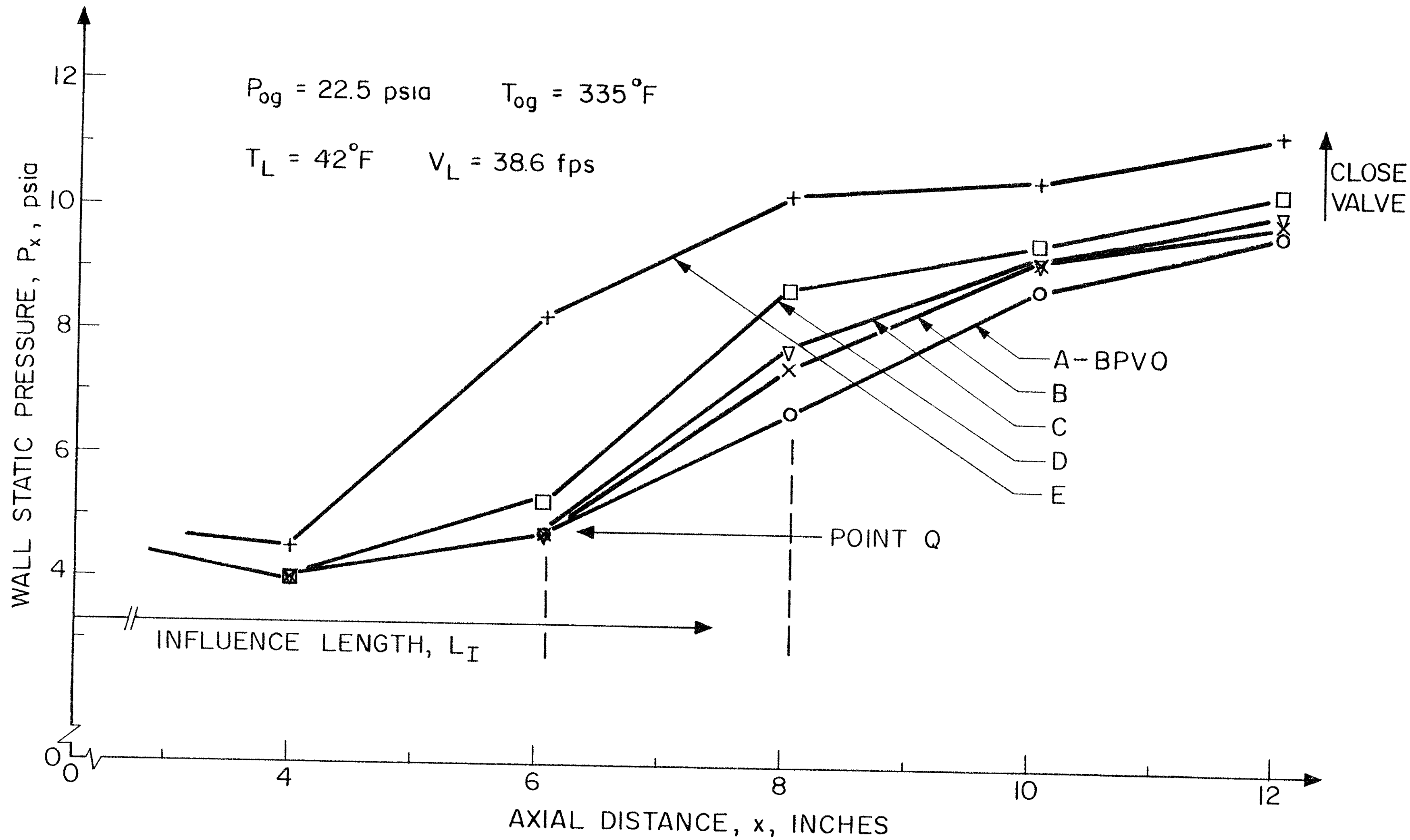

FIGURE 46 EFFECT OF BACK PRESSURE, ON STATIC PRESSURE NEAR POINT Q

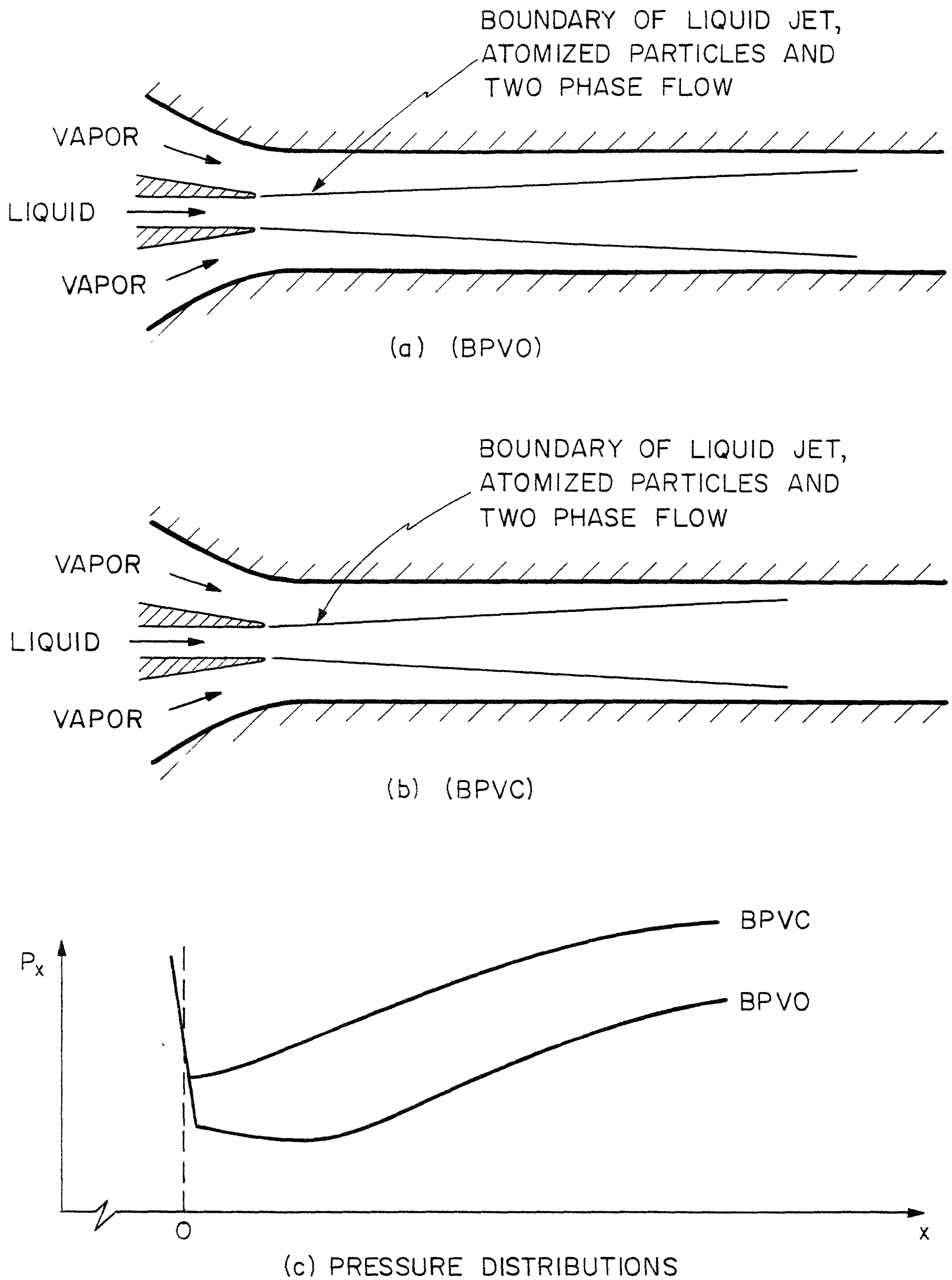

FIGURE 47 DIAGRAM OF CE OPERATION AT p_{og} = 22.5 psia AND V_L = 38.6 fps WITH BPVO AND BPVC

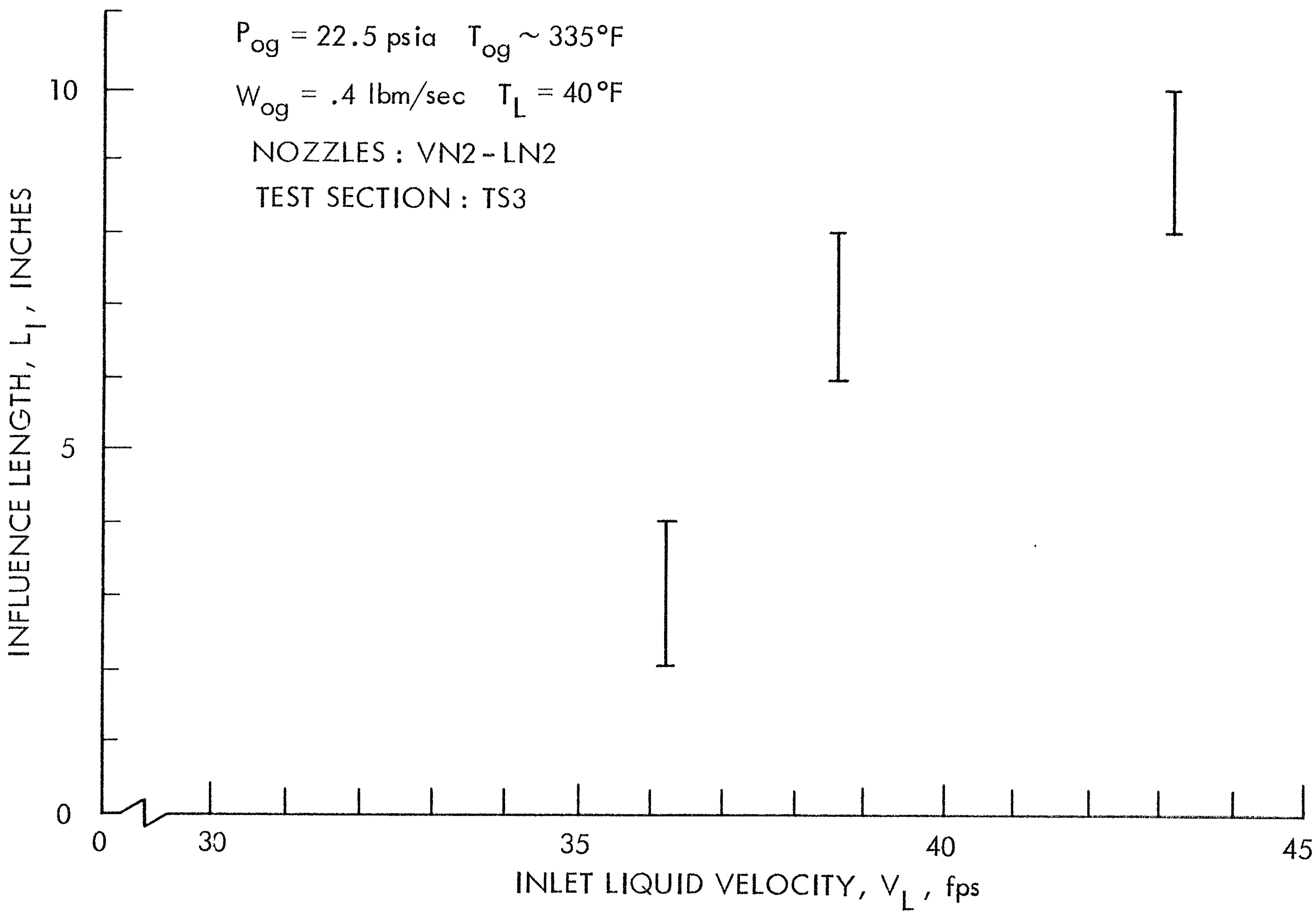

FIGURE 48. VARIATION OF INFLUENCE LENGTH WITH INLET LIQUID VELOCITY

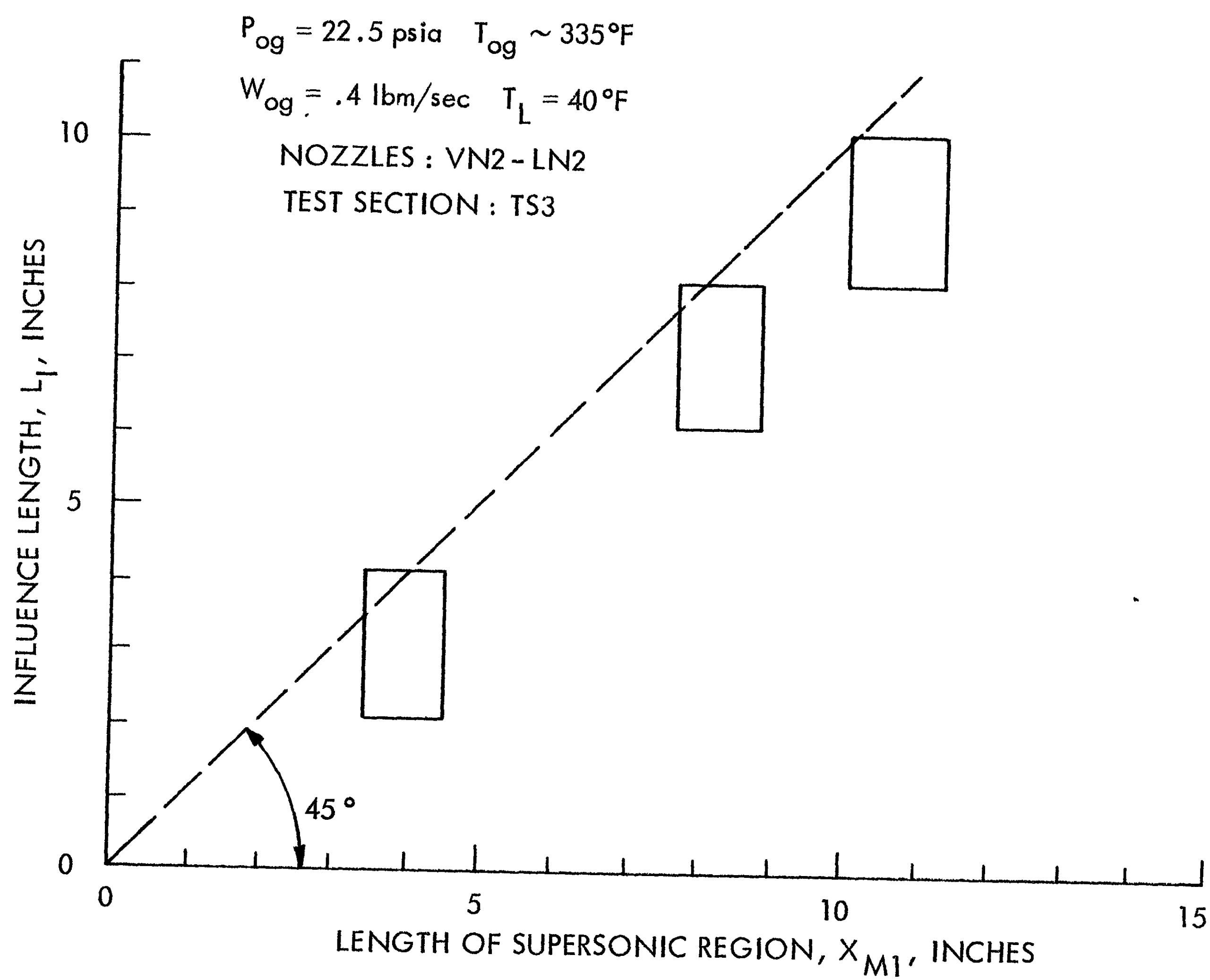

FIGURE 49. COMPARISON OF INFLUENCE LENGTH AND LENGTH OF SUPERSONIC REGION

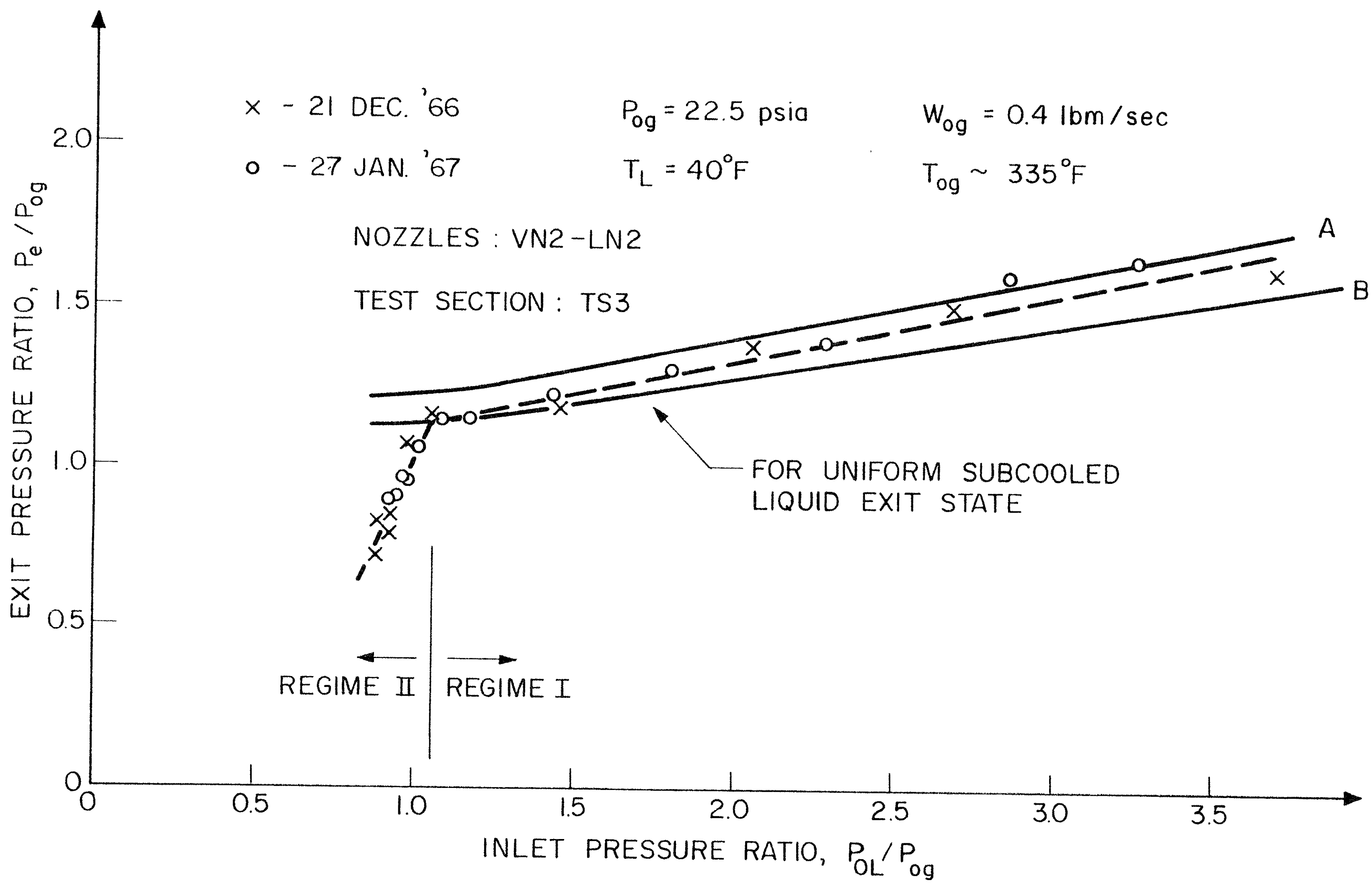

FIGURE 50 OVERALL PRESSURE PERFORMANCE (BPVC)

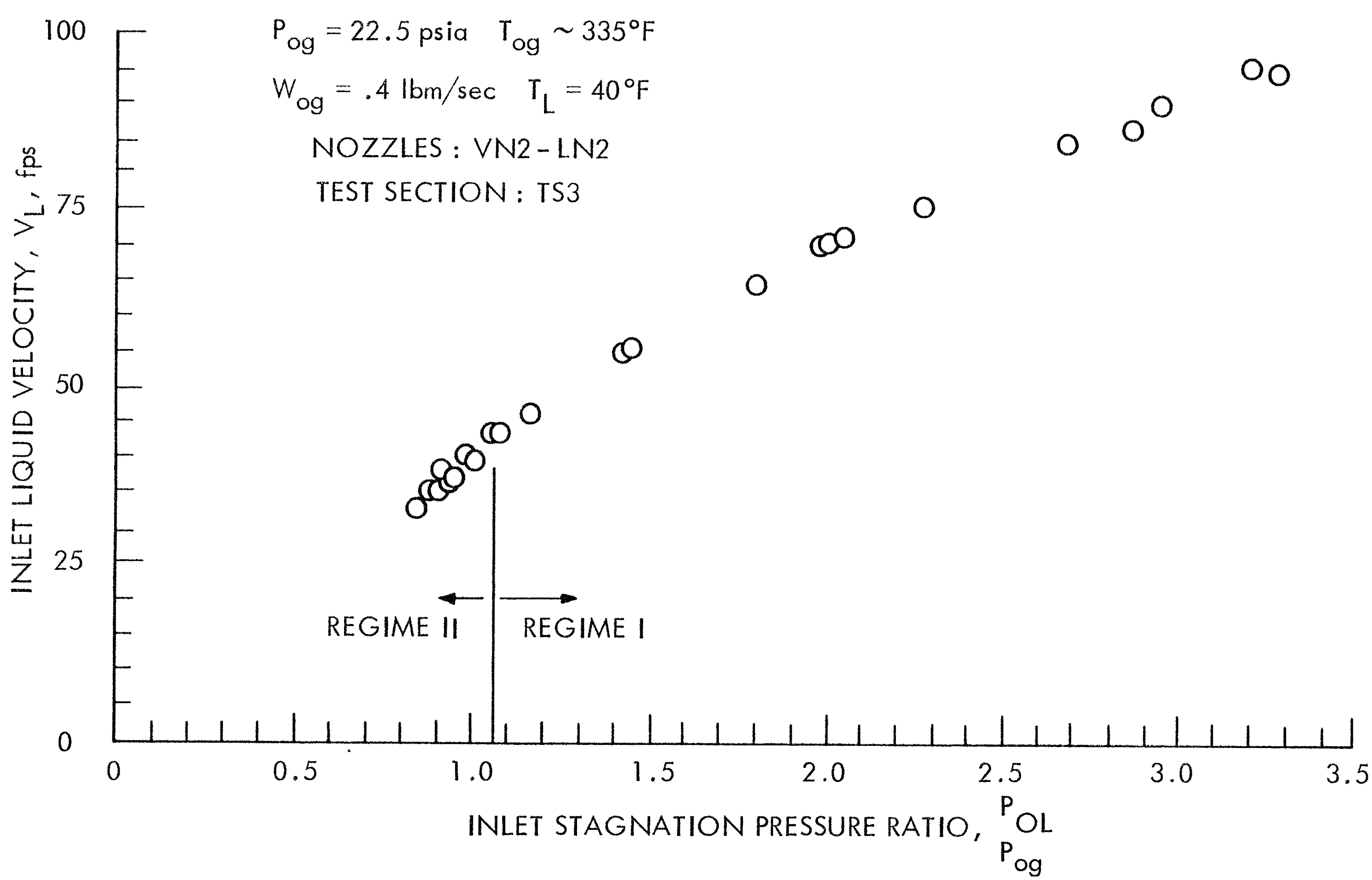

FIGURE 51. VARIATION OF INLET LIQUID VELOCITY WITH INLET PRESSURE RATIO (BPVO)

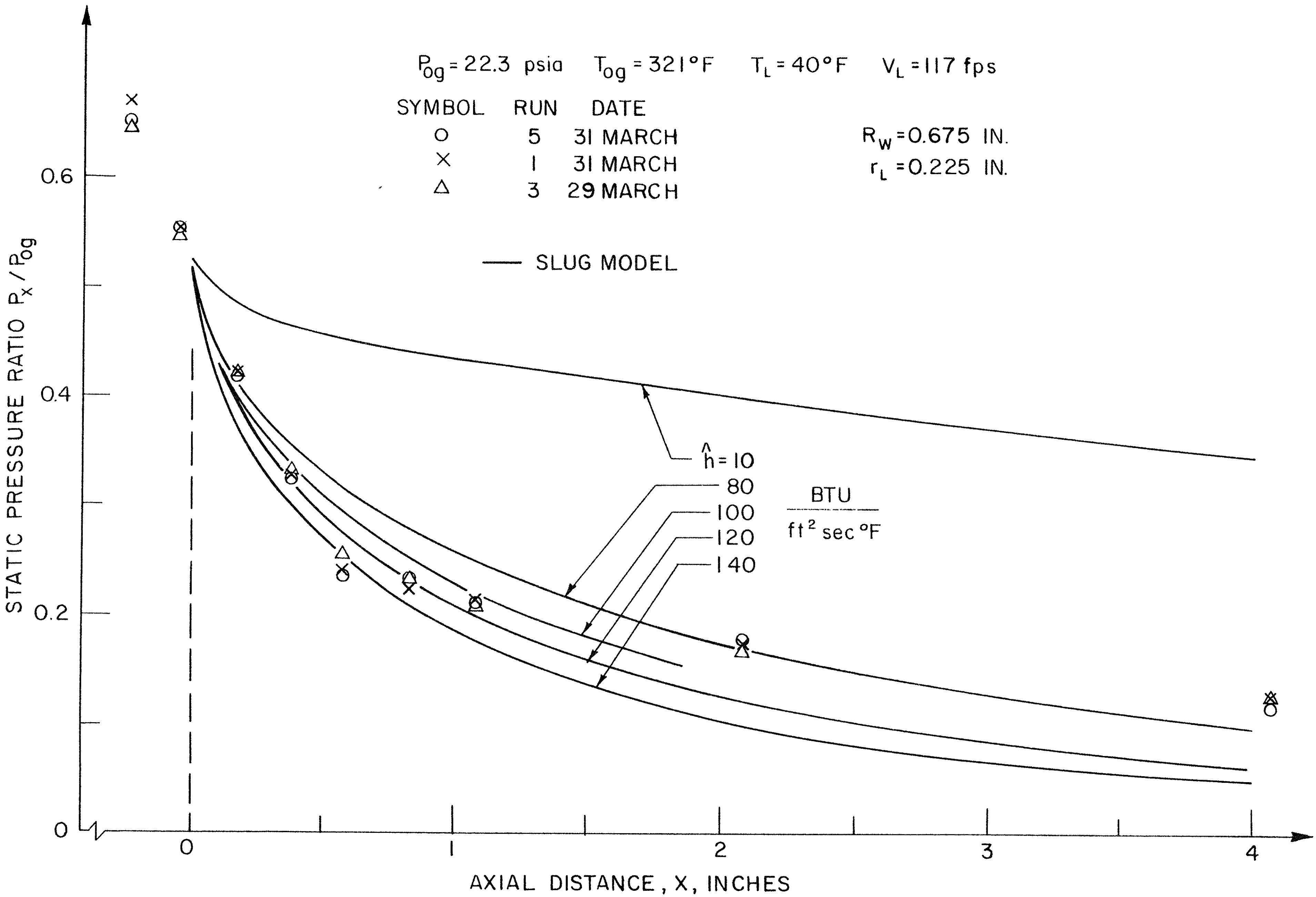

FIGURE 52 EFFECT OF HEAT TRANSFER COEFFICIENT ON AXIAL VARIATION OF STATIC PRESSURE

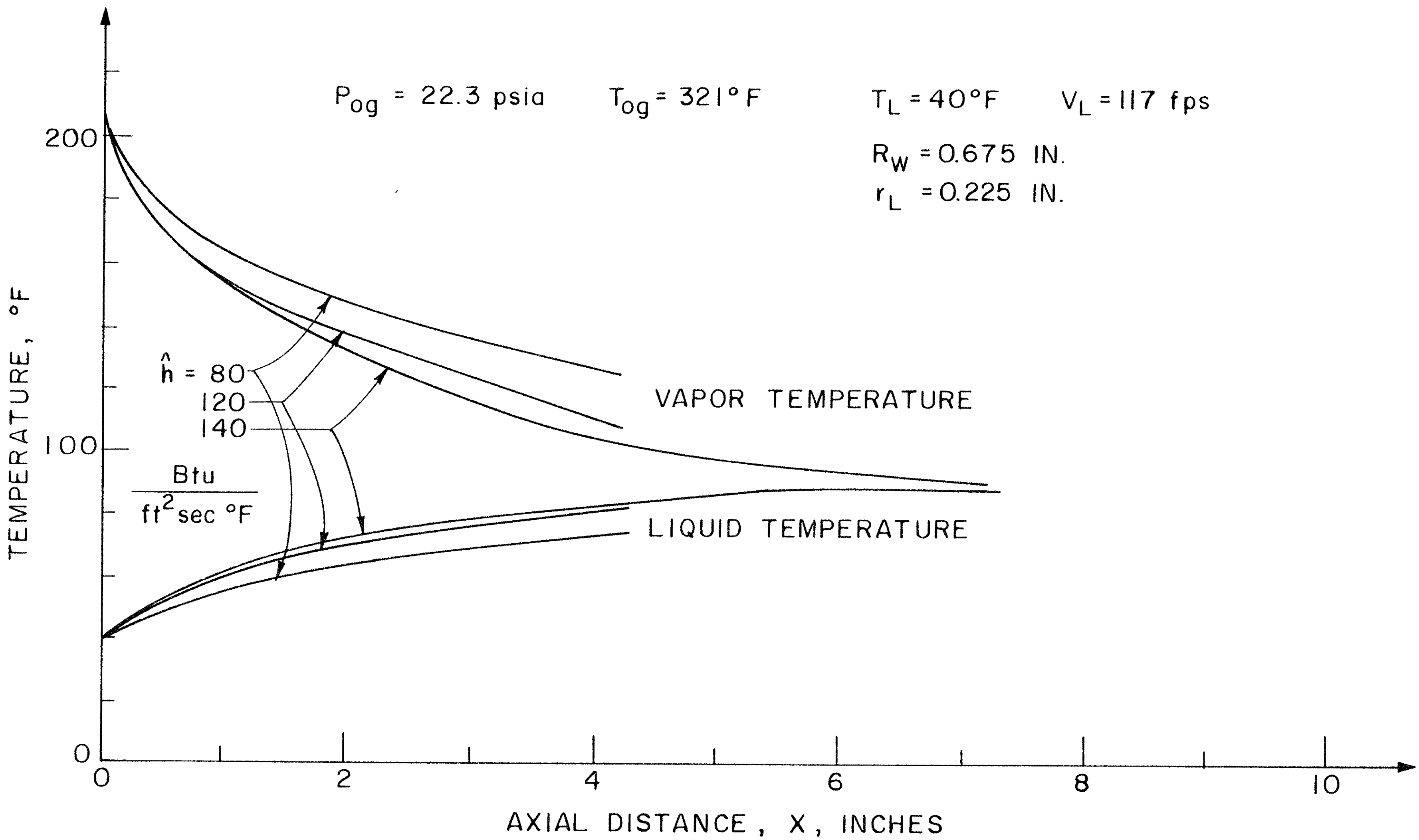

FIGURE 53 EFFECT OF HEAT TRANSFER COEFFICIENT ON AXIAL VARIATIONS OF LIQUID AND VAPOR TEMPERATURES – SLUG MODEL

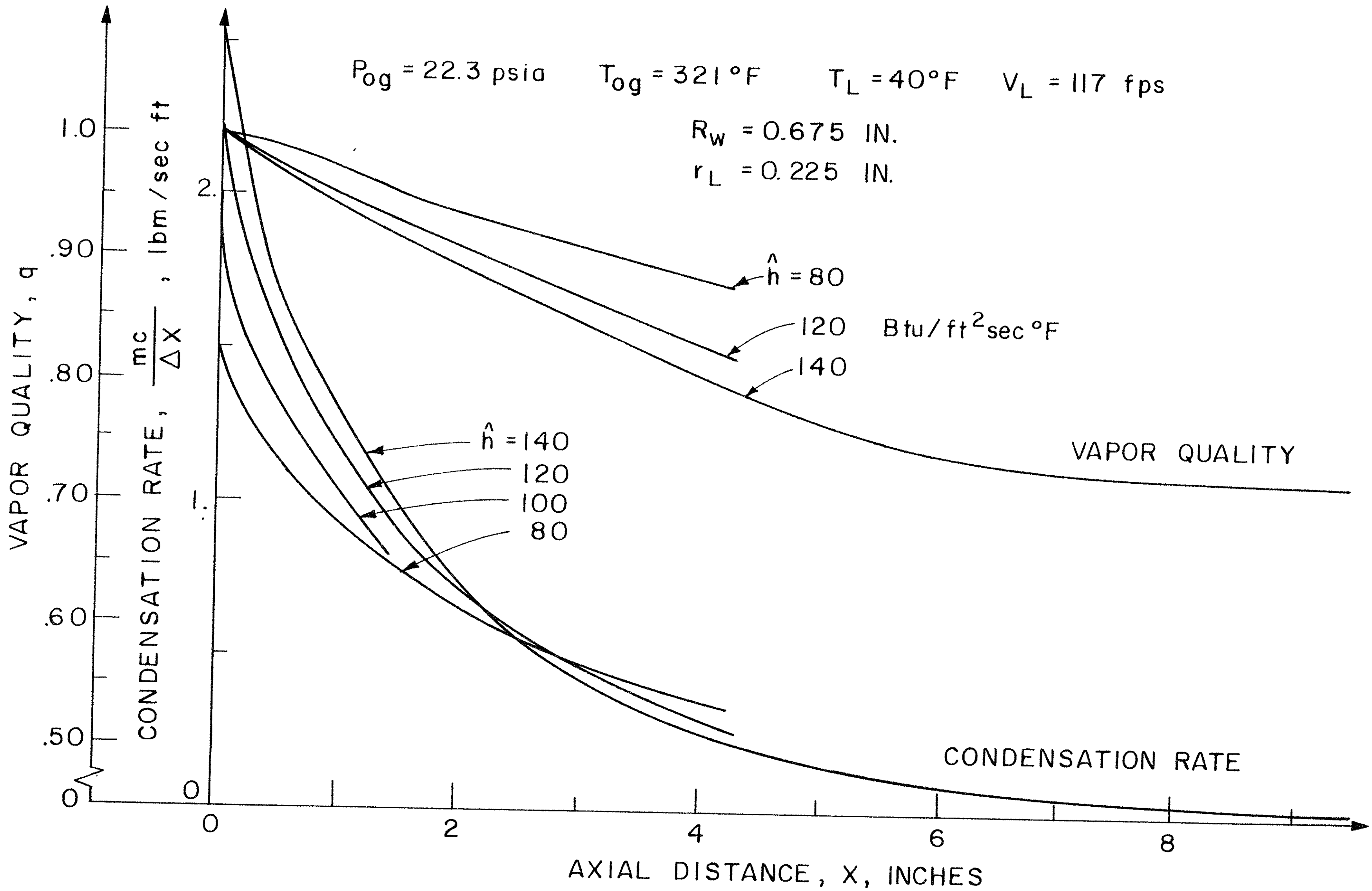

FIGURE 54 EFFECT OF HEAT TRANSFER COEFFICIENT ON AXIAL VARIATIONS OF VAPOR QUALITY AND CONDENSATION RATE - SLUG MODEL

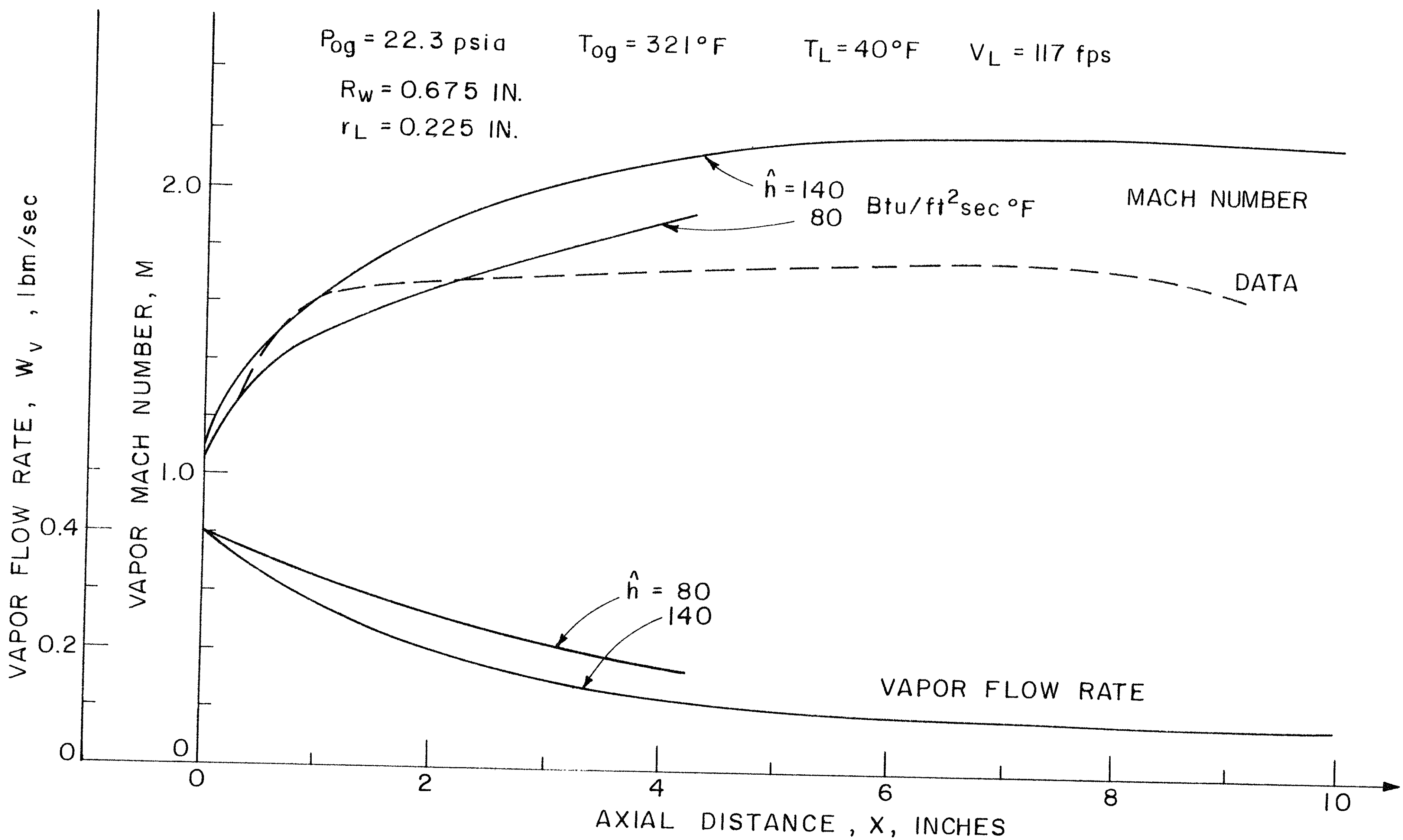

FIGURE 55 EFFECT OF HEAT TRANSFER COEFFICIENT ON AXIAL VARIATIONS OF VAPOR MACH NUMBER AND FLOW RATE – SLUG MODEL

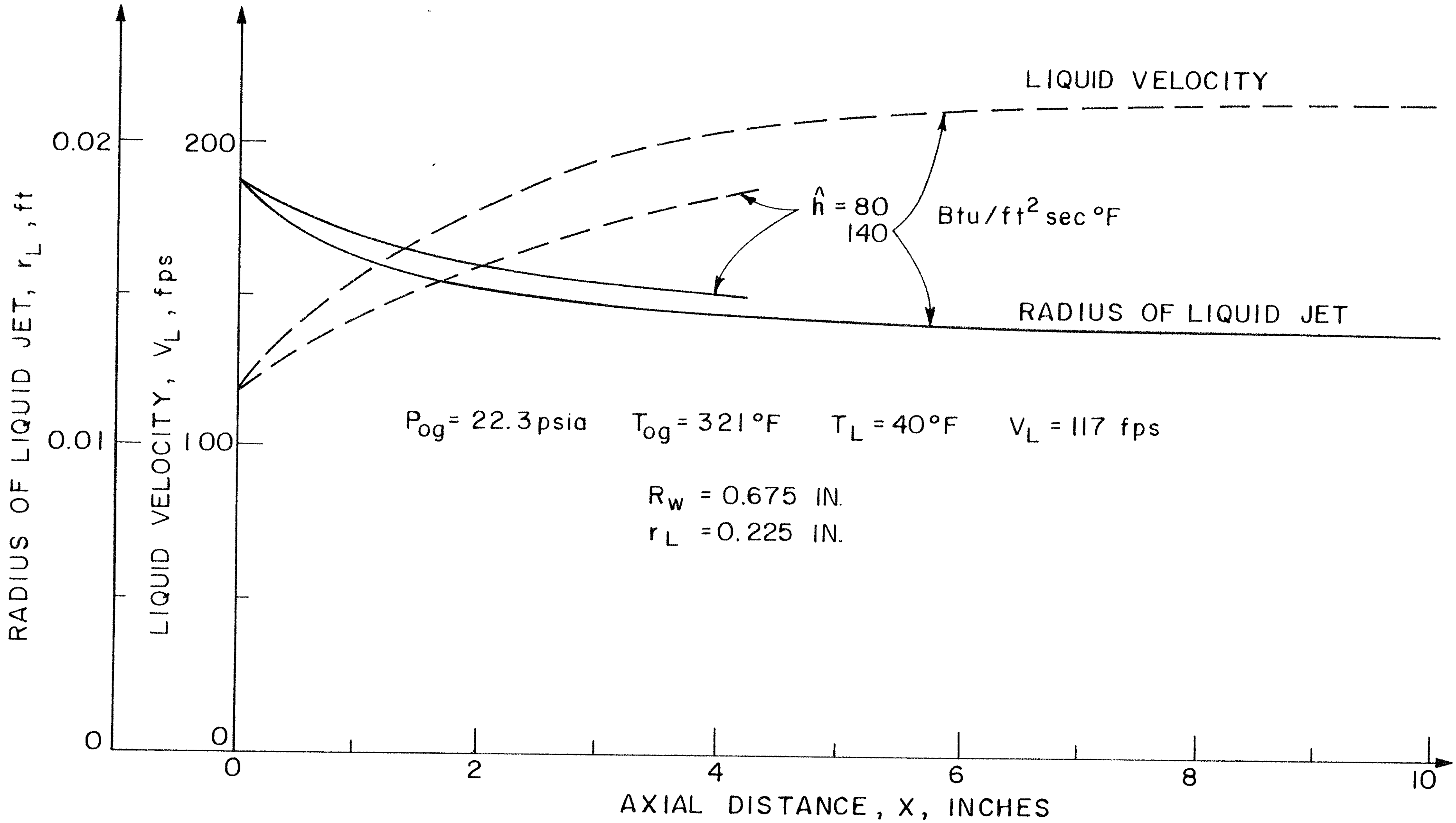

FIGURE 56 EFFECT OF HEAT TRANSFER COEFFICIENT ON AXIAL VARIATIONS OF LIQUID JET RADIUS AND LIQUID VELOCITY – SLUG MODEL

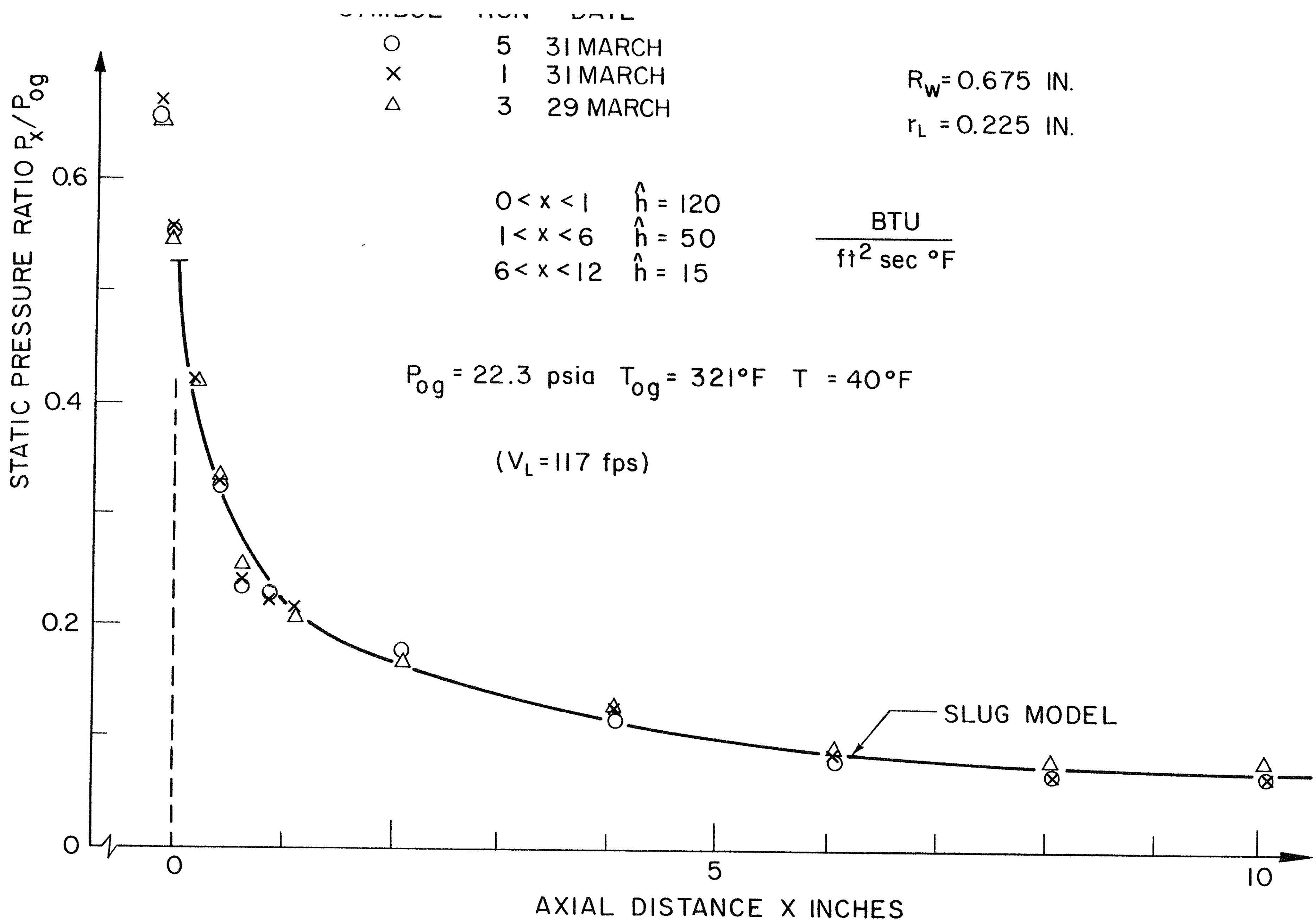

FIGURE 57 AXIAL VARIATION OF STATIC PRESSURE

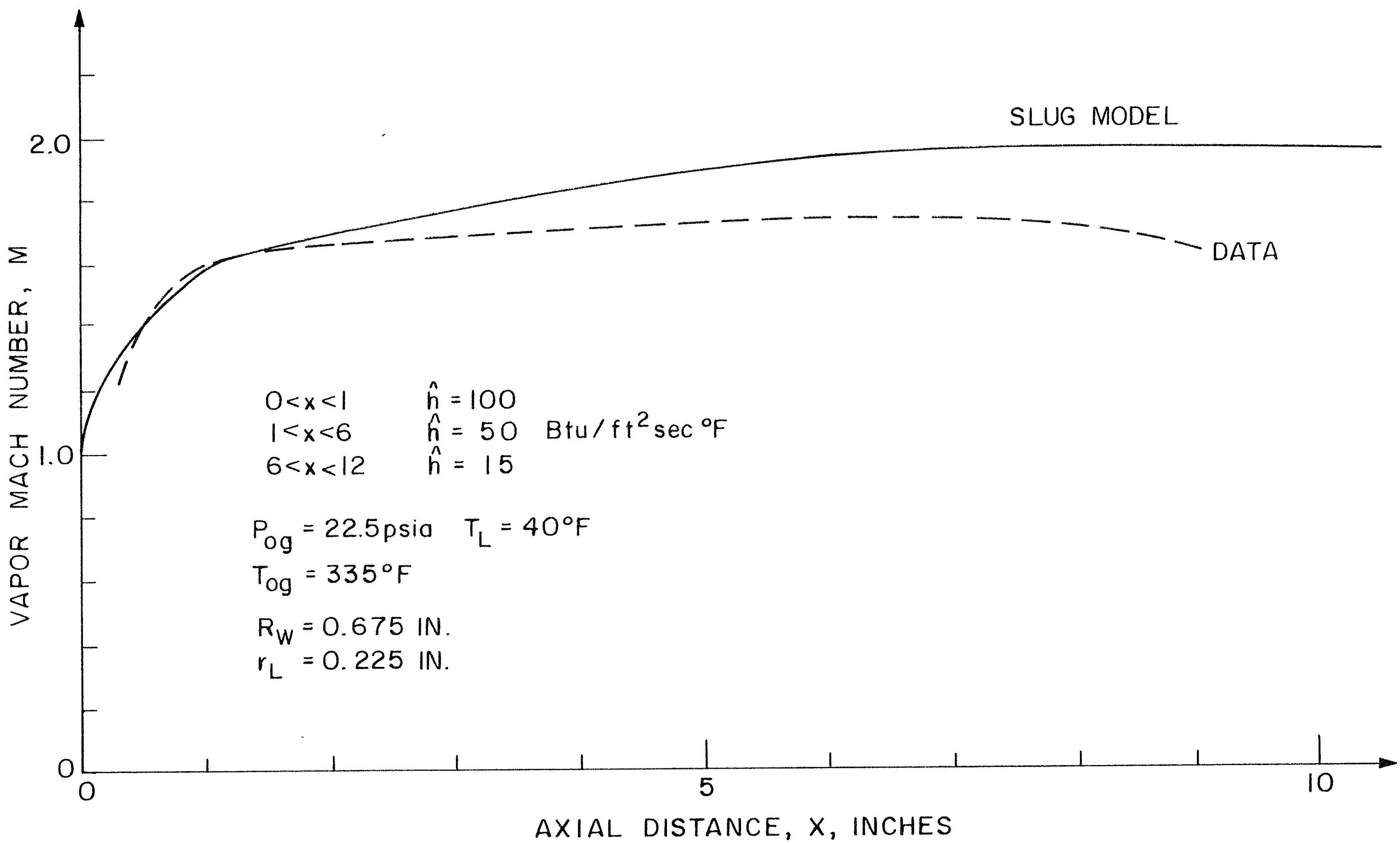

FIGURE 58 AXIAL VARIATION OF VAPOR MACH NUMBER (V_L = 117 fps)

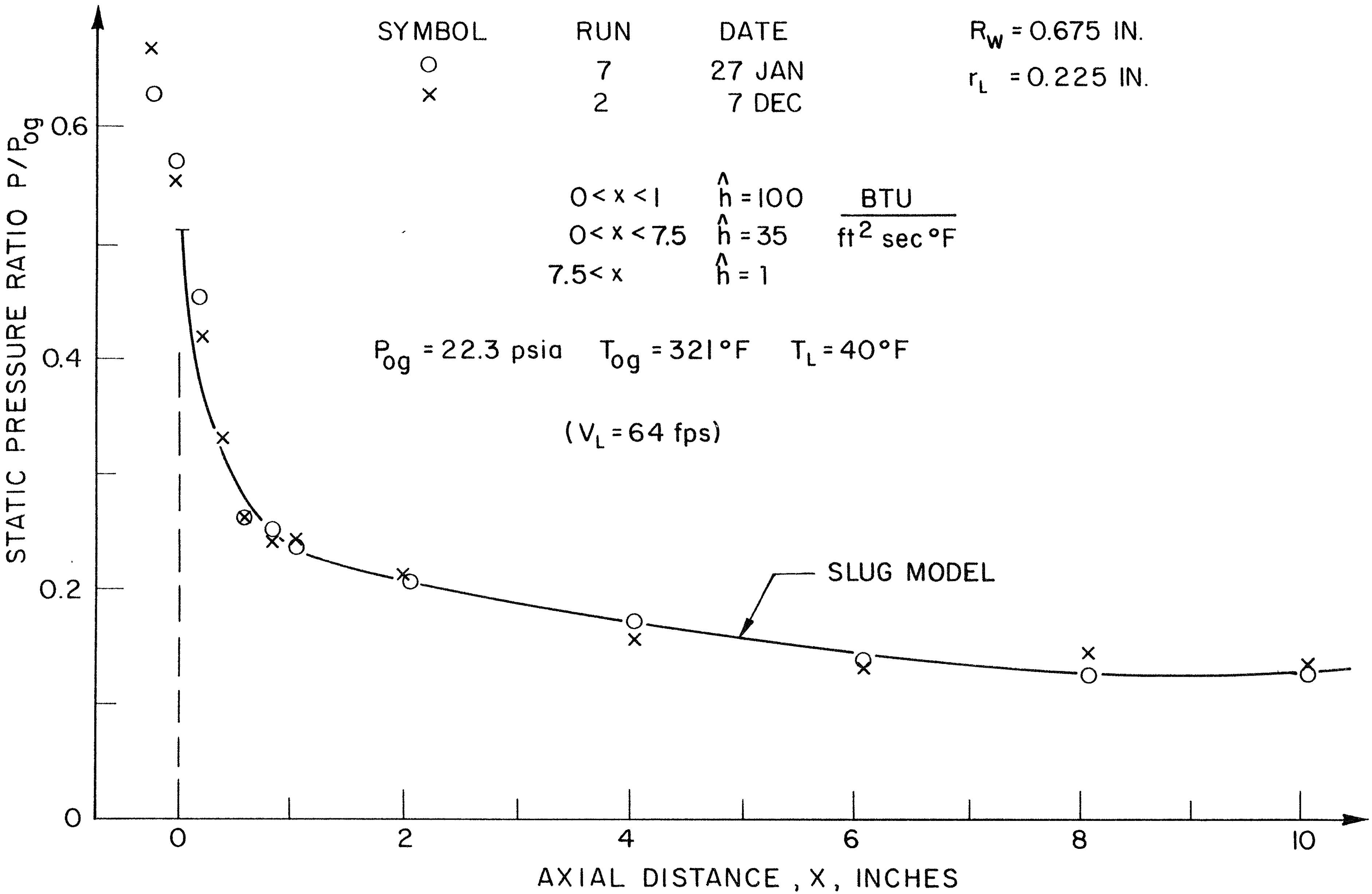

FIGURE 59 AXIAL VARIATION OF STATIC PRESSURE

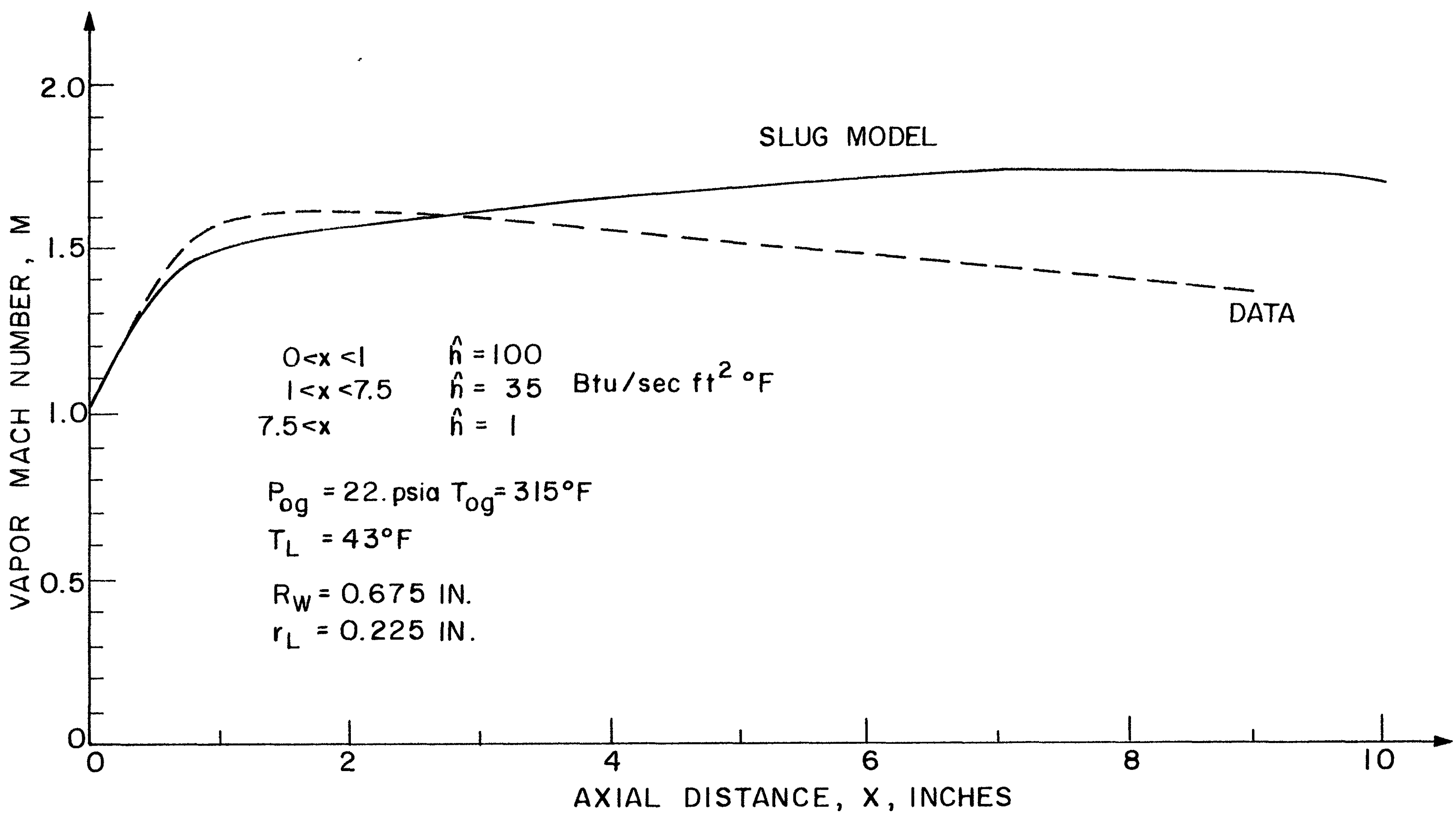

FIGURE 60 AXIAL VARIATION OF VAPOR MACH NUMBER (V_L = 64 fps)

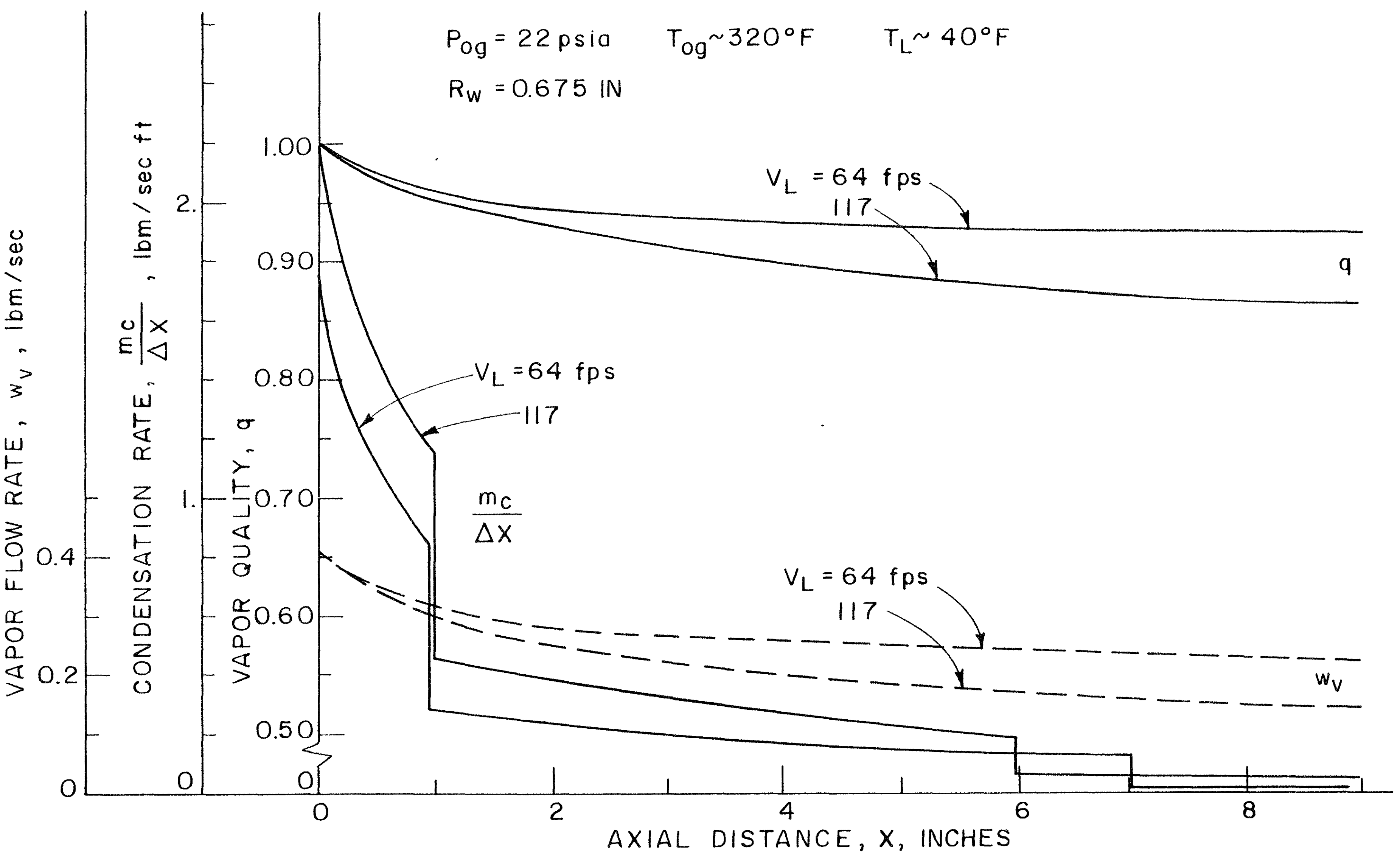

FIGURE 61 EFFECT OF INLET LIQUID VELOCITY ON AXIAL VARIATIONS OF VAPOR FLOW RATE, MASS QUALITY, AND CONDENSATION RATE – SLUG MODEL

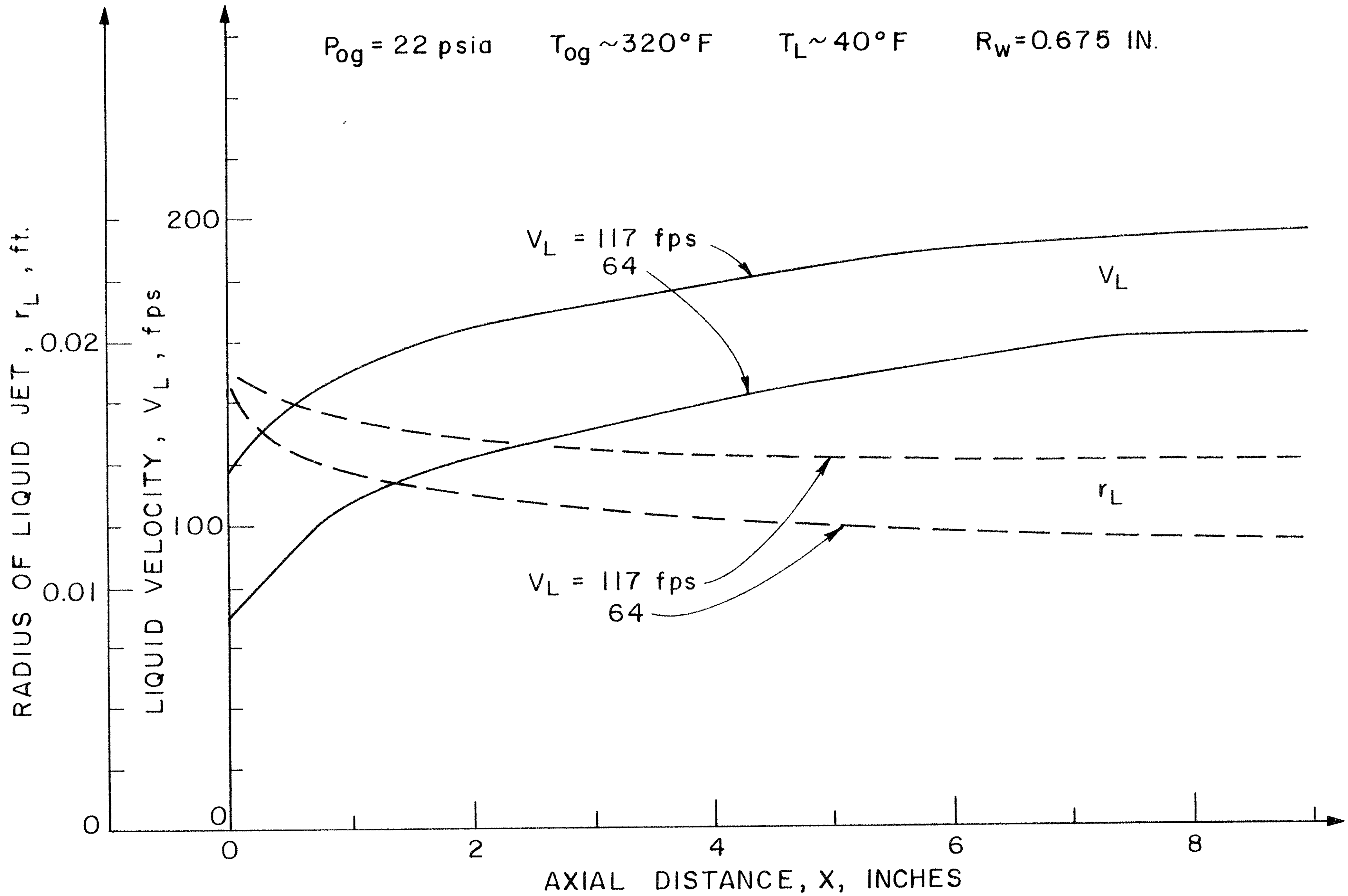

FIGURE 62 EFFECT OF INLET LIQUID VELOCITY ON AXIAL VARIATIONS OF LIQUID VELOCITY AND LIQUID JET RADIUS - SLUG MODEL

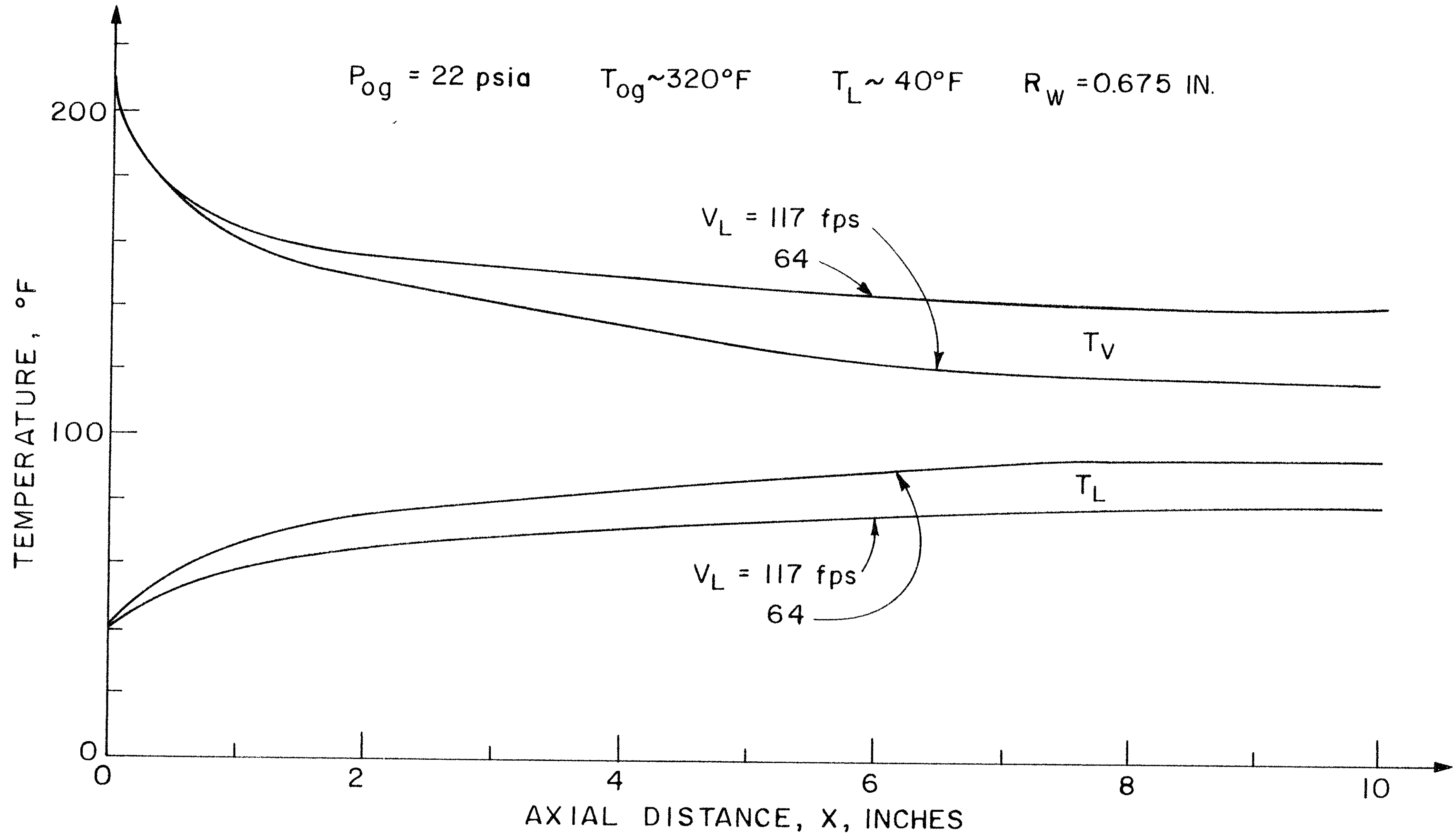

FIGURE 63 EFFECT OF INLET LIQUID VELOCITY ON AXIAL VARIATIONS OF LIQUID AND VAPOR TEMPERATURES - SLUG MODEL

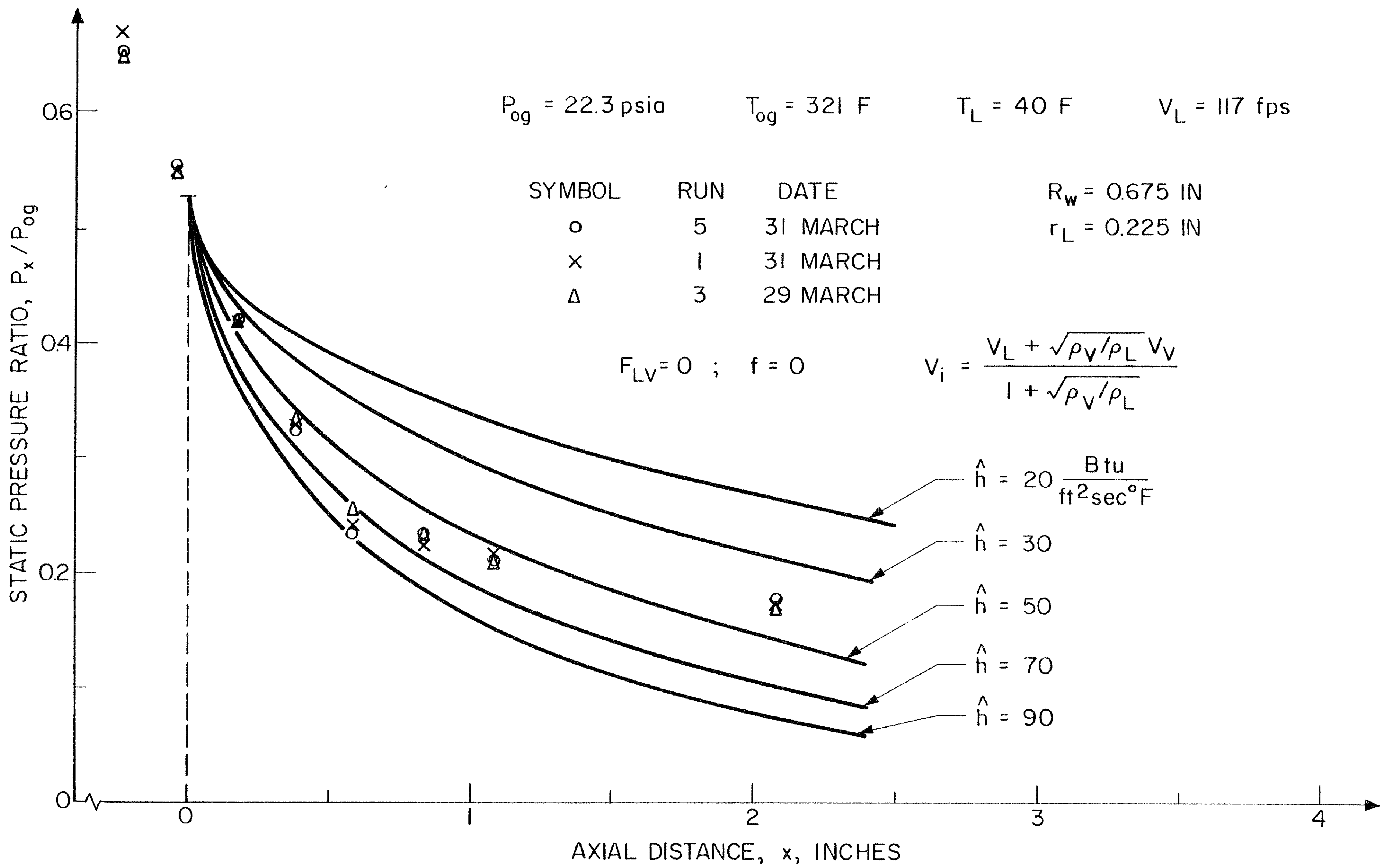

FIGURE 64 EFFECT OF HEAT TRANSFER ON STATIC PRESSURE DISTRIBUTION – SHEAR MODEL

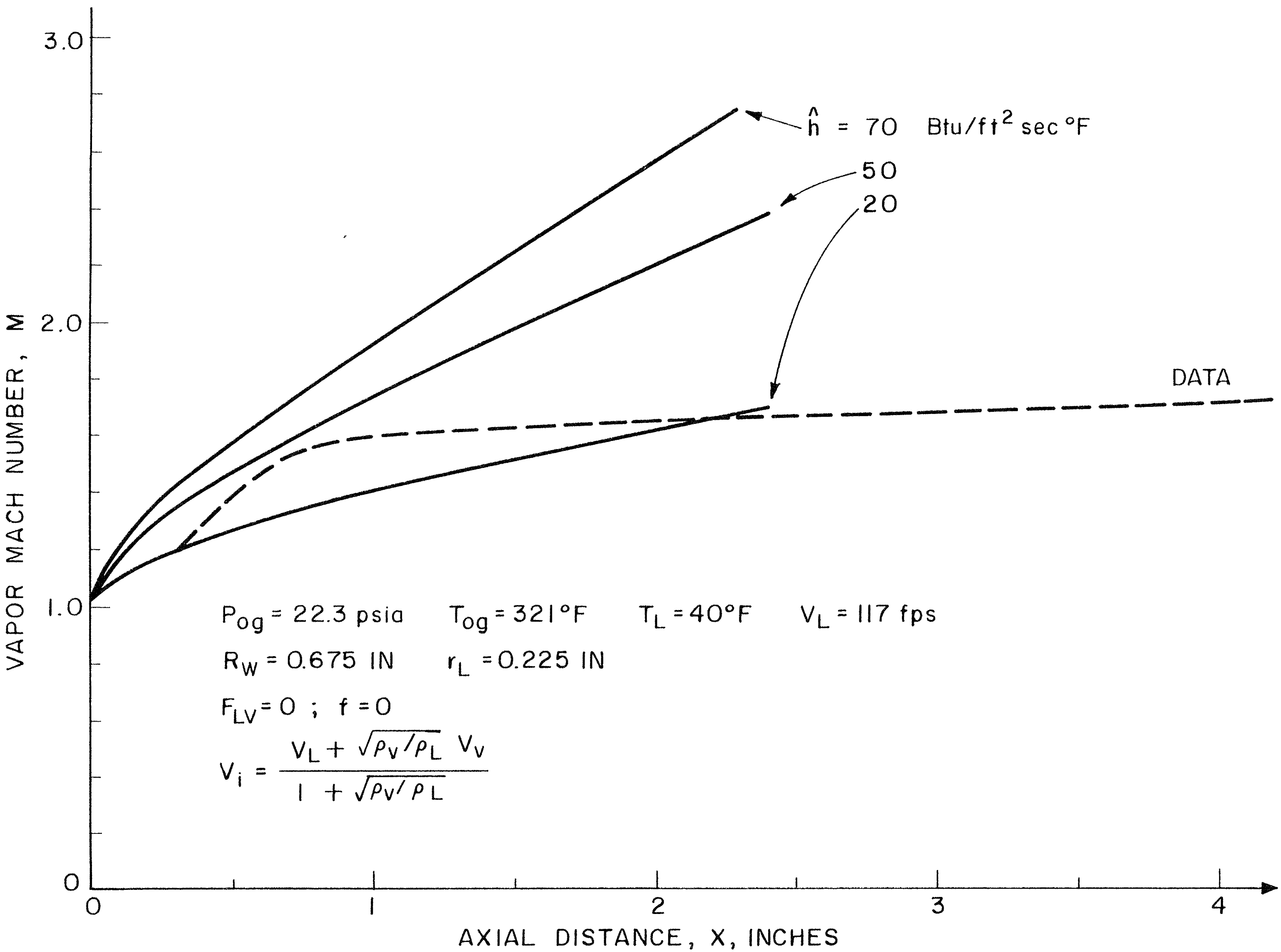

FIGURE 65 EFFECT OF HEAT TRANSFER ON VAPOR MACH NUMBER DISTRIBUTION - SHEAR MODEL

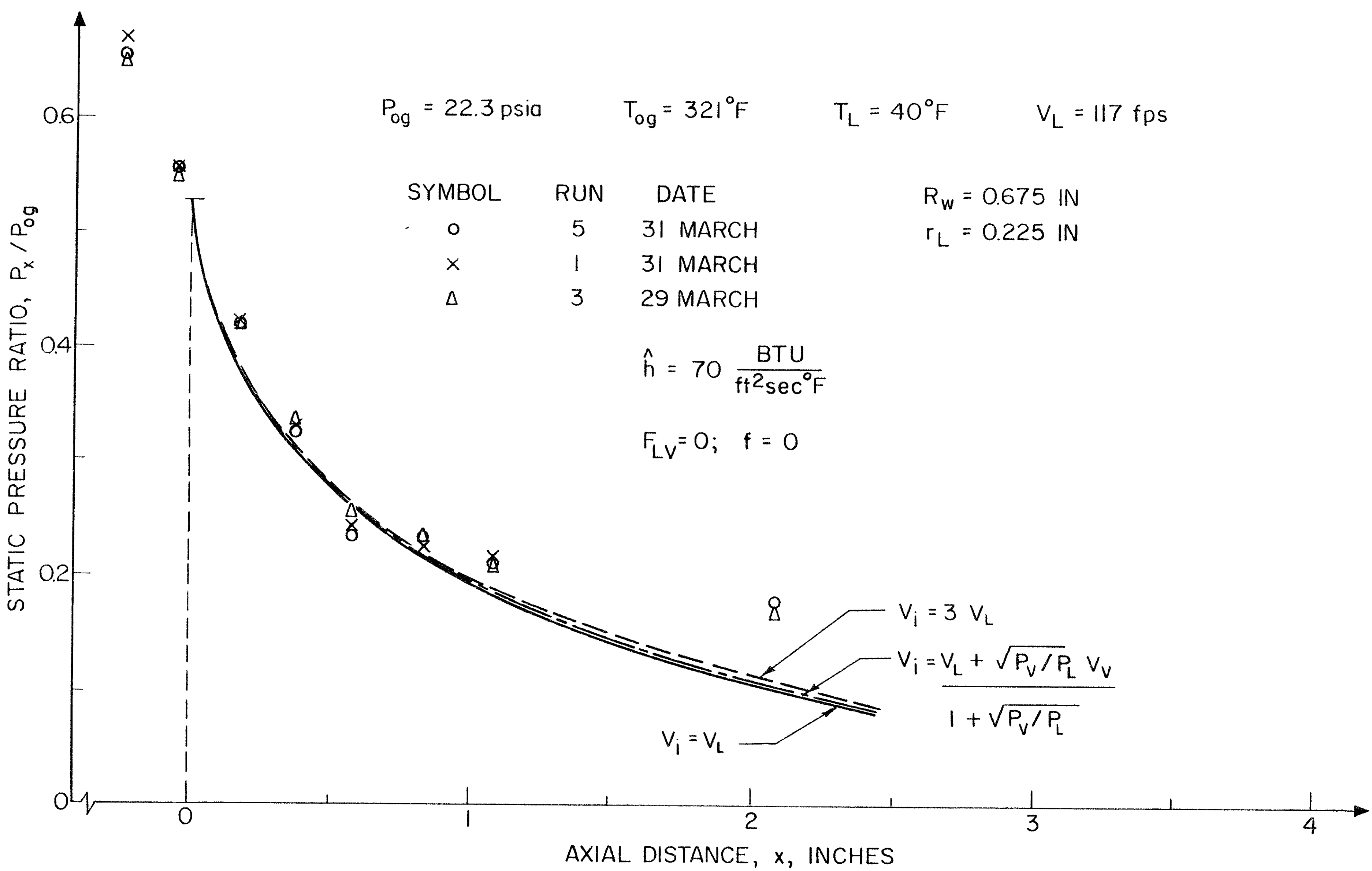

FIGURE 66 EFFECT OF INTERFACIAL VELOCITY ON STATIC PRESSURE DISTRIBUTION – SHEAR MODEL

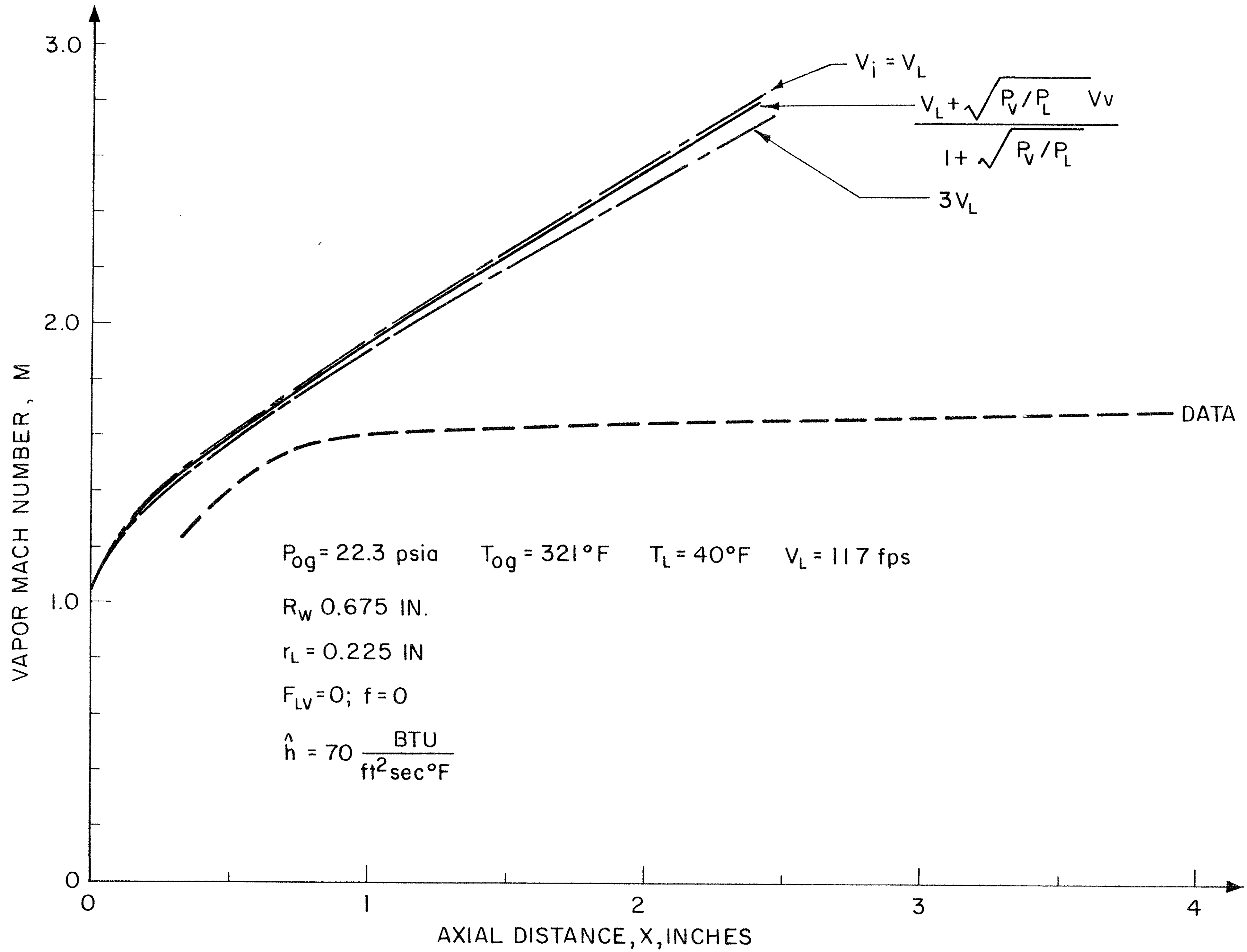

FIGURE 67 EFFECT OF INTERFACIAL VELOCITY ON VAPOR MACH NUMBER DISTRIBUTION – SHEAR MODEL

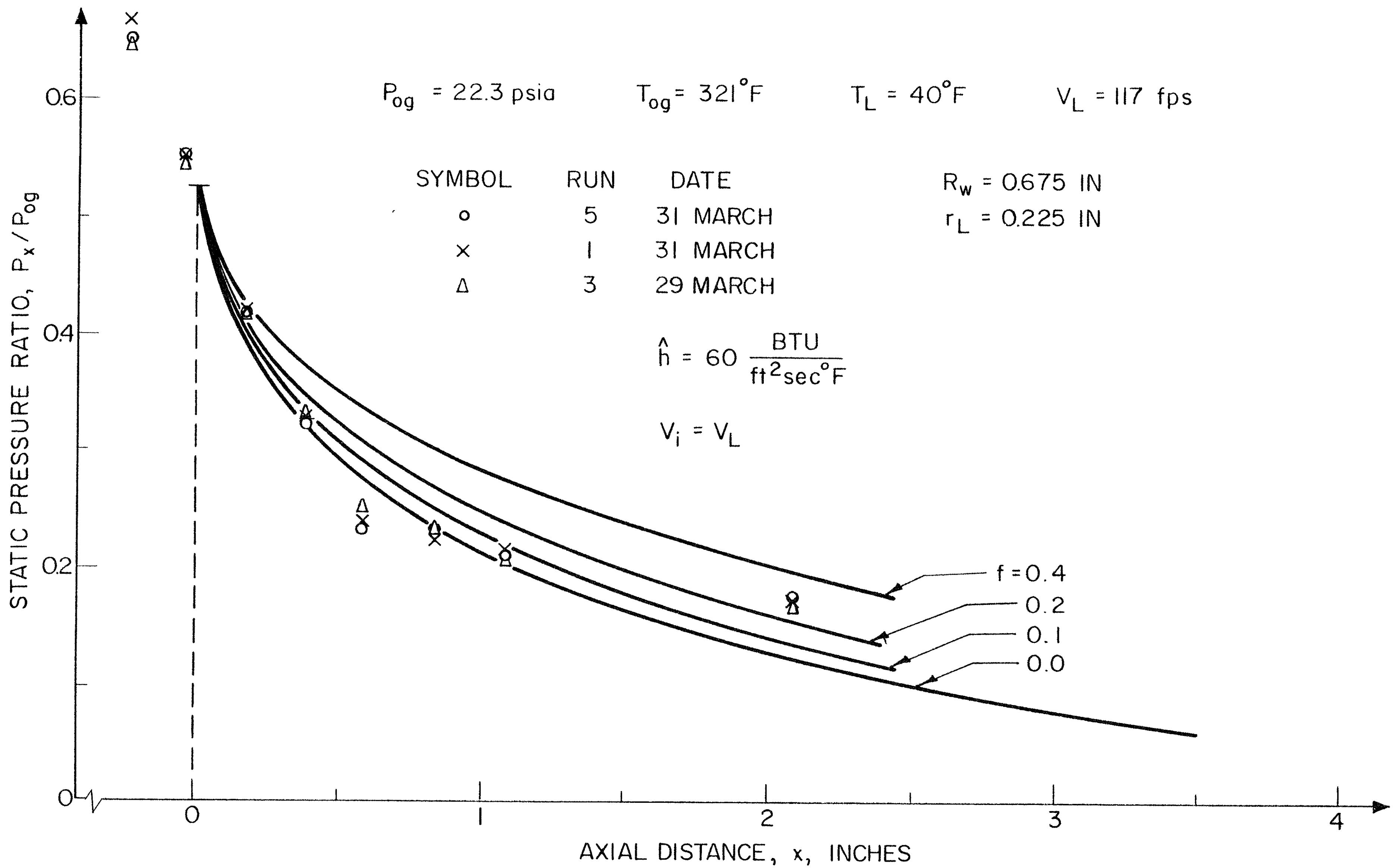

FIGURE 68 EFFECT OF INTERFACIAL SHEAR ON STATIC PRESSURE DISTRIBUTION – SHEAR MODEL

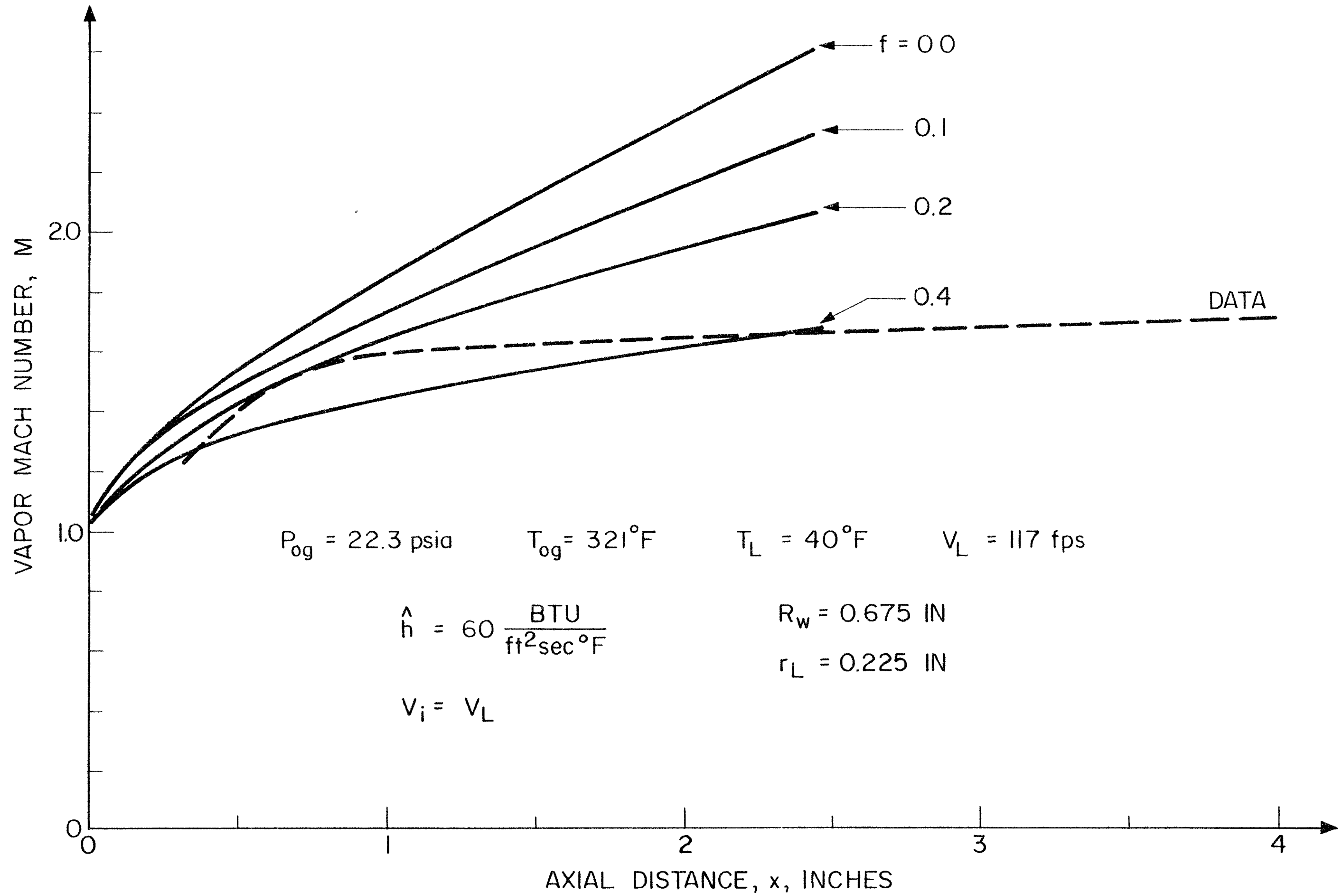

FIGURE 69 EFFECT OF INTERFACIAL SHEAR ON VAPOR MACH NUMBER DISTRIBUTION– SHEAR MODEL

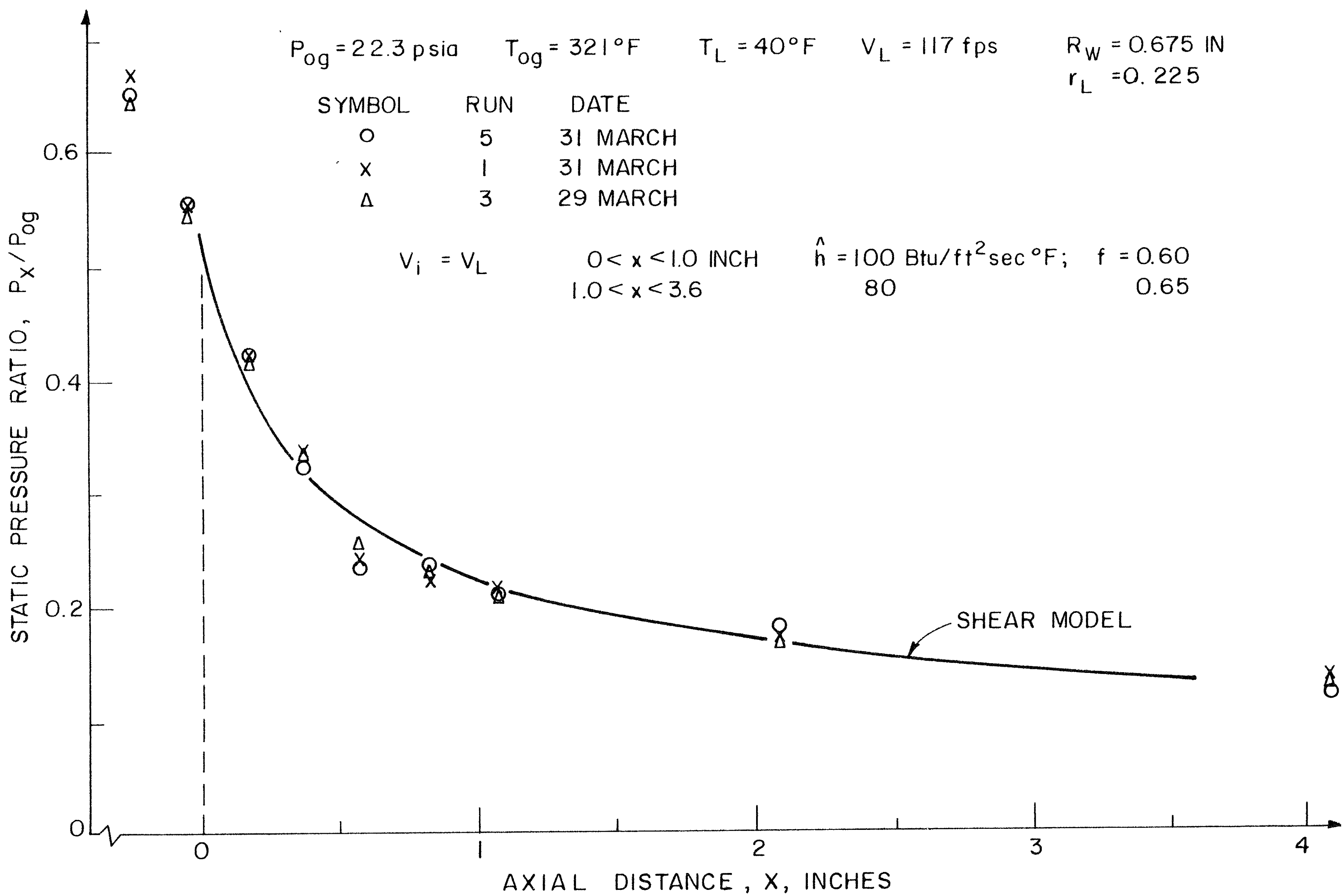

FIGURE 70 AXIAL VARIATION OF STATIC PRESSURE - SHEAR MODEL

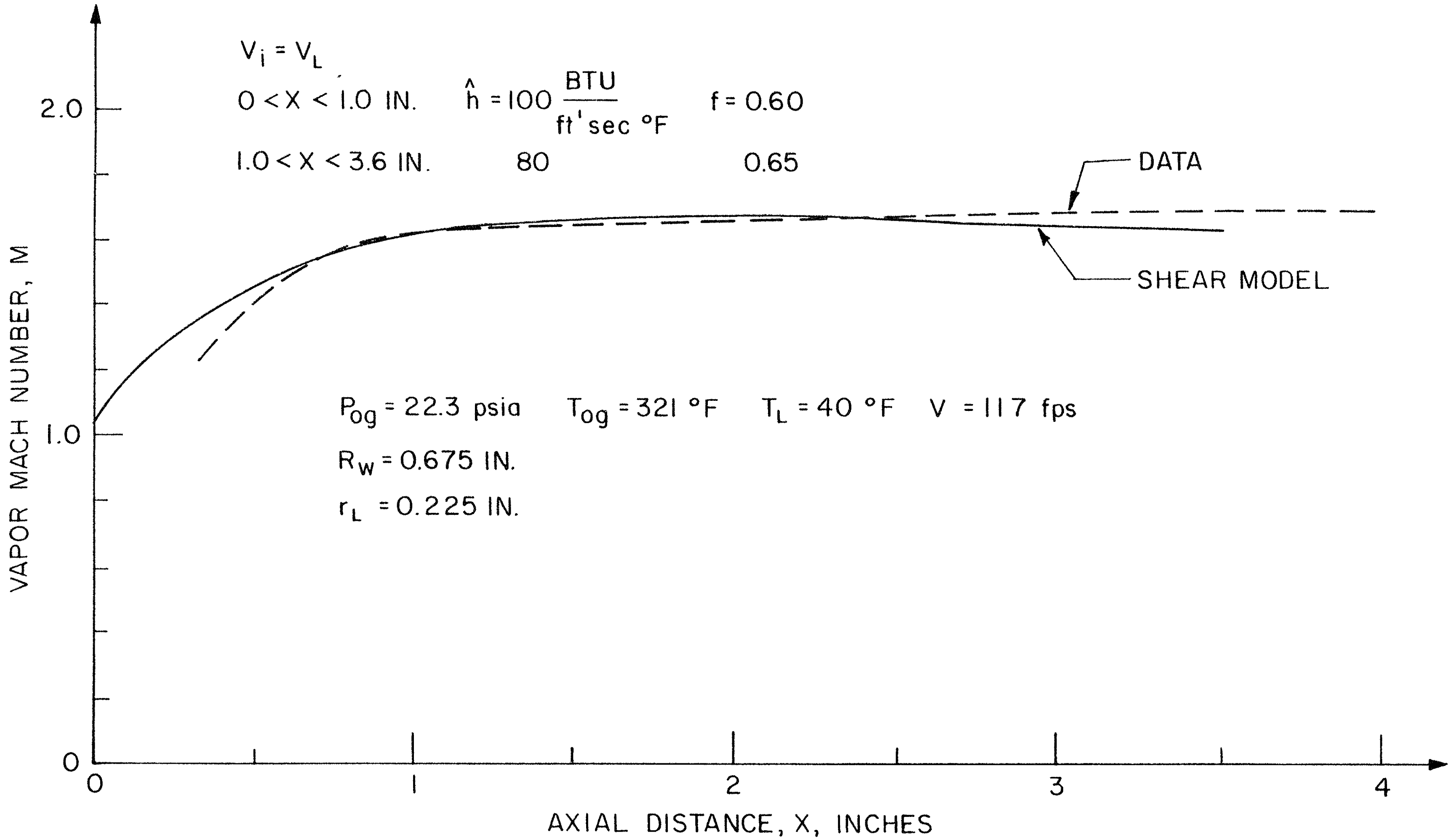

FIGURE 71 AXIAL VARIATION OF VAPOR MACH NUMBER-SHEAR MODEL